Fall 2020

Ocean-Atmosphere Interactions During Intraseasonal Oscillations in the Northern Indian Ocean

Heather Leigh Roman-Stork

OCEAN-ATMOSPHERE INTERACTIONS DURING INTRASEASONAL OSCILLATIONS IN THE NORTHERN INDIAN OCEAN

by

Heather Leigh Roman-Stork

Bachelor of Science
Boston College, 2016

Master of Science
Florida State University, 2018

Submitted in Partial Fulfillment of the Requirements

For the Degree of Doctor of Philosophy in

Marine Science

College of Arts and Sciences

University of South Carolina

2020

Accepted by:

Subrahmanyam Bulusu, Major Professor

Alexander Yankovsky, Committee Member

James L. Pinckney, Committee Member

Anthony Arguez, Committee Member

Cheryl L. Addy, Vice Provost and Dean of the Graduate School

DEDICATION

This dissertation is dedicated to my parents, Robin and Greg Roman-Stork, whose endless love and support have made this dissertation possible and who have always inspired me to be the best that I can be.

ACKNOWLEDGEMENTS

Thank you to all those who helped to make this dissertation possible. Thank you to my committee: Dr. Subrahmanyam Bulusu, my major advisor, Dr. Alexander Yankovsky, Dr. Jay Pinckney, and Dr. Anthony Arguez. In particular, thank you Subra for all your help through the years and all your hard work on my behalf. You always pushed me to be a better scientist and a better version of myself. I would also like to acknowledge and thank my coauthors, Dr. Subrahmanyam Bulusu, Dr. V.S.N. Murty, and Dr. Corinne Trott for their assistance and advice in preparing the bulk of this dissertation. Truly, this would not have been possible without you. Special thanks as well to Dr. Ebenezer Njadro for his patience and assistance in troubleshooting coding problems with me.

This research is supported through the United States Office of Naval Research's Oceanic Control of Monsoon Intraseasonal Oscillations in the Tropical Indian Ocean and the Bay of Bengal (MISO-BOB) Award #N00014-17-1-2468, awarded to my major professor, Dr. Subrahmanyam Bulusu. My PhD research was also partially funded by the NASA/South Carolina Space Grant Consortium's Graduate Research Assistantship for 2018-2019. Additional funding was provided by the University of South Carolina's School of the Earth, Ocean and Environment (SEOE).

I would also like to thank the Office of the Vice President of Research at the University of South Carolina for awarding me the 2020 Breakthrough Graduate Scholar award and SEOE for awarding me the 2020 Marine Science Award for Outstanding Publication.

As always, a special thank you to my parents, Robin and Greg Roman-Stork, for their unending support, love, and guidance and for always being there for me when I needed them. Finally, I would like to thank my friends and colleagues in the Satellite Oceanography Lab—Corinne Trott, Brady Ferster, Casey Shoup, Rachel Nichols, and Ricky Brokaw— for their patience and advice, scientifically and otherwise, and for always agreeing to be my taste testers for new baked goods.

ABSTRACT

The Indian Ocean and the monsoon system are dynamically complex. In the Bay of Bengal (BoB) and southeastern Arabian Sea (SEAS), surface circulation is strongly influenced by the monsoons and notable local eddying that modulates the East India Coastal Current (EICC). In this study, the role of freshwater transported from the BoB into the SEAS in determining both the timing of monsoon onset and the strength of the ensuing monsoon is examined. It is found that the long-term decrease in moisture flux from the sea surface and freshwater transport into the SEAS, along with a rise in upper ocean heat content (OHC) over a 15-year duration after 1994, contributed to the lack of strong monsoons in recent years; the prevailing interannual and interdecadal variability in these parameters associated with the Indian Ocean Dipole (IOD) and El Niño Southern Oscillation (ENSO) events favored weaker and normal monsoons after 1994 until the strong monsoon of 2019. Both ENSO and the IOD are also found to modulate coastal Kelvin wave and Rossby wave propagation in the BoB, which impacts the mesoscale eddy field in the EICC region and further influences the precipitation associated with these eddies.

Intraseasonal oscillations (ISOs) significantly contribute to and modulate Indian monsoon rainfall. Satellite observations are used to monitor the 30-90-day, 10-20-day, and 3-7-day ISOs, and how they influence local atmosphere and ocean dynamics in the BoB. This research has shown the importance of using blended satellite altimetric observations and satellite-derived salinity to monitor ISOs in the BoB Indian Ocean. A multivariate

analysis of the atmospheric 10-20-day mode is further conducted to both assess its overall characteristics in multiple oceanic variables and analyze how this atmospheric signal interacts with the underlying ocean. Temperature is notably found to have a strong biweekly signal in the central and southern BoB down to 250 m, with the mixed layer temperature showing a marked decrease after the 10-20-day precipitation maximum. This study has shown the 10-20-day mode in the atmosphere to heavily influence ocean dynamics, emphasizing the importance of continued modeling and satellite observation efforts for the monitoring and forecasting of these events.

TABLE OF CONTENTS

LIST OF TABLES

LIST OF FIGURES

CHAPTER 1

INTRODUCTION

1.1 DESCRIPTION OF THE RESEARCH AREA

The Indian Ocean is one of the most dynamically complex and unique basins in the globe. While this dissertation encompasses oceanic and atmospheric processes that extend into the South China Sea, Western Pacific, and southern Indian Ocean, the bulk of this research is focused in the northern Indian Ocean, in particular the eastern Arabian Sea and Bay of Bengal (Figure 1). One of the primary features that makes the Indian Ocean so unique is that the winds and currents are seasonally reversing with the monsoons (Schott & McCreary, 2001). The Indian Monsoon system is a highly air-sea-land coupled system that consists of two monsoons: the northeast monsoon, which occurs from December to February, and the southwest monsoon, which occurs from June through September, where the monsoons are so named for the dominant wind direction over India. These monsoons dominate the dynamics in the Indian Ocean, particularly in the northern Indian Ocean (Schott & McCreary, 2001).

The two major basins in the northern Indian Ocean are the Arabian Sea and the Bay of Bengal. The Arabian Sea in an evaporation dominated basin characterized by high salinity, energetic eddying, and high biological productivity (Schott & McCreary, 2001; Trott et al., 2019). By contrast, the Bay of Bengal is a comparatively fresh basin with notably low saline waters in the northern Bay and Andaman Sea, where some of the world's

largest rivers regularly contribute freshwater (Schott & McCreary, 2001; Ramachandran et al., 2018). Eddying in the Bay of Bengal is largely concentrated along the East India Coastal Current (EICC), the western boundary current in the Bay, and around the Andaman and Nicobar Islands (Patnaik et al., 2014; Dandapat & Chakraborty, 2016; Cheng et al., 2018). The Arabian Sea and Bay of Bengal exchange waters around the tip of India and Sri Lanka seasonally, where high salinity water is transported by the West India Coastal Current (WICC) and other currents into the Bay of Bengal during the southwest monsoon season, and low salinity water from the Bay is transported by the EICC and the North Equatorial Current (NEC) into the Arabian Sea during the northeast monsoon season (Figure 1; Schott & McCreary, 2001; Shenoi et al., 1999). This salinity exchange between these basins heavily impacts local dynamics and in particular plays a key role in the onset of the southwest monsoon.

1.2 Overview of Southwest Monsoon Onset

The southwest monsoon onsets in climatology on June 1 over the southwestern state of Kerala (pink star in Figure 1), although this onset varies by as much as 1-2 weeks interannually (Wang et al, 2009). The timing and strength of monsoon onset is critically important to forecast as this has dire implications for agriculture, economics, and the well-being of over a billion people in India and neighboring countries. Onset is an air-sea-land coupled process and understanding the ocean dynamics involved is a major focus of this dissertation.

Oceanic processes leading to southwest monsoon onset begin in October and November of the previous year in the Bay of Bengal (Shenoi et al., 1999). At this time, the

second downwelling Kelvin wave arrives in the Bay and continues around the coast of the Bay as a coastal Kelvin wave. This coastal Kelvin wave interacts with the EICC and can help weaken or strengthen its propagation and transport of low salinity waters out of the Bay, depending on factors that include the phase of the Indian Ocean Dipole (IOD) and El Niño-Southern Oscillation (ENSO), which impact the equatorial wind stress perturbations that trigger Kelvin wave propagation (Rao et al., 2010; Nienhaus et al., 2012). By December, the low salinity water carried by the EICC reaches Sri Lanka and the tip of India and is then transported by the EICC and NEC into the southeastern Arabian Sea by January (Figure 1), where it creates a fresh pool (Shenoi et al., 1999). The Lakshadweep High (LH), an anticyclonic circulation in the Lakshadweep Sea, helps to circulate this freshwater into the southeastern Arabian Sea. The timing, strength, and position of the LH helps to determine the extent of this fresh pool and how confined the freshwater is to the coast. The fresh pool in the southeastern Arabian Sea allows for the development of a barrier layer (a layer embedded in the isothermal layer and below the mixed layer) in this region, that can be as thick as 60 m, which in turn prevents entrainment cooling and allows for local sea surface temperatures (SSTs) to increase dramatically (Nyadjro et al., 2012; Shenoi et al., 1999).

These SSTs can reach temperatures in excess of 30ºC, which leads to the development of the Arabian Sea Mini Warm Pool (ASMWP) during March and April (Chacko et al., 2012; Deepa & Oh, 2014; Nyadjro et al., 2012; Rao et al., 2015; Vinayachandran & Shetye, 1991). The ASMWP is a subset of the larger Indian Ocean warm pool and equatorial Indian Ocean (Vinayachandra & Shetye, 1991), and it has been shown to impact the onset and strength of the southwest monsoon (Deep & Oh, 2014;

Neema et al., 2012; Vinayachandran et al., 2007). The ASMWP's exceptionally high SSTs create the conditions necessary for an aggregation of heat and moisture necessary for monsoon onset and the genesis of the monsoon onset vortex in May, which then allows for the monsoon to onset in climatology around June 1 (Shenoi et al., 1999). For this reason, it is crucial that the freshwater transport into the southeastern Arabian Sea and related mixed layer dynamics are more fully understood so that monsoon onset forecasting can be improved.

1.3 Intraseasonal Oscillations

While the onset of the southwest monsoon is extremely important to forecast, it is not the only determiner of monsoon strength and timing. Intraseasonal oscillations (ISOs) heavily impact southwest monsoon rainfall over the Indian subcontinent and modulate the active (flood) and break (drought) phases of the monsoon. Of these ISOs, the most prominent are the Madden Julian Oscillation (MJO), Boreal Summer Intraseasonal Oscillation (BSISO), quasi-biweekly oscillation, and oscillations in the monsoon trough.

The MJO is the dominant mode of intraseasonal variability in the tropics, impacting not just southwest monsoon variability, but tropical cyclone activity and weather globally. The MJO is characterized by alternating phases of eastward propagating enhanced and suppressed convection along the equator (Zhang, 2005; Wheeler & Hendon, 2004; Straub, 2013). The MJO occurs on a 30-90-day timescale, has a phase speed of 5 m/s, wavelength of 10,000 km, and impacts monsoon onset, rainfall, and other tropical systems, including ISOs, in the Indian Ocean (Zhang, 2005). While the MJO may propagate around the globe, it is most often generated in the western or central Indian Ocean by a downwelling Rossby

wave (Webber et al., 2010; 2012). Although it is eastward propagating, it often releases a northward propagating branch, often referred to as the BSISO or monsoon intraseasonal oscillation (MISO), which has both 30-60-day and 15-30-day modes and is characterized by a northward propagating system of convection, usually in the Bay of Bengal (Vecchi & Harrison, 2002; Krishnamurti et al., 2017).

The 10-20-day quasi-biweekly mode consists of a westward-propagating meridional double-cell structure in the Bay of Bengal, where the northernmost cell is centered on 15-20ºN and the southernmost cell is centered around the equator (Chatterjee & Goswami, 2004). The northernmost cell is generated by a breaking Rossby wave in the upper atmosphere in the South China Sea or Western Pacific (Ortega et al., 2017) before propagating westward into the Bay of Bengal. The southernmost cell is generated in the Indian Ocean and the two cells become phase-locked around the Bay of Bengal before propagating westward over India, contributing to monsoon rainfall, and reaching its demise in the Arabian Sea and southern Indian Ocean (Chatterjee & Goswami, 2004; Kikuchi & Wang, 2009). The 10-20-day mode has a phase speed of 4.5-6 m/s and a wavelength of 6,000 km (Chatterjee & Goswami, 2004; Chen & Chen, 1993).

The 3-7-day ISO consists of oscillations in the monsoon trough and serves as the primary control on the active and break phases of the southwest monsoon (Krishnamurti & Bhlame, 1976; Subrahmanyam et al., 2020). This 3-7-day mode is primarily centered over India and the northern Bay of Bengal but can have significant impacts on mixed layer dynamics in the entire Bay of Bengal (Subrahmanyam et al., 2020). The 3-7-day mode is heavily influenced by the other ISOs, especially the MJO, and this influence varies regionally. While its regional and temporal influence is small compared to other ISOs, the

3-7-day ISO is associated with more precipitation and can have devastating impacts on flooding and droughts in the southwest monsoon region.

While there has been extensive research into the atmospheric components of these ISOs, far less attention has been paid to the oceanic components. As ISOs are all highly air-sea coupled phenomena, it is vital that a further understanding of these oceanic processes is developed, and this serves as a major motivator for this dissertation.

1.4 Outline of the Dissertation

There are five additional chapters in this dissertation. Chapter 2 is entitled "The Role of Salinity in the Southeastern Arabian Sea in Determining Monsoon Onset and Strength" and is published in *Journal of Geophysical Research: Oceans*. This chapter uses reanalysis data from 1980 to 2016 in order to understand how freshwater fluxes and mixed layer processes in the southeastern Arabian Sea impacted the timing and strength of the southwest monsoon during this time. Trends in various oceanic and atmospheric parameters are analyzed during this time in order to understand the drought in strong monsoons between 1994 and 2019.

Chapter 3 is entitled "Monitoring Intraseasonal Oscillations in the Indian Ocean using Satellite Observations" and is published in *Journal of Geophysical Research: Oceans*. This study uses satellite observations from NASA's Soil Moisture Active Passive (SMAP) mission and blended altimetry, in conjunction with precipitation and surface wind, in order to further our understanding of ISO dynamics in the Indian Ocean. Additionally, this study aims to understand to what extent various remotely sensed oceanic parameters can capture these ISO signals.

Chapter 4, “Quasi-biweekly oscillations in the Bay of Bengal in observations and model simulations,” and is published in the Bay of Bengal special issue of *Deep Sea Research: Part II*. This chapter analyzes the 10-20-day ISO in the Bay of Bengal using a combination of satellite observations and ocean model simulations from the Nucleus for European Modeling of the Ocean (NEMO). The overall propagation of this ISO in the Bay is analyzed, as well as how the atmospheric ISO is translated into the Bay.

Chapter 5 is entitled, “Mesoscale Eddy Variability and its Linkage to Deep Convection over the Bay of Bengal using Satellite Altimetric Observations,” and is published in the 25 Years of Altimetry special issue of *Advances in Space* Research. This chapter endeavors to characterize the mesoscale eddy field in the Bay of Bengal as well as connect eddy processes to observed patterns of atmospheric convection in the Bay. To do this, an automatic eddy tracking algorithm is applied to daily blended sea level anomalies derived from altimetry from 1993 to 2018.

Finally, Chapter 6 presents the major conclusions of this dissertation, summarizing the findings of Chapters 2-5.

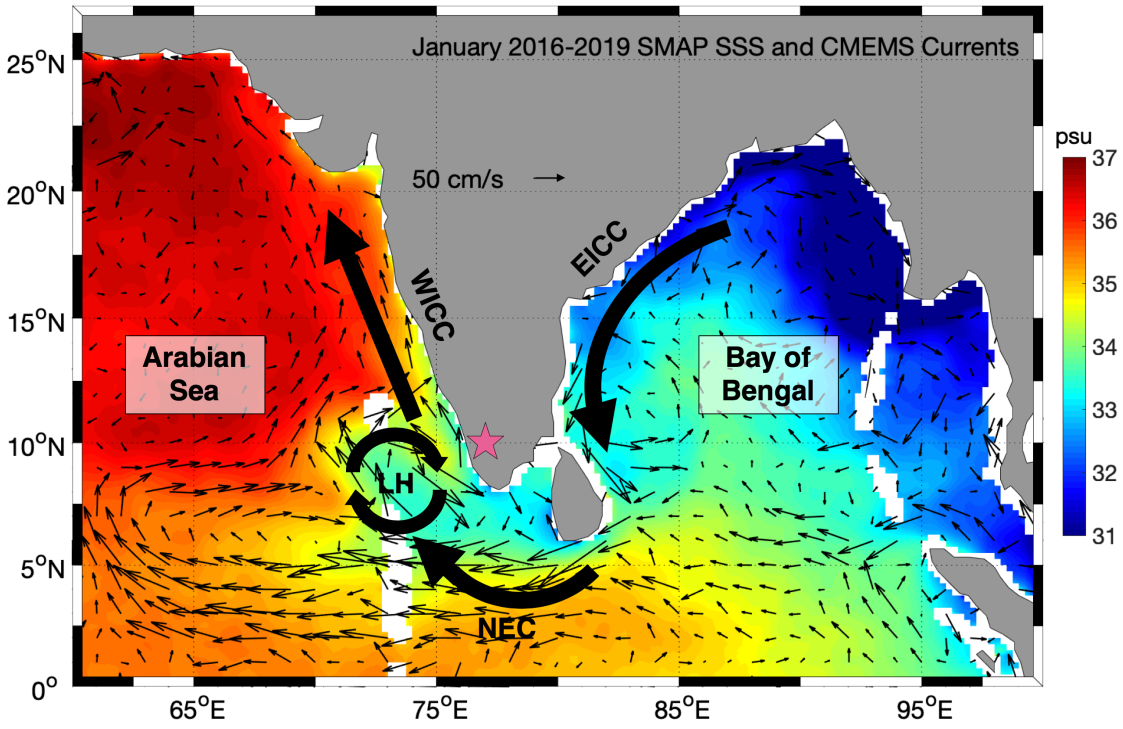

Figure 1.1. Monthly average sea surface salinity (SSS) from NASA's Soil Moisture Active Passive (SMAP; shaded; psu) overlaid with geostrophic currents derived from CMEMS blended altimetry (think black vectors; cm/s) for January 2016-2019. Major surface features are indicated by thick black vectors: The East India Coastal Current (EICC), West India Coastal Current (WICC), North Equatorial Current (NEC), and Lakshadweep High (LH). The pink star indicates the relative location of Kerala, India where the southwest monsoon onsets.

CHAPTER 2

THE ROLE OF SALINITY IN THE SOUTHEASTERN ARABIAN SEA IN DETERMINING MONSOON ONSET AND STRENGTH[1]

[1]Roman-Stork, H.L., B. Subrahmanyam, and V.S.N. Murty (2020). The Role of Salinity in the Southeastern Arabian Sea in Determining Monsoon Onset and Strength. Journal of Geophysical Research: Oceans, 125, https://doi.org/10.1029/2019JC015592.

ABSTRACT

In this study, we examine the role of freshwater transported from the Bay of Bengal (BoB) into the southeastern Arabian Sea (SEAS) in determining both the timing of monsoon onset and the strength of the ensuing monsoon. To do this, we use a combination of satellite-derived salinity data and reanalysis products from 1980 to 2016 in order to discuss seasonal, interannual, sub-decadal and long-term decadal variability in various atmospheric and oceanic contributors such as ocean heat content (OHC), freshwater transport, ERA5 instantaneous moisture flux, mixed layer depth (MLD) and barrier layer thickness (BLT). The salt budget in the SEAS reveals the dominance of meridional freshwater advective transport that brings in variability in salinity and thus in salinity stratification, as well as in mixed layer processes. We find that these parameters exhibit the prevalence of a long-term decadal variability (with trends of increasing/decreasing phases over a 15-year duration) over which interannual (3-year trend) and interdecadal (7-year trend) variability trends are superimposed. The patterns of both the 3- and 7-year trends follow each other closely and relatively high amplitudes are seen in the 3-year trends. The long-term decrease in moisture flux and freshwater transport into the SEAS along with a rise in OHC over a 15-year duration after 1994 contributed to a lack of strong monsoons in recent years; the prevailing interannual and interdecadal variability in these parameters associated with the Indian Ocean Dipole (IOD) and El Niño Southern Oscillation (ENSO) events favored weaker and normal monsoons after 1994.

2.1 INTRODUCTION

The Indian monsoon system is one of the most complex meteorological phenomena in the world and directly impacts the lives of over a billion people, the global climate, and world economy. Given its incredible importance, it is critical that we understand the dynamics and characteristics of this coupled land-ocean-atmosphere phenomenon. The southwest monsoon that occurs from June to September in climatology is responsible for the most rainfall over Indian subcontinent. Monsoon onset over Kerala (MOK) occurs on June 1 in climatology, but there is a great deal of interannual variation, usually within a week or so (Wang et al., 2009). Given the importance of the southwest monsoon, a great deal of research has been dedicated to improving our forecasting of the monsoon onset. If onset forecasts are off by even a day, there can be serious impacts on agriculture, local preparedness, and both local and global economics. As such, it is critically important that we understand all of the factors that contribute to the MOK.

One of the major contributors to MOK is the monsoon onset vortex (MOV), a low pressure system that develops over the southeastern Arabian Sea (SEAS; 6°-13ºN, 65°-75ºE) in May, roughly 16 days prior to MOK, particularly encompassing the Arabian Sea Mini Warm Pool (ASMWP) with sea surface temperatures (SSTs) greater than 28ºC to 30ºC (Chacko et al., 2012; Nyadjro et al., 2012; Deepa & Oh, 2014; Rao et al., 2015). The ASMWP is a subset of the larger Indian Ocean Warm Pool in the equatorial Indian Ocean (Vinayachandran & Shetye, 1991), with exceptionally high temperatures and unique dynamics that allow for it to be the initiation location for the southwest monsoon. Given the importance of the ASMWP, there have been a number of studies that have explored the characteristics of the ASMWP and its dynamic relation to not only the onset of the

monsoon, but also the strength of the monsoon (Deepa & Oh, 2014; Nagamani et al., 2016; Neema et al., 2012; Nyadjro et al., 2012; Rao et al., 2015; Vinayachandran et al., 2007; Vinayachandran & Shetye, 1991).

A number of field experiments have been conducted during the southwest monsoon seasons in the north Indian Ocean to understand the air-sea interaction processes and upper ocean variability and their coupling, such as the Bay of Bengal Monsoon Experiment (BOBMEX; Bhat et al., 2001), the Joint Air-Sea Monsoon Interaction Experiment (JASMINE; Webster et al., 2002), and the Arabian Sea Monsoon Experiment (ARMEX-I) during June-July 2002 and ARMEX-II during March-June 2003 (Sengupta et al., 2008). ARMEX-I had the goal of studying intense convective precipitation off the west coast of India associated with the monsoon. ARMEX-II studied the life cycle of the ASMWP, and its data analysis showed that ASMWP SSTs could exceed 30-32ºC, followed by a thin (10-20 m) mixed layer, and net surface heat gain of 80-100 W/m2 into the ocean (Sengupta et al., 2008). Further analysis of fluxes found that upper ocean stratification and heat fluxes warmed the SSTs on a subseasonal timescale (Sengupta et al., 2008).

Neema et al. (2012) investigated the thermal characteristics of the ASMWP using satellite observations and reanalysis products and model simulations. They used a threshold of 30.25 ºC to define the warm pool and found that the ASMWP reached its maximum spatial and thermal extent two weeks prior to the onset of the southwest monsoon and that it began to dissipate immediately after the monsoon onset took place. They also noticed that in many cases, larger and warmer ASMWPs were associated with stronger monsoon years, whereas smaller, lesser warm ASMWPs were associated with weaker monsoons. This study also found that the salinity of the warm pool and the strength of the warm pool

were highly correlated, with lower salinities leading to stronger ASMWPs (Neema et al., 2012).

Neema et al., (2012) was not the first to note the importance of salinity to the development of the ASMWP. The hallmark study by Shenoi et al. (1999) also suggested the importance of low salinity waters in the development of the ASMWP and provided a schematic for the life cycle of ASMWP. The surface winds and currents reverse between the northeast and southwest monsoon seasons and at the end of the southwest monsoon in October, the currents and winds once again reverse from southwesterly to northeasterly. This reversal of currents coincides with the arrival of the coastally trapped second downwelling Kelvin wave along the coast of India from the eastern boundary of the basin (Nienhaus et al., 2012). This coastal Kelvin wave in the Bay of Bengal helps to enhance the East India Coastal Current (EICC), transporting lower salinity waters from the Bay of Bengal from October through December. These low salinity waters reach Sri Lanka around December and after rounding the tip of India and reach the SEAS region in January through February, depending on the timing of the coastal Kelvin wave and the strength of the EICC. These low saline waters create stable stratification in the SEAS region and create a barrier layer (Shenoi et al., 2005; ARMEX-I). The northward propagating downwelling coastal Kelvin wave radiates downwelling Rossby waves as it travels along the west coast of India. These Rossby waves thus contribute to the development of higher sea level in the SEAS region, called the Lakshadweep High (LH), and modulates the local pycnocline and barrier layer thickness (Rao & Sivakumar, 1999). The arrival of low saline waters and development of LH in the SEAS along with the increased solar radiation (as the Sun marches northward across the equator), creates the conditions necessary for warming of

SSTs, leading to the development of the ASMWP in March. By May, as the Intertropical Convergence Zone (ITCZ) moves northward, the MOV may develop and help trigger monsoon onset around June 1 (Rao & Sivakumar, 1999; Shenoi et al., 1999).

Given that precipitation is the defining characteristic of the monsoon, many studies have focused on the atmospheric components of the monsoon. Recently Deepa and Oh (2014) used the National Center for Environmental Prediction/National Center for Atmospheric Research (NCEP/NCAR) reanalysis product from 1982 to 2011 to study the observed decrease in monsoon onset vortices, though the intensity of ASMWP increased in recent years. The analyzed patterns of upper and lower tropospheric wind convergence and divergence fields showed that divergent winds were dominating the lower troposphere (850 hPa) and convergent winds were dominating the upper troposphere near the tropopause, thus inhibiting convection. This pattern of reduced moisture convergence near the surface would contribute to fewer instances of MOV formation.

Other studies have approached the problem from the other direction with a focus on the oceanographic processes that involved in monsoon onset. Rao et al. (2015) used satellite-derived SST to study the strong and weak ASMWP regimes in order to determine the factors that contribute to ASMWP strength. They found that upper ocean salinity structure of the ASMWP was important for the size and maximum strength of the ASMWP, where stronger ASMWPs were associated with low saline waters over a deeper layer than the weaker ASMWP regimes. Their research highlighted the importance of the Rossby waves in the SEAS region for warming of the ASMWP. The type of Rossby wave and its strength was found to be important, with weaker regimes of ASMWP having more upwelling Rossby waves and strong regimes of ASMWP having more downwelling

Rossby waves. An upwelling (downwelling) Rossby wave would lead to the shoaling (deepening) of the pycnocline and barrier layer, thereby creating conditions for a weak (strong) ASMWP.

The structure of the low saline waters in the ASMWP was the focus of a study by Nyadjro et al. (2012), who analyzed the role of salinity and upper layer heat and salt budgets in the formation of the ASMWP using Hybrid Coordinate Ocean Model (HYCOM), satellite-derived salinity, and Argo floats. Their research found that the low saline waters in the SEAS usually cap the top 60 m in January and February and that the minimum in salinity is concurrent with the formation of the barrier layer. Net surface heat fluxes peaked shortly after the increased salinity stratification, which created conditions ideal (no vertical mixing and trapping of the net heat gain in the salinity stratified layer) for ASMWP development in March through April. The ASMWP was found to collapse in May due to increase in sea surface salinity (SSS) and the associated weakening of stratification.

Beyond understanding the characteristics and dynamics of the ASMWP, others have striven to understand the interannual variability of the ASWMP (Sankar et al., 2011; Rao et al., 2015). Sankar et al. (2011) used NCEP/NCAR reanalysis products from 1948 to 2009 to study the impact of the El Niño-Southern Oscillation (ENSO) and Indian Ocean Dipole (IOD) on the MOK. They found that years with advanced MOK had persistent westerlies before MOK and enhanced convection over the SEAS and Bay of Bengal, and the opposite was true for delayed MOKs. They also found that the localized Hadley circulation associated with the monsoon was stronger during advanced MOKs compared to delayed MOKs (Sankar et al., 2011). Both La Niñas and negative IOD phases were found

to support increased moisture over India, whereas El Niños and positive IOD phases were found to inhibit this. These findings are complicated by more recent research, which found that the ASMWP was more developed during El Niños than during La Niñas (Rao et al., 2015). As ENSO and IOD are both found to influence the strength and timing of the second downwelling Kelvin wave's arrival in the Bay of Bengal and the subsequent coastal Kelvin wave that interacts with the EICC, it is evident that the influences of both ENSO and IOD on both the ASMWP and MOK will be more complex (Rao et al., 2010).

Studies on the ASMWP, MOK, and strength of the monsoon have been varied, but there has yet to be a focused study on the impact of freshwater in the SEAS on monsoon strength. We hope that this is the first study using satellite-derived salinity from multiple satellite missions to analyze low salinity waters in the SEAS region and to analyze long-term trends in various air-sea coupled parameters for different monsoon regimes –strong, weak and normal monsoon years. The goal of this research is two-fold: 1) to determine the role of freshwater and salinity in the SEAS region for the ensuing strong, weak, and normal southwest monsoon regimes, and 2) to analyze the interannual, interdecadal and decadal trends in various air-sea coupled parameters to determine why there has not been a strong monsoon since 1994, and what role the freshwater transport and salinity may have to this. To do this, we use a combination of reanalysis datasets from 1980 to 2016 and the information on each year's monsoon strength from the Indian Institute of Tropical Meteorology (IITM), Pune. We use a composite analysis of all the strong, weak, and normal monsoon years during the 1980 to 2016 time period. Here, strong (weak) monsoons years were defined wherein the all India Summer Monsoon Rainfall (ISMR) exceeded (was far below) the long-term mean ISMR by more than 10%, and normal monsoons were

considered to be within the 10% threshold, as to identify the differences in the air-sea coupled processes that prevailed over the SEAS region during these different regimes. Over this time period, there were found to be 3 strong monsoons, 10 weak monsoons, and 24 normal monsoons (Table 2.1). This paper is organized as follows: data and methods are given in Section 2.2, the results and discussion on the findings cover Section 2.3, and Section 2.4 concludes this study.

2.2 DATA AND METHODS

A. DATA

A.1. REANALYSIS PRODUCTS

In this study to determine the influence of freshwater and salinity into the SEAS region, multiple salinity products are used. The Simple Ocean Data Assimilation v3.12.2 (SODA) monthly ocean reanalysis product available on a 0.5º horizontal grid with 50 vertical layers is used from 1980 to 2016 (Carton, Chepurin, & Chen, 2018; Carton, Chepurin, Chen, et al., 2018). SODA v3.12.2 has observational data assimilation and is forced with JRA-55DO with the Coupled Ocean-Atmosphere Response Experiment version 4 (COARE4) bulk formulae for surface forcing. This SODA product is obtained from the University of Maryland at https://www.atmos.umd.edu/~ocean/index_files/soda3.12.2_mn_download_b.htm. Previous versions of SODA have been used in multiple studies in the Indian Ocean and the reanalysis is found to have superior mixed layer dynamics (D'Addezio et al., 2015; Grunseich et al., 2011; Karmakar et al., 2018; Li et al., 2018; Zhou & Murtugudde, 2013).

In this study, we have also used a second ocean reanalysis product i.e., The Ocean ReAnalaysis System 5 (ORAS5) from the European Centre for Medium-Range Weather Forecasts (ECMWF; Zuo et al., 2019). ORAS5 has 75 vertically stratified layers and uses the Nucleus for the European Modeling of the Ocean (NEMO) v3.4 for its ocean model with a coupled sea ice model and ERA-Interim and WAVE forcing with observational data assimilation. ORAS5 is available from 1979 to present at monthly temporal resolution on a 0.25□ horizontal grid and is obtained from Integrated Climate Data Center (ICDC) at the University of Hamburg (http://icdc.cen.uni-hamburg.de/projekte/easy-init/easy-init-ocean.html). A recent study by Karmakar et al. (2018) compares multiple ocean state products for the tropical Indian Ocean, and ultimately concludes that ORAS5 as the best product to use in the region, with the highest correlations and lowest errors compared to observations.

The ERA5 reanalysis product, available from ECMWF from 1979 to present for the atmosphere, land and ocean, is used in this study. Total instantaneous moisture flux is obtained from ERA5 on a monthly timescale at one integrated pressure level for the entire air column from 1980 to 2016 on a 0.25º horizontal grid, 10-meter winds (both zonal and meridional), evaporation, precipitation, and surface net heat flux are obtained on a monthly timescale from 1980 to 2016. ERA5 is the successor to ERA-Interim and ERA-40, which have long been reliably used in tropical regions, the Indian Ocean, and monsoon studies (Uppala et al., 2005) and is obtained from the Copernicus Climate Change Service (C3S). ERA-Interim was also successfully used in moisture budget studies, finding it to be comparable to that of NASA's Modern Era Retrospective-analysis for Research and Applications (MERRA), (Cullather & Bosilovich, 2011).

A.2. OBSERVATIONAL PRODUCTS

Monthly gridded Argo float data is obtained from the Asia-Pacific Data-Research Center (APDRC) at the International Pacific Research Center (IPRC) on a 1º horizontal grid with 27 vertical depth levels. Argo float data is available in its gridded form from 2005 to present. The European Space Agency's (ESA) Soil Moisture and Ocean Salinity (SMOS) version 3 Level 3 SSS product is obtained from L'OCEAN Centre Aval de Traitement des Données SMOS (CATDS). SMOS is available at 0.2º gridded horizontal resolution from 2010 to present, with data for every 4 days. The National Aeronautics and Space Administration (NASA) Aquarius version 5 SSS (Combined Active Passive (CAP) algorithm) Level 3 data are obtained from the Physical Oceanography Distribution Active Archive Center (PO.DAAC) and processed by the Jet Propulsion Lab (JPL). Aquarius is available monthly from 2011 to present on a 1º horizontal grid. NASA's Soil Moisture Active Passive (SMAP) SSS is also obtained from PO.DAAC and processed by JPL as a monthly product with 0.25º horizontal resolution. SMAP is available from 2015 to present. Satellite-derived salinity has been used in several studies of the Indian Ocean but is underutilized in monsoon studies on the whole (Murty et al., 2004; Nyadjro et al., 2012; Nyadjro & Subrahmanyam, 2016; Paris & Subrahmanyam, 2018; Subrahmanyam et al., 2018).

Outgoing longwave radiation (OLR) is obtained from the National Oceanic and Atmospheric Administration's (NOAA) National Center for Environmental Information (NCEI). The NOAA-NCEI OLR product is available from 1979 to present on a 2.5º horizontal grid and monthly temporal resolution. All India summer monsoon rainfall totals

from 1871 to 2016 as monthly mean data are taken from IITM, and is obtained from ftp://www.tropmet.res.in/pub/data/rain/iitm-regionrf.txt.

Monsoon onset data were obtained from the India Meteorological Department (IMD), as well as previous studies (Pai and Rajeevan, 2009; Ordoñez et al., 2016). ENSO phases are based on the NOAA and NCEP Oceanic Niño Index (ONI) and a previous study by Grunseich et al. (2011). IOD phases are obtained from the Australian Bureau of Meteorology as annual phases. Monsoon regimes (strong, weak, or normal) data are also obtained from IITM and these regimes are based on a 10% departure from the long-term mean, where a season with more (less) than 10% of the long-term mean would be a strong (weak) monsoon (Ordoñez et al., 2016; Pai & Rajeevan, 2009).

B. METHODS

B.1. FRESHWATER FLUXES

Surface freshwater flux (F_w; kg m^{-2} s^{-1}) is calculated using SODA and ORAS5 reanalysis products for the northern Indian Ocean as outlined in the papers by Aagaard and Carmack, (1989), Wijffels et al. (1992), Serreze et al., (2006) and Smedsrud et al., (2010):

$$F_w = \frac{S_{ref} - SSS}{S_{ref}} V \qquad (2.1)$$

where S_{ref} is the reference salinity for the Indian Ocean (S_{ref} = 34.67 psu), *SSS* is the sea surface salinity and *V* is the volume flux, F_w is represented as either the zonal or meridional flux per unit area for zonal or meridional current velocity. The freshwater flux is computed for the top 5 m layer.

B.2. FRESHWATER TRANSPORTS

Depth-integrated transports (kg/s) are calculated for the upper 0-45 m layer in the northern Indian Ocean for each SODA and ORAS5 layer using the equations for:

Depth-integrated zonal salt transports:

$$F_{S,u} = \int_{H}^{z_0} \int_{0}^{L} \rho u(y,z) S(y,z) dy dz \qquad (2.2)$$

Depth-integrated meridional salt transports:

$$F_{S,v} = \int_{H}^{z_0} \int_{0}^{L} \rho v(x,z) S(x,z) dx dz \qquad (2.3)$$

Depth-integrated zonal mass transports:

$$F_{M,u} = \int_{H}^{z_0} \int_{0}^{L} \rho u(y,z) dy dz \qquad (2.4)$$

Depth-integrated meridional mass transports:

$$F_{M,v} = \int_{H}^{z_0} \int_{0}^{L} \rho v(x,z) dx dz \qquad (2.5)$$

Depth-integrated zonal ($F_{FW,z}$) and meridional ($F_{FW,m}$) freshwater transports:

$$F_{FW,z} = F_{M,u} - F_{S,u} \qquad (2.6)$$

$$F_{FW,m} = F_{M,v} - F_{S,v} \qquad (2.7)$$

where ρ is the density calculated at each depth using the equation of state of seawater, u (v) is the zonal (meridional) current velocity (m/s) at depth, *dy* (*dx*) is the difference (in m) between latitudinal (longitudinal) grid points, and *dz* is the layer thickness (in m). *S* is salinity in units of kg/kg (10^{-3} psu). *H* is the water depth (45 m in this study) and z_0 is the

ocean surface, and L is the meridional (zonal) distance of the box considered (D'Addezio et al., 2015; Nyadjro et al., 2011; Wijffels et al., 1992).

B.3. Ocean Heat Content

Upper ocean heat content (OHC) in the 0-45 m layer is calculated using both SODA and ORAS5 as in Nyadjro et al. (2012):

$$OHC = \int_{H}^{z_0} \rho C_p T dz \qquad (2.8)$$

where ρ is the density of seawater calculated at each depth using the equation of state, C_p is the specific heat capacity of seawater (4000 J kg^{-1} K^{-1}), H is the water depth (45 m in this study), z_0 is the ocean surface, and T is the mean temperature over dz, the depth thickness in meters.

B.4. Mixed Layer Depth, Isothermal Layer Depth, and Barrier Layer Thickness

In the study of north Indian Ocean, the Mixed Layer Depth (MLD), Isothermal Layer Depth (ILD), and Barrier Layer Thickness (BLT) are calculated for the SEAS region using both SODA and ORAS5 products following the methods of de Boyer Montégut et al. (2004). MLD was calculated using a 0.03 kg/m^3 density criteria as the threshold value with an equivalent temperature difference, dT, of 0.2°C used for both MLD and ILD calculations (de Boyer Montégut et al., 2004). In this study, it was found that 0.03 kg/m^3 is appropriate for near-equatorial regions with strong diurnal variability, which has been considered for this study. We have chosen 10 m as the reference depth to avoid the diurnal variability of the surface ocean. BLT is calculated as the difference between ILD and MLD.

B.5. SALINITY GRADIENTS

The SSS gradient is calculated following Nyadjro and Subrahmanyam (2016), who used salinity gradients in the Indian Ocean to describe the location of salinity fronts and position of the ITCZ. The meridional SSS gradient is described by:

$$\nabla_y SSS = \frac{SSS(i,j+1) - SSS(i,j-1)}{2\Delta Y} \qquad (2.9)$$

where i is the longitudinal grid point, j is the latitudinal grid point, and ΔY is change in latitude in meters between grid points.

B.6. SALT BUDGET

A salt budget was calculated for three regions in the near equatorial northern Indian Ocean, with three boxes in the SEAS, south of Sri Lanka, and in the Bay of Bengal. Boxes were chosen in order to determine the dominant processes in each region, so as to better understand the role of salinity in determining monsoon onset and strength in the SEAS. To calculate the salt budget, a methodology similar to Nyadjro and Subrahmanyam (2016) was followed, using the equation:

$$\frac{\partial S}{\partial t} = S\,\frac{E-P}{h} - u\frac{\partial S}{\partial x} - v\frac{\partial S}{\partial y} - w\frac{\partial S}{\partial z} + R \qquad (2.10)$$

where S is ORAS5 salinity, E and P are evaporation and precipitation from ERA5 reanalysis, h is the calculated MLD from ORAS5, u and v are ORAS5 zonal and meridional currents, respectively, and w is the vertical velocity. R is taken to be additional processes, such as river runoff, that are not directly accounted for in either the models or in this salt

budget. As *w* is not readily available in ORAS5, it is calculated through Ekman pumping and mixed layer vertical motion, as in Nyadjro and Subrahmanyam (2016):

$$w = \frac{curl(\tau)}{\rho f} + \frac{\partial h}{\partial t} \qquad (2.11)$$

where τ is the wind stress calculated from ERA5 10 m winds and drag coefficients, ρ is the seawater density calculated from ORAS5 temperature and salinity, and *f* is the Coriolis parameter calculated at each point. Vertical salinity gradients were calculated from ORAS5 to be the difference between the surface and 10 m below the MLD, as in Nyadjro and Subrahmanyam (2016). The terms are defined as, and later plotted as, salinity tendency ($\frac{\partial S}{\partial t}$), surface freshwater flux ($S\ \frac{E-P}{h}$), zonal advection ($u\frac{\partial S}{\partial x}$), meridional advection ($v\frac{\partial S}{\partial y}$), and entrainment ($w\frac{\partial S}{\partial z}$), where the total is taken to be the right side of equation 10 without the residual term.

2.3 Results and Discussion

A. Monthly Variability of SSS Products in the SEAS

To begin our analysis, we start with the composite distribution of satellite derived SMAP SSS in December in the northern Indian Ocean that highlights the distinct characteristics of very high salinity (>36 psu) waters in the northern and eastern Arabian Sea and very low salinity (<30 psu) waters in the northern/northeastern Bay of Bengal (Figure 2.1a). Some of the riverine low salinity waters also escape into the interior Bay into an eddy off the east coast of India, and some low salinity waters flow equatorward along the east coast of India, up to east coast of Sri Lanka and into the SEAS. One can also see the movement of high salinity waters into the interior Bay from the southern Bay of Bengal.

Various satellite derived SSS products from SMOS, SMAP, Aquarius and the reanalysis products of SODA SSS and ORAS5 SSS were compared for the SEAS region (black box in Figure 2.1a). These five products are found to be comparable and well correlated (correlation coefficient of 0.9 and 0.95) with Argo SSS (Figure 2.1b). Each SSS product shows a standard deviation between ±0.5 and ±0.75 psu. When compared with Argo, the other five products were found to be within a root mean squared difference of 0.25. This is consistent with the findings of other studies in the Indian Ocean, which found satellite salinity products (e.g. Aquarius, SMOS, and SMAP) to have a comparable standard error (Grunseich & Subrahmanyam, 2013; Guan et al., 2014). SODA SSS and ORAS5 SSS were found to be the closest to Argo. As both the products take the sea "surface" to be 5 m and satellites measure skin salinity, this may account for the divergence in values, particularly when compared to ORAS5, which has a surface at 0.5 m that allows it to be closer to the satellite values. As these products fall within 0.25 psu accuracy, they are reasonable to use for monsoon studies in the SEAS region.

All six products were also found to be in phase at monthly resolution from 1980 to 2016 for their respective time periods (Figure 2.1c). While maximum amplitudes within one standard deviation ranged from 34 psu to 36.5 psu in the region, their time variations were consistent across the products. The minimum SSS is resulted from the advection of low salinity surface waters from the western Bay of Bengal via the EICC and the higher SSS waters of northern Arabian Sea are advected along the west coast of India during southwest monsoon season (Shenoi et al., 2005). One can also notice interannual variability in SSS during this 36-year period.

Since our main focus is on the cases of strong, weak, and normal monsoon regimes, we will examine the occurrence of low salinity water, freshwater flux and freshwater transport into the SEAS region, as well as track the distributions of these parameters from October of the previous year to May so as to examine the impact they have on the ensuing monsoon season. Figure 2.2 presents the monthly mean SSS from SMOS, SMAP, Aquarius, ORAS5, and SODA for October, December, February and April over the periods of data availability of each product (Section 2.1). In comparing the satellite salinity products with the reanalysis products, it is clear that the increased spatial resolution of SMAP and SMOS allows for a better, more complete picture of the freshwater transport from the Bay of Bengal into the SEAS region. All three products are capable of capturing this signal on a monthly timescale, though SMAP is able to reach the closest to the coastlines, given that the sensor also captures soil moisture over land and does not experience the issues SMOS has had with radio frequency interference (RFI). SMOS does not have the close coastline of SMAP but is fairly high resolution and agrees well with SMAP. Aquarius is the coarsest of the products and does not reach close to coastlines but is in close agreement to ORAS5 simulations and is the closest to Argo of the satellite products. This may be in part due to the high accuracy of the Aquarius product in the region, as well as the similar spatial resolutions of the products. That being said, Aquarius does not cover the coastal waters of India and Sri Lanka, and experiences issues around the Maldives, which limits its use in studying salinity and freshwater exchanges in those regions. By October, low salinity waters occupy the western Bay of Bengal north of 12°N and open sea areas, while high salinity waters occupy the west coast of India up to the SEAS region. By December, these low salinity waters flow equatorward and reach SEAS

region *via* the east coast of Sri Lanka, and by February the SEAS region is occupied with relatively low salinity waters, while the SSS along the east coast of India shows a seasonal increase. By April, the SEAS region is occupied with relatively high salinity waters and in the Bay of Bengal the low salinity waters are now confined to the northeastern Bay of Bengal, and northern Andaman Sea. These patterns are more clearly seen in SMAP and SMOS.

Compared to the satellite products, SODA largely still captures the seasonal salinity exchange between basins but lacks the magnitude of low salinity water in the northern Bay in October and December, which leads to a much lower signal in the SEAS overall than in the satellite products. By comparison, ORAS5 shares a spatial pattern very close to the satellite products, especially SMAP and SMOS, just as its accuracy is seen to be very close to satellites in Figure 2.1b. These spatial similarities suggest that ORAS5 is a suitable stand in for satellite salinity for a long-term study of monsoon variability in salinity. As in Figure 2.1, the differences in SODA and ORAS5 for surface salinity is due largely to the level given as the surface, with SODA having a surface layer at 5 m depth and ORAS5 having a surface at 0.5 m depth, allowing ORAS5 to better reflect satellite-derived salinity values.

Moving forward, it is critically important that we are able to so clearly capture this exchange between basins as it has important implications for future forecasting and studies of monsoon dynamics in the oceans. Satellite salinity allows us to have unprecedented synoptic observations both spatially and temporally, which will greatly help in monitoring of freshwater transport from the Bay of Bengal into the SEAS region. As this freshwater transport is important for the development of salinity stratification and formation of thin mixed layer, the barrier layer, and subsequently the ASMWP and monsoon onset vortex, it

is critical that we maintain these observations for monsoon predictability. Table 2.1 displays the strength of monsoon, phases ENSO that were prevailing during the monsoon year and occurrence of IOD events during the monsoons from 1980 to 2016. Also mentioned in the Table 2.1 is the monsoon onset date (4th column) over the Kerala coast.

B. Variability of SSS and Currents for Preconditioning of the Southwest Monsoon

We have examined the monthly distribution of several ocean parameters from October to May for composite strong, weak, and normal southwest monsoon seasons. These years are selected based on the criterion of all India total rainfall in the respective year of southwest monsoon based on the IITM criteria (Section 2.1.2; Table 2.1). Earlier studies (Aparna et al., 2012; Grunseich et al., 2011) show that the climatic events of El Niño, La Niña and IOD impact the flow of EICC, and hence bring about variability in the advection of low salinity waters and freshwater transport from the Bay of Bengal into the SEAS region. As we analyze composite seasons, this variability is largely averaged out.

Based on the hypothesis presented by Shenoi et al. (1999), the reversal of the EICC towards the equator in October following the collapse of southwest monsoon traps freshwater in the EICC and perpetuates it around India in winter. By December-January, freshwater from the EICC should reach the tip of India and begins entering the SEAS region, creating stable stratification and formation of a barrier layer, which is conducive to the development of the ASMWP and later, the MOV. Figure 2.3 shows the bimonthly distributions of ORAS5 SSS superimposed with ORAS5 geostrophic surface currents for the months of October, December, February and April of the composite years leading into and during composite strong, weak, and normal monsoon regimes.

Following the demise of the southwest monsoon season in October, low salinity waters in the Bay of Bengal arise from the precipitation over the Bay and inflow of huge riverine freshwater flux into the basin, and flow equatorward through the EICC along the east coast of India (Figure 2.3, 1st row). By December of each year, we can trace these low salinity waters flowing along the east coast of India, along the east coast of Sri Lanka and their way into the SEAS region by the EICC and strong westward flow south of Sri Lanka and northwestward flow into the SEAS region (Figure 2.3, 3rd row). By February, though the EICC reverses to flow poleward, the SEAS region is occupied by the low salinity waters, as the westward flow of the North Equatorial Current (NEC) also brings in low salinity waters into the SEAS. By April, some traces of low salinity waters are still present near the coast in the SEAS region clearly seen two months prior to the ensuing southwest monsoon in each year.

In comparing the strong, weak, and normal monsoon seasons, it becomes clear that the weak and normal monsoon years have the greatest EICC transport into the SEAS region, with northward propagation of freshwater up to 15ºN in the Arabian Sea. The strong monsoon composite does not demonstrate this characteristic and it is likely a result of many fewer strong monsoons being added to the composite, resulting in IOD forcings acting on the weak and normal monsoon regimes and not the strong composite regime. While both the weak and normal monsoons have the highest early arrival of freshwater in the SEAS region by February, the strong monsoon year has the lowest salinity values in the SEAS region in April, suggesting a more prolonged, steady influx of freshwater into the region, most likely from the Andaman Sea via the NEC.

As the freshwater entering the SEAS region during a strong monsoon season cannot be coming alone from the EICC, it must be coming from somewhere else, given the pronounced pattern of lower salinity waters in April compared to the weak and normal monsoon seasons. Following the surface currents (Figure 2.3), it can be seen that freshwater from the northern Bay is carried into the Andaman Sea from where it is carried across the southern Bay, then moves around the tip of India into the SEAS region.

Composite bimonthly distributions of ORAS5 sea surface height (SSH) superimposed with surface geostrophic currents for October to April show the development of the Lakshadweep High in the SEAS leading into and during different monsoon regimes (Figure 2.4). The basin scale distributions of SSH show lower SSH in the Arabian Sea basin and higher SSH in the Bay of Bengal, in contrast to and in association with the distributions of SSS in both the basins. The impact of arrival of low salinity waters into the SEAS region is seen as the development of higher SSH region, known as the 'Lakshadweep High' (LH) by December and February (Figure 2.4, 2nd and 3rd rows) and its westward propagation by the radiating Rossby waves from the SEAS to the interior Arabian Sea. In February and March, the LH drifts far westward towards the Somali coast. By April, the LH has dissipated completely from the SEAS region (Figure 2.4, 4th row). High SSH is seen along the east coast of India wherein the low salinity waters are advected equatorward by the EICC, and by February, a large-scale anticyclonic gyre occupies the Bay of Bengal with a poleward flowing EICC (Murty et al., 1993; Shetye et al., 1996).

The LH is a necessary feature for the formation of the MOV (Shenoi et al., 1999). While all three monsoon years show a well-developed LH, the weak and normal monsoons have the highest amplitude LH in February, whereas the strong monsoon has the smallest

and lowest amplitude LH. In April, SSH for the weak monsoon year remains high in the SEAS region and between 6ºN and 12ºN, whereas the normal, and especially strong, monsoon years have more moderate SSH.

C. The Meridional Salinity Gradient and Local Convection

The meridional salt gradient in the northern Indian Ocean was calculated using ORAS5 SSS at 0.5 m depth, (Figure 2.5). The salinity gradient partially stems from E-P, and so if evaporation or moisture flux increases (decreases) in a grid of the reanalysis product, then we would expect a positive (negative) meridional salt gradient. Moisture convergence and flux are also functions of evaporation, where more positive (negative) values would decrease (increase) the salinity gradient. The negative (positive) OLR anomalies suggest more (less) convection and therefore more (less) precipitation, which would lead to a negative (positive) meridional salinity gradient in the reanalysis product. While this methodology is most commonly used to study salinity fronts, it can also be used in the tropics to determine the relative position and strength of the ITCZ over the ocean and has been shown to present at multiple depths using both SMOS and Argo (Nyadjro & Subrahmanyam, 2016). Similar to their study, we also find that the southernmost ascending branch of the localized Hadley circulation near the equator is most prominent in the SSS gradient due to the high evaporation, and therefore higher salinity values associated with it. This southernmost branch is located over the SEAS region, and thus it contributes to the salinity, surface latent heat fluxes, and moisture fluxes in that region. Here, though there is some coincidence between the meridional salinity gradient and OLR anomalies, there are deviations between them due to processes beyond evaporation and precipitation influencing salinity in the area.

In comparing different monsoon regimes, we find that the SSS gradient is strongest from April-June in a strong monsoon regime, particularly in the SEAS region and Bay of Bengal prior to monsoon onset. These salinity gradients, particularly in the SEAS, weaken once the monsoon onsets in June and convection sets over the region, as seen in the OLR anomalies. The normal monsoon has the smallest gradient values in the SEAS region. The weak monsoon has a moderate SSS gradient that weakens as in the other years. This suggests at least a loose relationship between monsoon strength and the SSS gradient in the SEAS via local Hadley circulation.

D. Mixed Layer Salt Budget in the SEAS

In order to determine the dominant processes controlling salinity in the mixed layer in the SEAS region, a salt budget is constructed using ORAS5 and ERA5 reanalysis products in equations 2.10 and 2. 11. We decompose the salt budget into composite strong, weak, and normal monsoon years to understand how the processes that control salinity vary between monsoon regimes (Figure 2.6). Overall, we find mixed layer salinity in the SEAS to be overwhelmingly dominated by horizontal advection, particularly meridional advection, with entrainment and surface fluxes playing a much smaller role. This is consistent with previous studies of the region, which also found entrainment and surface freshwater fluxes to be small (Nyadjro et al., 2012; Nyadjro & Subrahmanyam, 2016; Zhang & Du, 2012). Here salinity is shown to decrease during the winter months when freshwater is transported into the SEAS via the EICC and NEC, and again increases following monsoon onset until once again there is an influx of low saline water. This seasonal pattern is in contrast to Nyadjro et al. (2012), which found the salinity tendency to reach its minimum in the summer months at the height of the southwest monsoon, but is

consistent in both shape and magnitude with Zhang and Du (2012). These results reaffirm the importance of understanding the magnitude and dynamics involved with transport of low saline water in the EICC and NEC into the SEAS. Though surface freshwater fluxes are given to be small here compared to advective processes, they should not be disregarded, as evaporative processes and moisture fluxes can still heavily influence local precipitation in the region, and thus monsoon strength and onset.

We find that surface freshwater fluxes are more negative during strong monsoon years during the monsoon season, suggesting an increase in positive moisture flux as the system becomes precipitation dominated (negative E-P), whereas weaker monsoon regimes will be more evaporation dominated (positive E-P), where SFWF is in terms of E-P, where a precipitation (evaporation) dominated system would have negative (positive) values. By comparison, moisture flux follows surface flux conventions where positive (negative) values are presentative of surface gains (losses), and thus a positive SFWF implies a negative moisture flux. During strong monsoon regimes, zonal advection is also more negative prior to monsoon onset, suggesting an increase in westward advection from the NEC in February and March of a strong monsoon year. This is consistent with Figures 2.7 and 2.8, where zonal freshwater fluxes were seen to be comparatively high prior to monsoon onset for strong monsoon years. Meridional transport is also higher during strong monsoon regimes, suggesting an increase in northward transport into the SEAS through May, particularly during March and April. Given the timing of arrival, it is likely that it is the NEC, not the EICC, which is more important in determining monsoon regime strength based on salinity. The southward meridional salinity advection into the SEAS by the West India Coastal Current (WICC) brings high salinity waters (Shenoi et al., 2005; ARMEX-I)

and northward salinity advection in winter months by the EICC and NEC into the SEAS brings low salinity waters, together playing a major role in controlling salinity in the SEAS. The latter brings in salinity stratification, develops the barrier layer, and increases OHC during winter months. The former, during the southwest monsoon season, annihilates the barrier layer by the weakening of salinity stratification, deepens the mixed layer, and increases OHC.

E. Variability of Surface Freshwater Flux and Freshwater Transport

Having established the relative dominance of horizontal advection in determining salinity in the SEAS, it is next useful to discuss the origins and strength of this advection during different monsoon regimes. Figures 2.7 and 2.8 represent the bimonthly distributions of meridional and zonal surface advective freshwater flux (m2/s) respectively for the months of October, December, February and April for the years of three monsoon regimes and the preceding years. One can notice the equatorward freshwater flux along the east coast of India in October and December and its entry into the SEAS by February and April (Figure 2.7, 1st row to 4th row). By February, the SEAS region freshwater flux has peaked in all regimes, with some variability, several months prior to the ensuing southwest monsoon. The freshwater flux decreases into the SEAS in April for all regimes. While high freshwater fluxes are observed along the east coast of India from February to April, the NEC strongly contributes to the westward freshwater flux into the SEAS at this time (Figure 2.8, 3rd and 4th rows).

The seasonal reversal of the EICC can most clearly be seen between December and February in all monsoon regimes, with no nominal difference in magnitude between

regimes. In December and February, the normal and weak monsoons have the highest amount of northward freshwater flux into the SEAS region, whereas the strong monsoon barely has any. The pattern of northward and southward propagation in the SEAS region is suggestive of an eddy, specifically the LH, which is well developed for the normal and weak monsoons (Figure 2.4).

Whereas the weak and normal monsoon seasons had the strongest meridional freshwater flux into the SEAS region, the strong monsoon season has the strongest overall zonal freshwater flux in the Bay of Bengal from December to April (Figure 2.8). As was seen in the salinity in Figure 2.3 and the salt budget in Figure 2.6, the westward zonal freshwater flux during the strong monsoon season is suggestive of a larger influx of freshwater compared to the brief burst of freshwater as in the other monsoon regimes. Furthermore, the majority of the freshwater during the strong monsoon season appears to originate in the Andaman Sea via the NEC, not the EICC, which remains strong through April, as in Figure 2.3. This further suggests that the dominant zonal freshwater flux is the NEC, particularly during strong monsoon years.

To quantify the freshwater transport in the upper 45 m layer from the Bay of Bengal to SEAS, we used ORAS5 reanalysis data and selected four transects: one zonal section off the central east coast of India at 15°N, 82°-85°E (considering the depth occupancy of low salinity waters and width of the EICC), one zonal section from 3°-6ºN, 85ºE in the southern Bay of Bengal, one meridional section south of Sri Lanka at 80°E, 3°-6°N and one zonal section in the SEAS region at 10°N, 72°-75°E. Calculations were also performed with SODA reanalysis but did not show a substantial difference. Accordingly, we calculated the monthly sectional mean meridional freshwater transport off central east coast

section, zonal freshwater transports at 85°E and 80°E and meridional freshwater transport at 10°N. The monthly time series of freshwater transport at each of the section are presented for the three monsoon regimes and their preceding years (Figures 2.9a-l), where year 1 precedes year 2, which is the designated monsoon regime year.

In Figure 2.9, the movement of freshwater from the EICC in the Bay of Bengal, near Sri Lanka, and around the tip of India in the SEAS can be traced. In October-December at 15ºN, southward transport can be observed. In both 3-6ºN transects during winter and early spring, there is clear westward transport during all monsoon regimes. At the tip of Sri Lanka, though differences between regimes are small, the normal and weak monsoons have the highest amplitude westward transport from October to April, consistent with high EICC output. Into the SEAS, the weak monsoon receives the most freshwater from November to December (Figure 2.8k), followed by the normal monsoon from October to February (Figure 2.9l).

Salt transports follow the same temporal patterns as their freshwater counterparts but are lower amplitude (figure not shown). Similar to the freshwater transports (Figure 2.9), the strong and weak monsoons have the highest salt transports around the EICC (figure not shown). However, the strong monsoon has the highest salt transport into the SEAS region, but freshwater transport lasts for a longer period of time. This suggests that the water transported during the strong monsoon year was more saline as southern Bay of Bengal waters enters the SEAS region. Given the meridional salt gradient near the equator and the potential equatorial origin of incoming water during the strong monsoon regime, it follows that the salt transport would also be higher at this time (Figures 2.3 and 2.5).

F. VARIABILITY IN MIXED LAYER PROCESSES

To further our discussion of salinity variability in the mixed layer during different monsoon regimes, Figure 2.10 presents the depth-time sections of temperature (contours) and salinity (shading) in the upper 140 m from both SODA (1st row) and ORAS5 (2nd row) for monsoon regimes and their preceding years in the SEAS region. The variation of BLT is shown by a white curve. While there is low interannual variability in the pattern of isotherms in each product, the occurrence of freshwaters in the upper 40 m is clear in all the years, with a slight variation in the magnitude and period of extent of freshwaters in each product. For example, in the strong monsoon regime, SODA salinity is weaker compared to the intense low salinity in ORAS5 beyond April, which coincides with warmer (30°C) temperatures. In the weak regime, low salinity waters are present through May, coinciding with warmer temperatures (30°C). In the normal regime, there is little variation in the salinity between products, and freshwater extend beyond April. From May to November, the ASMWP (>28°C) is present and extends up to 60 m (approximately coincides with the base of the 28°C isotherm). The thermocline deepens from December to March in association with the development of the anticyclonic LH.

The timing and occurrence of the low salinity layer and formation of the barrier layer for a strong monsoon season is largely consistent between products. The barrier layer is rapidly formed following the freshwater flux in January/February but falls apart within 2 months as temperatures reach their maximum and the ASMWP is formed. In all products, the weak monsoon regime has the strongest low salinity signal, followed by the normal monsoon regime, whereas the salinity values for a strong monsoon are much higher overall during the strong monsoon. Especially in ORAS5, the strong monsoon year has the highest

salinity values both at depth and at the surface following the annihilation of the barrier layer. Given the location of the ITCZ and the ascending branch of the local Hadley circulation, as well as values of moisture flux and surface latent heat fluxes, it is likely that the high evaporation associated with this region contributed to the higher salinity values. Advection of high salinity waters from the northern Arabian Sea via the WICC would offset these parameters, resulting in the observed variability.

These results are consistent with those of previous studies, which found a deeper freshwater pool and barrier layer to be associated with a stronger ASMWP (Rao et al., 2015). Observational studies based on the ARMEX program found that ASMWP temperatures could exceed 30ºC (Sengupta et al., 2008). As their study and our salt budget analysis also have connections to surface fluxes, it is useful now to look at the relationship between the barrier layer, net surface heat fluxes, and upper ocean content (OHC) in the upper 45 m layer (Figure 2.11).

By directly comparing the seasonal cycles of BLT, OHC, and moisture fluxes, we can better understand the factors that contributed to the strength of the ensuing monsoon. As seen in Figure 2.11, BLT is largely in agreement for most of the year between regimes but has the highest discrepancy during February due to the advection of low salinity waters, the subsequent development of a thin mixed layer, and the consequent thickening of BLT. Whereas the normal and weak monsoon years have their peak around 25 m, the strong monsoons have shallower barrier layers in February by as much as 20 m. This decrease in BLT corresponds with the increase in net surface heat flux (not shown). It is the collapse of the barrier layer, particularly from February to May, that allows the OHC to increase, due to increase in net surface heat gain, and the ASMWP to develop (Figure 2.11). The

upper layer OHC (0-45 m layer) exhibits a bimodal seasonal distribution with minimum OHC in winter (January) and July to August (peak southwest monsoon period). The SEAS attains maximum OHC from April to May (formation of ASMWP) and a secondary maximum in October to November (post-southwest monsoon period); however, the amplitude of the seasonal cycle in OHC is large, with a peak maximum in May and peak minimum in August.

It should be noted that ERA5 moisture fluxes (and surface latent heat fluxes) also increase from March to June, as surface winds pick up as monsoonal flow begins over the Arabian Sea. Moisture flux values, however, show the greatest discrepancies between regimes. During the weak monsoon regime, moisture flux is negative from May to September contributing moisture by evaporation from the surface to atmosphere. During the normal monsoon regime, moisture flux is near zero during the southwest monsoon season. Strong monsoons, by contrast, are evaporation dominated during much of February and March, then overwhelmingly are more precipitation (positive moisture flux) dominated during the monsoon season. It may be noted that the negative sign of moisture fluxes denotes a loss of water vapor due to increased evaporation from the sea surface. The decrease in moisture flux from July to November over the SEAS region corresponds to decrease in specific humidity difference during the southwest monsoon season, though the monsoonal wind speed increases during this period.

Previous studies have shown that moisture transport and fluxes from the ocean can significantly contribute to monsoon precipitation totals, along with flooding and drought phases of the monsoon, thus making this discrepancy in moisture flux between monsoon

regimes a possible explanation for the differences between monsoon seasons (Gimeno et al., 2010, 2016; Levine & Turner, 2012).

G. LONG-TERM VARIABILITY IN THE MIXED LAYER PROCESSES

Following our analysis of composite monsoon regimes, it is now useful to turn our attention to interannual variability and trends in monsoon strength, specifically with the intention of identifying which variables are most responsible for the observed long-term trends in monsoon strength. Until the 2019 strong monsoon season, 1994 was the strongest monsoon in recent memory, and so it is important to identify the controlling forces behind the observed monsoon variability.

The long-term salt budget for the SEAS region (Figure 2.12) reaffirms the findings in Figure 2.6 that mixed layer salinity in the SEAS is overwhelmingly advection dominated, as is consistent with previous studies of the region (Nyadjro et al., 2012; Nyadjro & Subrahmanyam, 2016; Zhang & Du, 2012). We find that westward zonal advection leading into a stronger monsoon year is typically larger than during weak monsoon years and that the magnitude of the meridional advection does not play a significant role in monsoon strength. There are no significant trends in the salt budget beyond meridional advection, which is strongly related to IOD and ENSO phase oscillations. Overall, however, it is clear that salinity in the SEAS is overwhelmingly dominated by horizontal advection into the region, with surface freshwater fluxes playing a relative minor role. As monsoon variability overall is small, however, and moisture fluxes have been shown to vary considerably between monsoon regimes (Figure 2.11), it cannot be overlooked. It is therefore useful now to turn our attention to the dominant mixed layer

processes that contribute to both salinity variability in the mixed layer and monsoon strength.

The long-term (1980 to 2016) anomaly (seasonal cycle removed) time series of moisture flux, meridional freshwater transport (normalized by its standard deviation), MLD, BLT, and 0-45 m layer OHC with their associated 3-year and 7-year trends superimposed have been plotted in order to best show these trends (Figure 2.13). These 3- and 7-year moving means are calculated as a low pass filter to remove lower frequency variability above the given time period. Necessarily, the 3-year mean will have most IOD and ENSO variability while the 7-year mean will represent a half-wavelength of decadal-scale variability. The different scales for these trends for each parameter are shown on the right y-axis. As BLT is determined as the difference between the ILD and MLD, it is important to determine whether thermal processes or changes in salinity are principally responsible for changes in BLT observed from 1980 to 2016. It is seen that the amplitudes of interannual and interdecadal MLDA are positive and weaker from 1980 to 1996 and changes to a large negative phase (shoaling of MLD) from 1996 to 2014. It can be seen further that the advancement of monsoon occurred mostly during this long-term decadal variation of negative phase of MLDA. Interestingly, the strong monsoon year of 1994 coincides with change over from the positive phase to negative phase of MLDA, wherein the amplitude of variation is nearer to zero, and the monsoon advanced by 5 days (Table 2.1) under the basin scale influence of both El Nino and IOD. In the time series of BLTA, one can notice the long-term decadal variation of 15-years in interannual and decadal variations (3-year and 7-year trend curves) with a large positive amplitude in 1993 and 2007, and a large negative amplitude in 2002. Through these time series, we can see a clear

3-year oscillatory pattern associated with BLT anomalies that may, at least in part, be related to the phases of ENSO and the IOD. From 1988 to 1993, there is an increase in BLT. From 1993 to 2002 there is a decrease, and then again from 2002 to 2007 there is a strong decrease. This suggests that for a given year BLT in the SEAS region is more fully controlled by the preceding year's IOD and ENSO phase than any other governing mechanism. This theory is supported by the work of previous studies, which have shown ENSO and the IOD to have a profound impact on the strength of the coastal Kelvin wave propagation around India into the SEAS region, which greatly enhances or suppresses EICC transport (Nyadjro et al., 2012; Rao et al., 2010; Sankar et al., 2011). The sequential delay in the MOK for most of the monsoon years from 1993 to 2005 occurs during the decreasing trend of BLTA and the sequential advancement in the MOK occurs during the increasing trend of BLTA from 2006 to 2011, though some exceptions are seen with the coincidence of ENSO and IODs. Since we have used the monthly means of all parameters, we can attribute the delay or advancement in MOK qualitatively as due to the long-term decadal oscillation in the above upper ocean processes. The largest change in MLD appears after 2005, possibly as a result of the La Niña leading to greater transports of low salinity waters into the SEAS. This suggests, however, that it is changes in OHC and surface fluxes which are responsible for the observed trends.

The trends in normalized meridional freshwater transport into the SEAS are antiphased with the BLT anomaly trends. There occurs a long-term decadal variation in meridional freshwater transport with a decreasing trend from 1988 to 2002 and also from 2002 to 2009. The amplitude of this decadal variation is high and is clearer in the 3-year trend curve. Owing to the prevailing interannual variability in the northward freshwater

transport, the freshwaters (in the 0-45 m layer) reach the SEAS west of 72°E and returns equatorward (resulting in negative freshwater transport between 72°E and 75°E) under the influence of the anticyclonic (clockwise) flow of the Lakshadweep High. These freshwaters maintain a shallow MLD due to salinity stratification and the 3-year and 7-year trends in the MLD anomaly show a very little variation. The interannual and intradecadal variability in the flow pattern of the LH brings in similar variations in the thermocline and hence in the ILD and MLD anomalies (Figure 2.S1). The large variations in the ILD anomaly and weaker MLD changes brought about large variations in the BLT anomalies. Thus, one can see the opposing patterns in the 3-year and 7-year trends in the meridional freshwater flux and BLT anomalies. Since the ILD and BLT are affected by the circulation variability of the LH at interannual and intradecadal periods, the 0-45 m layer OHC is affected at these periods. As such one can see a clear long-period negative phase in OHC anomalies from 1980 to 1999 and a positive phase from 1999 to 2016. However, 3-year trend in OHC shows variation in amplitude with alternating positive phase and negative phases of decadal and intradecadal periods. From 2007 onwards, the interannual variability in OHC is positive with a progressive increase in positive OHC anomaly. This interannual variability in OHC coincides with that in meridional freshwater transport. The long-term variation of meridional freshwater transport in the EICC region of the Bay of Bengal does not exhibit any long-term trends, but the long-term variation of zonal freshwater transport at the section south of Sri Lanka does show a weak decadal oscillation, with a positive trend from 1980 to 1995 and a negative trend from 1996 to 2010.

While there appears to be a strong oscillatory pattern in the OHC time series, even when detrended, the most pronounced and statistically significant periods occur on the

order of seasonal and annual time-scales. While not statistically significant, there is a strong period of oscillation between 3 and 6 years, which are likely related to ENSO and IOD years (figure not shown). Given the role of freshwater flux, and the influence ENSO has on modulating SSTs and the EICC through coastally trapped Kelvin wave propagation in the Bay of Bengal, this may provide a possible mechanism for which ENSO may act on SEAS OHC, as well as the influence both ENSO and the IOD have on SSTs in the region. The most striking feature of the OHC time series, however, is not the spikes during El Niño events, but rather the overall trend. Our calculated upper ocean OHC shows a clear increase in SEAS OHC from 1980 to 2016, particularly in the later years, after 2002. This trend is consistent with recent studies, which have shown OHC in the northern Indian Ocean and the SEAS to be increasing, (Li et al., 2018; Nagamani et al., 2016). These studies have also speculated that this increase in OHC in the SEAS compared to the surrounding waters in the equatorial Indian Ocean (Nagamani et al., 2016) may help explain the lack of strong monsoons since 1994. These studies, however, used 0-400 m and 0-300 m OHC, not the salinity stratified upper ocean OHC. Nyadjro et al. (2012) used the upper 0-40 m OHC to analyze short term controls of OHC in the ASMWP from 2003 to 2006, finding that IOD and ENSO phases strongly contributed to OHC, as well as the strength and timing of the ASMWP development and demise.

Even more so than OHC, the ERA5 moisture flux shows a very clear downward trend from 1994 to 2005, suggesting that moisture flux, along with other related factors, are likely responsible for the lack of recent strong monsoons. As ERA5's moisture flux and surface latent heat fluxes are strongly related, it follows that surface fluxes, especially moisture and latent heat fluxes are largely responsible for the drop off of monsoon strength.

This is consistent with previous studies of the ASMWP, which found surface heat fluxes to place a critical role in the development of the ASMWP, especially in increasing the strength of the ASMWP (Rao et al., 2015; Sengupta et al., 2008). It is worth noting that the BLTA also decreases at the same time as the moisture flux trend decreases, which may have contributed to the decrease in monsoon strength. The study by Nyadjro et al. (2012) showed that the minimum in salinity in the SEAS, which corresponded to the formation of the barrier layer, led to an increase in net heat flux that allowed for the formation of the ASMWP in spring. If latent heat fluxes, moisture fluxes, and BLT also decreased from 1994 to 2005 that would account for the overall drop in monsoon strength during that time.

Given the strong relationship between atmospheric fluxes, barrier layer development, and freshwater transport, it becomes important to determine how strong of an impact OHC has on influencing these fluxes. To determine this, Figure 2.14 shows scatter plots of OHC anomalies and moisture flux anomalies for the 3- and 7- year trends, along with the corresponding wave coherence transforms. In considering only normal and strong monsoon years, we find that the 3 (7) year trends have an R2 value of 29% (64%). When only weak monsoon years are considered, the R2 values change to 59% and 57%, respectively. This suggests that more normal and strong monsoon years can be explained by longer term trends, on the order of 7+ years (decadal variation), whereas weaker monsoons are more likely to be explained by interannual variability on the order of 3-years (corresponding to IOD and ENSO events), which is clearly shown in the wave coherence plots. Wave coherence transforms of both trends show statistically significant periods of oscillation between 2 and 3 years, particularly during weak monsoon years.

Previous studies have identified winds as critical drivers of monsoon variability (Deepa & Oh, 2014; Kurian & Vinayachandran, 2007; Webster et al., 2002). Convergence and divergence of winds aloft and at the surface can either inhibit or support convection, which contributes not only to the formation of a monsoon onset vortex, but monsoon precipitation as a whole via moisture fluxes and moisture flux convergence (Deepa and Oh, 2014). Winds also contribute to changes in surface heat fluxes, entrainment, and air-sea processes, which make them critically important for determining monsoon strength and variability. Moisture fluxes necessarily rely on winds as well as humidity and heat fluxes, and so it follows that we must finally consider winds in our investigation.

Figure 2.15 shows ERA5 10 m zonal wind anomalies from 1980 to 2016, along with the associated trends. We can see that the zonal winds have the same overall trend as moisture flux, with a peak in 1993 and decreases after 1994. Interannual peaks do not always correspond with monsoon strength, with some of the largest peaks occurring during weak monsoon years. As at least two of these peaks occur immediately after an El Niño, it is possible that this became a factor in the wind strength. This finding is supported by previous work, such as the 2002 study by Webster et al., which analyzed the coupled nature of the monsoon to find that strong monsoons associated with La Niñas had stronger wind-induced ocean heat fluxes and content, whereas El Niño (weak) monsoon regimes had less wind-driven ocean heat variability. This further suggests a strong connection between OHC and wind variability in the SEAS region and in relation to the monsoon system overall.

Another interesting feature of the zonal winds, moisture flux, and OHC trends is the marked change after 2013, which corresponds to a long period of weak monsoons. While all of these factors, in their respective trends, combined would seem to suggest the

prevalence of strong monsoons, or at least normal monsoons that are almost strong, instead we see the opposite. The reason for this is likely found in the meridional freshwater transport into the SEAS, the trends of which all decrease drastically after 2012, but along with increased MLD and ILD. As the amount of negative freshwater transport trend suggests an influx of high salinity waters, this would weaken the salinity stratification, help MLD deepen, and BLT thinning (Figure 2.S1;2.13). The upward trend in BLT from 2002 on can be attributed to ILD deepening and the slight shoaling of MLD. With lower freshwater transports, MLD would be shallow and, if the LH is also present, the ILD would also deepen, leading to the observed BLT trends. During this time, preconditions were not necessarily met for a strong or even a normal monsoon season, but rather the monsoons were much weaker than normal. It then follows that while the decrease in moisture fluxes, latent heat fluxes, and zonal winds, and though OHC increases (from the decrease in latent heat flux) can account for the lack of strong monsoons after 1994, it is the decrease in freshwater transport and BLT in the SEAS that can account for the prevalence of weak monsoons in the recent years.

Finally, we must now consider rainfall. IITM JJAS rainfall from 1980 to 2016 shows clear 3- and 7-year trends, along with a longer, 15-year cycle. The trends in monsoon rainfall follow most closely the trends in BLT and moisture flux, while showing a slight decrease overall in accordance with increased OHC. The observed trends and relationship between OHC, moisture flux, and rainfall are indicative of the climatic oscillations associated with global climate change. An increase in OHC and increase in negative moisture flux (more evaporation) is what is expected of a warming ocean and an atmosphere capable of holding more moisture. Climate change impacts may then explain

the observed patterns in decreased monsoon strength over the past few decades as part of the negative phase of the climate change signal. In the years since 2016, this oscillatory pattern has also become more clear, with monsoons arriving later with extended periods of draught followed by highly active phases influenced by depressions over the Bay of Bengal (Bhat et al., 2001). As the climate oscillation pattern shifts into its positive phase, it is likely that we will begin to see more normal monsoons than weak, although periods of severe flooding remain likely, even during drought years. The 2019 monsoon season, by example, was the first strong monsoon season since 1994, further confirming the positive phase of the climate oscillation. It is therefore likely that it is these short-lived monsoon depressions and intraseasonal oscillations in the Bay of Bengal which will become increasingly more important for monsoon predictability and preparedness in the years to come.

2.4 CONCLUSIONS

While there have been a multitude of studies surrounding the role of the SEAS region in the monsoon onset and monsoon strength, the specific role of freshwater transports into this region has been largely neglected. In analyzing the freshwater transport into the SEAS region and the associated barrier layer development, we have found that both are critical components in the 'perfect storm' of variables that must all be right in order to facilitate a strong monsoon season.

Prior to the strong 2019 monsoon season, 1994 was the last strong monsoon in recent memory (India Meteorological Department, 2019), and the lack of strong monsoons has been the basis for a great deal of research and speculation. We find long-term decadal variation in a negative phase over a 15-year period in instantaneous moisture flux, a similar

negative phase in zonal wind speed at 10 m height, and BLT, all contributed to the lack of strong monsoons since 1994, but that the increase in OHC and decrease in meridional freshwater transport are why there have been more weak monsoons in recent years. As freshwater transport influences the MLD and BLT, it helps the thermal processes in the SEAS region that ultimately determine the monsoon strength, such as OHC and moisture flux. These trends are likely caused by a number of factors, but IOD and ENSO both play a significant role in determining the interannual variability, and thus the strength of the monsoon, particularly regarding the thermal structure of the ASMWP and the amount of EICC transport into the SEAS. We find that IMSR follows a similar short-term oscillatory pattern to 10 m zonal winds, BLT, and freshwater transport (anti-phased), and that the long-term 15-year trends are inversely related to the OHC trend. Given the nature of increasing OHC and decreasing moisture flux related to the changing climate, it is likely that the 15-year trend will continue, interacting with the shorter-term influences of the patterns of wind, BLT, and freshwater transport. The interplay of these oscillatory periods ultimately determines the monsoon strength and will continue to have an increasing amount of influence as the climate changes. At present, our confidence in how climate change will impact large-scale climate oscillations, such as ENSO and IOD, is fairly low, and improving our understanding of this will also help us to understand how the monsoons will change in the coming years.

Critically beyond the changing climate, the freshwater transport into the SEAS does not always find its origin in the EICC region, where most of the IOD and ENSO modulated variability in transport originates. Instead, strong monsoon years find a substantial amount of freshwater originating in the Andaman Sea region, transported to the SEAS via the NEC.

Low salinity waters in this region have influences from both river runoff and the Indonesian Throughflow, both of which can have a substantial impact on monsoon strength. As intraseasonal oscillations in the Bay of Bengal are also shown to have an impact on Indonesian Throughflow waters and river runoff, it is also important that we develop a stronger understanding of how these intraseasonal oscillations impact monsoon strength. Given the role and importance of freshwater transports into the SEAS for monsoon variability, further research is required into the role of the NEC and Andaman Sea in determining monsoon characteristics.

Table 2.1. Year-wise southwest monsoon strength (1st column), and occurrences of ENSO phase (2nd column), and IOD phase (3rd column), and date of monsoon onset over Kerala (MOK; 4th column) from 1980 to 2016.

Year	Monsoon Strength	ENSO	IOD	MOK
1980				3-Jun
1981				30-May
1982	weak	El Niño	positive	30-May
1983	strong	La Niña	positive	12-Jun
1984		La Niña		1-Jun
1985	weak			24-May
1986	weak	El Niño		12-Jun
1987	weak	El Niño		1-Jun
1988	strong	La Niña		2-Jun
1989		La Niña	negative	4-Jun
1990				18-May
1991		El Niño		2-Jun
1992			negative	5-Jun
1993				3-Jun
1994	strong	El Niño	positive	28-May
1995		La Niña		10-Jun
1996			negative	9-Jun
1997		El Niño	positive	12-Jun
1998		La Niña	negative	3-Jun
1999		La Niña		22-May
2000		La Niña		1-Jun

2001				26-May
2002	weak	El Niño		9-Jun
2003				13-Jun
2004	weak	El Niño		3-Jun
2005		La Niña		7-Jun
2006		El Niño	positive	26-May
2007		La Niña		28-May
2008		La Niña		31-May
2009	weak	El Niño		23-May
2010		La Niña	negative	31-May
2011		La Niña		29-May
2012			positive	5-Jun
2013				1-Jun
2014	weak	El Niño	negative	6-Jun
2015	weak	El Niño	positive	5-Jun
2016	weak	La Niña	negative	8-Jun

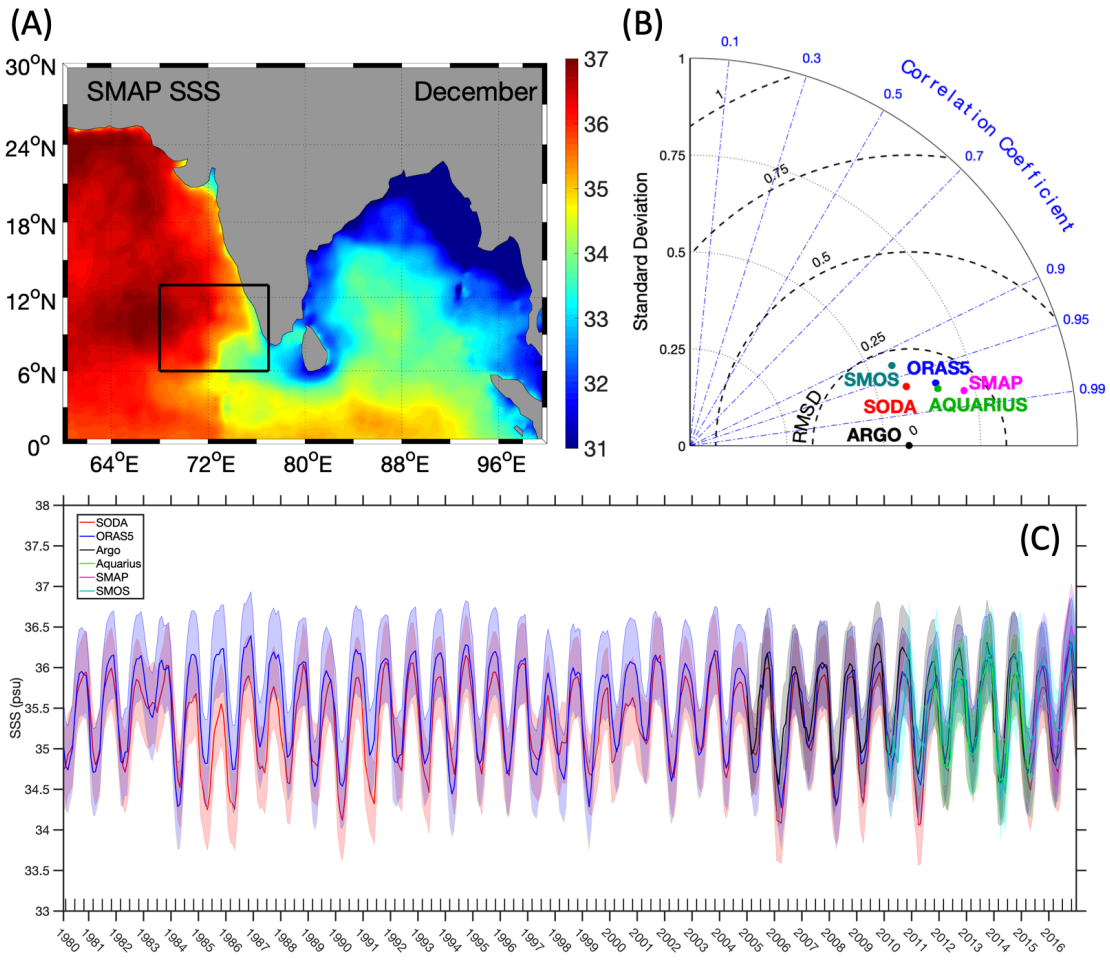

Figure 2.1. A) Monthly averaged SMAP sea surface salinity (SSS) for December 2016-2018 (shaded; psu) and the black box indicates the SEAS region (6°-13ºN, 65°-75ºE); B) Taylor diagram comparing multiple SSS products for the SEAS region; and C) Comparison of time series of various products of SSS with one standard deviation (shaded) for the SEAS region from 1980 to 2016.

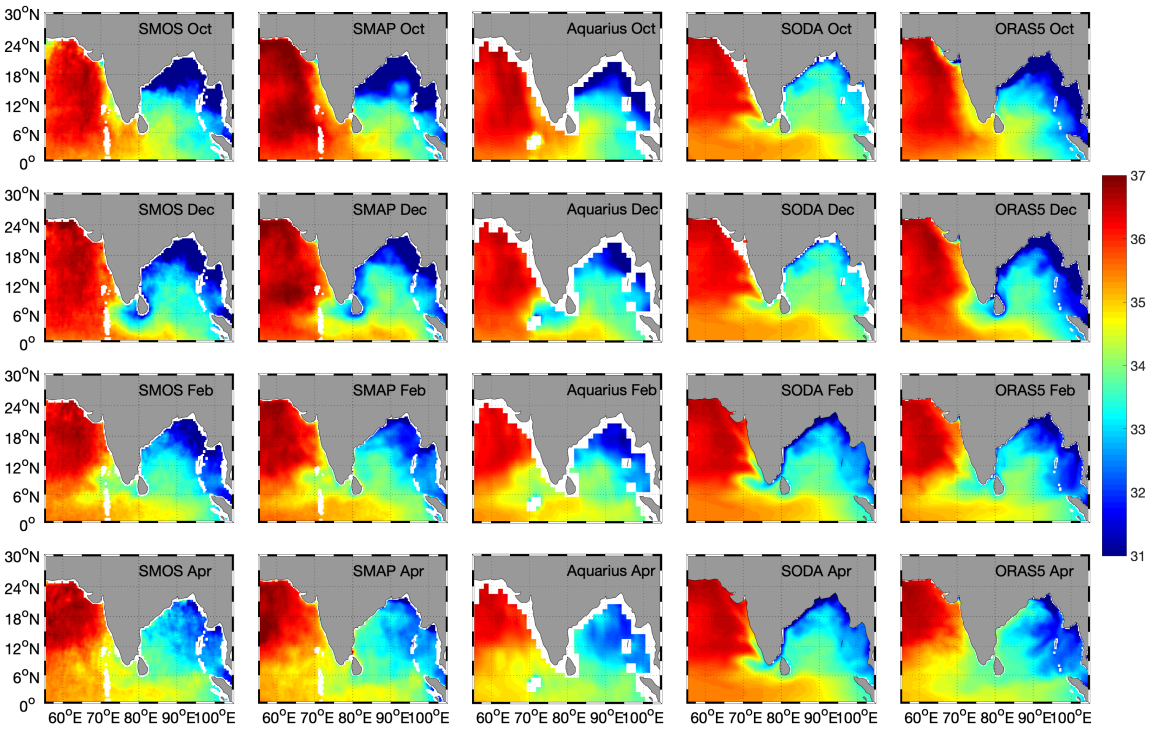

Figure 2.2. Bimonthly distributions of satellite-derived and model simulated sea surface salinity (shaded; psu) for October (1st row), December (2nd row), February (3rd row), and April (4th row) from SMOS (1st column; 2010-2017), SMAP (2nd column; 2016-2018), Aquarius (3rd column; 2012-2014), SODA (4th column; 2010-2016), and ORAS5 (5th column; 2010-2016).

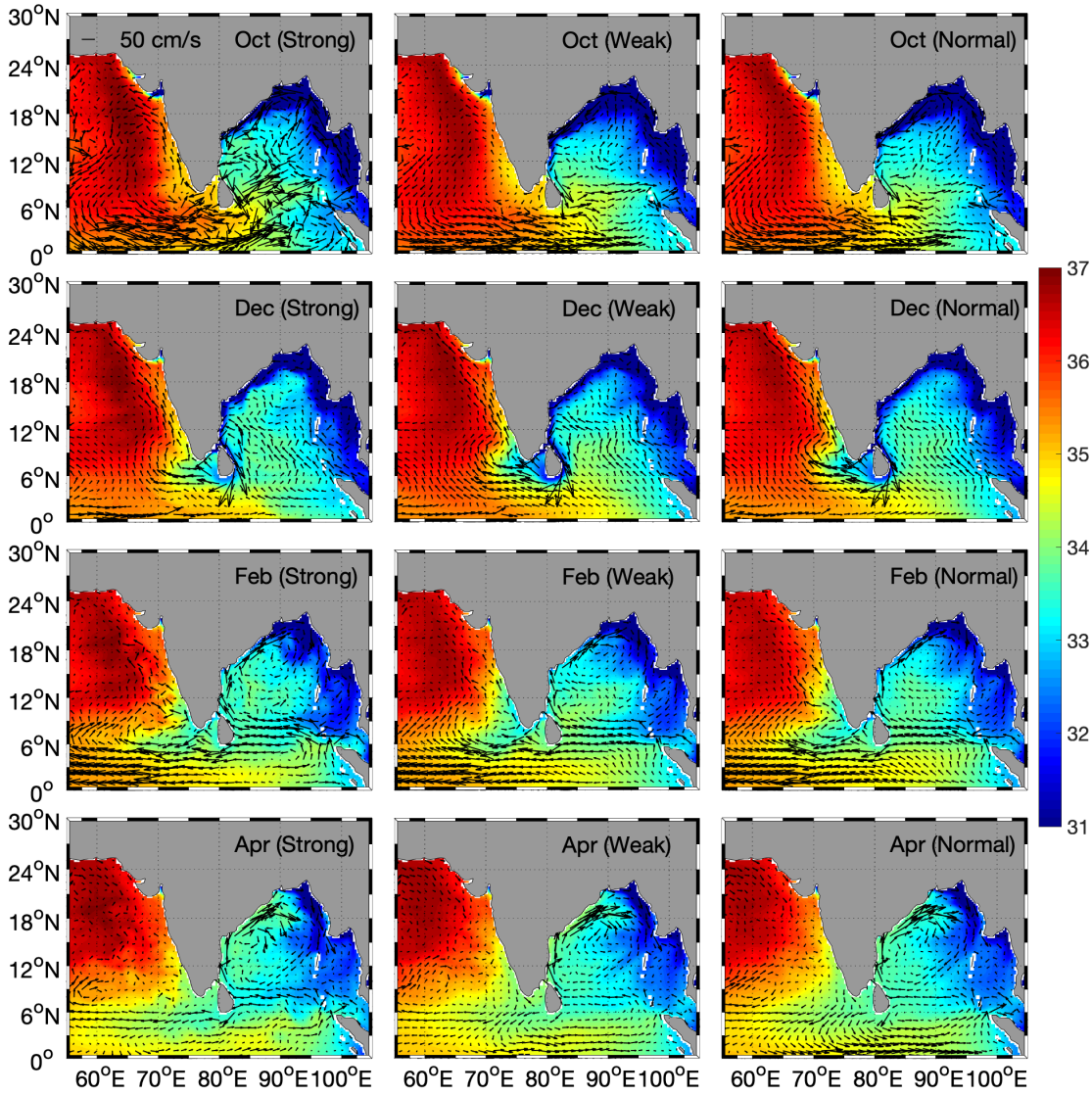

Figure 2.3. Composites of bimonthly distributions of ORAS5 sea surface salinity (psu; shaded) with overlaid ORAS5 geostrophic surface currents (cm/s; vectors) for October (1st row), December (2nd row), February (3rd row), and April (4th row) with overlaid ORAS5 geostrophic surface currents (cm/s; vectors) leading to the ensuing strong (left), weak (middle), and normal (right) southwest monsoon season.

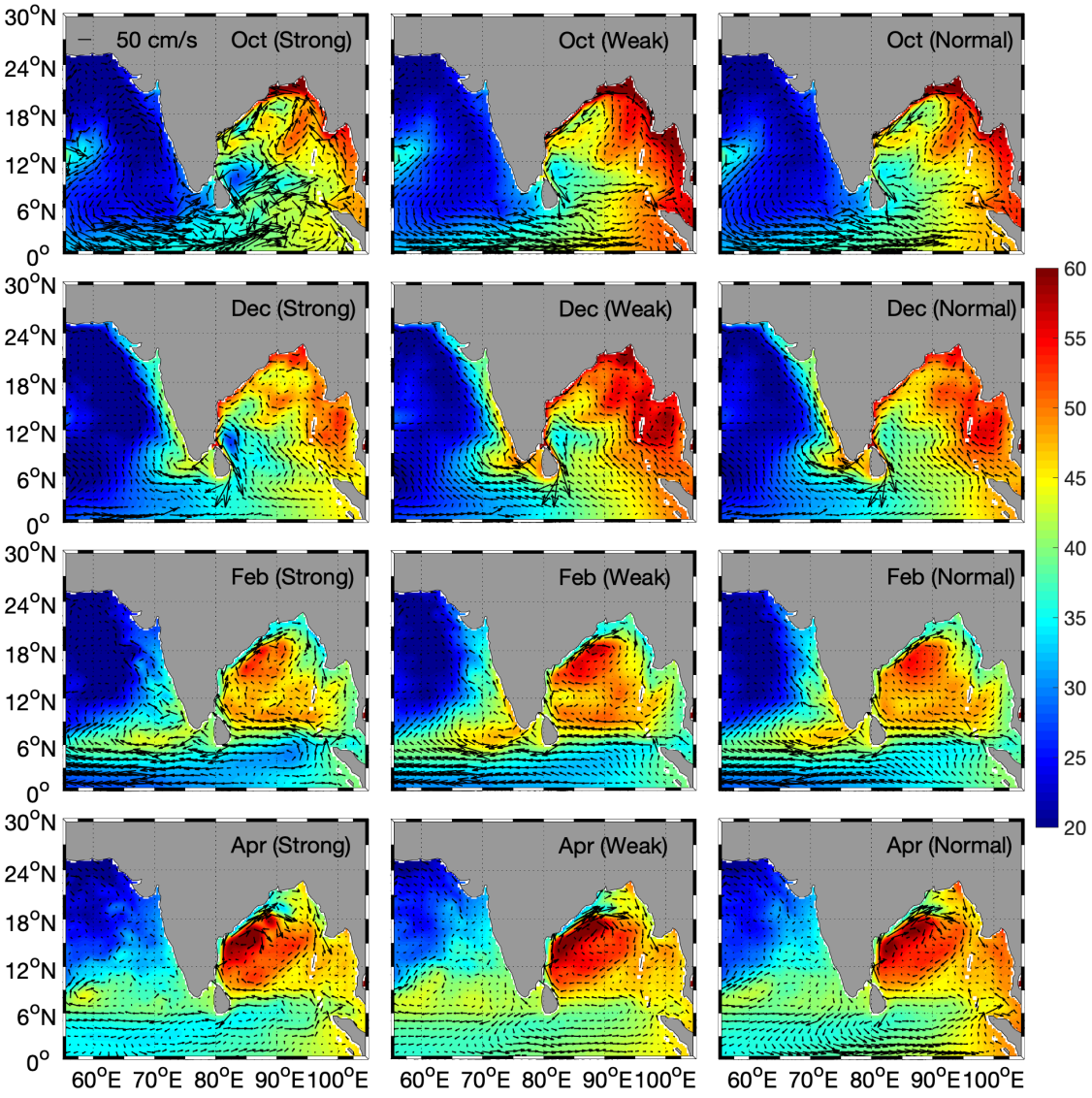

Figure 2.4. Composites of bimonthly distributions of ORAS5 sea surface height (cm; shaded) with overlaid ORAS5 geostrophic surface currents (cm/s; vectors) for October (1st row), December (2nd row), February (3rd row), and April (4th row) leading to the ensuing strong (left), weak (middle), and normal (right) southwest monsoon season.

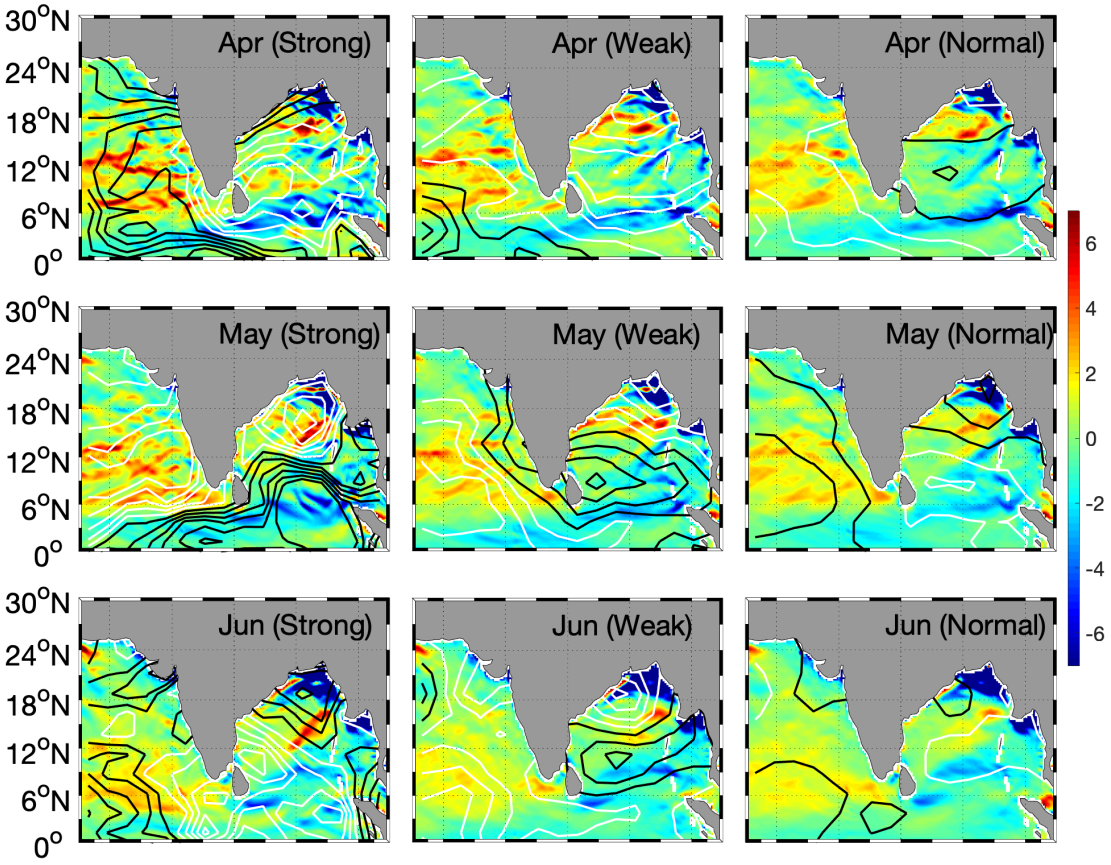

Figure 2.5. Composites of monthly distributions of ORAS5 meridional salt gradient (*10^2 psu/km) overlaid with NOAA-NCEP OLR anomaly contours as a proxy for ITCZ strength and position in the northern Indian Ocean for April (1st row), May (2nd row), and June (3rd row) during the strong (left), weak (middle), and normal (right) southwest monsoon season. Black (white) contours every 2 W/m^2 from 0 to ±10 to indicate negative (positive) OLR anomalies.

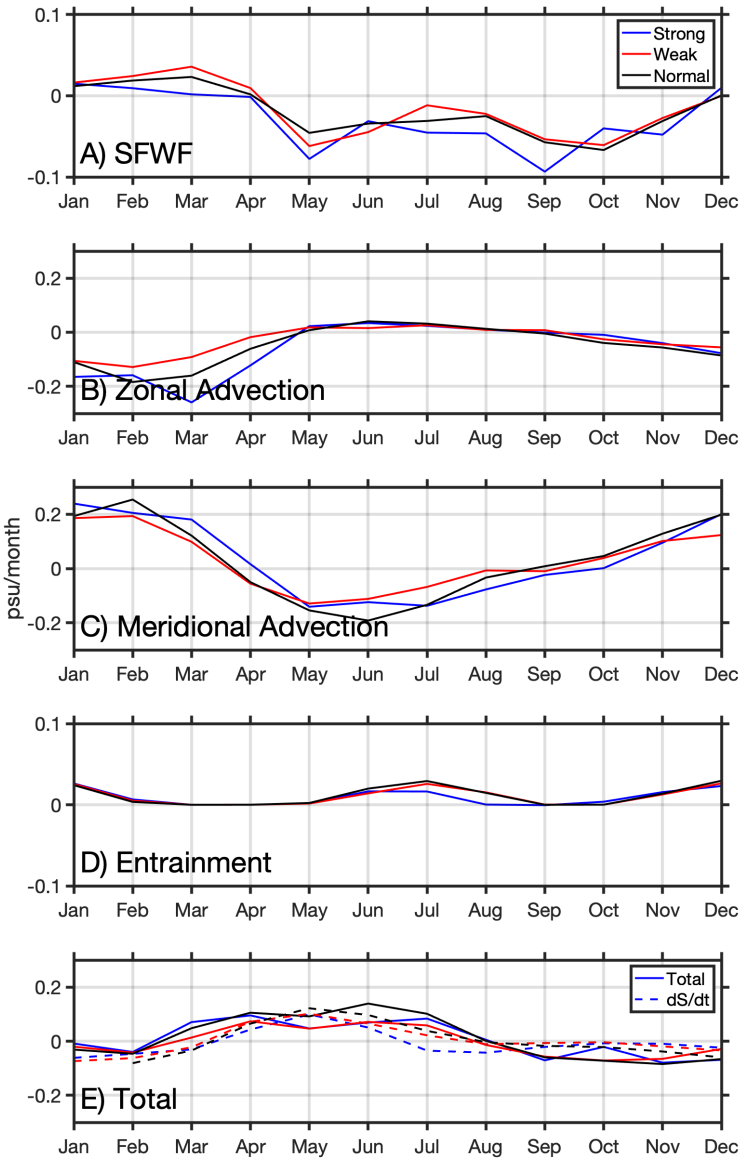

Figure 2.6. Composite time series of salt budget terms in psu/month a) surface freshwater flux (SFWF), b) zonal advection, c) meridional advection, d) entrainment, and e) the sum of terms a-d (solid lines) and the salinity tendency (dS/dt; dashed lines) for the SEAS region (6°-13ºN, 65°-75ºE) comparing a composite strong (blue), weak (red), and normal (black) southwest monsoon season.

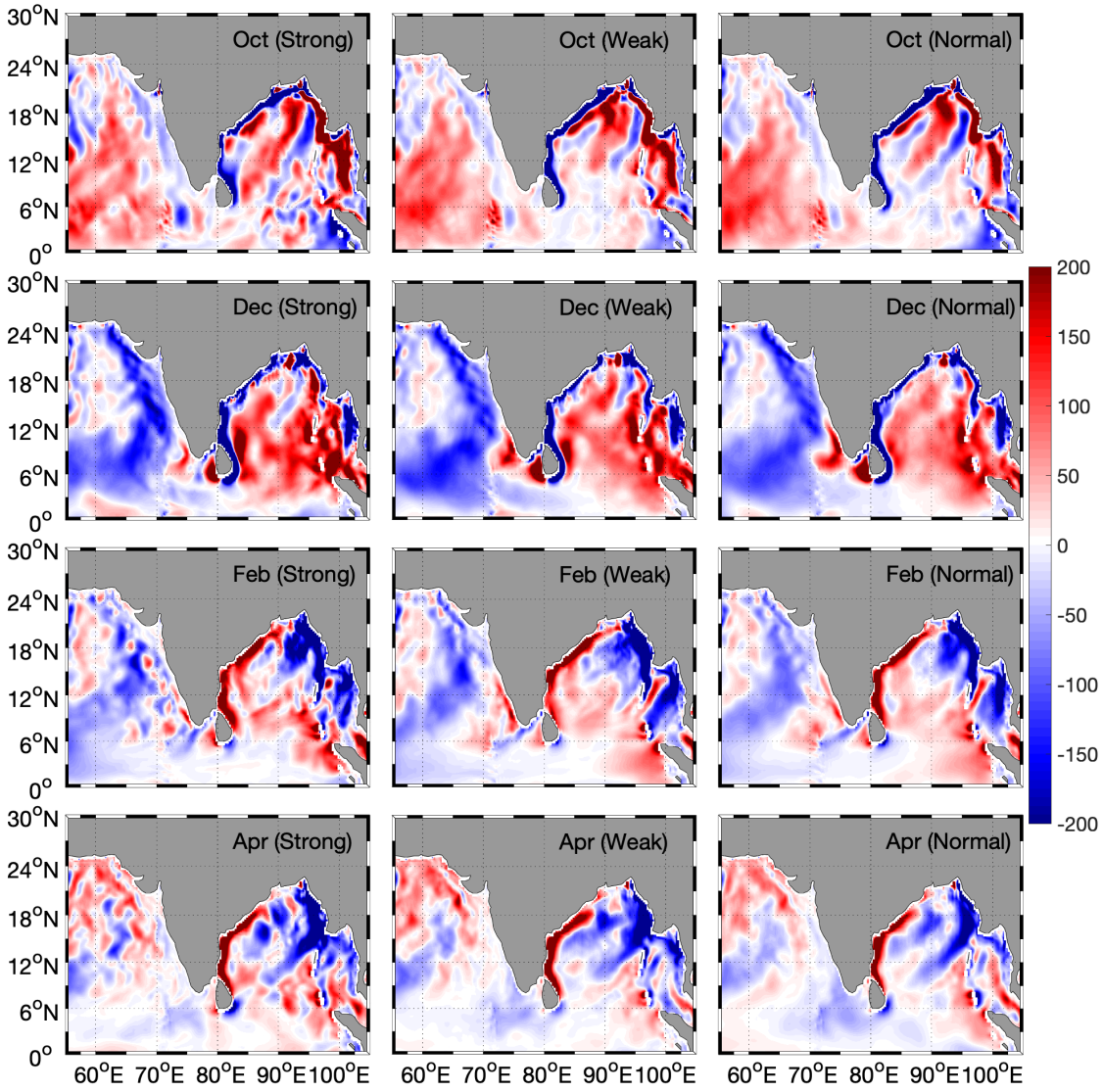

Figure 2.7. Bimonthly distributions of meridional surface advective freshwater flux (m^2/s) in the northern Indian Ocean for October (1st row), December (2nd row), January (3rd row) and April (4th row) leading to the ensuing strong (left; 1994), weak (middle; 2009), and normal (right; 2006) southwest monsoon season.

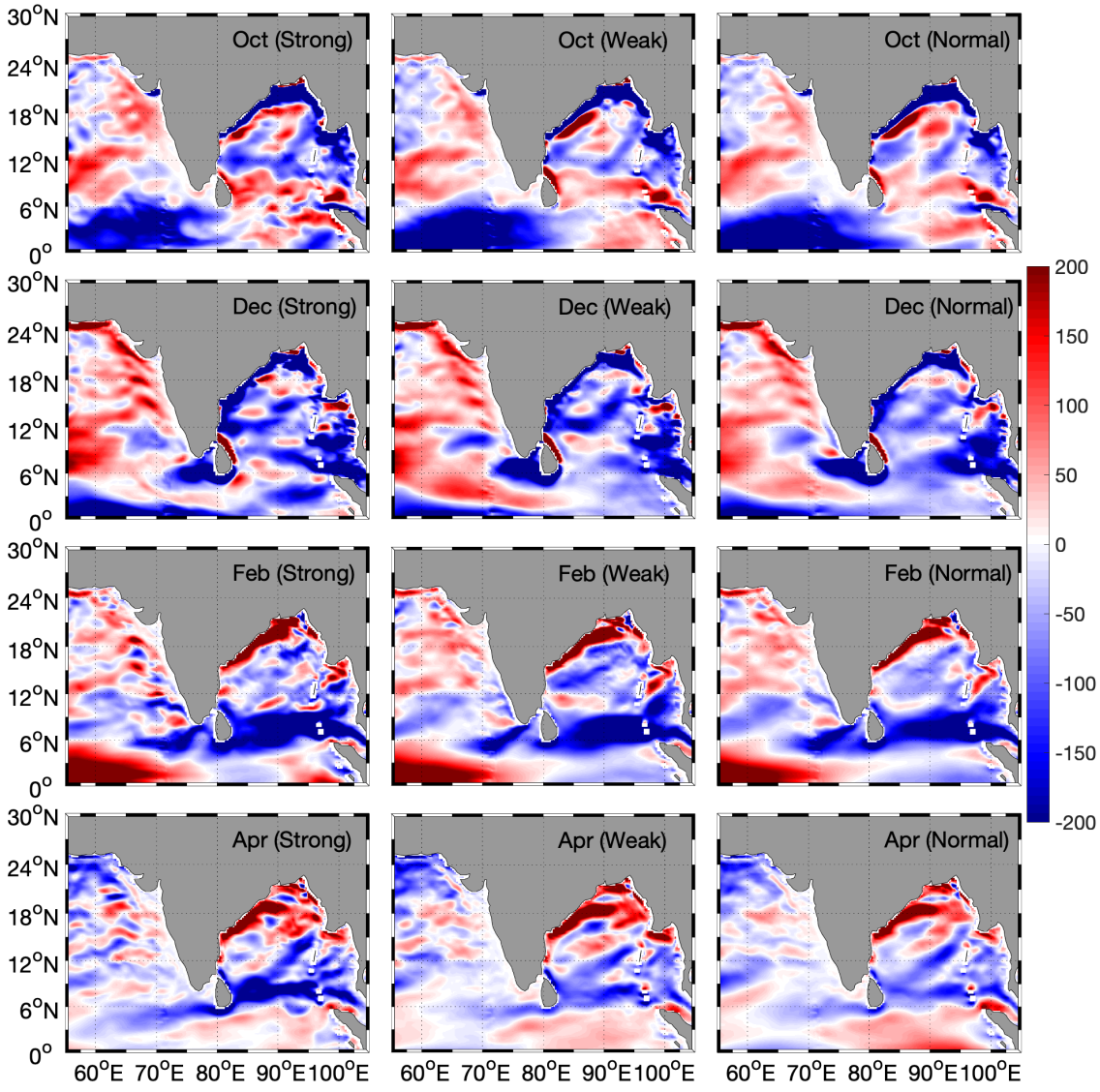

Figure 2.8. Bimonthly distributions of zonal surface advective freshwater flux (m^2/s) in the northern Indian Ocean for October (1st row), December (2nd row), January (3rd row) and April (4th row) leading to the ensuing strong (left; 1994), weak (middle; 2009), and normal (right; 2006) southwest monsoon season.

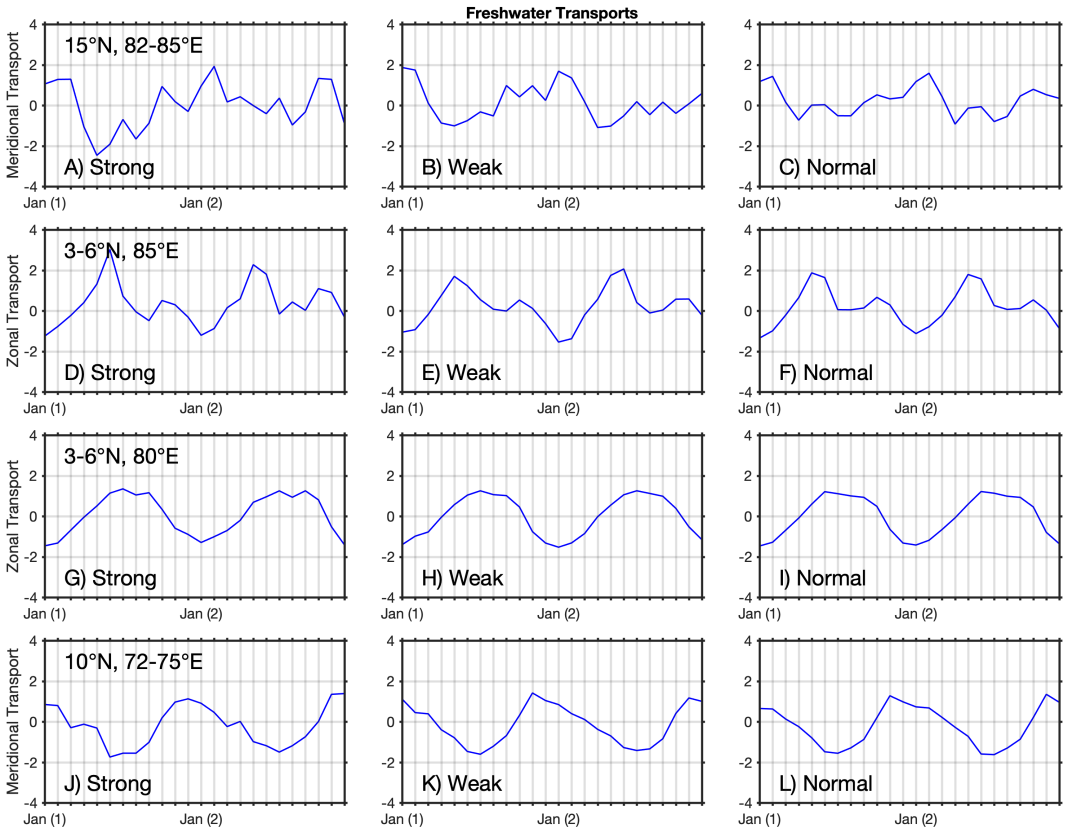

Figure 2.9. Time series of 0-45 m ORAS5 freshwater transports (blue; *10^8 kg/s), normalized to their own standard deviation and layer thickness, in sections at (A-C) 15ºN, 82°-85ºE, (D-F) 3°-6ºN, 85ºE, (G-I) 3°-6ºN, 80ºE, and (J-L) 10ºN, 72°-75ºE in the Bay of Bengal, South of Sri Lanka and SEAS leading to the ensuing composite strong (left), weak (middle), and normal (right) monsoon year.

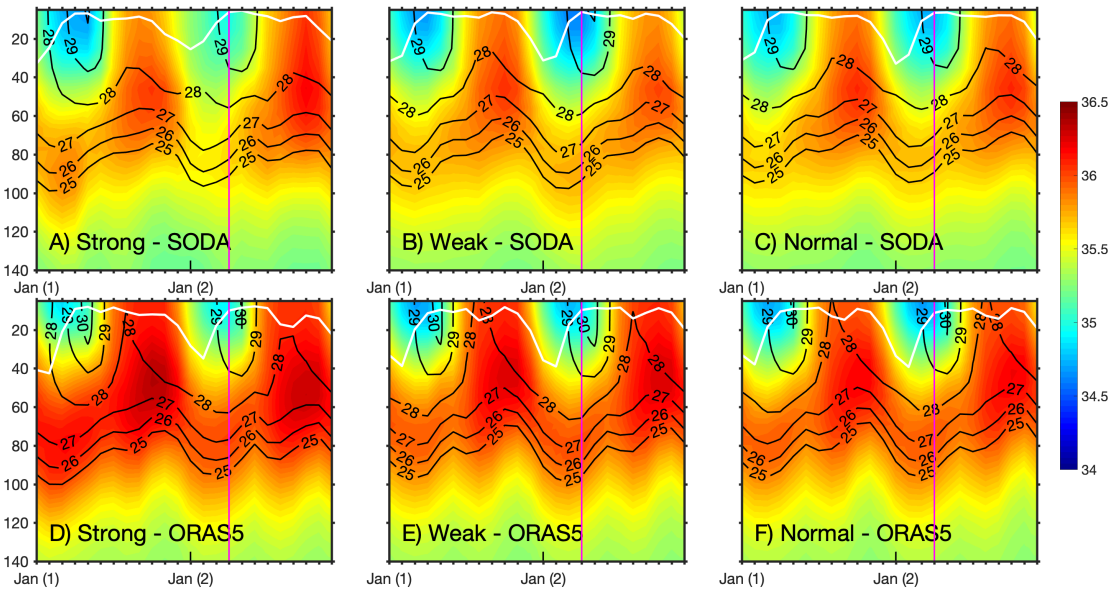

Figure 2.10. Composite time-depth plots of (A-C) SODA and (D-F) ORAS5 products of salinity (shaded; psu) and temperature (contours; °C) with overlaid barrier layer thickness (BLT in m, white line) calculated for each product in the SEAS region (6°-13ºN, 65°-75ºE) leading to and during a strong (1st column), weak (2nd column), and normal (3rd column) monsoon. A pink vertical line is drawn for April month of the given monsoon season.

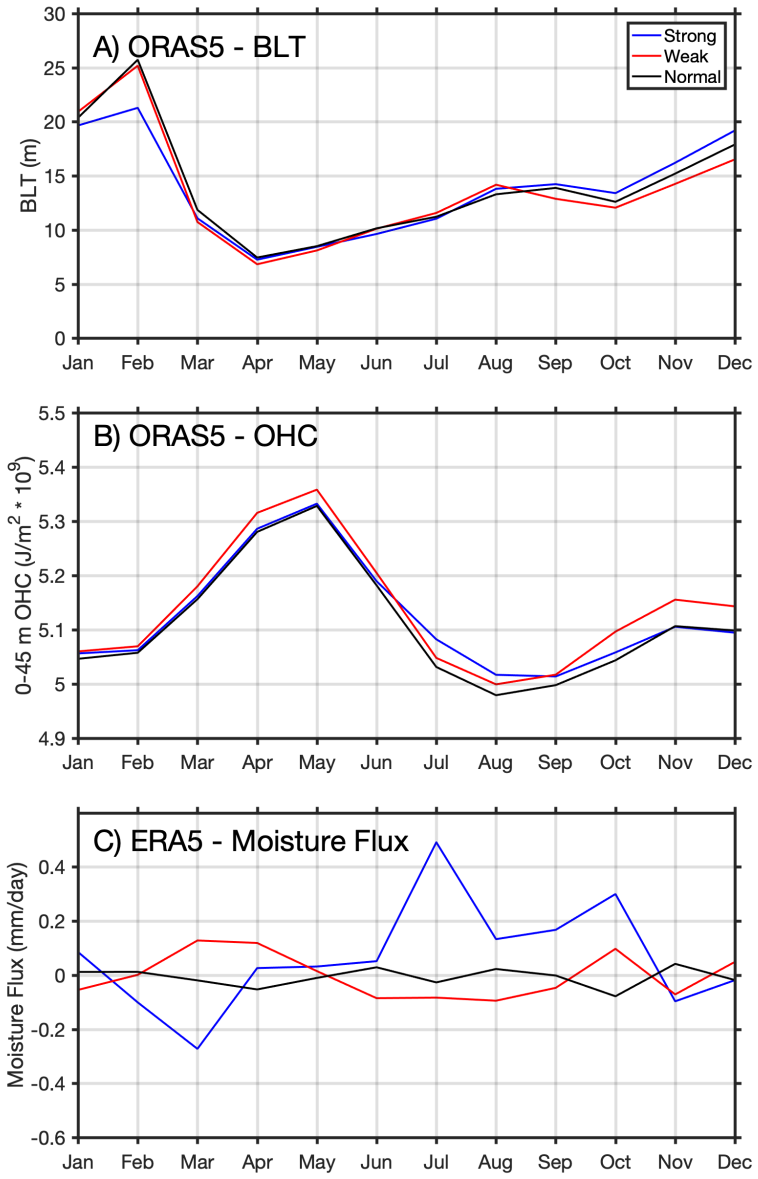

Figure 2.11. Composite time series of a) ORAS5 barrier layer thickness (BLT; m), b) ORAS5 upper ocean (0-45 m) heat content (*10^8 J/m^2), and c) ERA5 instantaneous moisture flux (mm/day) for the SEAS region (6°-13ºN, 65°-75ºE) comparing a composite strong (blue), weak (red), and normal (black) southwest monsoon season.

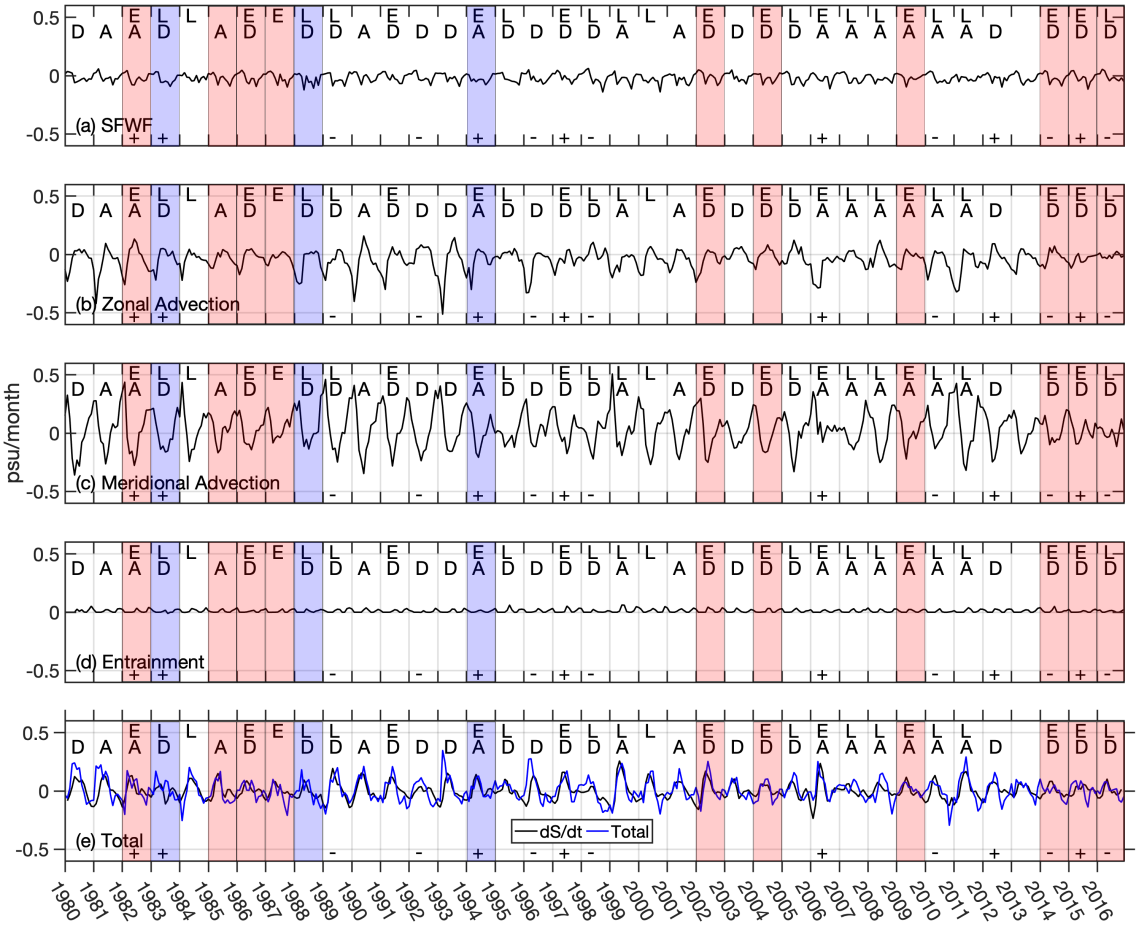

Figure 2.12. Individual terms of the mixed layer salt budget for the SEAS region (6-13ºN, 65-75ºE) from 1980 to 2016 using ORAS5 and ERA5 reanalysis, where (a) is the surface freshwater flux (SFWF), (b) is the zonal advection averaged in the mixed layer, (c) is the meridional advection averaged in the mixed layer, (d) is the entrainment in the mixed layer, and (e) is both the mixed layer salinity tendency (black) and the sum of SFWF, advection, and entrainment (blue). Red (blue) shading indicates a drought (flood) monsoon year. MOK is indicated as being delayed (D) or advanced (A), IOD phase is given as a (+) for a positive year and a (-) for a negative year, and El Niños (La Niñas) are indicated by an E (L).

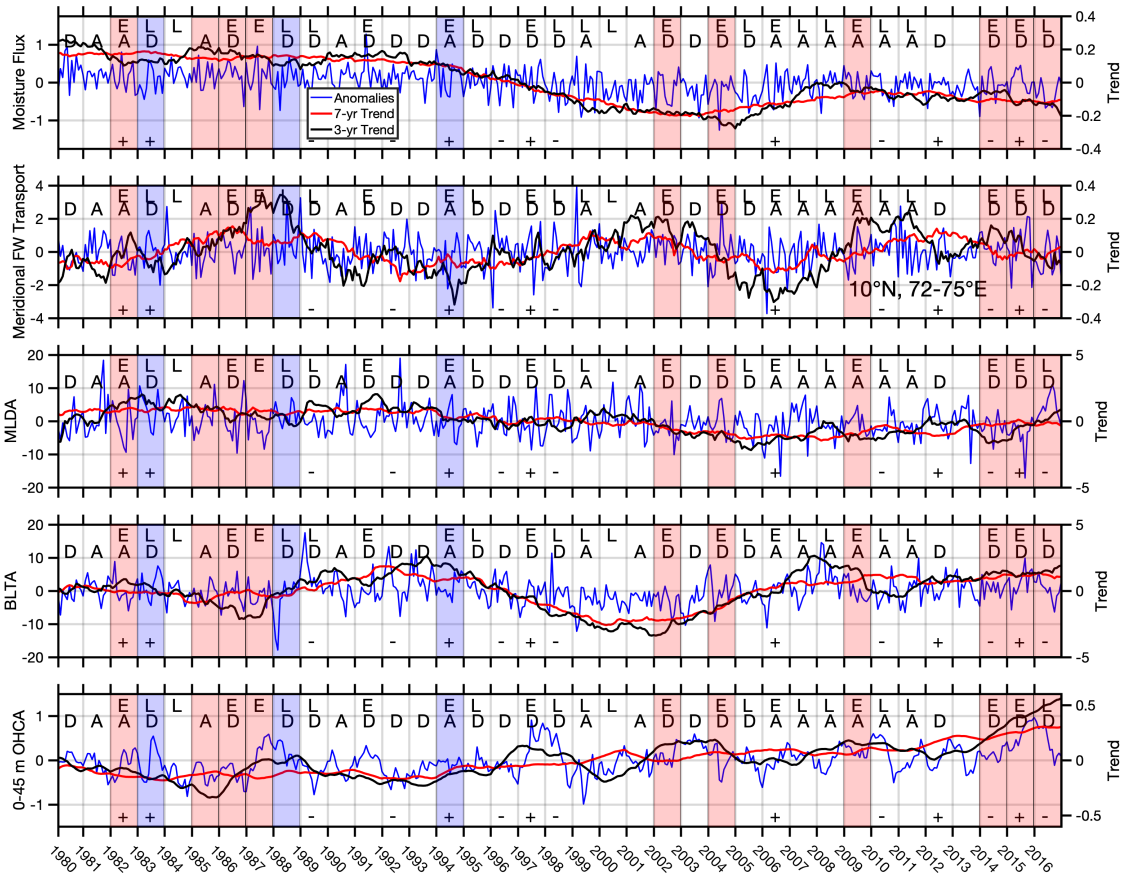

Figure 2.13. Time series of ERA5 instantaneous moisture flux anomalies (1st row; blue; mm/day), ORAS5 0-45 m layer meridional freshwater transport anomalies (normalized with its Standard Deviation) at 10ºN, 72-75ºE (2nd row; blue; * 10^8 kg/s), ORAS5 MLD anomalies (3rd row; m), ORAS5 BLT anomalies (4th row; blue; m), and ORAS5 0-45 m layer OHC anomalies (5th row; blue; J/m^2 *10^8). Red (black) curves indicate a 7-year (3-year) moving mean, whereas red (blue) shading indicates a drought (flood) monsoon year. Occurrences of El Niño (La Niña) are indicated by the letter E (L), MOK is indicated as being delayed (D) or advanced (A), and the occurrences of positive (+) phase and negative phase (-) of an IOD year is also marked.

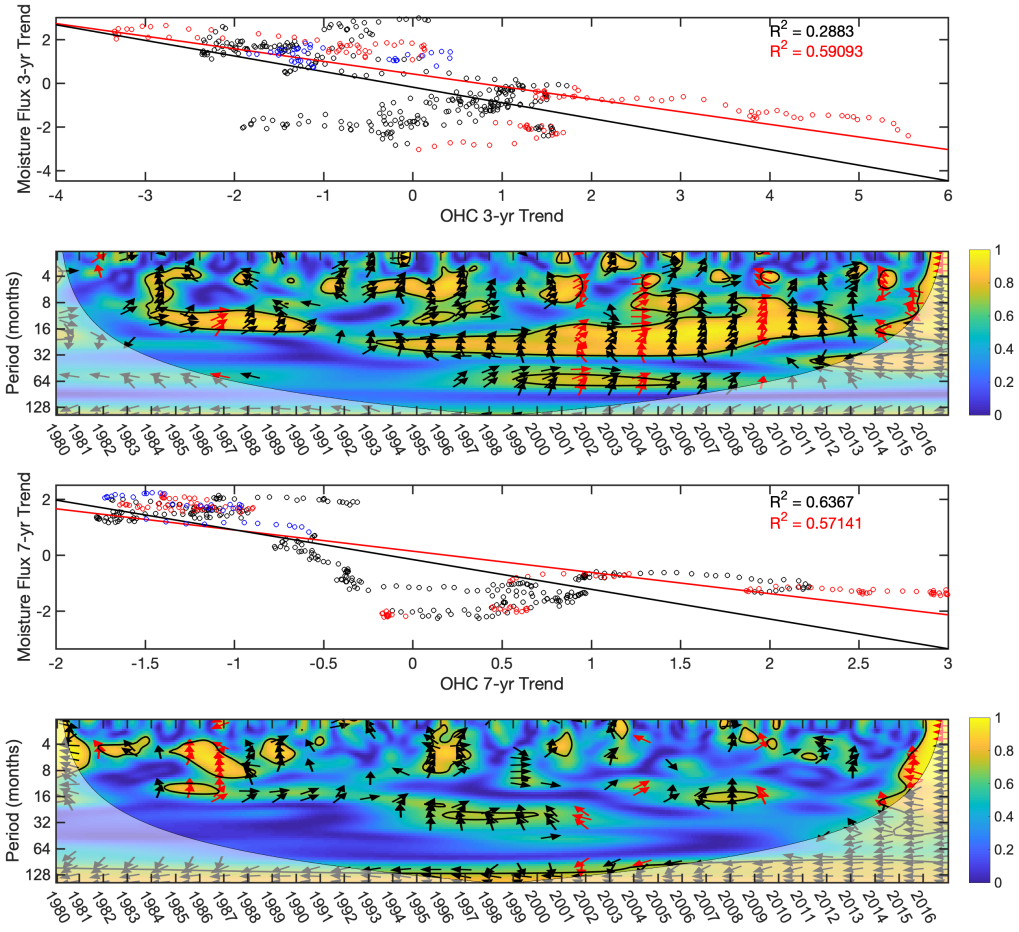

Figure 2.14. Scatter plots of 0-45 m OHC anomalies (*10^8 J/m^2) vs. moisture flux anomalies (mm/day) for the (1st row) 3-year trend and (3rd row) 7-year trend, where strong monsoons are in blue, weak monsoons are in red, and normal monsoons are in black. Wave coherence transforms of the 3-year trends (2nd row) and of the 7-year trends (4th row). Red (black) trend lines indicate weak (normal) monsoon trends. Wave coherence shading indicates an R^2 value and black outlines indicate 95% significance. Arrows indicate when the time series are in phase (to the right), anti-phase (to the left), or if the moisture flux trend leads (pointing up) or lags (pointing down) the OHC trend. White shading indicates the cone of influence where the time series is too short for patterns to be statistically significant (Grinsted et al., 2004).

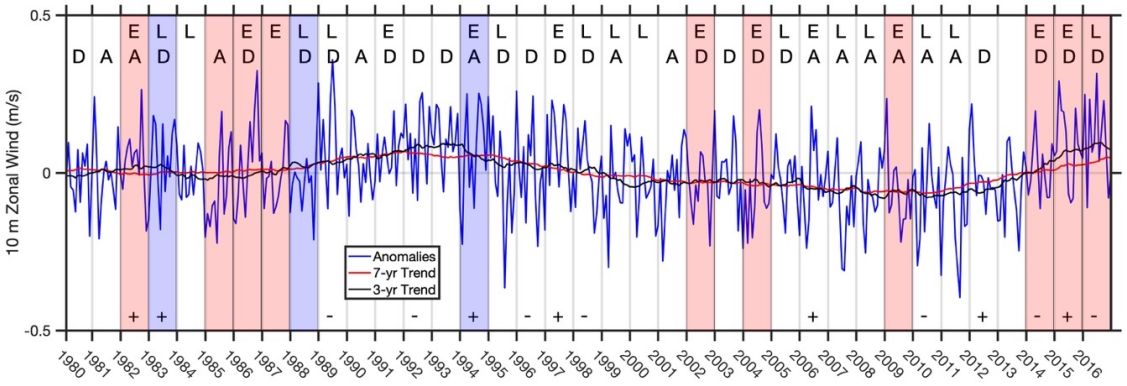

Figure 2.15. Times series of ERA5 10 m zonal wind anomalies (blue; m/s). Red (black) lines indicate a 7-year (3-year) moving mean, whereas red (blue) shading indicates a drought (flood) monsoon year. MOK is indicated as being delayed (D) or advanced (A), IOD phase is given as a (+) for a positive year and a (-) for a negative year, and El Niños (La Niñas) are indicated by an E (L).

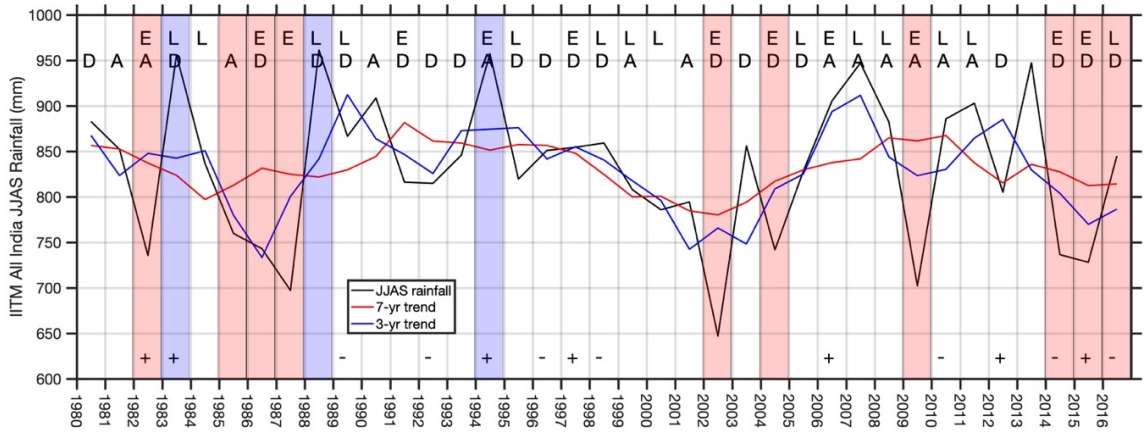

Figure 2.16. Time series of IITM All India JJAS rainfall (blue; mm/season) from 1980 to 2016. Red (black) lines indicate a 7-year (3-year) moving mean, whereas red (blue) shading indicates a drought (flood) monsoon year. MOK is indicated as being delayed (D) or advanced (A), IOD phase is given as a (+) for a positive year and a (-) for a negative year, and El Niños (La Niñas) are indicated by an E (L).

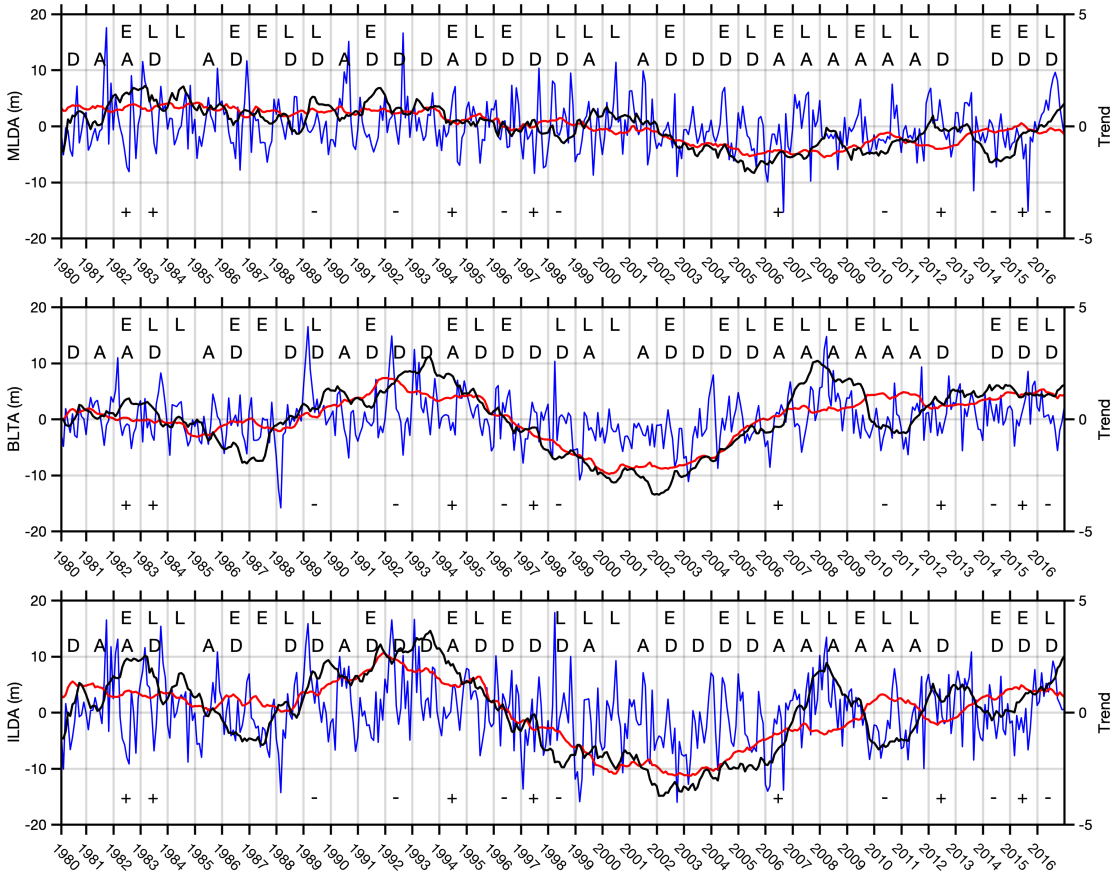

Figure 2.S1. ORAS5 mixed layer depth anomalies (MLDA; top; m), barrier layer thickness anomalies (BLTA; middle; m), and isothermal layer depth anomalies (ILD; bottom; m) for the SEAS region. Red (black) lines indicate a 7-year (3-year) moving mean. MOK is indicated as being delayed (D) or advanced (A), IOD phase is given as a (+) for a positive year and a (-) for a negative year, and El Niños (La Niñas) are indicated by an E (L).

CHAPTER 3

MONITORING INTRASEASONAL OSCILLATIONS IN THE INDIAN OCEAN USING SATELLITE OBSERVATOINS[2]

---

[2]Roman-Stork, H. L., Subrahmanyam, B., & Trott, C. B. (2020). Monitoring intraseasonal oscillations in the Indian Ocean using satellite observations. Journal of Geophysical Research: Oceans, 125, e2019JC015891. https://doi.org/10.1029/2019JC015891

ABSTRACT

Intraseasonal oscillations (ISOs) in the Indian Ocean play a significant role in determining the active (wet) and break (dry) cycles of the southwest monsoon rainfall. In this study, we use satellite-derived precipitation, sea level anomalies (SLAs), sea surface salinity (SSS), sea surface temperature, and surface winds to monitor the 30-90-day, 10-20-day, and 3-7-day ISOs, and how they influence local dynamics. The main focus of this work, however, is showing the importance of using SLA and SSS to monitor ISOs. Mixed Rossby gravity waves were found to induce convection associated with the southern cell of the 10-20-day mode, with surface winds from the northern cell modulating coastal Kelvin waves in the Bay of Bengal. The 10-20-day SSS response is instead more closely related to wind-induced upwelling in the central Bay of Bengal and river runoff in the northern Bay. The 3-7-day mode was found to have a weak oceanic signal, as the monsoon trough is mainly positioned over land, though SSS captured the structure of the signal most clearly. This study highlights the need for high spatial resolution SLA in order to adequately capture 3-7-day oscillations in the monsoon trough.

3.1 INTRODUCTION

The Indian monsoon system is dynamically complex and highly variable, influenced by multiple interannual and intraseasonal processes that modulate its seasonal rainfall. Of these, intraseasonal oscillations (ISOs) are primary contributors to southwest monsoon rainfall variability characterized by active (wet) and break (dry) phases. There are several ISOs that operate on different timescales, the most prominent being the 30-90-day, the 10-20-day, and the 3-7-day oscillations (Goswami et al., 1998, 2003; Pillai & Chowdary, 2016). The 30-90-day mode commonly describes the Madden-Julian

Oscillation (MJO), with a northward propagating phase referred to as either the monsoon intraseasonal oscillation (MISO) or boreal summer intraseasonal oscillation (BSISO; Ajayamohan et al., 2011; Girishkumar et al., 2017; Krishnamurti et al., 2017; Madden & Julian, 1971; Wheeler & Hendon, 2004; Zhang, 2005). The 10-20-day mode, or quasibiweekly oscillation, is a westward propagating system over the Bay of Bengal (BoB) and equatorial Indian Ocean (Chatterjee & Goswami, 2004; Kikuchi & Wang, 2009; Murakami, 1976; Roman-Stork et al., 2019). The 3-7-day mode is due to oscillations in the monsoon trough and is chiefly responsible for the active and break cycles of the southwest monsoon that have spectral peaks between 4 and 5 days (Trott et al., 2019). These ISOs are responsible for a significant portion of monsoonal variability, and while there has been extensive ISO research on the atmospheric side, there remains a gap in knowledge and understanding how oceanic parameters respond to and influence both the atmosphere and other oceanic parameters. As intensification and modulation of ISOs, and therefore their magnitude of influence on monsoonal rainfall, is due to air-sea coupling, it is critically important that we better understand the behavior of the complex oceanic processes involved.

As the MJO and MISO are primarily atmospheric phenomena, the overwhelming majority of research has gone into understanding the related atmospheric dynamics and how the MJO impacts other atmospheric processes, such as tropical cyclones (Sobel & Maloney, 2000). In recent years, however, there has been an increased interest into how the ocean impacts MJO initiation and propagation, as well as the impact both the MJO and MISO have on the ocean (Chen et al., 2017; Cheng et al., 2013; Krishnamurti et al., 2017;

Matthews, 2008; Straub, 2013; Vecchi & Harrison, 2002; Webber et al., 2010, 2012). Webber et al. (2012) found the triggering mechanism for MJO initiation in the western Indian Ocean to be a highly coupled process. The seasonal reversal of winds in the Somali Current region trigger an equatorial Kelvin wave response that propagate eastward across the Indian Ocean and reflect back as a downwelling Rossby wave. This Rossby wave deepens the mixed layer and thermocline, warming sea surface temperatures (SSTs), and triggering atmospheric MJO convection (Aiyyer & Molinari, 2003; Chen et al., 2017; Grunseich, Subrahmanyam, Arguez, 2011; Grunseich, Subrahmanyam, Murty, et al., 2011; Grunseich & Subrahmanyam, 2013; Hendon et al., 1998; Li et al., 2015; Matthews, 2008; Webber et al., 2010, 2012). Using satellite altimetry data, Grunseich and Subrahmanyam (2013) were able to confirm the impact Kelvin and Rossby waves have on MJO initiation, showing that satellite observations can be used to accurately monitor and predict these ISOs.

While Kelvin and Rossby waves have been clearly seen in sea surface height (SSH) and SSTs for years (Webber et al., 2010, 2012), studies of MJO sea surface salinity (SSS) variability did not come into prominence until the launch of the National Aeronautics and Space Administration's (NASA) Aquarius mission in 2011 and the Soil Moisture Active Passive (SMAP) mission in 2015 (Grunseich & Subrahmanyam, 2013; Grunseich, Subrahmanyam, & Wang, 2013; Grunseich, Subrahmanyam, Murty, et al., 2011; Shoup et al., 2019; Subrahmanyam et al., 2018). Grunseich, Subrahmanyam, and Arguez (2011), Grunseich, Subrahmanyam, Murty, et al. (2011) found the SSS response to vary depending on the seasonal occurrence of the MJO, with the SSS response found to be much weaker and with a longer period than the atmospheric MJO overall.

The northward propagating MISO in the BoB has been the focus of a number of studies analyzing the SST, SSS, SSH, ocean currents, and ocean heat content in the BoB on intraseasonal timescales (Ajayamohan et al., 2011; Chen et al., 2017; Cheng et al., 2013; Girishkumar et al., 2013, 2017; Krishnamurti et al., 2017; Rao et al., 2011; Subrahmanyam et al., 2018; Trott & Subrahmanyam, 2019; Vecchi & Harrison, 2002). These studies have found that MISO SST variability in the northern BoB can serve as a predictor for active and break cycles (Vecchi & Harrison, 2002) and that there is a 4-day lag between atmospheric wind forcing and the ocean response (Krishnamurti et al., 2017). This highlights the complex nature of this coupled system, where certain oceanic parameters may lead and trigger atmospheric events, whereas other changes occur in response to them. In this study, we intend to explore this interplay of parameters further.

Although the MJO and MISO are the dominant ISOs, the 10-20-day mode still contributes significantly to monsoon variability (Chatterjee & Goswami, 2004). There are 10-20-day spectral peaks in atmospheric variability globally (Kikuchi & Wang, 2009); however, the most relevant to the southwest monsoon is most predominant over the BoB and ranges from the western Pacific to the Arabian Sea (AS). The 10-20-day mode in the Indian Ocean consists of a double cell structure of atmospheric convection, with the northern cell centered over 15–20°N and the southern cell positioned around the equator in the BoB (Chatterjee & Goswami, 2004; Chen & Chen, 1993; Krishnamurti & Ardanuy, 1980; Roman-Stork et al., 2019). The northern cell is generated by breaking Rossby waves in the upper atmosphere over the Pacific Ocean, which triggers convection over the South China Sea (Ortega et al., 2017). This convective cell then propagates westward into the BoB where it rapidly intensifies. The southern cell is generated in the Indian Ocean itself

and becomes phase-locked with the northern cell in the BoB before the entire system propagates westward and slowly weakens over India. The northern cell reaches its demise over the AS, and the southern cell breaks apart in the southern Indian Ocean (Kikuchi & Wang, 2009; Roman-Stork et al., 2019).

While the structure and dynamics of the 10-20-day mode in the atmosphere are reasonably well understood, the corresponding signature and dynamics in the ocean are less so, with few studies focused on the ocean (Chatterjee et al., 2013; Miyama et al., 2006; Roman-Stork et al., 2019; Sengupta et al., 2001; Sengupta et al., 2004; Subrahmanyam et al., 2018; Trott et al., 2019; Trott & Subrahmanyam, 2019). Ocean currents and meridional surface winds in the eastern equatorial Indian Ocean were found to exhibit strong biweekly variability, with fluctuations in this wind stress exciting a westward wave response that is associated with a pattern of upwelling and downwelling along the coastal boundary (Sengupta et al., 2001; Sengupta et al., 2004). Within the BoB, SSS responses have been found to be predominantly forced by river runoff in the northern Bay and by wind-induced Ekman processes in the central Bay for all ISOs, with the signal in the northern Bay being the strongest (Roman-Stork et al., 2019; Subrahmanyam et al., 2018; Trott et al., 2019). Mixed Rossby Gravity (MRG) or Yanai waves in the Indian Ocean that also occur on biweekly timescales and have been shown to have the same structure as the 10-20-day mode (Chatterjee et al., 2013; Miyama et al., 2006; Sengupta et al., 2004).

The 3-7-day oscillations in the monsoon trough, or tropical convergence zone, are representative of the active (wet) and break (dry) cycles of the monsoon (Gadgil & Asha, 1992; Gadgil & Joseph, 2003; Goswami et al., 2003; Krishnamurti & Bhalme, 1976; Trott et al., 2019). The monsoon trough is primarily positioned over land around 25°N

(Krishnamurti & Bhalme, 1976), with only a secondary mode over the ocean (Gadgil & Asha, 1992), and so the 3-7-day mode in the ocean is much weaker than the other ISOs. These active and break phases are heavily influenced by other ISOs, both through the cascading of energy and through dynamic interactions of these ISOs with the monsoon trough (Gadgil & Asha, 1992; Trott & Subrahmanyam, 2019). While there have been numerous studies that have examined the impact of various oceanic and atmospheric processes on active and break cycles of the monsoon (Gadgil & Joseph, 2003), very few have directly focused on the 3-7-day mode in the ocean (Subrahmanyam et al., 2018; Trott et al., 2019; Trott & Subrahmanyam, 2019).

As ISOs are the primary contributors to the active and break cycle of the southwest monsoon, it is critically important that we develop a better understanding of feedback with the ocean. By furthering our understanding of the dynamics involved, it will be possible to improve our forecasting and monitoring of ISOs and active and break cycles of the monsoon, which motivates this research. In this study, we take a multiparameter approach to understanding ISO variability and dynamics using satellite observations in the Indian Ocean, BoB, and AS with the overall goal of showing how ocean-observing satellites can be used to monitor these events. Our research combines satellite-derived precipitation, sea level anomalies (SLAs), and SSS observations to understand how these ocean properties influence one another and the atmosphere for the first time. This research is structured as follows: section 3.2 presents the data and methodology, section 3.3 both presents and discusses the findings of our study, and section 3.4 concludes the study.

3.2 DATA AND METHODS

A. OCEAN PARAMETERS

SLA from blended altimetric observations originally developed by AVISO+ (Archiving, Validation, and Investigation of Satellite Oceanography) are used in this study at daily temporal resolution on a 0.25° grid from 2015 through 2018 and are obtained from the Copernicus Marine and Environmental Monitoring Service (CMEMS; marine.copernicus.eu). This blended product combines all altimeter mission observations from Jason-1, Jason-2, Jason-3, Sentinel-3A, HY-2A, Saral/AltiKa, Cryosat-2, Topex/Poseidon, ENVISAT, GFO, and ERS 1/2 (Ducet et al., 2000; Le Traon et al., 1998) and has been reliably used in the Indian Ocean (Li et al., 2018; Rao et al., 2011). SSS data from NASA's SMAP mission were taken from the Physical Oceanography Distributed Active Archive Center (PO.DAAC) at NASA's Jet Propulsion Lab (JPL) and is processed with the Combined Active Passive (CAP) algorithm as SMAPv4.2 (Entekhabi et al., 2010; Fore et al., 2016). SMAP SSS is available from April 2015 through present on a 0.25° grid globally and is found to resolve salinity variability in the Indian Ocean, including around coastlines (Agarwal et al., 2016; Prend et al., 2018; Subrahmanyam et al., 2018). SMAP-CAP was chosen because the addition of the CAP algorithm has been shown to significantly improve ISO identification, particularly along the coast (Shoup et al., 2019) and has the daily temporal resolution necessary to resolve higher frequency ISOs. SST data were taken from National Oceanographic and Atmospheric Administration (NOAA)'s Optimally Interpolated SST version 2 (OISSTv2) from daily blended Advanced Very High Resolution Radiometer observations (AVHRR; Reynolds et al., 2007). OISST is available from NOAA National Center for Environmental Information (NCEI) with 0.25° horizontal

grid spacing and was obtained from 2015 to present. OISST is a widely used product in the tropics and has been widely used in ISO studies in the region (Girishkumar et al., 2017; Murty et al., 2004).

B. ATMOSPHERIC PARAMETERS

Daily precipitation data from the NOAA Global Precipitation Climatology Project (GPCP) version 1.2 were obtained from 2015 to present on a 1° horizontal grid from NOAA's NCEI (Huffman et al., 1997) and has been shown to adequately capture intraseasonal and monsoon variability (Rao et al., 2011; Vinayachandran et al., 2002; Zhang, 2005). Surface wind observations were taken from the Cross-Calibrated Multi-Platform version 2.0 (CCMPv2.0) product available from Remote Sensing Systems (RSS) every 6 hours at 0.25° horizontal grid spacing. CCMP combines surface vector wind observations from scatterometers, moored buoys, and the ERA-Interim 10-m winds from the European Centre for Medium-Range Weather Forecasts (ECMWF) to create a global blended wind field at high temporal resolution (Atlas et al., 2009, 2011). CCMP winds have been reliably used in monsoon studies in the Indian Ocean (Chen et al., 2017; Li et al., 2015; Zhang et al., 2017).

C. METHODS

To isolate the various ISO signals, box-averaged time series, time-latitude, and time-longitude sections were bandpass filtered with a fourth-order Butterworth bandpass filter, both backward and forward, to eliminate edge effects and isolate each periodicity (Krishnamurti et al., 2017; Roman-Stork et al., 2019; Shoup et al., 2019; Subrahmanyam et al., 2018; Trott et al., 2019). Wavelet analysis was also conducted to identify dominant

periodicities and ISOs, following the methodology of Grinsted et al. (2004). Using box-averaged bandpass filtered time series of GPCP precipitation over the Indian Ocean, spatial composites were constructed based on the methodology in Roman-Stork et al. (2019). Ensemble Empirical Mode Decomposition (EEMD) analysis was performed on the time series to identify the relevant intrinsic mode functions (IMFs) for each ISO, and the relevant IMFs were averaged together to create an ISO time series (Huang & Wu, 2008; Wu & Huang, 2009). IMFs 4 and 5 were averaged for the 30-90-day ISO, IMFs 2 and 3 were averaged for the 10-20-day ISO, and IMFs 1 and 2 were averaged for the 3-7-day ISO. Peaks greater than 1 standard deviation above the mean were then used to construct composites. Spatial composites were spatially filtered following the methodology in Roman-Stork et al. (2019) using a wavelength-based bandpass filter for ISO wavelength to isolate events. The 30-90-day composites were filtered between 5,000 and 10,000 km, the 10-20-day composites were filtered between 3000 and 6000 km, and the 3-7-day composites were filtered between 1,000 and 9,000 km (Hendon et al., 1998; Miyama et al., 2006; Sengupta et al., 2004).

3.3 Results and Discussion

A. ISOs Throughout the Indian Ocean

ISOs in the Indian Ocean are some of the major controllers of the active and break cycles of southwest monsoon precipitation; however, there is significant variability of ISO strength as a function of periodicity and location, particularly with regard to the two basins in the northern Indian Ocean. The strongest ISOs of all periodicities are in the BoB (Figure 3.1u), and the weakest are those averaged over the full Indian Ocean (Figure 3.1m). In the unfiltered signal, a seasonal pulse is seen that is strongest in the BoB and over all periods

less than 90 days. The 30-90-day signal shows significant interannual variability, with high-amplitude events aligning with a strong MJO, such as in 2015. Though the MJO is a tropical event, it is interesting that there is no high-amplitude signal in the larger Indian Ocean box (taken only between 20°N and 20°S). This may indicate dominance of MISO rather than MJO events within this band but is likely a result of the box size of the Indian Ocean washing out the signal. The 10-20-day signal is also strongest in the BoB due to the location of the northern cell of the double cell structure, which has the majority of the rainfall and propagation associated with the 10-20-day signal (Chatterjee & Goswami, 2004; Kikuchi & Wang, 2009; Krishnamurti & Ardanuy, 1980; Roman-Stork et al., 2019). The 3-7-day ISO in the BoB is strongest during the southwest monsoon season and in the BoB, clearly responding to the positioning of the monsoon trough. Other seasons are too dry to note any ISO activity in precipitation. There is also a seasonal pulse in the AS in the 3-7-day signal, though it is weaker than that in the BoB, again indicative of the location of the monsoon trough and possibly tropical cyclone activity. There is one unusually high-amplitude precipitation event at the very beginning of the 2014 summer monsoon season that may be attributed to Cyclonic Storm Nanauk (Deb et al., 2016) and its interactions with the monsoon trough and MJO activity that modulated the observed ISOs.

Previous studies of ISO SSS have shown SMAP-CAP to be the most robust satellite salinity product for observing ISOs (Shoup et al., 2019; Trott et al., 2019) as it has the spatial resolution, proximity to the coast, and accuracy necessary to adequately capture ISO signals. Salinity variability in the unfiltered SMAP-CAP data is close to ±0.5 psu in the BoB and AS ±0.3 psu in the Indian Ocean (Figure 3.2), where total variability is higher than the global SMAP-CAP accuracy (0.2 psu; Fore et al., 2016). The 30-90-day ISO in

SSS clearly shows well-known major MJO events, such as the one in October–November 2015 and throughout 2017 (Trott et al., 2019). The SSS 10-20-day signal in the BoB has a strong seasonal pulse, which is due both to the precipitation seen in Figure 3.1 and to the seasonal discharge of river water from the Ganges-Brahmaputra river basin. Peaks are typically seen in April and October. The 10-20-day signal in the AS and the Indian Ocean show individual events in October 2015 and April 2018, but no other strong pulses. The 3-7-day signal is stronger in the basins than the Indian Ocean and is extremely noisy, reflecting the overall location of the monsoon trough and the synoptic-scale weather variability on this timescale.

The variability of SLA is large in the BoB and AS during the propagation of ISOs in these basins. The clearest seasonal cycle in SLA is seen in the AS, consistent with the vertical motion induced by monsoon winds and the cycle of Rossby waves that propagate across the basin (R. R. Rao et al., 2010; Shankar & Shetye, 1997; Sreenivas et al., 2012). Figure 3.3q clearly shows the dominance of the seasonal cycle on SLA. The BoB shows a weaker seasonal cycle and significantly more intraseasonal variability. For the 30-90-day signal, the 2017 MJOs are seen in the Indian Ocean, pulses are seen in the AS in 2015 and 2017, and in the BoB are seen in 2016–2017. As there is a relationship between Rossby waves and MJO initiation, due to local mixed layer dynamics and changes in upper ocean stratification, it is likely that these anomalous signals in SLA are due to the anomalous Rossby waves that led to these MJO events (Roundy, 2008; Roundy et al., 2009; Webber et al., 2010, 2012). The 10-20-day ISO is relatively noisy and is due to downward cascading of energy from higher-period equatorial oscillations (Cheng et al., 2013, 2017; Trott & Subrahmanyam, 2019), eddying, and MRG waves (Chatterjee et al., 2013; Sengupta et al.,

2001). The 3-7-day signal is very noisy, but a larger amplitude signal in the BoB can still be seen, followed by the AS and then the IO.

B. INTRASEASONAL OSCILLATIONS (30-90-DAYS)

The atmospheric spatial structure of the 30-90-day ISO (MJO) has been well documented in previous research (Matthews, 2008; Pai & Rajeevan, 2009; Waliser et al., 2005; Webber et al., 2012; Wheeler & Hendon, 2004; Zhang, 2005) and is most often described as alternating phases of enhanced and suppressed convection over the equatorial Indian and Pacific Oceans as an eastward propagating system. Spatial lag composites of MJO events from 2015–2018 were constructed based on a box-averaged time series of daily precipitation over the entire Indian Ocean (20°S–20°N, 40–100°E), with the peak of enhanced convection (precipitation) in the Indian Ocean at day 0 (Figure 3.S1 in the supporting information). From day −20 to day −10, the suppressed phase (dashed boxes in Figure 3.S1) dominates the Indian Ocean, with the enhanced phase (solid boxes in Figure 3.S1 beginning to generate around day −10. By day −5, the enhanced phase has generated in the western/central Indian Ocean and begins to propagate eastward across the basin. The timing and location of this initiation of this enhanced phase of the MJO align with composites of SLA, which show a downwelling Rossby wave in the same location shortly before (Figure 3.4), which follows the initiation theory posed by Webber et al. (2012). By day +5, a northward propagating branch of the enhanced convective cell moves into the BoB and continues to propagate northward into the BoB through day +15. This northward propagating cell is representative of the MISO and has both a 15-30-day mode and a 30-60-day mode (Krishnamurti et al., 2017; Lawrence & Webster, 2002; Sharmila et al., 2013; Suhas et al., 2013; B. Wang & Xie, 1997). Once this northward propagation moves into

the BoB, the enhanced precipitation moves over the Maritime Continent, with the suppressed phase once again dominating the Indian Ocean basin between days +10 and +20, creating a roughly sinusoidal oscillation of precipitation in the Indian Ocean.

Spatially filtered lag composites of SLA for the 30-90-day ISO further reveal the spatial structure and dominance of planetary waves in the equatorial Indian Ocean that (Figure 3.4) that lead to the genesis of MJO and MISO convection (Figure 3.S1). Even when filtered, the SLA signal remains strong and well within satellite accuracy, closely following the phase and propagation of the 30-90-day signal at the equator. Throughout the 41-day composite, a downwelling Rossby wave clearly propagates westward across the Indian Ocean basin, seeming to interact with eastward propagating Kelvin waves that modify the wave's amplitude. This positive SLA signal arrives in the central Indian Ocean at day −5 as the enhanced convection arrives and increases in strength, suggesting that the downwelling Rossby wave helped to trigger and enhance the convection in a similar way as proposed for MJO initiation of primary events in Webber et al. (2012), where the downwelling Rossby wave depresses the thermocline, increases SSTs, and triggers convection. While the Webber et al. (2012) theory was focused on events triggered in the western Indian Ocean, MJO events have been known to initiate in various equatorial regions, including the central Indian Ocean (Matthews, 2008; Straub, 2013). Given the manner in which the 30-90-day composites were constructed over the Indian Ocean, it is likely that the events captured by these composites were of this nature. The northward propagating signal in the BoB is less apparent in the spatially filtered composites. While there is a slight change in SLA in the BoB, it is largely dwarfed by the higher amplitude equatorial signals present.

The spatial structure of the 30-90-day ISO in SSS has been studied in Grunseich et al. (2013), Guan et al. (2014), and Shoup et al. (2019), with SMAP-CAP having been shown to have the most robust, and accurate, spatial signal, particularly in coastal areas. The spatially filtered SSS composites in Figure 3.4 reflect a similar pattern to previous studies (Grunseich & Subrahmanyam, 2013; Guan et al., 2014; Shoup et al., 2019) with the suppressed (enhanced) phase typically having higher (lower) SSS signals. Previous studies, however, only performed composite analysis or isolated individual events, not spatially filtering and isolating the signal. Spatially filtering the SSS field reveals a short lag between the location of convection and the salinity response, suggesting that the direct freshening of the surface ocean due to enhanced precipitation is not the dominant control on SSS on the 30-90-day time scale at the MJO wavelength. The spatial pattern of SSS following the enhanced phase of convection (day +5 through day +20) more closely follows the atmospheric signal, with higher salinity dominating during the suppressed phase of convection. The SSS signal leading into the convective phase, however, appears unreflective of the atmospheric component of the MJO.

A composite time series of precipitation, SLA, and SSS more fully describes the interplay of parameters that leads to the strong 30-90-day precipitation signal in the Indian Ocean (Figure 3.S2). As seen in Figure 3.4 the SLA signal lead the precipitation signal by 5 days. This suggests, as in Figure 3.4, that a Rossby wave depresses the thermocline and increases SSTs, which agrees closely with the initiation theory proposed by Webber et al. (2012). These air-sea interactions with SSTs and winds then trigger the convection that leads to the strong precipitation signal at day 0 and the initiation of an event. As seen in Figure 3.5, SSS increases after day 0 with the decrease in precipitation and return to the

suppressed phase of the MJO. From days −20 to 0, however, SSS was already decreasing. This suggests that another seasonal signal, likely Indonesian Throughflow waters, were already lowering the salinity before MJO initiation occurred, and that it was the suppressed phase and increased evaporation that instead altered the SSS (Roman-Stork et al., 2019; Shoup et al., 2019).

To further analyze the propagation of the 30-90-day signal in the ocean, bandpass filtered Hovmöller diagrams were constructed. Figure 3.6 describes the longitudinal propagation of SLA, SSS, and SST in the Indian Ocean from 2015 to 2018 that has been bandpass filtered for the 30-90-day signal. The most direct relationship between parameters seen in the 30-90-day ISO is between SST and local winds (Figure 3.7), indicating strong air-sea interactions (Rao et al., 2011). Not only do independent ISO bands align and favor the longer-period boundary of the 30-90-day window, but the 2018 intensification of the 30-90-day signal is mirrored in both SST and winds. This indicates that wind is the primary driver of SST variability, as suggested in Krishnamurti et al. (2017), likely due to wind-induced vertical motion and mixing. The SSS and SLA signals are dominated by local advection, Kelvin waves, and Rossby waves, which are also wind induced. The phase speed of both eastward (figure not shown) and westward propagating waves was calculated from the SLA time-longitude plots, with the eastward speed being calculated from an eastward filtered time-longitude plot using an FFT. Phase speeds were found to be nearly equal, with the westward (eastward) phase speed being roughly 1.5 (1.7) m/s. This eastward phase speed is roughly equivalent to that of an equatorial Kelvin wave in the Indian Ocean (Sprintall et al., 2000).

While the composite time series establishes the lag between parameters (Figure 3.S2), it does not describe the propagation of these signals. Figure 3.8 shows the composite time-longitude and time-latitude bandpass filtered plots of the 30-90-day ISO in multiple variables. The ISO is most clearly seen in precipitation, which captures both the overall eastward propagation of the MJO and northward propagation of the MISO signal clearly. SSS follows a similar propagation pattern to precipitation, although with the 5-day lag observed in Figure 3.S2. SLA does not propagate as clearly as SSS, with the most robust signals occurring at coasts and along the equator. The lack of coherent zonal propagation in SLA may also be attributable to the interplay of multiple planetary waves that constructively and destructively interfere with one another, as seen in Figure 3.4 (Masunaga, 2007). While precipitation and SSS both have a clear meridional propagation, SLA does not. SLA does increase between 5°N and 15°N over the course of the ISO period; however, this is an offequatorial extension of the planetary waves at the equator. Satellite altimetry most clearly captures planetary wave propagation in equatorial and coastal margins, and so any open-ocean ISO propagations into the BoB that are of a much smaller amplitude are not as readily visible.

C. INTRASEASONAL OSCILLATIONS (10-20-DAYS)

The 10-20-day ISO is characterized by a double cell structure centered over the BoB (Chatterjee & Goswami, 2004; Kikuchi & Wang, 2009; Roman-Stork et al., 2019). The northernmost cell is centered along 15–20°N, and the southernmost cell is centered near the equator. The northern cell is generated by breaking Rossby waves in the upper atmosphere and forms as a small convective cell over the South China Sea before it propagates westward into the BoB (Ortega et al., 2017; Wang & Chen, 2017). The

southernmost cell, by contrast, is generated in the Indian Ocean. These two cells become phase-locked and then propagate westward over India, where the northern cell then reaches its demise over the AS and the southern cell reaches its demise in the southern Indian Ocean. The life cycle of the 10-20-day ISO can be clearly seen in Figure 3.S3, which shows a spatial lag composite of precipitation anomalies from 2015 to 2018, as well as the propagation and life cycle of both cells over a 15-day period.

Previous studies of 10-20-day SSS have been largely restricted to the BoB (Roman-Stork et al., 2019; Trott et al., 2019) and showed that the majority of the SSS response was due to river runoff and upwelling. Throughout the full Indian Ocean, however, the SSS response is fairly weak and largely confined to the equatorial region when filtered for the 10-20-day wavelength (Figure 3.9). This signal is likely a response to the southern cell over the eastern equatorial Indian Ocean, although an overall salinification of the BoB can be observed as in Roman-Stork et al. (2019) following the passage of the double cell with a roughly 4-day lag between the precipitation peak and the increase in salinity. The consistent magnitude and sign change of salinity between both the central BoB and eastern equatorial Indian Ocean suggests that a similar mechanism may be responsible for both observed patterns.

While the salinity structure of the 10-20-day ISO is poorly understood, there have been a number of studies that have focused on the biweekly nature of MRG waves in the region and several studies have noted the possible connection to the 10-20-day ISO (Miyama et al., 2006; Sengupta et al., 2001). The wavelength filtered (3,000–6,000 km) spatial lag composite shows a clear equatorial and off-equatorial signal indicative of an MRG wave, which has been shown to share a similar wavelength as the 10-20-day ISO

and have a 10-20-day periodicity in the eastern equatorial Indian Ocean (Miyama et al., 2006; Sengupta et al., 2001). The highest amplitude signals remain at the coastal boundary in the eastern Indian Ocean, which is consistent with the findings of Trott et al. (2019), which found the highest 10-20-day signal in SLA in the BoB to be at the eastern coastal boundary (Figure 3.10). Considering the structure and timing of the southern cell of the 10-20-day ISO, it is likely that this MRG wave is responsible for the genesis and propagation of the southern cell.

The time-longitude plots of SLA, SSS, SST, and surface winds allow us to better understand the dynamics of the oceanic propagation of the 10-20-day signal for both the northern and southern cell (Figures 3.11–3.14). SLA has a strong coastal signal and tends to peak at the Indian coastline at about 77.5°E (Figures 3.11a–3.11d). Zonal propagation of the 10-20-day ISO is continuously strongest in SLA (as seen by the sloping in Figures 3.11a–3.11d), which is due to the signal propagation of Rossby and Kelvin waves, shown in the coastal intensification (high-amplitude ISO) and shifts between westward and eastward propagation (Trott & Subrahmanyam, 2019). The passage of the northern cell through the BoB has been shown to deepen the mixed layer in the central and near-equatorial BoB, which would modulate heat storage as a response to the ISO (Roman-Stork et al., 2019). The amplitude of the southern cell at the equator is much stronger in SLA, particularly between 80 and 100°E, likely related to MRG wave dynamics in the region that induce convection associated with the southern cell (Figure 3.12; Sengupta et al., 2004). The 10-20-day signal has a much stronger relationship between SSS and winds than that seen in the 30-90-day signal, particularly during the summer monsoon of 2015 and throughout all of 2017 and 2018. SSS does not show a clear seasonal preference except for

a slightly stronger signal in springtime across the full basin. SST has a clear basin-wide signal that shows minimal latitudinal propagation and notable zonal changes in amplitude. There are strong 10-20-day ISO events in temperature in the western Indian Ocean during the summer monsoon seasons of 2015 and 2017 (with a moderate signal in 2018) and across the full basin during November-December of 2016, 2017, and 2018.

Multivariate time-longitude and time-latitude lag composites of the northern cell of the 10-20-day ISO further reinforce the dominance of the signal in the BoB. In precipitation, there is a clear westward and northward propagation of precipitation from 100 to 80°E in the BoB (Figure 3.S3). In Figure 3.15a, the signal largely disappears over land, which can be due to both the cell moving northward out of the 10–20°N range and weakening over India before it reaches its demise in the AS. SSS has a weak northward propagation but remains fairly strong at both the coastal boundary and central BoB suggesting a coastally trapped signal as seen in SLA (Figure 3.15e), and Ekman pumping in the central BoB, as described in Roman-Stork et al. (2019). The northern cell does not have a strong SLA signal outside of the coastal boundaries, suggesting a coastal wave propagation in response to 10-20-day wind forcing and equatorial wave activity at the coastal boundary as the dominant mode of SLA variability for this ISO, which is consistent with the 30-90-day ISO as well.

While the northern cell is characterized by strong westward and slight northward propagation, the southern cell is largely stationary, with only slight longitudinal propagation, largely in the eastward direction where it becomes phase locked with the northern cell, before propagating only slightly westward (Figures 3.S3 and 3.S4). As with the northern cell, the majority of 10-20-day precipitation occurs east of 70°E, although

there is a low amplitude signal on the west coast of India where the double cell reaches its demise. SSS shows no latitudinal propagation and only a weak westward propagation throughout, suggesting that the SSS response is more closely tied to SLA than in response to surface freshening from precipitation. As with the northern cell, the strongest SSS signals occur at the coastal boundary near 100°E, as in SLA (Figures 3.S4c and 3.S4e). SLA also has a weak westward propagation and a strong southward propagation, suggestive of an off-equatorial Rossby wave and coastally trapped Kelvin wave (Chatterjee & Goswami, 2004; Sengupta et al., 2004).

D. INTRASEASONAL OSCILLATIONS (3-7-DAYS)

The 3-7-day ISO is characterized by oscillations in the monsoon trough, which during the southwest monsoon are centered over 25°N (Gadgil & Asha, 1992; Krishnamurti & Bhalme, 1976). These oscillations occur on the same timescale of the active and break cycle of the monsoon and are heavily influenced by tropical cyclone activity and other ISOs (Gadgil & Asha, 1992; Goswami et al., 2003). To construct composites of 3-7-day events, a time series of precipitation over the monsoon trough region (20–30°N) was taken, as opposed to the entire Indian Ocean, as in the 30-90-day and 10-20-day ISO composites (Figure 3.16). The 5-day composites were constructed of 3-7-day events, where the composite length was chosen based on the average event period, which was found to be 4–5 days, and is akin to the period of active and break cycles of the monsoon.

In precipitation, the 3-7-day ISO appears largely stationary over northern India, with higher precipitation over India from days −2 to 0 and lower precipitation over India during days +1 and +2. This pattern is largely reversed over the northern BoB, where there

is lower precipitation during days −1 and −2 and higher precipitation from days 0 through +2. This is similar to the climatological OLR composites of active and break cycles of the monsoon (Joseph & Sijikumar, 2004).

As the majority of the 3-7-day precipitation occurs over land, the bulk of the SSS signal is in response to equatorial and BoB precipitation. In particular, there appears to be significant freshening of the northern BoB in response to precipitation. River runoff in the BoB has been shown to significantly impact salinity and mixed layer processes in the northern and western BoB, which would account for the spatial distribution of SSS and SLA variability seen in Figure 3.16. This same signal can also be seen in the northeastern AS, suggesting that river runoff from the monsoon trough in the north of both basins is responsible. The 3-7-day mode is analogous to the tropical convergence zone in the atmosphere, which has been shown to be out of phase with that in the ocean (Gadgil & Asha, 1992). This relationship would contribute to the observed differences found, where there is little spatial coherence between parameters.

The 3-7-day SLA response is noisy over the full Indian Ocean, even when filtered for the 3-7-day wavelength (Figure 3.16). The structure is apparent, but the signal amplitude is very low and is outside the current accuracy of altimeters. Comparing SLA and SSS, SMAP has a 1,000 km swath, which allows it to capture both the structure and magnitude of the 3-7-day response more reliably. Altimeters, by contrast, have an along-track footprint that is only 2 km wide on a flat surface. Even the upcoming Surface Water and Ocean Topography (SWOT) altimetry mission will have a 120 km swath, an order of magnitude smaller than SMAP. This difference in swath size and methodology allows for blended SLA from multiple altimeters to capture the structure, but not the amplitude of the

3-7-day signal, which means that SSS is a more robust tool for the study of the 3-7-day ISO than SLA (Durand et al., 2010; Subrahmanyam et al., 2018; Trott et al., 2019; Trott & Subrahmanyam, 2019).

There is clear northward propagation of the 3-7-day ISO in precipitation (Figure 3.S5). The northward propagation is strong enough that the high-amplitude 3-7-day ISO events are over India during the summer monsoon season. This pattern is very similar for all years of study. There is sparse rainfall north of 10°N from November–March (consistent with the northeast monsoon season). Strong cyclones in the AS and BoB also operate on a 3-7-day timescale and contribute to the active and break cycles of the monsoon, as well as interact with the monsoon trough (Goswami et al., 2003). As these time-latitude plots are from 20°S–20°N, they do not completely capture activity of the actual monsoon trough, but rather the activity just south of it, which is why activity is strongest during the boreal summer in the northern part of the basin, which coincides with both the southwest monsoon and tropical cyclone season. This is the opposite in the southern Indian Ocean, where the Australian monsoon is strongest during boreal winter.

The northward propagation here in SMAP matches that of precipitation (Figure 3.17). This suggests that SSS better mirrors precipitation than SLA, as in Figure 3.16. Figure 3.17 shows a better meridional structure of the ISO signal than SLA, as the full meridional span of the ISO is clear, as opposed to the noise of the SLA signal (Figure 3.18). Following the southwest monsoon, the 3-7-day ISO is strongest above 15°N and likely also reflects some shorter-term fluctuations in river discharge, likely induced by precipitation from oscillations in the monsoon trough, which was seen in Figure 3.16. The strength of

the observed signal is similar to seen in Subrahmanyam et al. (2018), which showed SMAP SSS in the BoB to have a similar amplitude and propagation.

Compared to the SSS time-latitude plots, the all Indian Ocean time-latitude plots for SLA are very noisy and peak around the equator. When plotted exclusively for the BoB (figure not shown), the signal is much stronger and more coherent, particularly in the southern Bay, which is consistent with previous studies in the region (Trott & Subrahmanyam, 2019). This is likely in response to more off-equatorial weather and planetary wave activity, as well as to the monsoon trough (Sreenivas et al., 2012). As the monsoon trough is mainly over both India and the BoB, the SLA signal is stronger over this basin. In order to fully see the structure and amplitude of these signals, however, it is necessary that we have both high spatial resolution altimeters and swaths that can capture the structure of the signal. The upcoming SWOT mission promises both a 120 km swath and high spatial resolution, which will greatly improve the usefulness of altimetry for studies of the 3-7-day ISO (Durand et al., 2010).

3.4 CONCLUSION

ISOs in the Indian Ocean are major controllers of the southwest monsoon active and break cycles and significantly contribute to monsoonal precipitation. They are highly coupled processes, and it is critically important for monitoring and forecasting of these ISOs that we understand the oceanic processes that influence them. This study highlights how SLA and SSS can be used to complement atmospheric data for monsoon forecasting and monitoring. Through our analysis of satellite-derived SLA and SSS, we have found that wind-driven planetary wave propagation and vertical motion are the primary mechanisms by which SLA and SSS influence and are influenced by ISOs in the Indian

Ocean. On 30-90-day timescales, Rossby waves and Kelvin waves in the equatorial Indian Ocean establish the conditions necessary for MJO initiation. SSS perturbations are found to precede MJO and MISO precipitation through wind-induced advection of low salinity waters. The SLA response to the 10-20-day mode is more varied, with MRG waves triggering the genesis of the southern cell and wind from the northern cell modulating coastal Kelvin waves in the BoB. The SSS response is much weaker than that of SLA, with SSS responding to changes in SLA, advection, and wind-induced upwelling. The 3-7-day ISO has a much weaker SLA and SSS signature, at least partially due to the persistence of the monsoon trough over land at 25°N. The 3-7-day SSS presents a slight northward propagation, particularly prior to the southwest monsoon season, but the SLA propagation is much weaker, with this propagation being strongest in the BoB. Future altimetry missions are anticipated to improve this.

While SLA best captures the conditions that lead to genesis of 30-90-day and 10-20-day ISOs, the current altimeter footprints are too small to adequately capture the 3-7-day signal. Given the amplitude of SLA signals in the AS and BoB, it is very difficult for a single altimeter to resolve ISO patterns, and so more altimetry missions with wide swaths are needed, such as the upcoming SWOT mission. Compared to existing altimetry missions, the SWOT mission has the potential to significantly improve ISO studies due to its 120 km swath, which is an improvement from the along-track footprints of existing altimeters. SSS is more useful for the monitoring of oceanic responses to ISOs rather than their prediction, but more clearly captures the ISO signal due to the wide swath (1,000 km for SMAP) and faster repeat cycle. SMAP is the most recent mission used for salinity, and there are no future NASA salinity missions planned. In order to further monitor and

understand these ISOs, continuous salinity missions are required. As neither SLA nor SSS experience the cloud interference that SST does, it is important to be able to use these parameters to monitor ISOs in real time. That being said, neither SSS nor SLA can track ISOs over land, which makes the monitoring of the 3-7-day and northern cell of the 10-20-day more difficult and requires them to be used in conjunction with atmospheric parameters. Further, SSS signals are contaminated by precipitation and river runoff, which is a disadvantage compared to SLA, which does not. As the Indian Ocean experiences monsoon conditions for the majority of the year, both clouds and precipitation pose a significant limitation in satellite observations of the region. SWOT is an all-weather satellite, and so the observations obtained from the mission will not experience the same limitations and issues that other sensors due in the region.

Ultimately, this research is most beneficial for the improvement of coupled atmosphere-ocean models and the assimilation of satellite data for monsoon studies, which will improve the predictability of ISOs and southwest monsoon precipitation. Active and break cycles of the monsoon are the most difficult aspect of the southwest monsoon to predict, but also have the greatest impact on agriculture, transport, economics, and the lives of over a billion people. Moving forward, it is crucial that we maintain and expand high-quality satellite-observations of the Indian Ocean so that the forecasting, monitoring, and modeling of ISOs and the southwest monsoon may be improved.

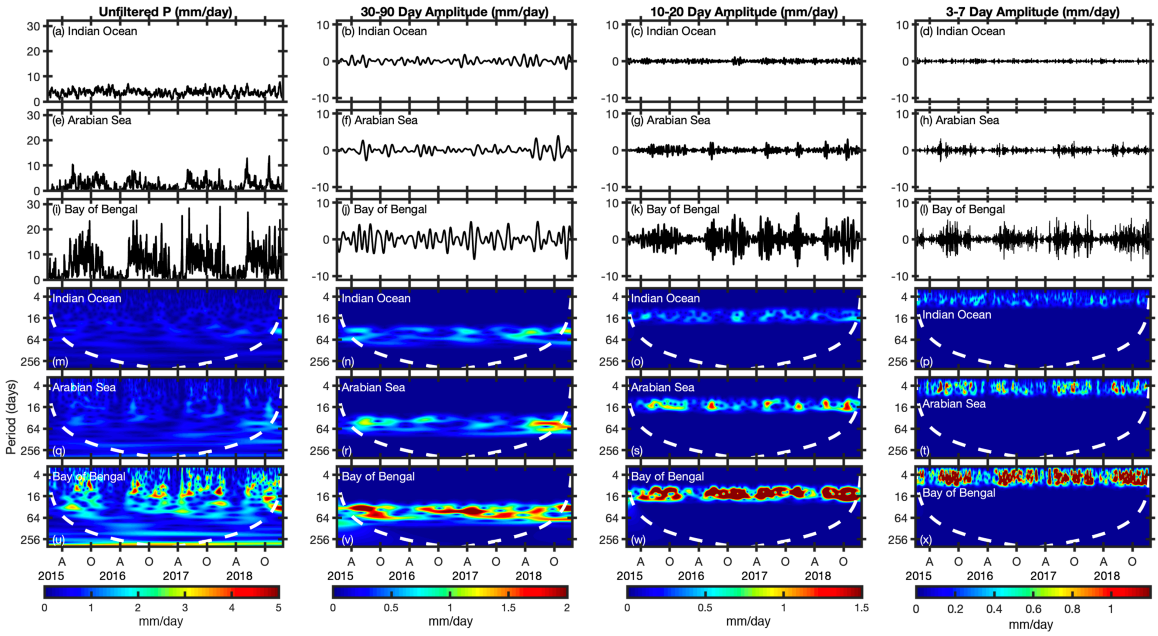

Figure 3.1. Time series and wavelets of Global Precipitation Climatology Project (GPCP) precipitation (mm/day) in the (a–d; m–p) Indian Ocean, (e–h; q–t) Arabian Sea, and (i–l; u–x) Bay of Bengal from 2015 to 2018 that are unfiltered (first column), 30-90-day filtered (second column), 10-20-day filtered (third column), and 3-7-day filtered (fourth column).

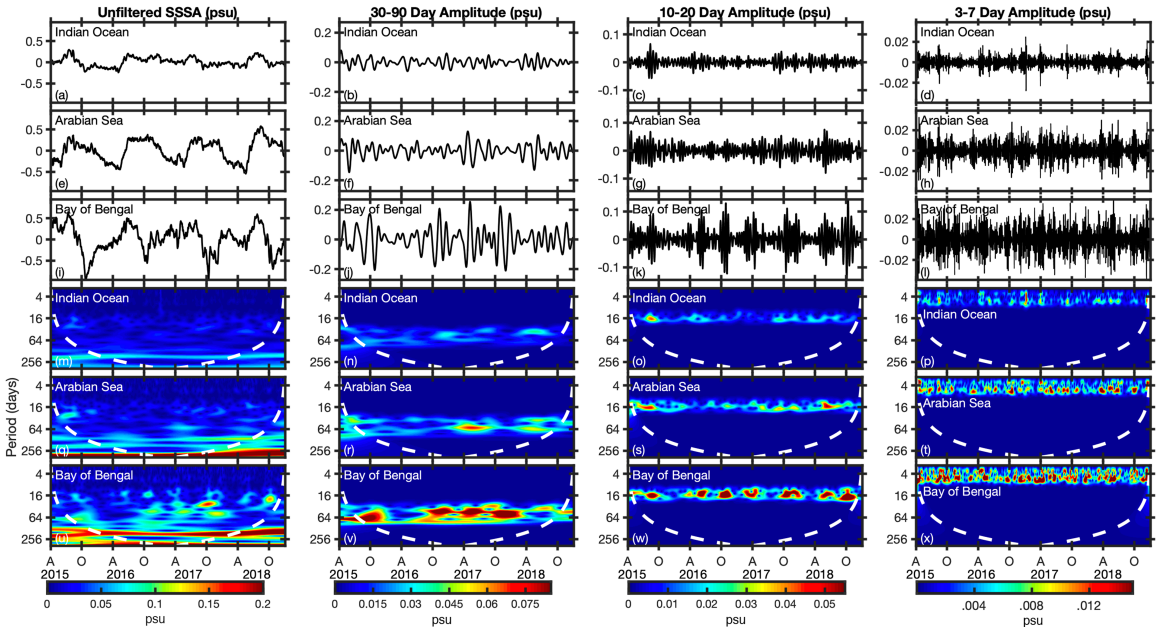

Figure 3.2. Time series and wavelets of Soil Moisture Active Passive-Combined Active Passive-sea surface salinity (SMAP-CAP SSS; psu) in the (a–d; m–p) Indian Ocean, (e–h; q–t) Arabian Sea, and (i–l; u–x) Bay of Bengal from 2015 to 2018 that are unfiltered (first column), 30-90-day filtered (second column), 10-20-day filtered (third column), and 3-7-day filtered (fourth column).

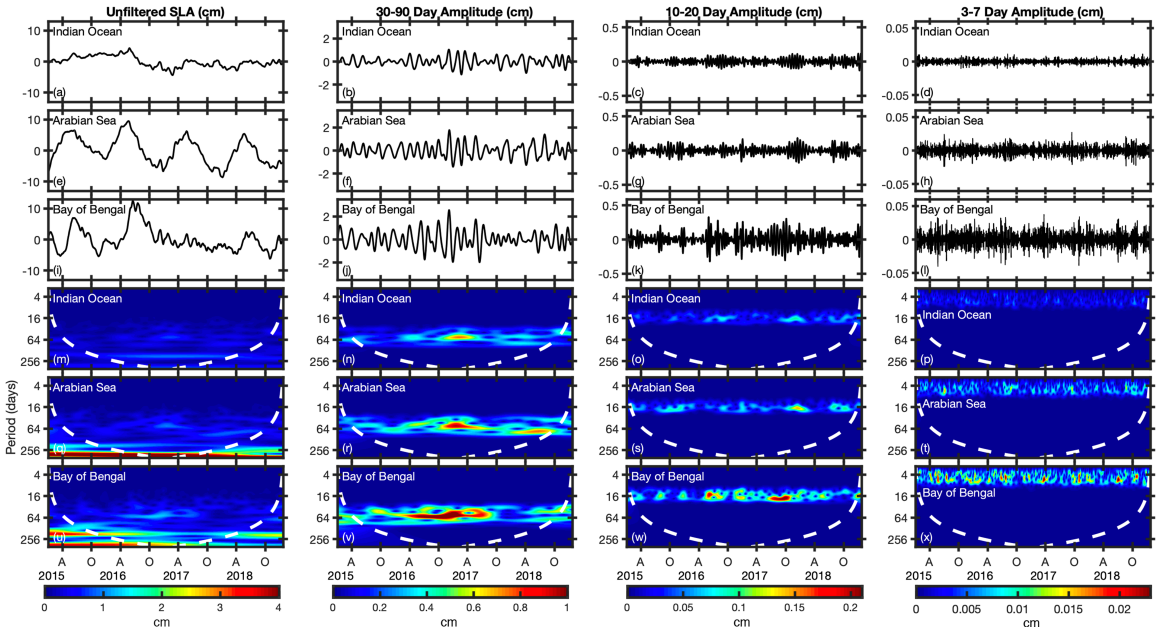

Figure 3.3. Time series and wavelets of Copernicus Marine and Environmental Monitoring Service sea level anomaly (CMEMS SLA; cm) in the (a–d; m–p) Indian Ocean, (e–h; q–t) Arabian Sea, and (i–l; u–x) Bay of Bengal from 2015 to 2018 that are unfiltered (first column), 30-90-day filtered (second column), 10-20-day filtered (third column), and 3- 7-day filtered (fourth column).

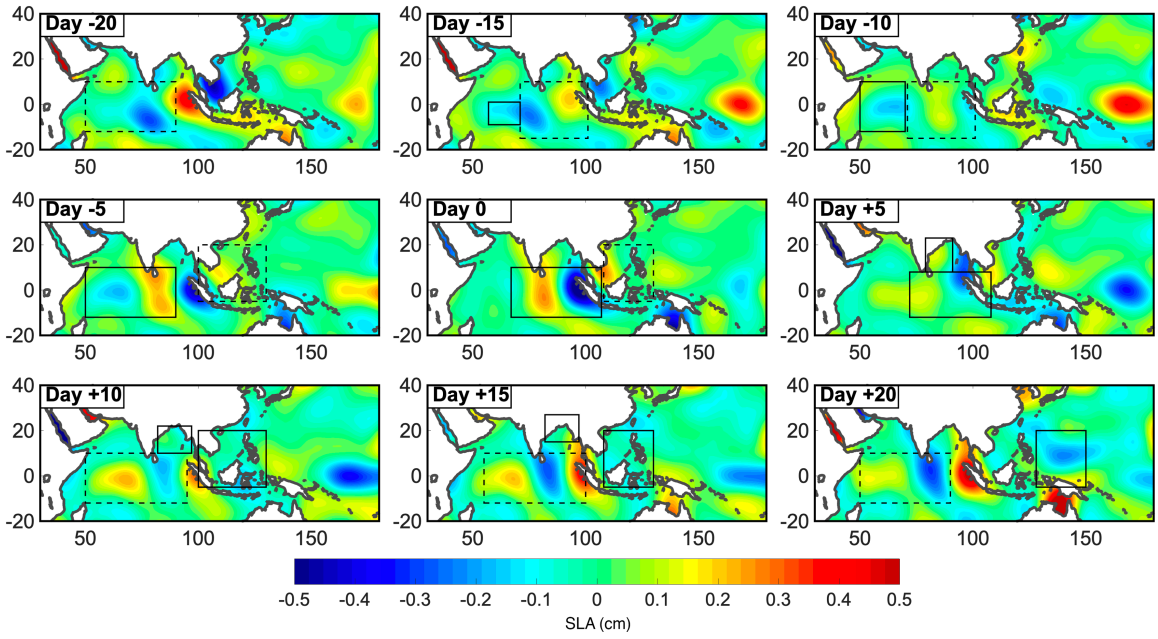

Figure 3.4. Deseasonalized Copernicus Marine and Environmental Monitoring Service sea level anomaly (CMEMS SLA; cm) composite of the 30-90-day intraseasonal oscillation in the Indian Ocean (20°S–20°N, 40–100°E) based on a box averaged time series of Global Precipitation Climatology Project (GPCP) precipitation from 2015 to 2018 and spatially filtered to the Madden-Julian Oscillation wavelength in the Indian Ocean.

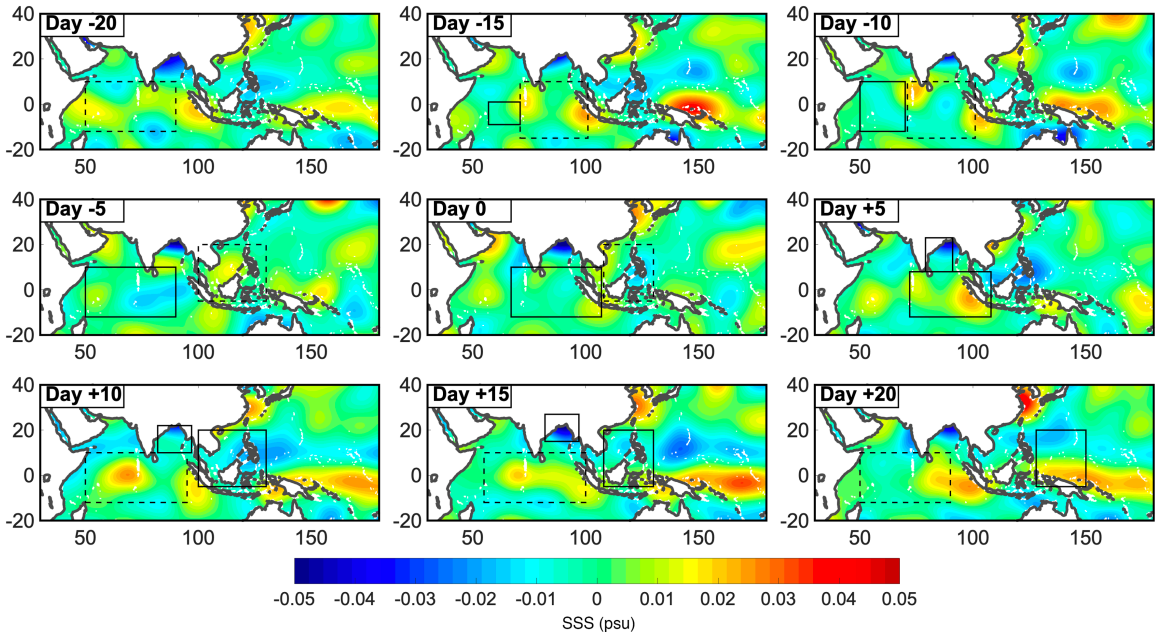

Figure 3.5. Deseasonalized Soil Moisture Active Passive-Combined Active Passive (SMAP-CAP) anomaly (psu) composite of the 30-90-day intraseasonal oscillation in the Indian Ocean (20°S–20°N, 40–100°E) based on a box averaged time series of Global Precipitation Climatology Project (GPCP) precipitation from 2015 to 2018 and spatially filtered to the Madden-Julian Oscillation wavelength in the Indian Ocean.

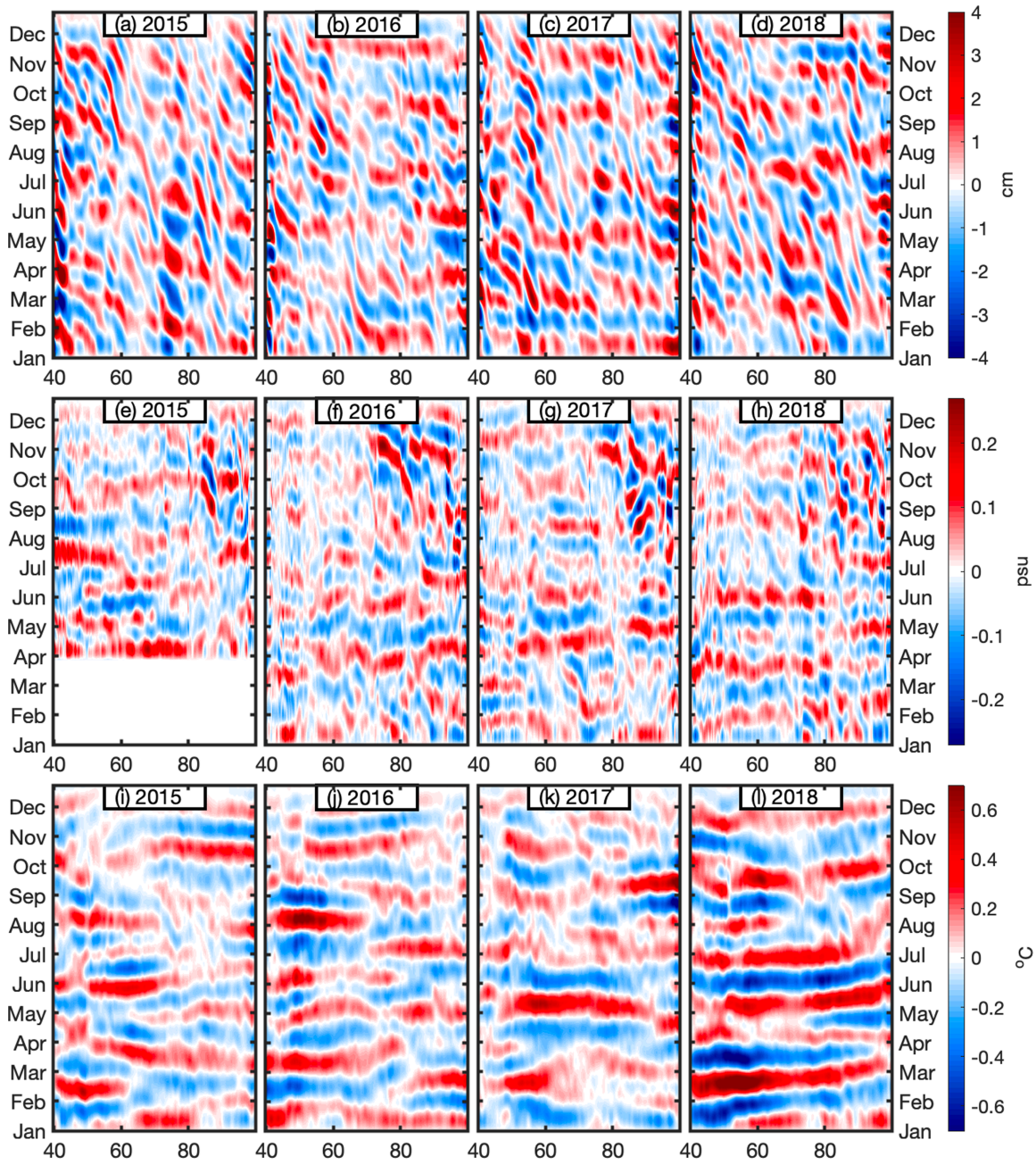

Figure 3.6. 30-90-day bandpass filtered time-longitude plots of (a–d) Copernicus Marine and Environmental Monitoring Service (CMEMS) sea level anomaly (cm), (e–h) Soil Moisture Active Passive-Combined Active Passive (SMAP-CAP; psu), and Optimally Interpolated Sea Surface Temperature (OISST; °C) from 2015 (a) to 2018 (i) in the Indian Ocean (20°S–20°N, 40–100°E).

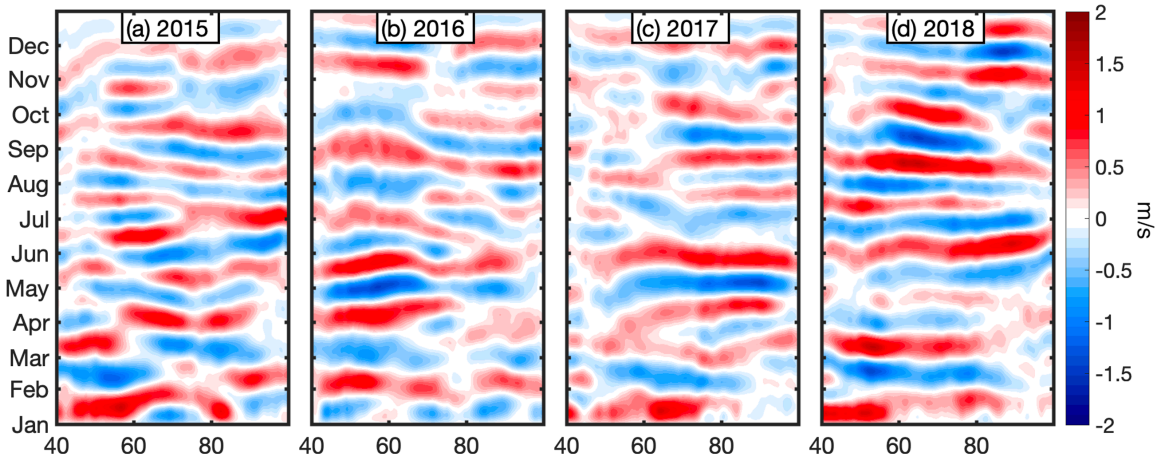

Figure 3.7. 30-90-day bandpass filtered time-longitude plots of Cross-Calibrated Multi-Platform version 2.0 (CCMPv2.0) surface wind magnitude (m/s) from (a) 2015 to (d) 2018 in the Indian Ocean (20°S–20°N, 40–100°E).

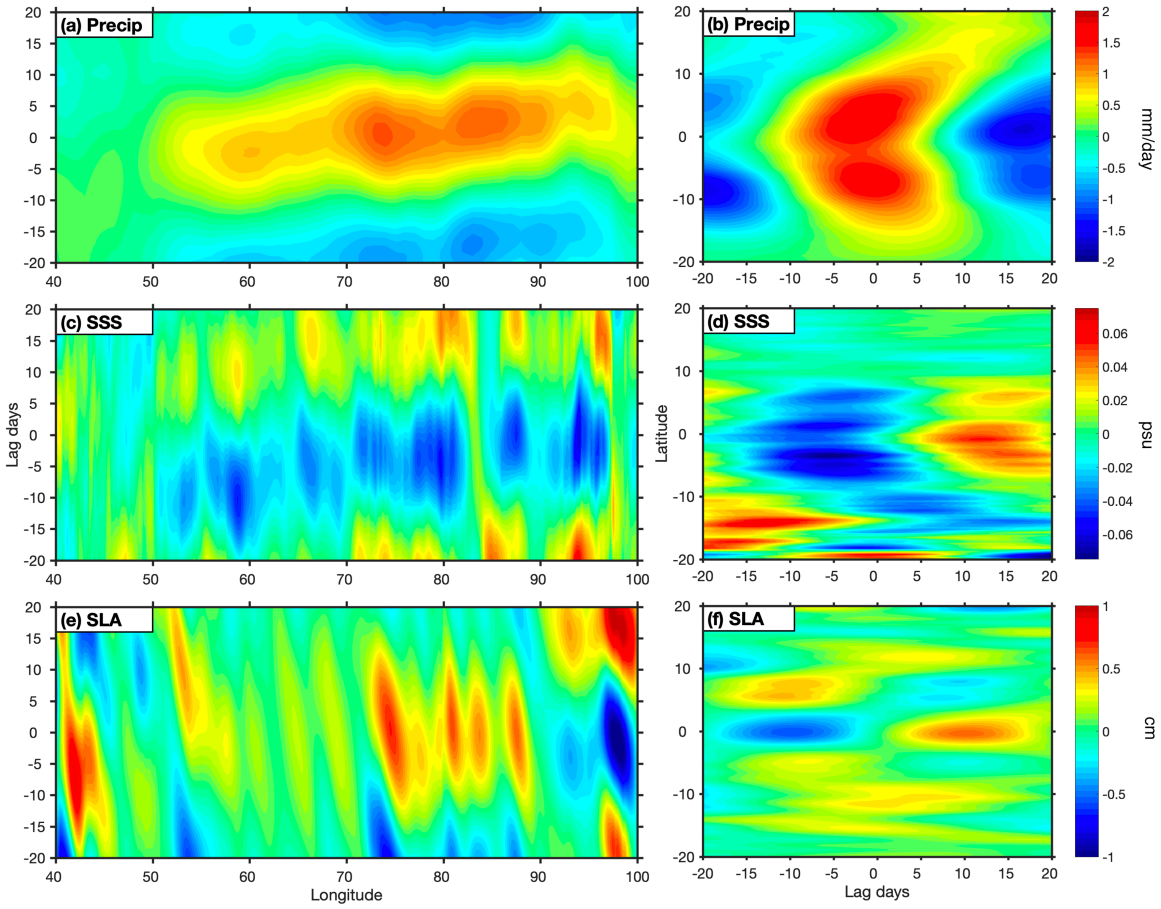

Figure 3.8. 30-90-day (a, c, and e) bandpass filtered time lag-longitude plots and (b, d, and f) time lag-latitude plots of deseasonalized Global Precipitation Climatology Project (GPCP) precipitation (a and b; mm/day), Soil Moisture Active Passive-Combined Active Passive (SMAP-CAP; c and d; psu), and Copernicus Marine and Environmental Monitoring Service sea level anomaly (CMEMS SLA; e and f; cm) from 2015 to 2018 in the Indian Ocean (20°S–20°N, 40–100°E).

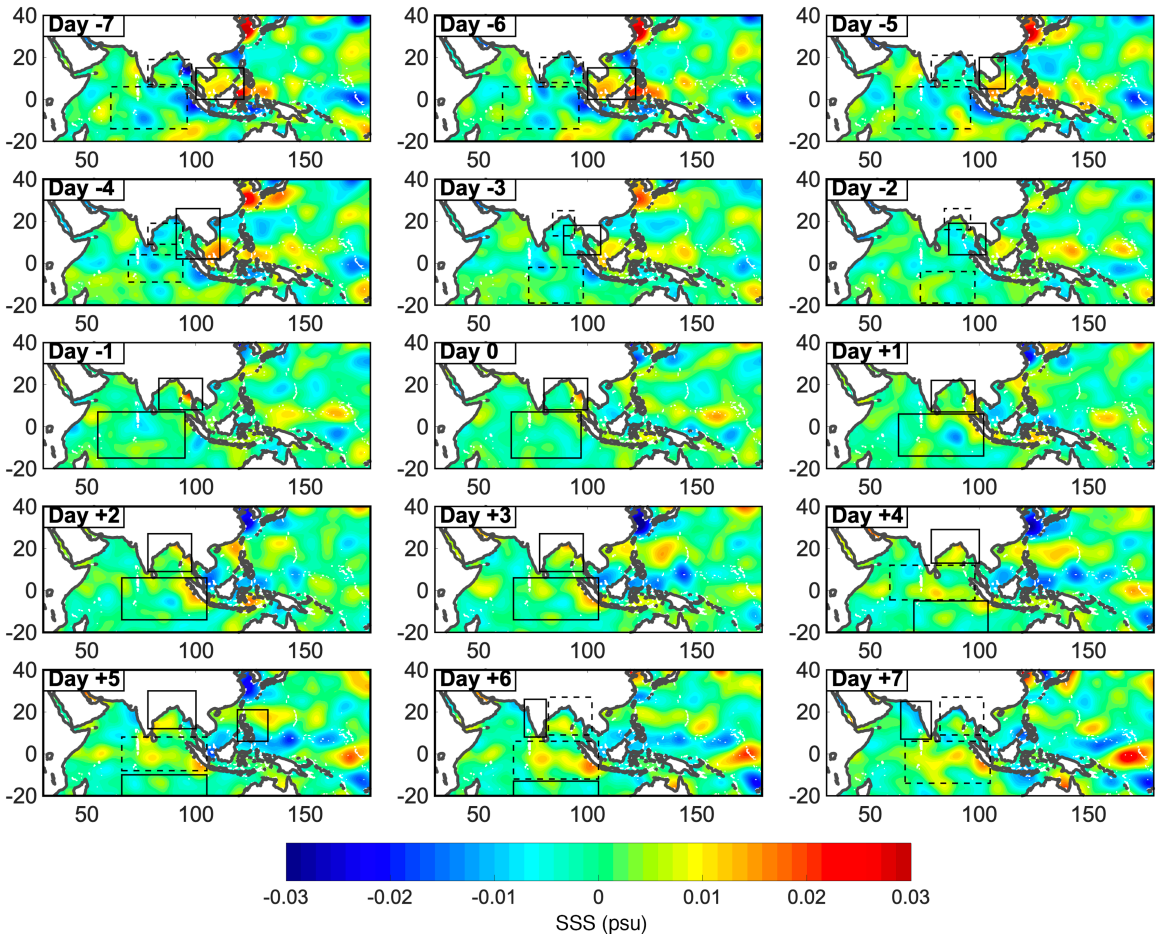

Figure 3.9. Deseasonalized Soil Moisture Active Passive-Combined Active Passive (SMAP-CAP) anomaly (psu) composite of the 10-20-day intraseasonal oscillation in the Indian Ocean (20°S–20°N, 40–100°E) based a box averaged time series of Global Precipitation Climatology Project (GPCP) precipitation from 2015 to 2018 and spatially filtered to the quasi-biweekly wavelength in the Indian Ocean.

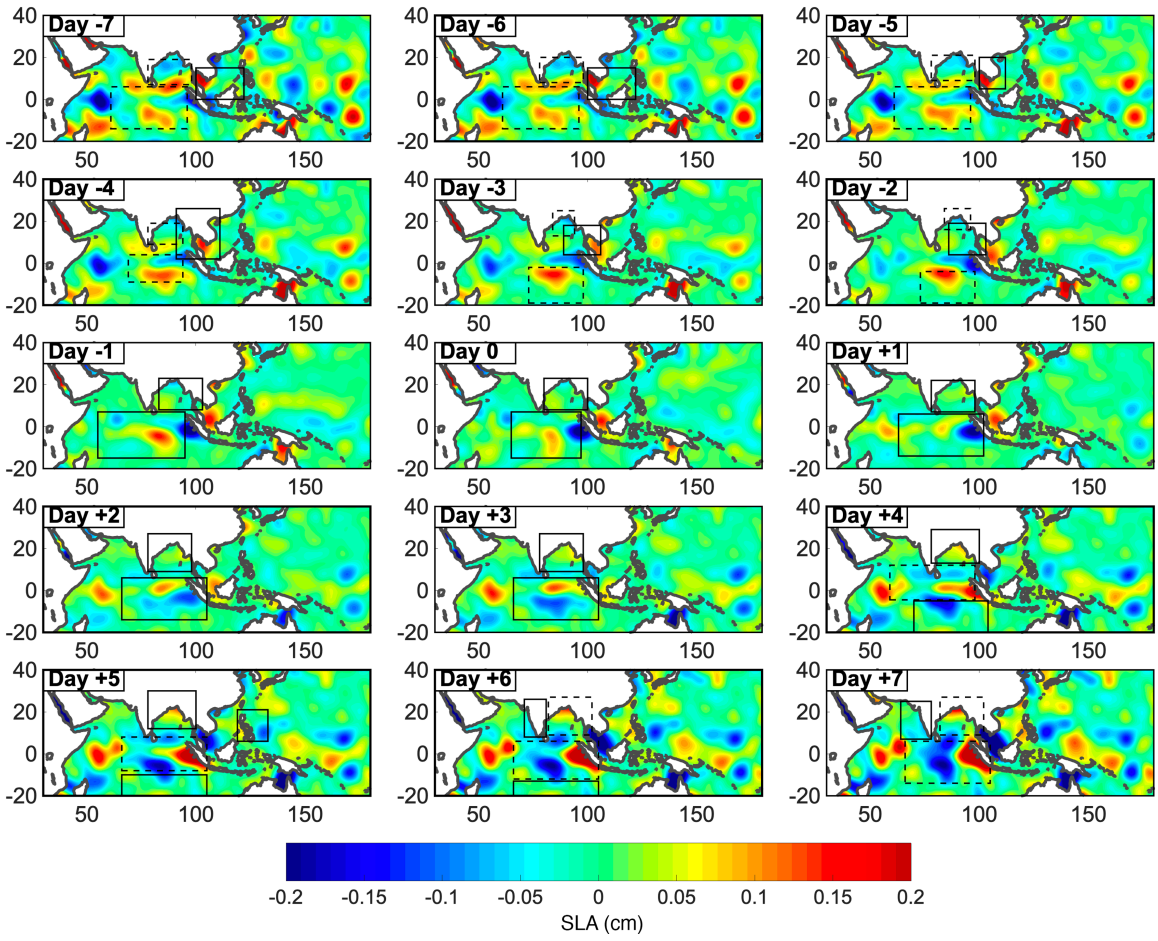

Figure 3.10. Deseasonalized Copernicus Marine and Environmental Monitoring Service sea level anomaly (CMEMS SLA) anomaly (cm) composite of the 10-20-day intraseasonal oscillation in the Indian Ocean (20°S–20°N, 40–100°E) based a box averaged time series of Global Precipitation Climatology Project (GPCP) precipitation from 2015 to 2018 and spatially filtered to the quasi-biweekly wavelength in the Indian Ocean.

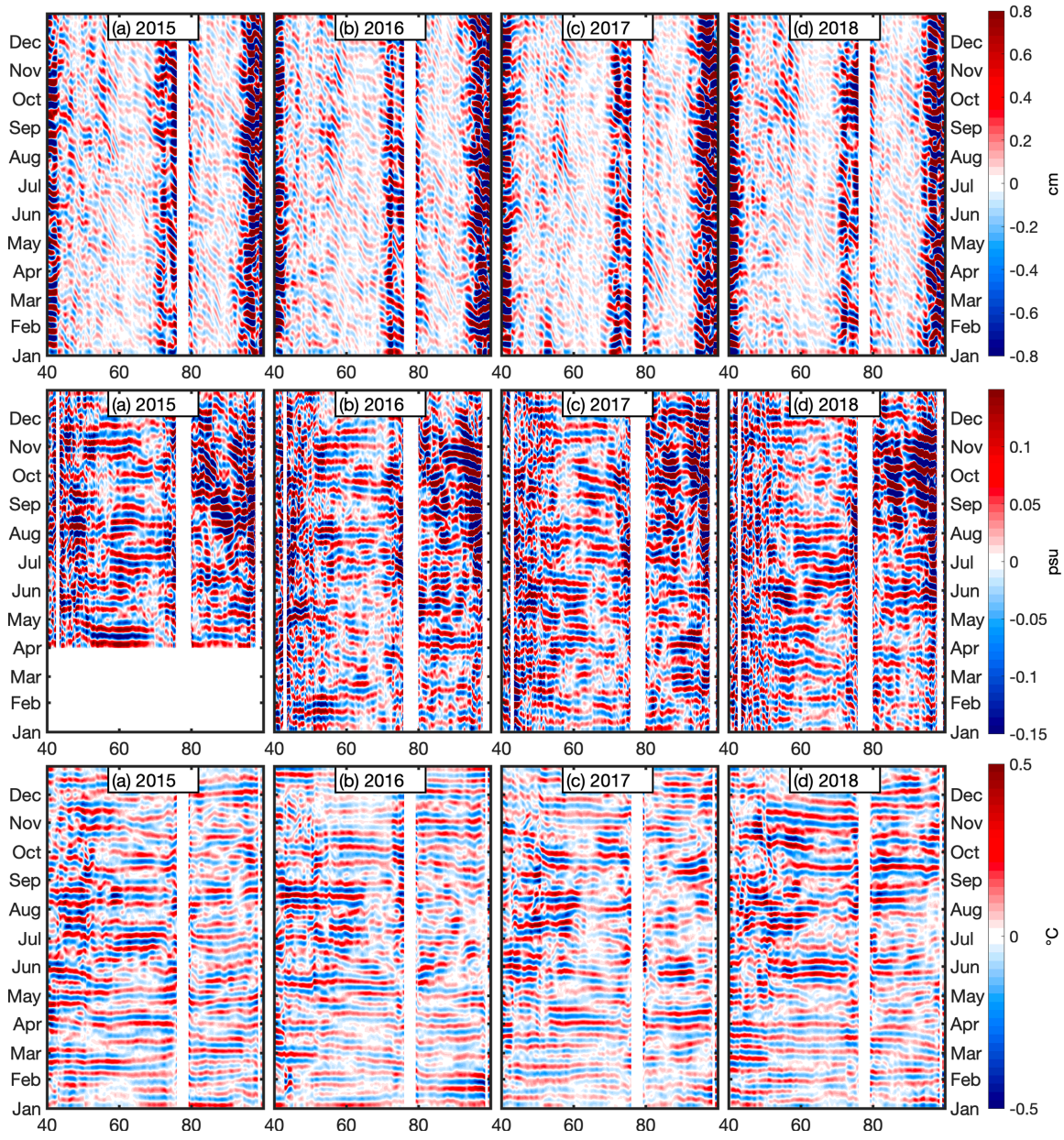

Figure 3.11. 10-20-day bandpass filtered time-longitude plots of Copernicus Marine and Environmental Monitoring Service sea level anomaly (CMEMS SLA; top; cm), Soil Moisture Active Passive-Combined Active Passive (SMAP-CAP; middle; psu), and Optimally Interpolated Sea Surface Temperature (OISST; bottom; °C) from (a) 2015 to (i) 2018 in the Indian Ocean, Bay of Bengal, and Arabian Sea (10–20°N, 40–100°E) for the northern cell of the double cell structure.

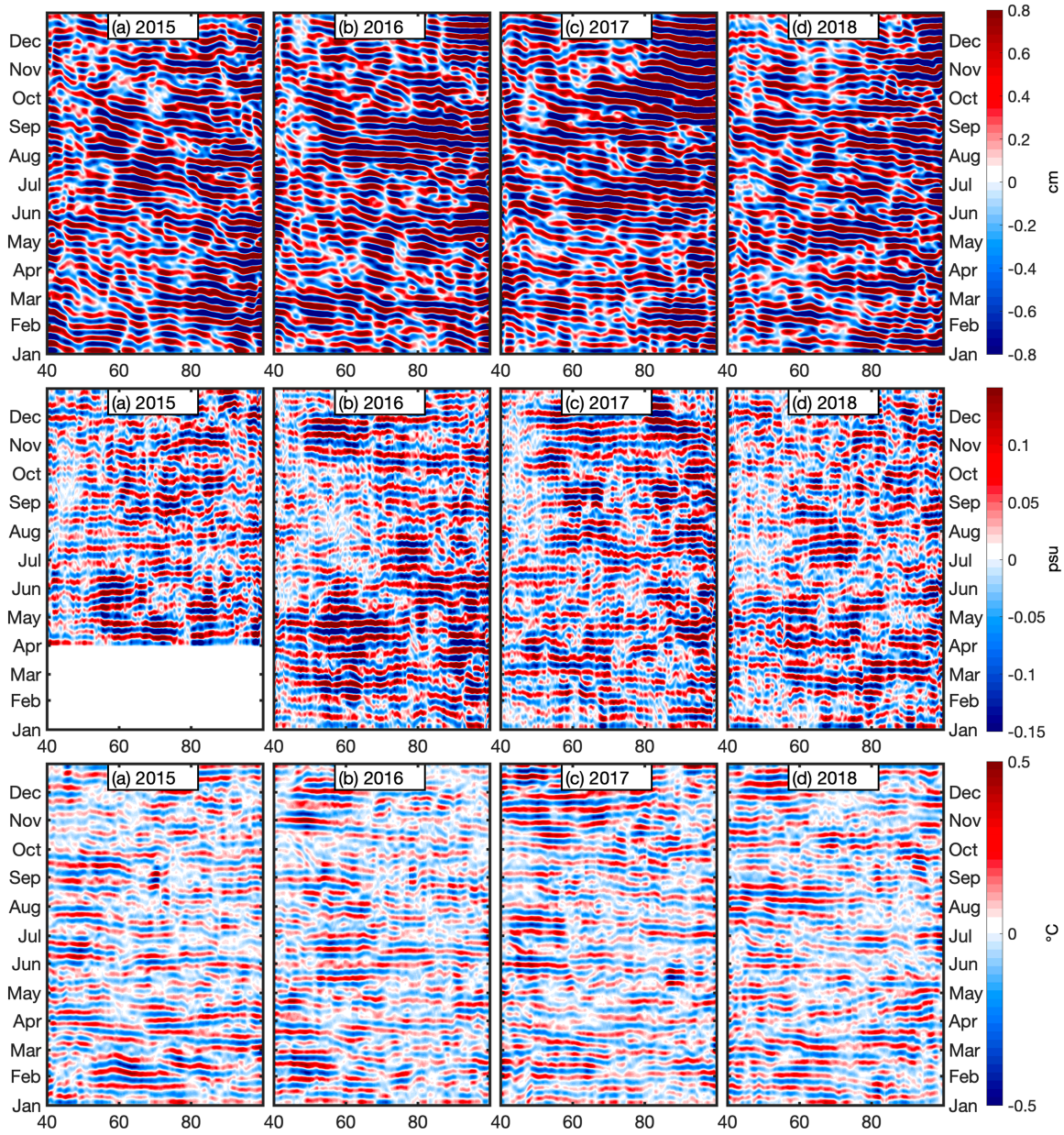

Figure 3.12. 10-20-day bandpass filtered time-longitude plots of Copernicus Marine and Environmental Monitoring Service sea level anomaly (CMEMS SLA) (top; cm), Soil Moisture Active Passive-Combined Active Passive (SMAP-CAP; middle; psu), and Optimally Interpolated Sea Surface Temperature (OISST; bottom; °C) from (a) 2015 to (i) 2018 in the Indian Ocean (5°S–0°N, 40–100°E) for the southern cell of the double cell structure.

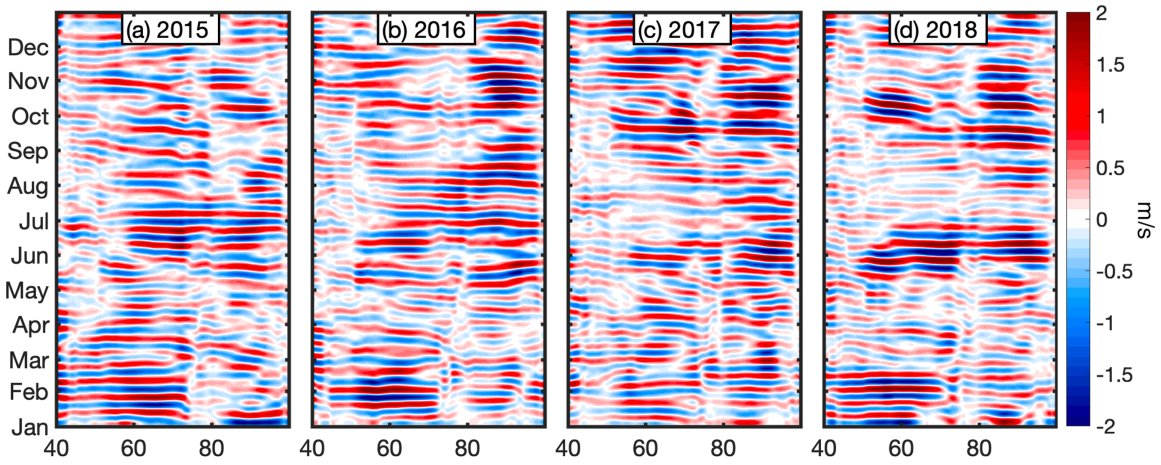

Figure 3.13. 10-20-day bandpass filtered time-longitude plots of Cross-Calibrated Multi-Platform version 2.0 (CCMPv2.0) surface wind magnitude (m/s) from (a) 2015 to (d) 2018 in the northern Indian Ocean, Bay of Bengal, and Arabian Sea (10–20°N, 40–100°E).

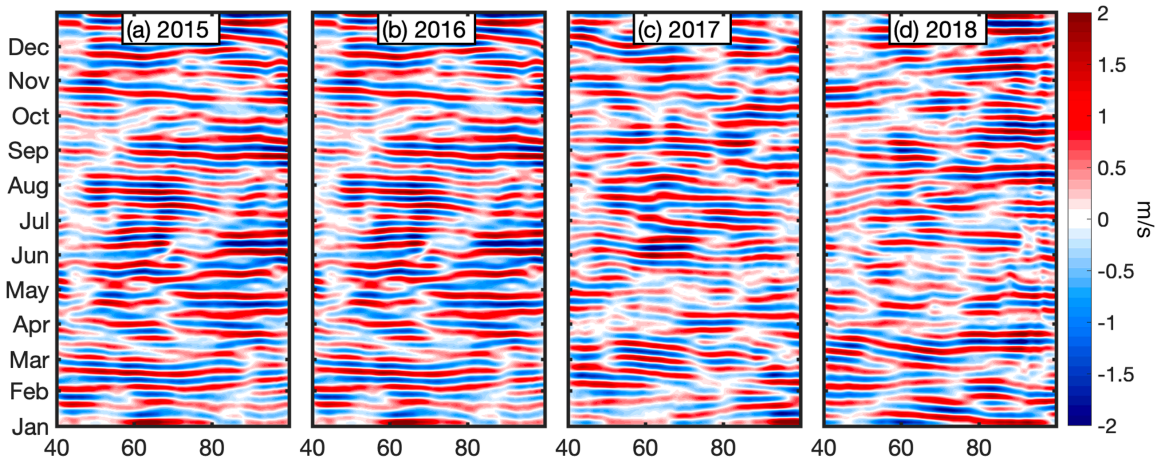

Figure 3.14. 10-20-day bandpass filtered time-longitude plots of Cross-Calibrated Multi-Platform version 2.0 (CCMPv2.0) surface wind magnitude (m/s) from (a) 2015 to (d) 2018 in the south equatorial Indian Ocean (0–5°S, 40–100°E).

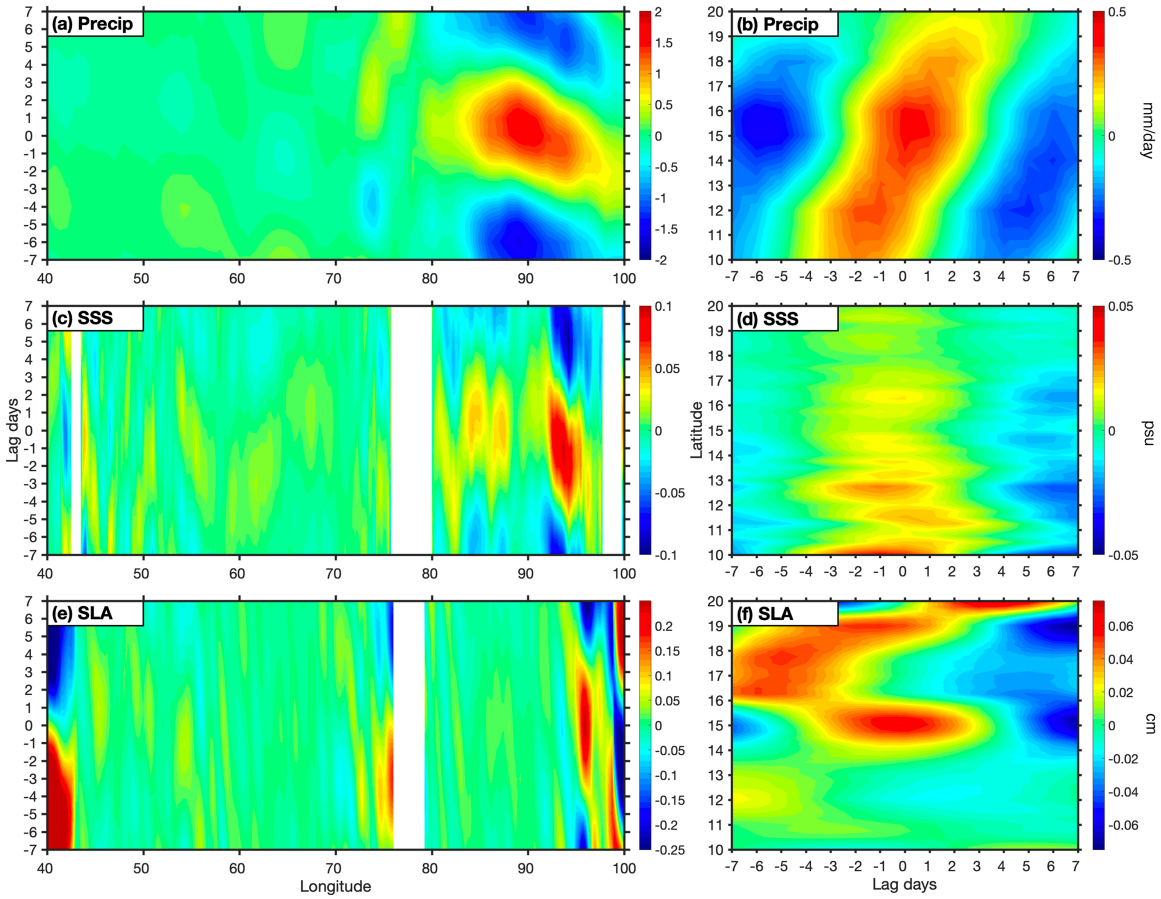

Figure 3.15. Composite 10-20-day bandpass filtered time lag-longitude plots of deseasonalized (a and b) Global Precipitation Climatology Project (GPCP) precipitation (mm/day), (c and d) Soil Moisture Active Passive-Combined Active Passive (SMAP-CAP; psu), and (e and f) Copernicus Marine and Environmental Monitoring Service sea level anomaly (CMEMS SLA; cm) from 2015 to 2018 in the Indian Ocean, Bay of Bengal, and Arabian Sea (10–20°N, 40–100°E) for the northern cell of the double cell structure.

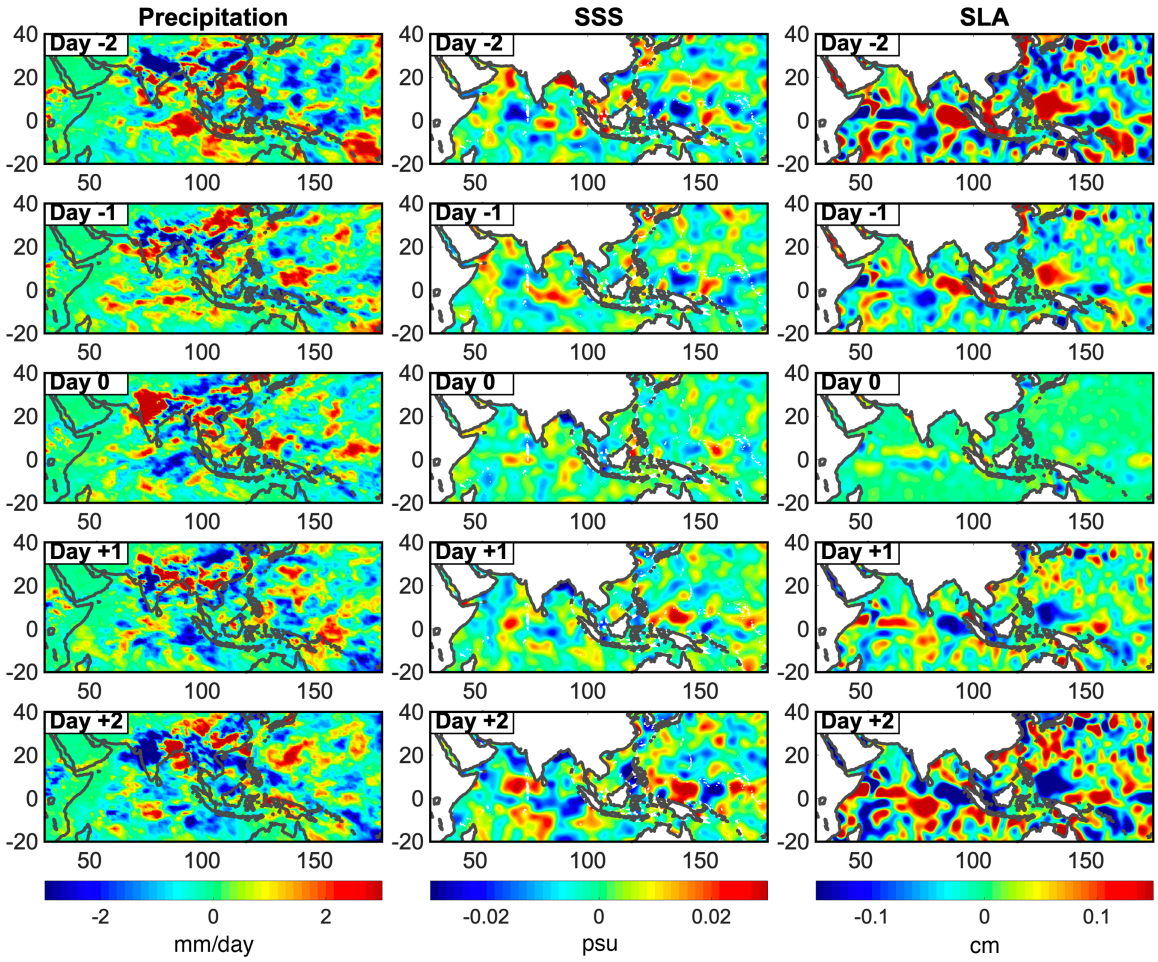

Figure 3.16. Deseasonalized Global Precipitation Climatology Project (GPCP) precipitation anomaly (left; mm/day), Soil Moisture Active Passive-Combined Active Passive (SMAP-CAP) SSS (middle; psu), and Copernicus Marine and Environmental Monitoring Service (CMEMS) blended altimetry sea level anomaly (SLA; right; cm) composites of the 3-7-day intraseasonal oscillation in the Indian Ocean (20–30°N, 40–100°E) based on a box averaged time series from 2015 to 2018 and spatially filtered to the 3-7-day wavelength in the Indian Ocean.

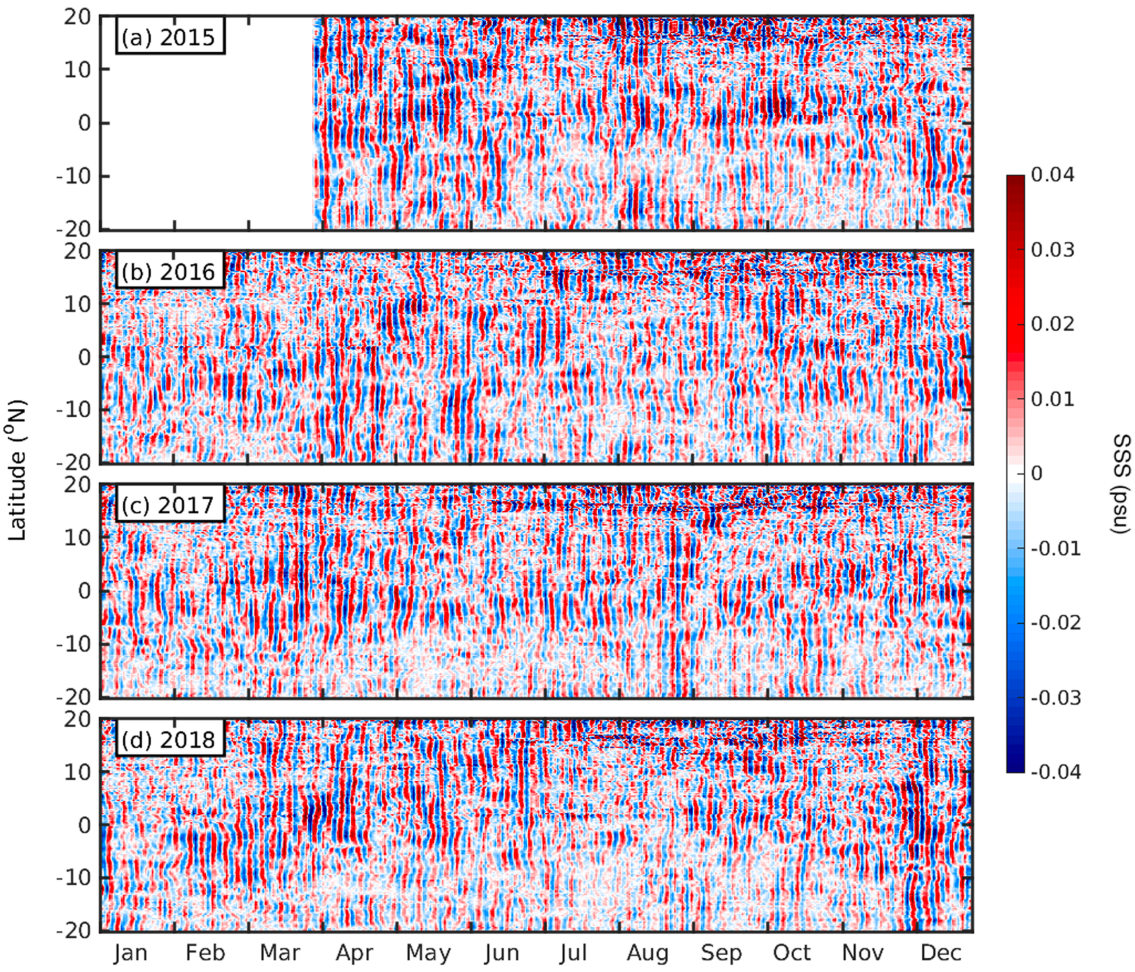

Figure 3.17. 3-7-day bandpass filtered time-latitude plots of Soil Moisture Active Passive-Combined Active Passive (SMAP-CAP) sea surface salinity (SSS; psu) from (a) 2015 to (d) 2018 in the Indian Ocean (20°S–20°N, 40–100°E).

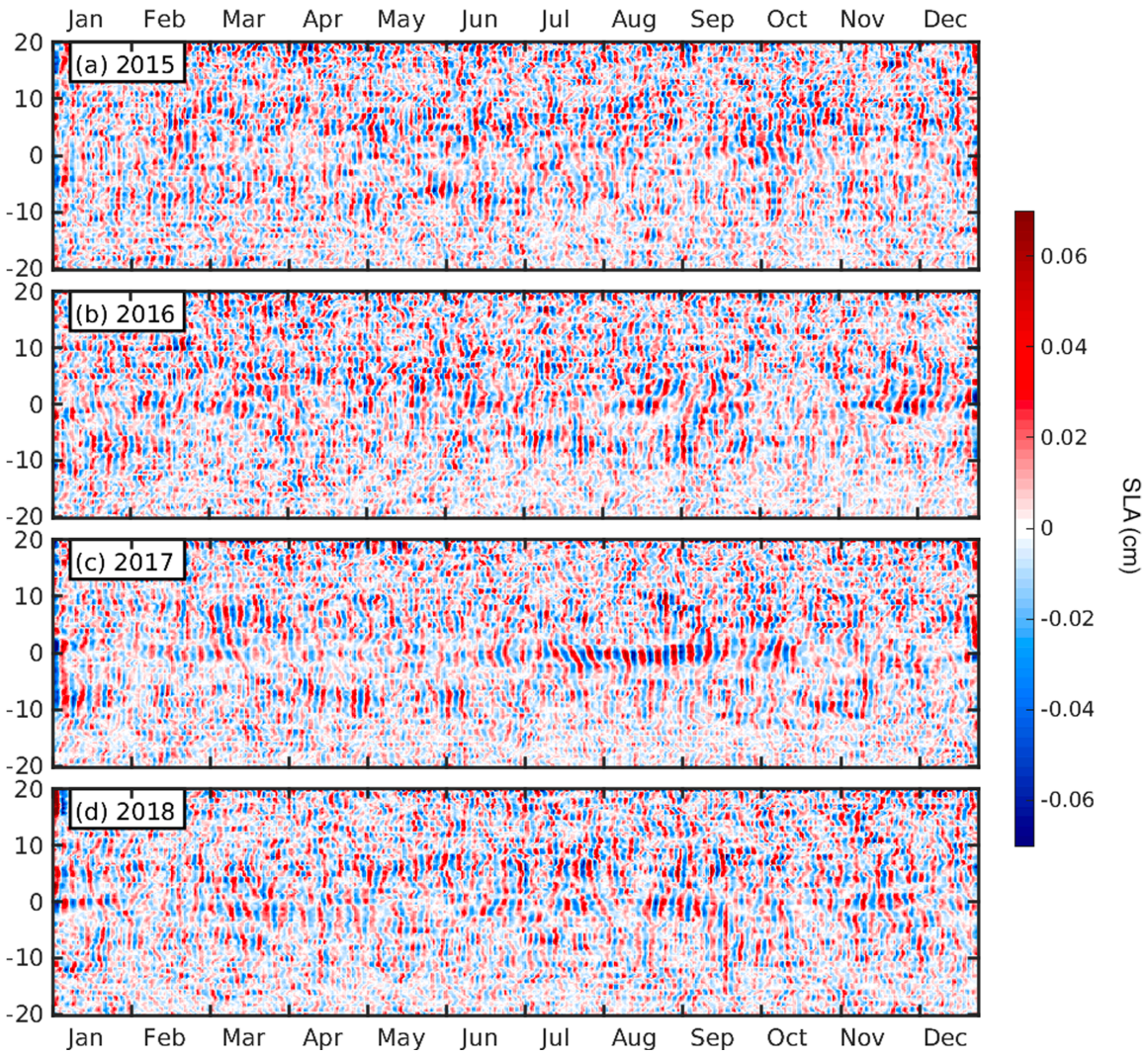

Figure 3.18. 3-7-day bandpass filtered time-latitude plots of Copernicus Marine and Environmental Monitoring Service sea level anomaly (CMEMS SLA; cm) from (a) 2015 to (d) 2018 in the Indian Ocean (20°S–20°N, 40–100°E).

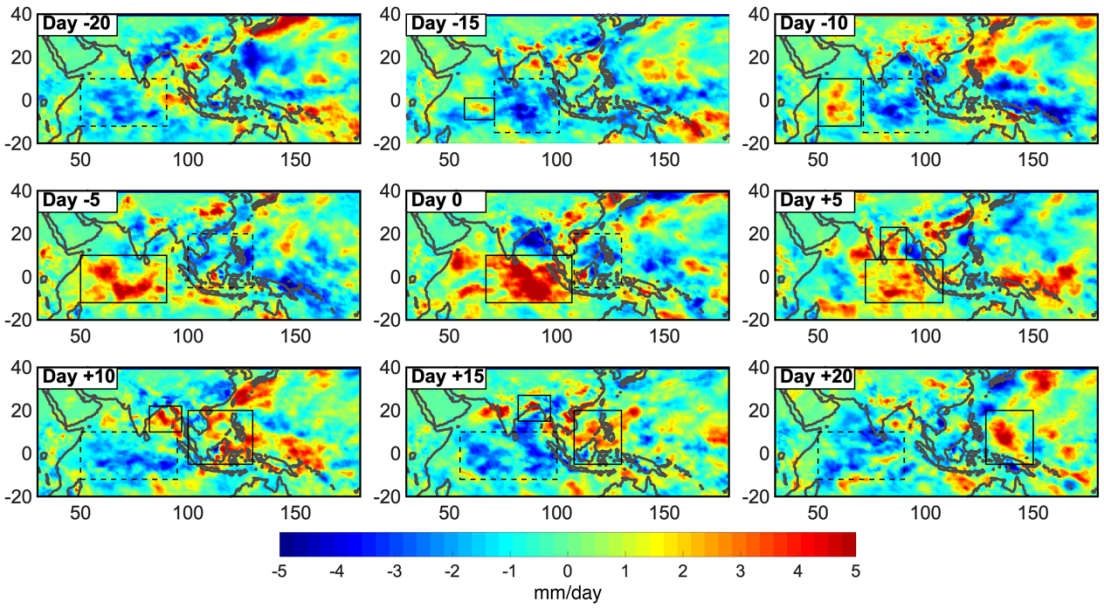

Figure 3.S1. GPCP precipitation anomaly (mm/day) composite of the 30-90-day ISO in the Indian Ocean (20ºS-20ºN,40ºE-100ºE) based a box averaged time series from 2015 to 2018 with the seasonal mean removed.

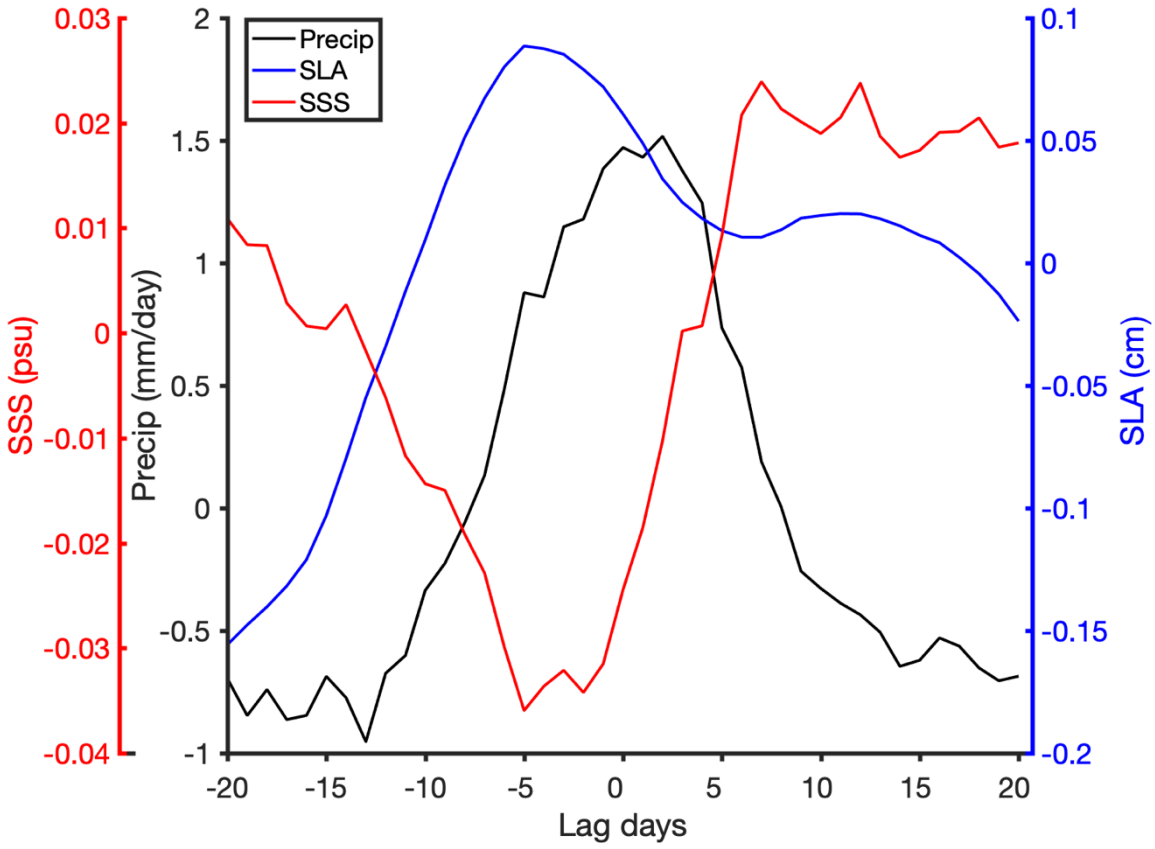

Figure 3.S2. Composite time lag plots of 30-90-day filtered GPCP precipitation (mm/day; black), CMEMS SLA (cm; blue), and SMAP-CAP SSS (psu; red).

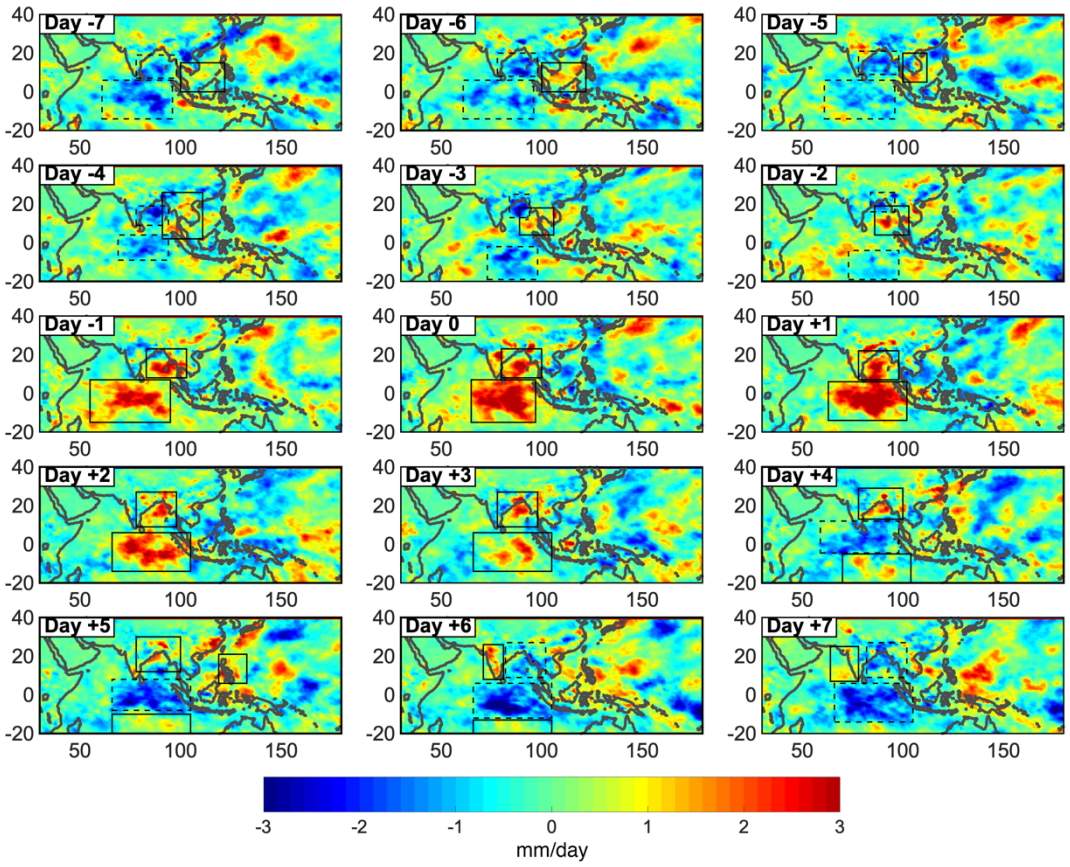

Figure 3.S3. GPCP precipitation anomaly (mm/day) composite of the 10-20-day ISO in the Indian Ocean (20ºS-20ºN,40ºE-100ºE) based a box averaged time series from 2015 to 2018 with the seasonal mean removed.

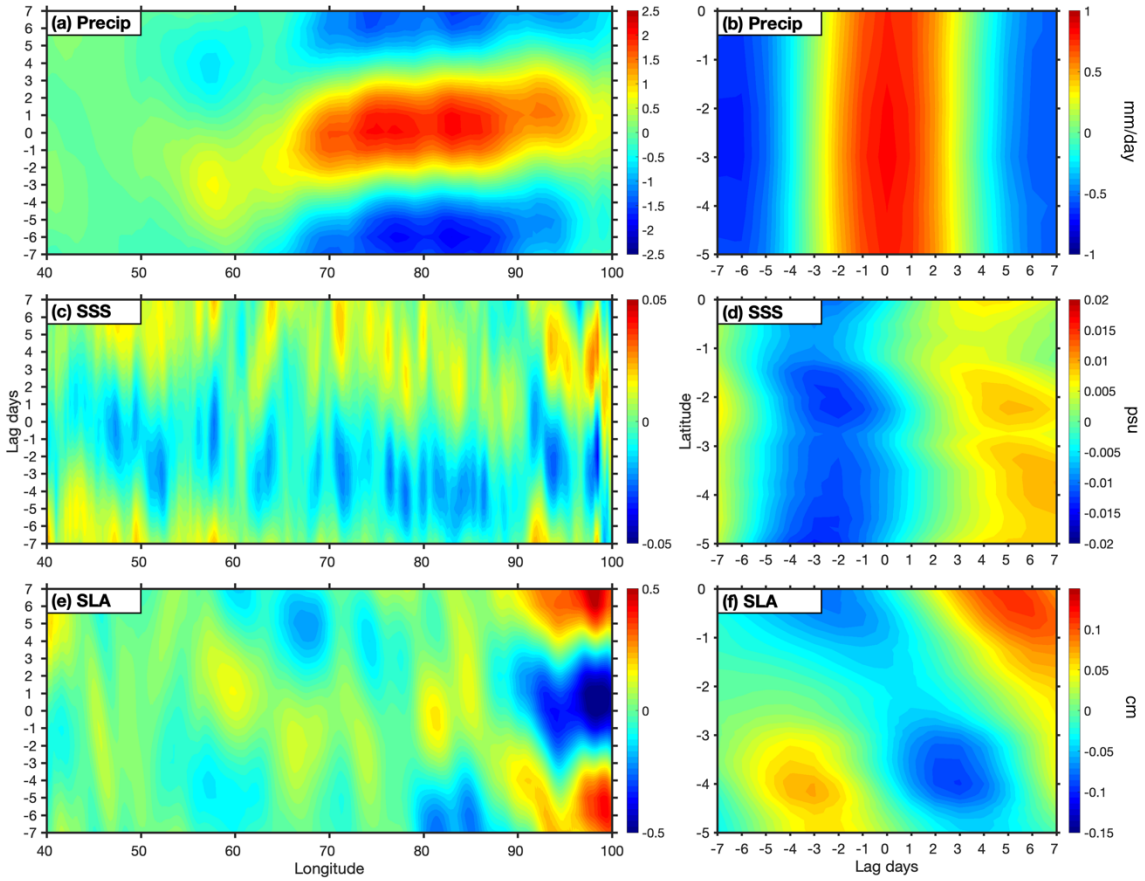

Figure 3.S4. Composite 10-20-day bandpass filtered time lag-longitude plots of deseasonalized GPCP precipitation (a-b; mm/day), SMAP-CAP (c-d; psu), and CMEMS SLA (e-f; cm) from 2015 to 2018 in the Indian Ocean (5ºS-0ºN,40ºE-100ºE) for the southern cell of the double cell structure.

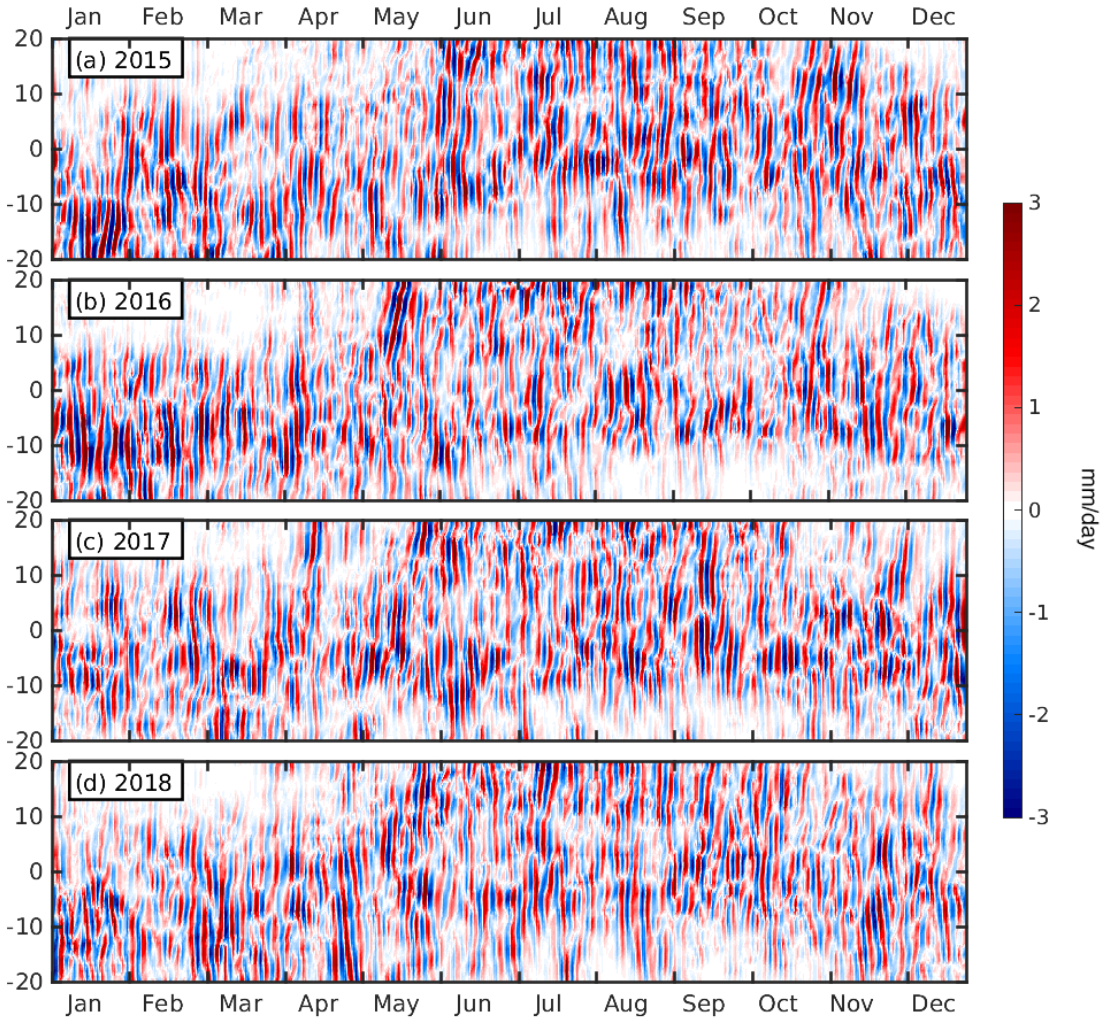

Figure 3.S5. 3-7-day bandpass filtered time-latitude plots of GPCP from 2015 (a) to 2018 (d) in the Indian Ocean (20ºS-20ºN,40ºE-100ºE).

CHAPTER 4

QUASI-BIWEEKLY OSCILLATIONS IN THE BAY OF BENGAL IN OBSERVATIONS AND MODEL SIMULATIONS[3]

[3]Roman-Stork, H. L., Subrahmanyam, B., & V. S. N. Murty (2019). Quasi-biweekly Oscillations in the Bay of Bengal in Observations and Model Simulations, Deep Sea Research II, https://doi.org/10.1016/j.dsr2.2019.06.017

Reprinted here with permission of publisher.

ABSTRACT

Intraseasonal oscillations (ISOs) significantly contribute to the variability and strength of rainfall associated with the Indian Summer Monsoon. The westward-propagating, 10–20-day, quasi-biweekly ISO (QBWISO), in association with the zonal double-cell structure, contributes to an increase in momentum and moisture from the western Pacific Ocean and South China Sea to the Bay of Bengal (BoB) and Indian subcontinent that intensifies monsoonal rainfall rates. The QBWISO also has a meridional double-cell structure positioned over 15–20ºN and 0–5ºN, with the northernmost cell significantly contributing to monsoonal precipitation. The atmospheric systems associated with this QBWISO, particularly the northernmost cell, induce shifts in circulation that directly impact the strength and timing of active and break monsoon periods, which are respectively characterized by wet and dry conditions. Here we conduct a multivariate analysis of the atmospheric QBWISO to both assess its overall characteristics in multiple oceanic variables and analyze how this atmospheric signal interacts with the underlying ocean. We utilize a combination of satellite observations and the Nucleus for European Modeling of the Ocean version 3.4 (NEMOv3.4) ocean model simulated temperature, salinity and mixed layer depth to examine the characteristics of QBWISO for the 2016–2018 Indian Summer Monsoon seasons. This study reveals that both the zonal and meridional double-cell structures in QBWISO precipitation are phase-locked during the southwest monsoon and positively enhance/suppress the precipitation over northern BoB leading to higher amplitudes in QBWISO sea surface salinity (SSS), compared to those in the central and southern BoB. The NEMO SSS also supports the occurrence of higher SSS anomalies at QBWISO period in the northern BoB. We find that NEMO temperature has a

strong biweekly signal in the central and southern BoB down to 250m depth, with the mixed layer temperature showing a marked decrease after the QBWISO precipitation maximum. Comparatively, at subsurface depths the QBWISO signal in NEMO salinity shows a slight increase in thermocline in the central and southern BoB, suggesting that the subsurface Arabian Sea high salinity water mass is affected by the QBWISO.

4.1 INTRODUCTION

Monsoon intraseasonal oscillations (MISOs) in the Indian Ocean greatly contribute to Indian Summer Monsoon rainfall over the Indian subcontinent and the surrounding region. There are several ISOs, with the 30–90-day Madden-Julian Oscillation (MJO) being the most well-known and well-studied. In recent years, however, another ISO has begun to gain attention for its significant contribution to monsoonal rainfall. The quasi-biweekly intraseasonal oscillation (QBWISO), with a period of 10–20 days, is one of the dominant ISOs in the Indian Ocean and is one of the main controls on the active and break cycles of the monsoon (Chatterjee and Goswami, 2004; Chen and Chen, 1993; Krishnamurti and Ardanuy, 1980).

The QBWISO was first characterized by Murakami (1976) as the dominant control of the active and break cycle of the Indian Summer Monsoon. He found these oscillations take the form of an atmospheric mesocyclone over the Bay of Bengal (BoB) region that is cyclonic during active phases and anticyclonic during break phases. This theory was further elaborated upon through wavenumber and spectral analysis (Krishnamurti and Ardanuy, 1980) as well as signal analysis (Chen and Chen, 1993), which revealed the mode to be westward propagating along the monsoon trough with a dominant wavelength of 6000 km and speed of 4.5–6ms−1. A strong biweekly oscillation is not unique to the BoB and Indian

Ocean regions; previous studies have shown there to be a dominant 10–20 day signal in atmospheric convection in the global tropics (Kikuchi and Wang, 2009; Wheeler and Kiladis, 1999). Wheeler and Kiladis (1999) performed spectral analysis of outgoing longwave radiation (OLR) between 15ºS and 15ºN, demonstrating that there was a strong westward propagating signal in zonal wavenumber frequency between 10 and 20 days, much as Krishnamurti and Ardanuy (1980) showed for surface pressure over India.

Past studies have focused predominantly on wavenumber (Krishnamurti and Ardanuy, 1980) and only recently have they begun to shift focus to a more dynamical approach in the atmosphere (Chatterjee and Goswami, 2004; Kikuchi and Wang, 2009). These studies further characterize the QBWISO as having a double-cell structure in the BoB, described either in terms of vortices or convective cells where the northernmost cell is centered on 15–20ÅãN and the southernmost cell is centered just north of the equator (Chatterjee and Goswami, 2004; Kikuchi and Wang, 2009). The southernmost cell was found to be generated in the Indian Ocean, while the northernmost cell, which significantly contributes to monsoonal rainfall, is generated in the western Pacific and propagates into the BoB. There it becomes phase-locked with the southernmost cell, then propagates over the Indian subcontinent before its demise in the region of the Arabian Sea (Kikuchi and Wang, 2009).

Further research has investigated a genesis mechanism for these events. Chatterjee and Goswami (2004) used a 2. layer model to find the QBWISO to have a Conditional Instability of the Second Kind (CISK)-like mechanism of generation and found the structure to be characteristic of an equatorial Rossby Wave made unstable trough a wave-boundary layer-CISK mechanism. Other studies have noted that the double-cell structure

is consistent with a Mixed Rossby Gravity (MRG) wave translated north of the equator (Sengupta et al., 2004; Sengupta and Ravichandan, 2001). More recent studies have discovered that breaking Rossby Waves in the upper atmosphere in the mid-latitudes over the western Pacific can trigger convective events over the South China Sea, providing a mechanism for genesis and formation that is consistent with the CISK-like mechanism and MRG wave analysis of previous studies (Ortega et al., 2017).

While most of the recent research into the QBWISO has focused on the atmospheric component of the oscillation, there remains only a small body of research dedicated specifically to the oceanic response, and most studies have only peripherally considered oceanic impacts of the 10–20-day period. There have been a number of past studies that have focused on the oceanic response to ISOs in the BoB and Indian Ocean (Girishkumar et al., 2017, 2013; Goswami and Chakravorty, 2017; Han et al., 2006; Y. Li et al., 2018; Senan et al., 2003; Vecchi and Harrison, 2002; Wang et al., 2006), but there is a limited body of work concerning the QBWISO events, (Agarwal et al., 2007; Sengupta et al., 2001, 2004; Sengupta et al., 2001a,b; Subrahmanyam et al., 2018). Previous ISO studies in the BoB have utilized the Research Moored Array for African-Asian-Australian Monsoon Analysis and Prediction (RAMA) moorings, models, and satellite observations to observe the oceanic response, but have focused primarily on surface processes.

A study by Sengupta and Ravichandan (2001) analyzed the sea surface temperature (SST) response to ISOs in the BoB, principally using buoy data. Their research found that active monsoon phases, which are strongly modulated by the QBWISOs, result in deep convection, as seen in OLR data, and strong surface winds, as derived from the Tropical Rainfall Measurement Mission (TRMM). They found that the SST response to ISOs

occurred with multi-week period and were dominantly controlled by net atmospheric heat fluxes.

A study by Agarwal et al. (2007) also utilized an ocean general circulation model (OCGM) and National Centre for Environment and Prediction (NCEP) reanalysis fluxes to study QBWISO changes in SST in the BoB. Their study found that changes in net heat fluxes and vertical mixing drove the changes they observed in their model in the central BoB, and that these results were consistent with buoy data, as in Sengupta and Ravichandan (2001). While robust, their study only included one monsoon season and two QBWISO events, suggesting the need for further research with a greater sample size.

A further study focused principally on the equatorial Indian Ocean, which includes the equatorial BoB, and used moored buoys and the Modular Ocean Model (MOM) version 2.2 to study wave propagation on a QBWISO timescale (Sengupta et al., 2004). Their work suggested that the meridional currents in the equatorial region had a strong biweekly oscillation and that the variability observed was characteristic of MRG waves. Their research also found that only the meridional component of the wind stress had a biweekly oscillation, and that these winds helped to drive the westward propagation characteristic of the QBWISO over the equatorial Indian Ocean. Further conclusions suggested a relation to vertical advection in this region.

In this study, we focus on the QBWISOs in the BoB and how the atmospheric signals are translated down into the ocean. Past studies of this type have principally concerned themselves with characterizing the 10–20-day signal in specific oceanic parameters, such as ocean currents, sea surface salinity (SSS), and SST (Agarwal et al., 2007; Sengupta et al., 2001, 2004; Subrahmanyam et al., 2018). While critically important

to understand, there remains a lack of work on the upper ocean response in the BoB to these QBWISOs. The goal of this research is to analyze the recent oceanic response to these atmospheric events, especially rainfall, using a combination of satellite observations and model simulations during the Indian Summer Monsoon season (May–October) from 2016 to 2018. Through analyzing how deep the QBWISOs penetrate the BoB, we can better understand the full oceanic response to the atmospheric signal beyond surface processes, as well as how strongly the ocean is affected by such activity on a short time scale. This paper is organized as follows: Section 4.2 presents the data and methods used, Section 4.3 describes the results and discussion of the study, and Section 4.4 summarizes the conclusions.

4.2 Data and Methods

A. Data

To analyze the oceanic response to QBWISOs in the BoB, a multivariate analysis was conducted using both satellite observations and model simulations. As the northernmost cell of the double-cell structure is largely defined by its significant contribution of rainfall to the BoB and Indian subcontinent, daily precipitation data from the joint National Aeronautics and Space Administration (NASA) and Japan Aerospace Exploration Agency (JAXA) Global Precipitation Measurement (GPM) mission was used to characterize the QBWISO events. GPM is the follow on to NASA's TRMM, which has been used in several studies to describe QBWISO events (Chatterjee and Goswami, 2004; Kikuchi et al., 2012; Kikuchi and Wang, 2009). As TRMM is no longer operational, GPM stands as a viable alternative to its predecessor's high-resolution precipitation in the tropics and has the advantage of both spanning through present years and having near global

coverage. Data were obtained from NASA's Earthdata database (https://pmm.nasa.gov/data-access/downloads/gpm) at 0.1ºx0.1º horizontal grid spacing and are available from March 2014-present.

SSS observations were taken from NASA's Soil Moisture Active Passive (SMAP) mission. The SMAP SSS product from NASA's Jet Propulsion Lab (JPL) is available at a horizontal grid spacing of 0.25ºx0.25º and a daily temporal resolution from April 2015 to present. While SMAP has a global repetition cycle of 8 days, its near-perfect global coverage at 3 days allows for a daily product produced through interpolation of an 8-day running mean. Previous studies have used SMAP to study ISOs in the BoB and found it to adequately represent the ISO signal (Subrahmanyam et al., 2018). SMAPv4.0 is used in this study as it is corrected for brightness temperature biases and galaxy contamination (Fore et al., 2016).

SST observations were taken from the National Oceanic and Atmospheric Administration's (NOAA) Optimum Interpolation Sea Surface Temperature version 2 (OISSTv2) data using the Advanced Very High Resolution Radiometer (AVHRR; Reynolds et al., 2007). Daily AVHRR SST data are available from NOAA at 0.25ºx0.25º gridded horizontal resolution from 1978 to present, (https://www.esrl.noaa.gov/psd/data/gridded/data.noaa.oisst.v2.highres.html). Previous ISO studies have used AVHRR derived SSTs and found them to be highly applicable in the Indian Ocean region for these purposes (Girishkumar et al., 2017; Li et al., 2018a,b, 2016; Murty et al., 2004).

B. MODEL SIMULATIONS

In this study, we have used European Centre for Medium-Range Weather Forecasting (ECMWF) ERA-Interim reanalysis daily evaporation, which is available in 1ºx1º horizontal grid spacing from 1979 to present as a daily product. While available as both forecast and reanalysis products, here only the reanalysis is used, (http://apps.ecmwf.int/datasets/data/interim-full-daily/levtype=sfc/). ECMWF has been widely used in the Indian Ocean and BoB in a variety of studies, including ISOs with great success (Cheng et al., 2018; D'Addezio and Subrahmanyam, 2018; Fu et al., 2007; Sanchez-Franks et al., 2018; Wang et al., 2006).

The global Nucleus for European Modeling of the Ocean version 3.4 (NEMOv3.4; Madec, 2008) was used extensively in this study. The model has been used to study several different oceans (Bernard et al.,2006; Penduff et al., 2010, 2007) and in the Indian Ocean to analyze the Indian Summer Monsoon response (Momin et al., 2013; Samson et al., 2017). The model is most well-known for being the oceanic component of the ECMWF reanalysis. NEMO ocean output files are available at 1/12º gridded horizontal resolution and 50 vertically stratified depths, providing eddy resolving high resolution model output. The model is initialized with the temperature and salinity climatology using World Ocean Atlas 2013 (https://www.nodc.noaa.gov/OC5/woa13/woa13data.html). NEMO incorporates river runoff monthly climatology obtained from the Dai and Trenberth estimates (Dai and Trenberth, 2002). The surface forcing data for the NEMO model integration is taken from Coordinated Ocean-sea ice Reference Experiment version 2 (CORE v.2), (Large and Yeager, 2009). NEMO's latest version has 10-day forecasts from 2016 to present available in daily temporal resolution. This version assimilates altimeter

data, in situ temperature and salinity vertical profiles, and satellite derived SST. The NEMOv3.4 period (2016–2018) provides the temporal framework for this study.

C. METHODOLOGY

To isolate the QBWISO signal in both the atmospheric and oceanic variables, a 4th order Butterworth recursive time (bandpass) filter was employed following the methodology of Krishnamurti et al. (2017). The bandpass filter uses a 10-day lower limit and 20-day upper limit to isolate the desired signal, where all data are double filtered (forwards and backwards) to eliminate edge effects. This technique is widely applied in ISO studies, most notably towards the 30–60-day Boreal Summer Intraseasonal Oscillation (BSISO) in SST and ocean heat content (Krishnamurti et al., 2017). Lags between unfiltered time series were performed using a cross-correlation MATLAB algorithm. This MATLAB algorithm (finddelay) estimates the normalized cross-correlation between two signals and estimates the lag based on the lag value for which the normalized cross-correlation has the highest absolute value.

All composites were created following a similar methodology of Chatterjee and Goswami (2004). A box-averaged time series for the BoB (80–100ºE, 0–20ºN) for GPM precipitation data was created from 2016 to 2018. Using this time series, an Ensemble Empirical Mode Decomposition (EEMD) principle component analysis was performed with 100 ensemble members and a 0.5 standard deviation in order to extract the individual Intrinsic Mode Functions (IMFs) that coincided with the desired time period (10–20 days), (Huang and Wu, 2008; Wu and Huang, 2009). It was found that IMFs 2 and 3 had periodicities that significantly overlapped with the 10–20-day time scale, and so the time series were combined and averaged. This raw IMF time series was then filtered using the

4th order Butterworth bandpass filter for the 10–20-day band. To create an index in GPM precipitation, the filtered IMF time series was then normalized to its own standard deviation. Composite events were identified as peaks above 1 standard deviation and further refined to only occur between May and October for the Indian Summer Monsoon season, resulting in 29 total identified events. Following the Chatterjee and Goswami (2004) methodology, 15 phases for the QBWISO were determined with Day 0 as the peak then subtracting and adding 7 days from Day 0 to obtain a full 15 phase oscillation, Day −7 to Day +7, respectively. Repeating the procedure by choosing troughs (Day −7) as the identifying event instead of peaks (Day 0) did not significantly alter the results. Composites were then constructed by averaging each phase together to create a full composite time series that was then applied to the spatial products. Repeating this procedure for one specific year or randomized events did not significantly alter the results or observed patterns.

Spatial filtering of composite maps was performed using a wavelength-based bandpass filter between 3000 and 6000 km, as the wavelength of the QBWISO signal has been shown to be 6000 km (Chatterjee and Goswami, 2004; Chen and Chen, 1993; Krishnamurti and Ardanuy, 1980).

4.3 Results and Discussion

A. Zonal and Meridional Double-Cell Structures in GPM Precipitation and Precipitation minus Evaporation Anomalies

To begin the assessment of the QBWISO, it is first advantageous to visualize how this ISO appears in precipitation. As precipitation is one of the principle ways in which convective double-cell manifests and impacts the people who live in this region, it is critical

to see how it evolves in the BoB, Indian Ocean, and western Pacific over the 15 phases. The QBWISO in GPM precipitation shows the characteristic meridional double-cell structure that has been described in the previous studies (Chatterjee and Goswami, 2004; Kikuchi and Wang, 2009), where one cell is centered over the northern BoB and the other cell is centered over the equatorial region (Figure 4.1). The life cycle of the northernmost cell of the double-cell becomes most apparent in this figure, denoted by a solid black box, as it forms in the western Pacific/South China Sea and propagates westward into the BoB where it rapidly intensifies between Day −1 and Day +1. Beginning at Day +2, this maximum in precipitation in the BoB weakens and begins propagating westward, for the northernmost cell and south/southwestward for the southernmost cell. The northernmost cell of the convective meridional double-cell terminates in the Arabian Sea after Day +4.

This overall pattern of the double-cell structure has been noted by previous studies in the Indian Ocean (Chatterjee and Goswami, 2004; Kikuchi and Wang, 2009), who also found the northernmost cell of the meridional double-cell structure contains the majority of the QBWISO precipitation. The generation and propagation of this northernmost cell in the western Pacific Ocean and South China Sea was also noted by Kikuchi and Wang (2009) in their global study of biweekly oscillations. They also found that a new cell begins to form in the western Pacific as the original cell is reaching its demise in the Arabian Sea. A more recent study focused on the South China Sea (Wang and Chen, 2017) used OLR to find that the northernmost cell of the double-cell is generated in the western Pacific, where it moves northwestward into the South China Sea and then westward into the Indian Ocean, as is shown in Figure 4.1. As such, our progression of precipitation from genesis to demise in the western Pacific into the Arabian Sea is in good agreement with past studies.

It is interesting to note that during both the negative phase (Day −7 to Day −3) and the positive phase (Day +4 to Day +7) of the QBWISO, there are negative anomalies of precipitation, i.e. dry conditions prevail over the BoB. In association with this negative precipitation anomaly in the meridional double-cell, there occurs a zonal double-cell structure with one cell of positive precipitation anomaly over the western Pacific and the other over the northern Arabian Sea. This zonal double-cell of positive precipitation anomaly is separated by the negative precipitation anomaly over the northern BoB; however, high precipitation conditions (positive anomalies of precipitation) of this meridional double-cell prevail over these two regions during Day −2 through Day +3 of the QBWISO. The zonal double-cell structure is, however, weak during the positive phase of the meridional double-cell structure wherein high precipitation occurs in the northern BoB.

While understanding the patterns of precipitation is valuable, a more useful measure of oceanic and atmospheric processes is precipitation minus evaporation (P-E), which helps to describe regions where precipitation or evaporation is more dominant. P-E has long been known to be suggestive of salinity, with precipitation, evaporation, and river runoff being the primary contributors to oceanic salinity values, not including mixing and advective processes. Composites of P-E show a similar overall pattern to the composites of precipitation, though with far less noise and a more pronounced change in conditions over the 10–20-day period (Figure 4.2). As in Figure 4.1, the most striking feature remains the northernmost cell of the meridional double-cell structure, which reaches its maximum positive P-E over the BoB from Day −1 to Day +1, with dominant precipitation (P > E) during this time. The dissipation region over the Arabian Sea, as well as the southern Indian

Ocean, is evaporation dominated (P < E). Compared to the precipitation only figure, the development of precipitation in the BoB is more clearly shown, where it becomes apparent that a disturbance is already present in the eastern BoB from Day −4, which then expands and intensifies at Day −1 and then weakens after Day +1.

As opposed to precipitation, however, the overall life cycle of the double-cell is far less apparent in P-E. While the overall sinusoidal pattern of precipitation in the BoB remains fairly intact when including evaporation, the overall propagation signal from genesis to demise largely disappears. This suggests that while we may see a P-E and salinity signal on a biweekly scale in the BoB, such a signal in salinity is unlikely to appear in the South China Sea or western Pacific. Given the prevalence of P-E in the BoB, however, salinity should present a reasonably strong signal. Previous studies (Subrahmanyam et al., 2018) have used SMAP salinity values in the BoB to analyze ISO signals and found the occurrence of biweekly ISO in SSS in the BoB. This suggests that at least SSS is impacted on a biweekly time scale but does not take into account processes with depth.

While Figs. 1 and 2 describe the spatial distribution and life cycle of precipitation during the QBWISO, the westward propagation of the zonal double-cell structure from the western Pacific region to northern BoB to the Arabian Sea can more clearly be seen through a Hovmöller diagram (Figure 4.3). Here the generation, propagation, and demise of the northernmost cell over the 15-day cycle can be seen. As noted by past studies (Kikuchi and Wang, 2009; Wang and Chen, 2017), the northernmost high precipitation cell in the western Pacific region is generated around 130ºE on Day −7 and then propagates westward into the BoB (90–100ºE) where it reaches its maximum between Day −3 and Day +3, after which it ends in the eastern Arabian Sea region (60–65ºE). From this diagram, propagation

speed can be calculated, and is found to be 4.8 m s−1, which agrees with previous findings of 4.5–6ms−1, (Chatterjee and Goswami, 2004; Chen and Chen, 1993; Krishnamurti and Ardanuy, 1980).

B. Comparison of 10-20 day Filtered Time Series of Precipitation, Sea Surface Temperature

While the QBWISO typically manifests through its atmospheric component, the underlying oceanic processes involved are critically important to understand. To assess the relationship between precipitation, SST, and SSS, satellite observations from GPM precipitation, OISST, and SMAP, respectively, were compared by region within the BoB, (Figure 4.4). Consistent with the spatial distribution of precipitation in previous figures (Figures 4.1, 4.2), the regional signal of precipitation is strongest in the northern and central BoB and is most prominent during the Indian Summer Monsoon season. Overall, SSTs have the strongest signal in the northern and central BoB as well, with the signal slightly leading precipitation in the summer months. Salinity has the most distinct signal, particularly in the northern BoB, that gradually weakens farther south, particularly in the latter half of 2017. Lag for SSS was calculated with respect to precipitation by region and it was found that in the central, southern, and equatorial BoB, SSS lags precipitation by approximately 100 days, which is consistent with previous studies that suggested a roughly 3 month lag (or P and SSS are in quadrature) between convection and SSS in the BoB (Murty et al., 2004). The northern BoB has a lag of 135 days, putting SSS in more than quadrature with precipitation and creating a full seasonal lag. This suggests that the salinity signal in the northern BoB is dominated by the freshwater fluxes from river runoff in the northern BoB as opposed to the precipitation and evaporation signal in the rest of the basin.

C. Spatial distributions of composites of 10-20-day filtered precipitation minus evaporation, SMAP sea surface salinity and optimum interpolation sea surface temperature anomalies

Analysis of the spatial distributions of composites of the 10-20-day filtered of P-E, SMAP SSS anomalies, and OISST anomalies in the BoB reveals a similar pattern to the time series analysis (Figure 4.5). Observational trends in P-E again show the western propagation and intensification of QBWISO precipitation within the BoB, particularly during Day -3 to Day +3. Accordingly, as in Figure 4.4, the northern BoB has the strongest signal of SSS, with an overall freshening trend in the northern BoB over the 15-day period. OISST anomalies in the northern BoB remain consistently low over the biweekly period, possibly as a result of the freshwater fluxes observed in SSS. SSTs exhibit an overall cooling trend that is nearly basin-wide during the biweekly period and is nearly uniform regardless of latitude, save positive anomalies in the northwest BoB from Day -7 to Day 0. SST ISO processes have been observed by previous studies (Agarwal et al., 2007; Han et al., 2006; Rao et al., 2011; Sengupta and Ravichandan, 2001; Vecchi and Harrison, 2002) in the BoB and have been largely attributed to a combination of vertical mixing processes and surface heat fluxes. Given the nature of the QBWISO and the horizontal advection that helps modulate SSS processes, it is likely that a combination of fluxes and mixing creates the SSS observed SSS trends.

A previous study by Subrahmanyam et al. (2018) also used SMAP salinity to look at ISOs in the BoB. This study, however, reported higher amplitudes of SSS than we see for the QBWISO in the northern BoB (Figs. 4, 5). Our results, however, also report higher amplitudes for 2018 than in Subrahmanyam et al. (2018). This difference is likely due to a

difference in boxes chosen for averaging purposes in time series (Figure 4.4). Overall, in both studies, higher amplitudes of SSS are seen in the northern BoB compared to the central and southern regions. It is proposed here that the QBWISO of the zonal and meridional double-cell structures in precipitation are in coherence and phase-locked during the Indian Summer Monsoon season. Every 7 days, the precipitation in the northern BoB is enhanced due to both the double-cell structure. Over the subsequent 7 days, precipitation is suppressed due to the negative phase of the double-cell and QBWISO. This pattern of enhancement (suppression) of precipitation leads to a decrease (increase) in SSS in the positive (negative) phase of the QBWISO. Combined with river runoff and horizontal salinity advection, and we see the stronger salinity signal in the northern BoB. Conversely, in the central and southern BoB, we do not see the same impact of the double-cell on salinity.

D. Spatial distributions of composites of 10-20-day filtered precipitation minus evaporation, NEMO model parameters of sea surface salinity, sea surface temperature and mixed layer depth anomalies

While satellite observations assist us in studying oceanic processes to an unprecedented spatial extent, they still only go skin deep, and thus models are required to understand other processes, especially with depth throughout the full basin. To directly compare with the satellite observations in Figure 4.5, composite anomalies of 10-20-day filtered P-E, NEMO SSS, NEMO SST, and NEMO mixed layer depth (MLD) is shown in Figure 4.6. NEMO SSS has the weakest signal of the oceanic variables, with little overall change over the 15-day phase cycle. In the QBWISO, the northern and northwestern BoB and north of Andaman Sea are dominated by positive SSS anomalies (corresponding to the

negative P-E anomalies) that are weakened with the introduction of strong negative anomalies characteristic of freshwater flux from riverine discharge in response to increased precipitation over land in the region. The central and southern BoB experience little change, but there is a slight increase in salinity anomalies in those regions, particularly from 85-95°E. The equatorial BoB has no apparent change in salinity.

Compared to SMAP SSS anomalies (SSSA), NEMO SSSA has a strong negative signal in the northern BoB over the 15-day phase cycle, (Figs. 5, 6). This stark contrast may be due to the way in which horizontal advective processes are modeled in NEMO, as well as how observational data are assimilated into the model. While the sign of the anomalies is different in the northern BoB, however, there remains an overall trend towards freshening in the northern BoB, as the NEMO positive anomalies become weaker and more negative anomalies emerge in that region. In the central and southern BoB, there are fewer competing processes governing salinity, and both observational and modeled SSS show weak positive anomalies that emerge.

NEMO SST changes are much more than SSS over the 15-day phase cycle, dominantly characterized by positive anomalies during the negative phase of the ISO in the northwest BoB and then by negative anomalies in central and southern BoB during the positive phase of the ISO (Figure 4.6). Corresponding to the positive SSSA in the northwestern BoB during the negative phase of QBWISO, the SST anomalies (SSTAs) are relatively negative in this region, suggesting the role of upwelling process dominating during the negative phase of QBWISO. The northern BoB experiences the majority of the positive SSTAs, whereas the central BoB appears to have the highest magnitude negative anomalies—the region coincident with the positive SSS anomalies. This SST signal is more

pronounced than in OISST (Figure 4.5), but follows a similar overall pattern, suggesting that NEMO models BoB temperatures reasonably well. It is likely that the vertical mixing processes in the NEMO model are dominantly controlling changes in SST.

MLD follows a similar pattern to precipitation, reaching its maximum depth around Day 0 at the same time as precipitation, though the spatial pattern appears to have a slight lag delay. As with P-E, MLD anomalies are negative in the days both leading and following the maximum change around Day 0, though the maximum changes are of a smaller magnitude and are highest in the southern BoB region. In the eastern BoB and southeastern BoB, corresponding to the positive SSSA, the SSTA are negative and MLD anomalies (MLDAs) are positive, suggesting the deepening of MLD. This process of mixed layer deepening strongly suggests that vertical mixing and mixed layer processes are responsible for the SST and SSS patterns seen in both satellite observations and NEMO simulations.

Still, the positive anomalies in NEMO SSS present something of a problem, as the East India Coastal Current (EICC) should be flowing along the east coast of India and contributing to horizontal advective processes. What is most likely contributing to this disparity are atmospheric processes, such as wind stress curl. Previous studies have shown that the meridional component of surface winds and wind stress curl is one of the dominant forces that control both the atmospheric and oceanic components of the QBWISO (Sengupta et al., 2004; Wang and Chen, 2017). Wind stress curl drives upwelling processes in the BoB during the southwest monsoon months (Murty et al., 1996), and thus could easily cause the SST and SSS signatures in NEMO, which would be cold and saline if upwelling were indeed involved. A 1998 study by Goswami et al. (1998) of surface winds over the Indian Ocean, including the BoB, showed that there is a strong biweekly

oscillation in surface winds over the BoB, particularly during active phase of the monsoon. This peak in wind and circulation over the central BoB region (~88°E) would drive upwelling, and vertical mixing in the BoB, which would result in the SSS and SST signatures seen in both observations and model simulations, (Goswami et al., 1998).

E. Response of upper ocean temperature and salinity to the QBWISO

Though the surface ocean processes are important, it is also critical to understand how subsurface processes respond to disturbances at the surface and to understand the broader impacts of the QBWISO on the greater ocean. Figure 4.7 describes NEMO ocean temperature at four different levels: 0, 25, 50, and 75 m over Day -7, Day 0, and Day +7, where anomalies shown are created by subtracting the seasonal mean. The progression of SSTs and spatial distribution are similar to those in Figure 4.6, with the highest negative values appearing in the central and southern BoB region as against the precipitation maximum at Day 0. The temperature anomalies become stronger with depth, with the surface signal being reflective of a much stronger signal in the subsurface in that region. The surface signal appears to have a constant magnitude down to 25 m, roughly the MLD, with anomalies of a higher magnitude and slightly different spatial patterns appearing at the levels below this. As the negative temperature anomaly develops in the subsurface, penetrating down at least to 75 m, and reaches the surface slightly later, it is likely that the surface signal seen is reflective of upwelling in that region, with deeper waters being pulled to the surface through Ekman pumping. The response of QBWISO in the water column is that temperatures are warmer during the negative phase of QBWISO (Day -7) and cooler during the positive phase (Day +7) (Figure 4.7).

To further investigate the change in temperature with depth, cross-sections over the central (10-15°N) BoB region were taken for Day -7, Day 0, and Day +7 (Figure 4.8). As in Figure 4.7, a subsurface cold anomaly can be seen around 85-88°E in the central BoB, with the highest magnitude anomaly at deeper levels. As the 15-day phase cycle progresses, however, this deep, cold anomaly is pulled to the surface, from 75 m at Day -7 to 50 m and a surface signature at Day +7. In the western (80-86°E) BoB, the warm anomaly that dominates the region at Day -7 slowly disappears and is replaced by much cooler waters by Day +7, suggesting a large cooling trend from 80-88°E over the entire period of oscillation. Conversely, the eastern BoB (94-98°E) experiences a slight warming trend, where the cold anomaly present at Day -7 disappears and is replaced by neutral waters by Day +7. The advection of cold waters towards the surface and cooling trend seen over the duration of the QBWISO suggests both upwelling and meridional transport of waters on either side of the BoB, such as the EICC on the western boundary. The changes in the temperature anomalies in the western BoB and eastern BoB would reflect the impact of large-scale thermocline and circulation changes in association with the westward propagating annual Rossby waves radiated from the coastally trapped Kelvin waves at the eastern boundary of the BoB.

The depth-time profiles for the northern, central, southern, and equatorial BoB in temperature, salinity, and MLD show clearly which regions are most significantly impacted by the ISO precipitation (Figure 4.9). The temperature-depth plots all show a similar pattern with varying magnitudes above MLD, with positive anomalies before the maximum precipitation event and negative temperature anomalies after the precipitation maximum. These spatial and depth patterns are strongly consistent with wind-driven upwelling,

particularly in the central and south BoB, which contributes to vertical mixing and changes in the mixed layer. In the central, southern, and equatorial BoB, MLD appears to share a similar pattern to precipitation, having a weakly sinusoidal signal with an oscillatory magnitude of roughly ±5 m. Below the MLD, the central BoB has the greatest change in temperature, sharing a similar pattern as the surface changes, with stronger cold anomalies during the negative phase of the QBWISO. This again suggests that meridional wind stress driven processes are the chief contributor, as the peaks in wind stress occur over the south and central BoB (Goswami et al., 1998).

The biweekly pattern in salinity is less pronounced than in temperature, or even in MLD (Figure 4.9). Over the biweekly time period, however, the positive salinity anomalies weaken and all but disappear below the mixed layer, suggesting a freshening trend driven by advective processes. In the central BoB, there are also high salinity anomalies above the mixed layer, but these patterns follow the same spatiotemporal distribution as the central BoB temperature anomalies, and thus are likely representative of the same upwelling as previously noted. Below the mixed layer in the central BoB, low salinity anomalies dominate the negative phase of the ISO and neutral to positive anomalies dominate the positive phase. The southern BoB has a very weak signal in salinity, though there is a slight shift towards higher salinity waters above the mixed layer during the positive phase following the precipitation maximum at Day 0. The equatorial BoB does not appear to have a biweekly change in salinity. This spatiotemporal distribution of temperature and salinity with depth suggests that upwelling and mixing are the dominant mechanisms that govern temperature over the biweekly period, whereas horizontal advection and freshwater input modulate salinity values.

Though salinity does not have as strong of a signal as temperature, it is still important to understand the observed changes (Figure 4.10). Over the 15-day phases of the QBWISO, there is a slight salinification of the central BoB above 50 m in the central and southern BoB and a slight freshening of the northern BoB surrounding the coast. It is interesting to note that though NEMO is an ocean model, the resultant riverine fluxes from the increased precipitation from the QBWISO can be observed in the northern BoB surrounding the coast, visible as strong negative salinity anomalies.

As the central BoB seems to exhibit the greatest change over the QBWISO, a composite cross-section of salinity was created, as was already done for temperature (Figure 4.11). As noted previously, the salinity signature is much weaker than in temperature, and the maximum changes in salinity largely occur above the mixed layer and above 75 m. In the eastern BoB, all observed change occurs in the mixed layer, with higher salinity anomalies dominant over the 15-day phase cycle. From Day -7 to Day 7, however, there is a slight salinification of the mixed layer between 92° and 94°E in the eastern BoB. From 80° to 88°E, the negative salinity anomaly that occurs between 50 and 75 m depth at Day -7 disappears almost entirely by Day +7, suggesting a flux of saltier waters into the region. When compared with the temperature cross-sections of this region in Figure 4.8, it is apparent that cooler, saltier waters are transported into the western central BoB between Day -7 and Day +7, with a net cooling and salinification of the area.

F. Comparison of unfiltered and 10-20-day filtered NEMO mixed layer depth in various regions of the Bay of Bengal

The MLD exhibits a slight oscillation on the biweekly time scale, appearing to follow a similar spatiotemporal pattern to precipitation, suggesting that the deepening of the mixed layer is a result of the precipitation and storm activity (Figure 4.12). To further analyze the behavior of the mixed layer in the BoB, box-averaged time series for each of the four regions were created and then filtered using a 10-20-day bandpass filter for 2016. What is most clear from the unfiltered time series is the seasonality of MLD activity. In January-March, there is limited activity in the northern and equatorial BoB, but the central and southern BoB experience slight changes. For the rest of the year, the central and southern BoB respond similarly, with a sudden uptake in activity and subsequent deepening of the mixed layer between May and October, a brief shallowing from October to November, and then a slight deepening again during winter. In the northern BoB, all of this activity is severely muted, with the only summer deepening occurring during between mid-May and the beginning of September. The winter deepening only occurs in the northern BoB during December and January. The equatorial BoB has the strongest and deepest MLD signal, peaking in late August and early September. While there is little to no winter signal in the equatorial BoB, the summer deepening begins in late May and then continues until mid-December, exhibiting a marked oscillatory pattern in the process. These results are consistent with the findings of Girishkumar et al. (2017), who used RAMA moorings to analyze mixed layer temperature in the BoB with respect to the 30-60-day ISO. Their study also showed a distinct seasonality, with a strong deepening of the mixed layer during the Indian Summer Monsoon season (Girishkumar et al., 2017).

Bandpass filtered time series of MLD in these same regions reveal a similar temporal distribution as the unfiltered time series, though only for QBWISO events (Figure 4.12). As in the unfiltered, the filtered MLD time series reveals very little activity in the northern BoB. The central BoB has a reasonably strong pattern, particularly during the summer monsoon season, though oscillations of this form appear to have a magnitude of <10 m, consistent with the composite MLD cross-sections and spatial patterns seen in previous figures. The southern BoB has a weaker signal than the central, though the pattern is more consistent across seasons. The equatorial BoB again has the strongest signal, though the filtered time series reveals several distinct patterns. the weakest MLD events occur in May and June in the equatorial BoB, with the strongest summer events occurring in August and September, followed by another series of events in November and December, indicative of the northeast monsoon as opposed to the southwest (summer) monsoon. Differences between the unfiltered and filtered time series appear primarily to be due not to seasonal signals, but to other ISOs. Particularly in the equatorial region, the MJO and the BSISO (or MISO) may be responsible for much of the MLD activity that is seen (Girishkumar et al., 2017). As these other ISOs are equator-based and northward propagating in the BoB region, it would account for the diminishing signal in the unfiltered time series. Mixed layer dynamics in the BoB on intraseasonal time scales are largely controlled by air-sea fluxes and wind stress (Girishkumar et al., 2017). Combined with the precipitation patterns, SST, and SSS, it seems increasingly apparent that wind stress, especially the meridional component of the wind, is the primary driver of QBWISO oceanic activity in the BoB, even as the precipitation and convective signal is mainly how the ISO is characterized.

G. Depth-time sections of 10-20-day filtered NEMO temperature and salinity in various regions of the Bay of Bengal

As one of the main goals of this research was to determine how deep the QBWISO signal penetrates the BoB, it was advantageous to plot both temperature and salinity with time and depth, while isolating the QBWISO signal through a bandpass filter (Figure 4.13). Through this analysis, temperature clearly has a stronger signal than salinity and penetrates far deeper into the BoB. In the northern and central BoB, temperature appears to have strong variability in the upper ocean above the mixed layer and then between 50 and 150 m depth. In the southern BoB, the strongest temperature signal occurs not at the surface, but rather between 50 and 250 m depth. In the equatorial region, much as with MLD in Figure 4.11, the QBWISO signal has two main parts: a lower energy signal in May and early June and a higher energy signal in August through October. This signal in the equatorial BoB, however, is strongest between 50 and 200 m depth.

The filtered signal in salinity is very weak, with maximum amplitude anomalies not exceeding 0.05. The northern BoB has the strongest surface and upper ocean signal (0-100 m), with the strongest signal occurring towards the end of the summer monsoon season. The central BoB has a relatively weak signal, with the highest signals being confined to the mixed layer. The southern BoB is similar, though the salinity signal could arguably penetrate down to 150 m. The equatorial region follows a similar temporal pattern to temperature, though much weaker and only extending down to 150 m instead of 250 m.

The spatiotemporal pattern of the QBWISO at depth suggests that in the equatorial and southern BoB, the transition months before and after the summer monsoon period

provide the greatest activity, further suggesting that the seasonal reversal of the oceanic currents may play a role in modulating the QBWISO signal, particularly during May and October. During August and September, however, the strong signal may be attributed to Indian Ocean Dipole (IOD) processes, particularly as 2016 was an extremely negative IOD year. While the link between IOD, the El Niño-Southern Oscillation (ENSO), and ISOs is still poorly understood, a recent study has suggested that ENSO phase plays a significant role in the timing of monsoon onset over the BoB through modulating ISO strength and timing (Li et al., 2018). 2016 was also a strong El Niño year, which slightly delayed onset in the BoB and led to a reasonably weak monsoon. While much research has been done on the relationship between ENSO, the IOD, and the monsoons, the dynamical relation between these oscillations and the QBWISO are not well understood, and further research will be required to establish how these different processes interact.

4.4 CONCLUSION

In this study, we used a combination of satellite observations and NEMO ocean model simulations to analyze the propagation and impact of the QBWISO in the BoB, with special attention to the examination of the extent of influence of QBWISO into the water column below surface. Our analysis reveals that the QBWISO in precipitation has both zonal double-cell structure and meridional double-cell structures with enhanced/suppressed precipitation for every 7 days in the northernmost cell in the northern BoB thus also impacting the SSS at QBWISO periods in the northern BoB. The zonal double-cell precipitation propagates westward from the western Pacific to the northern Andaman Sea and northern BoB in about 7 days with a propagation speed of about 4.8 m s^{-1}. This leads to an overall freshening in conjunction with river runoff in the northern BoB,

thereby decreasing SSS over 7 days and increasing SSS over the next 7 days due to reduced precipitation conditions (large negative precipitation anomalies) during the QBWISO. This brings in large amplitudes (±0.5 psu) in SSS in the northern BoB due to QBWISOs and it was particularly noticeable in 2018, compared to the QBWISO SSS amplitudes in the central and southern BoB, wherein the impacts of zonal and meridional double-cell structures in precipitation are at minimum. The QBWISO in NEMO SSS also reveals positive SSS anomaly in the northern BoB, and supports that noticed in the observations, and also the impacts of upwelling processes.

The QBWISO filtered time-series of GPM precipitation and SMAP SSS in the northern BoB, central BoB, southern BoB and equatorial box reveal that precipitation and SSS are in quadrature (a lag closer to 90 days with precipitation leading). In the northern BoB, the lag is high up to 135 days suggesting the horizontal advective process affects the SSS in addition to precipitation. The central BoB was also found to have a weak increase in salinity that peaked in amplitude 3 days after the precipitation maximum. SSTs were found to cool, particularly in the central and southern BoB over the biweekly period, with the peak in cold SSTs occurring at the same 3-day lag as SSS in the same region. When combined with known wind stress and surface wind patterns during the QBWISOs, it is proposed that the cooling and salinification of the central BoB is due to wind-induced upwelling in the central BoB. These processes, in turn, help to cause mixing in the upper ocean and deepen the mixed layer. Despite the majority of activity occurring above the mixed layer, there are still deeper ocean processes active on the biweekly time scale down to 250 m depth, suggesting that ocean currents and horizontal advective processes also play a critical role in QBWISO salinity and temperature regulation at depth, particularly in the

50-75 m depth range wherein the Arabian Sea high salinity water mass penetrates into the central BoB from the southwestern Bay during the southwest monsoon. While we have conducted a general study of recent ISO events, primarily using composite analysis, there is still a great deal of work to be done on QBWISOs. Further research is still needed to explore the differences between active and break monsoons and the influence of the IOD and ENSO on the QBWISO.

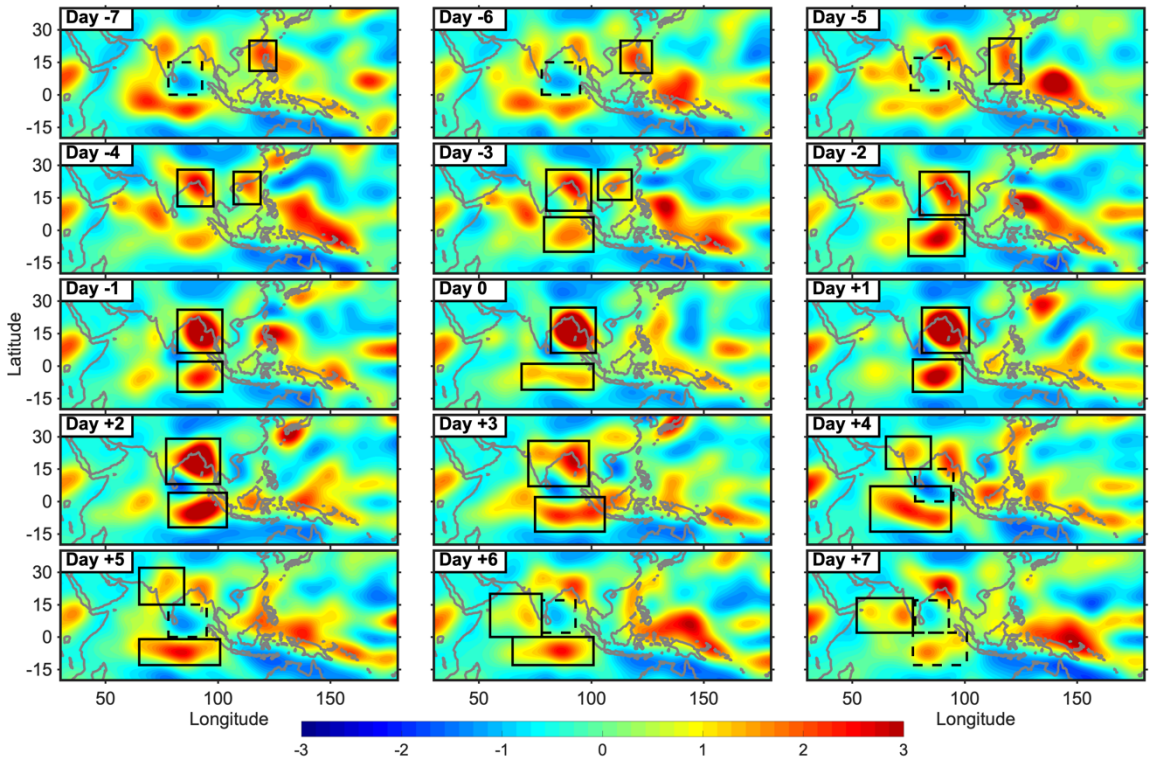

Figure 4.1. 10-20-day composite of GPM precipitation anomalies spatially bandpass filtered between 3000 and 6000 km during May-October, 2016-2018 (shaded; mm day^{-1}), where positive anomalies are in red and negative anomalies are in blue. Solid boxes indicate the life cycle of the westward propagation of the northernmost cell of the double-cell, as well as the double-cell over the Bay of Bengal. Dashed boxes indicate the negative phase of the double-cell over the Bay of Bengal region.

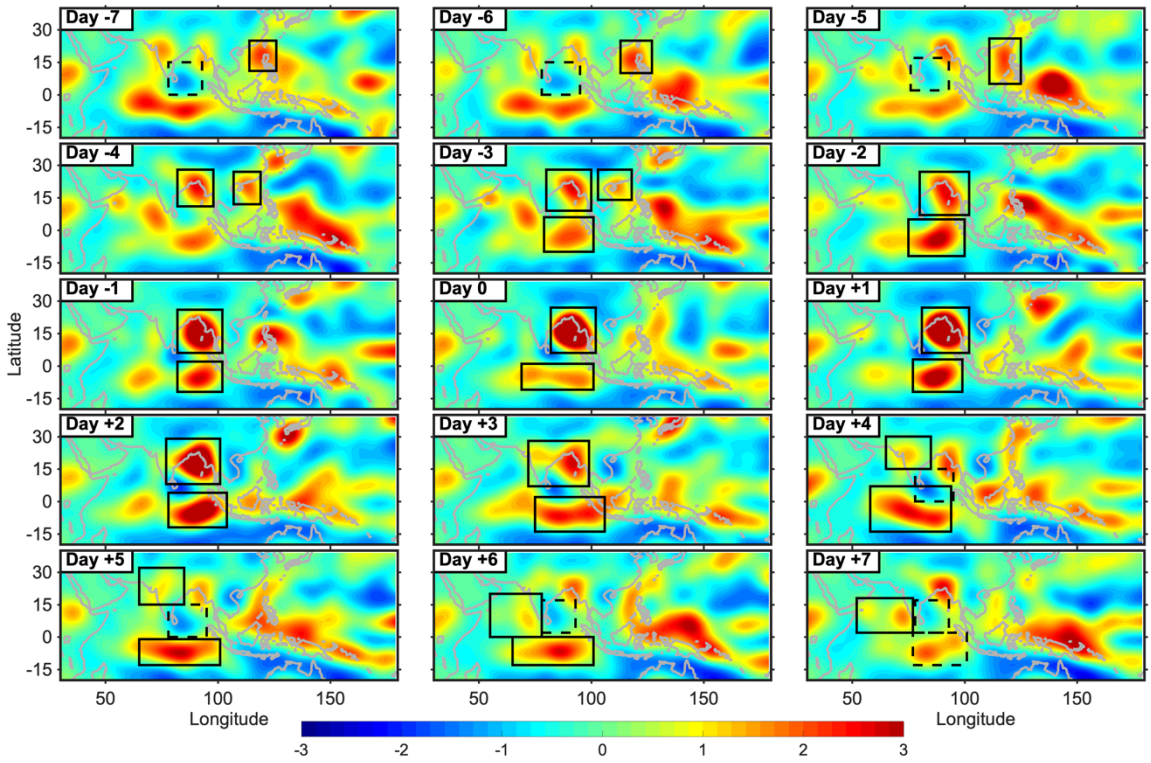

Figure 4.2. QBWISO composite of GPM precipitation minus ECMWF evaporation (P-E; mm day^{-1}) spatially bandpass filtered between 3000 and 6000 km during May-October 2016-2018. Solid boxes indicate the life cycle of the westward propagation of the northernmost cell of the double-cell, as well as the double-cell over the Bay of Bengal. Dashed boxes indicate the negative phase of the double-cell over the Bay of Bengal region.

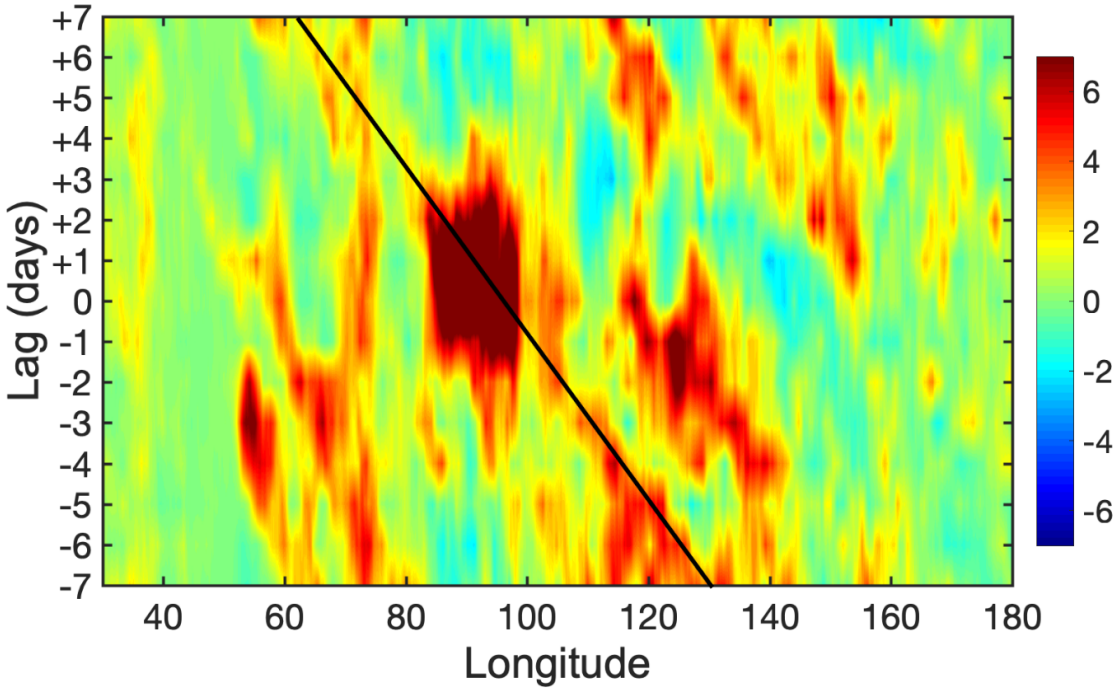

Figure 4.3. Unfiltered, latitudinally averaged (10-20°N) Hovmöller lag composite of GPM precipitation anomalies from May-October 2016-2018 (shaded; mm day^{-1}), where the black line indicates signal propagation.

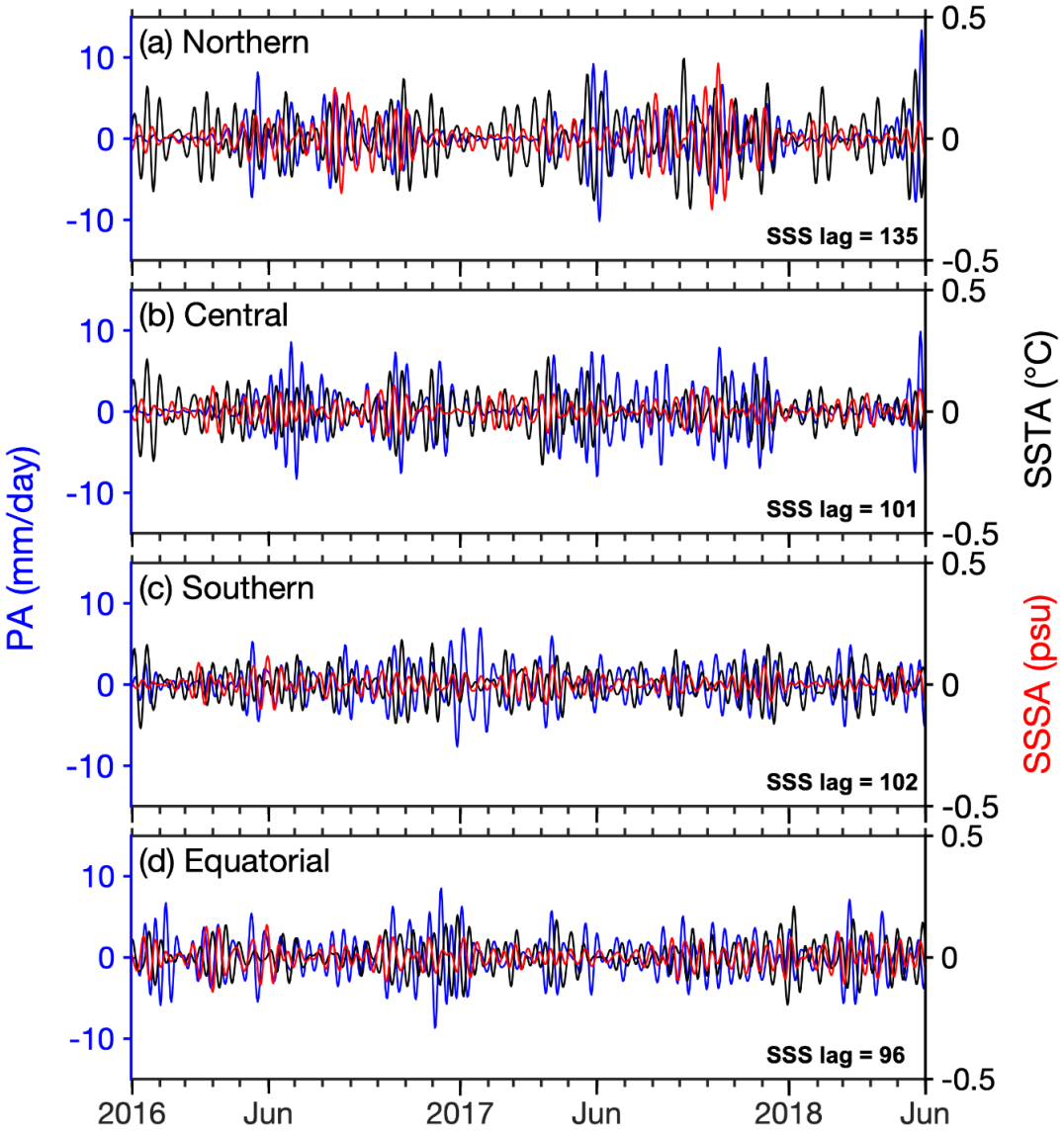

Figure 4.4. 10-20-day filtered regionally box-averaged time series of GPM precipitation anomalies (blue; left axis; mm day^{-1}), AVHRR OISST anomalies (black; right axis; °C), and SMAP SSS anomalies (red; right axis) for the (a) Northern (85-100°E, 15-20°N), (b), Central (85-100°E, 10-15°N), (c) Southern (85-100°E, 5-10°N), and (d) Equatorial (85-100°E, 0-5°N) Bay of Bengal for January 2016-October 2018. All lags are calculated with respect to precipitation using a normalized cross-correlation.

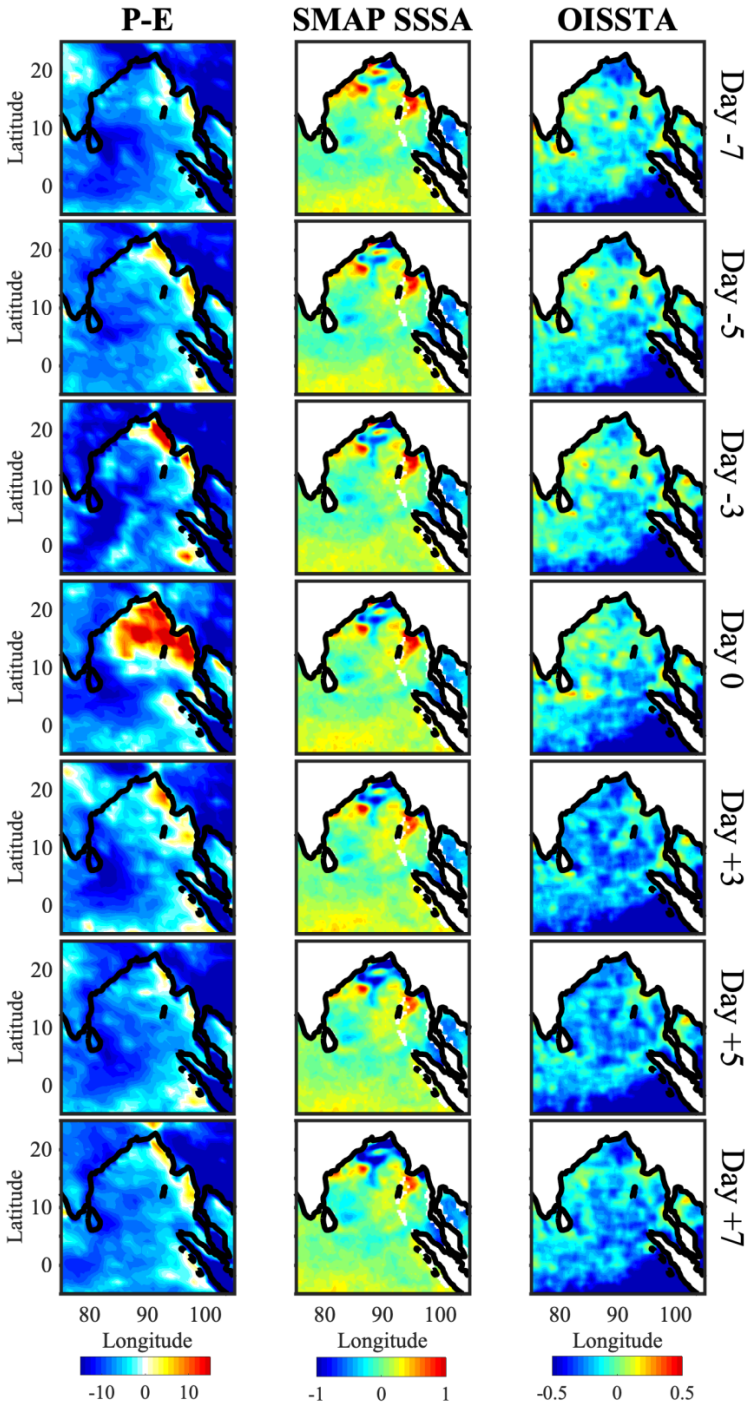

Figure 4.5. Unfiltered QBWISO composites of GPM precipitation minus ECMWF evaporation (P-E; mm day^{-1}), SMAP SSS anomalies (SMAP SSSA), and OISST anomalies (OISSTA; °C) for May-October 2016-2018.

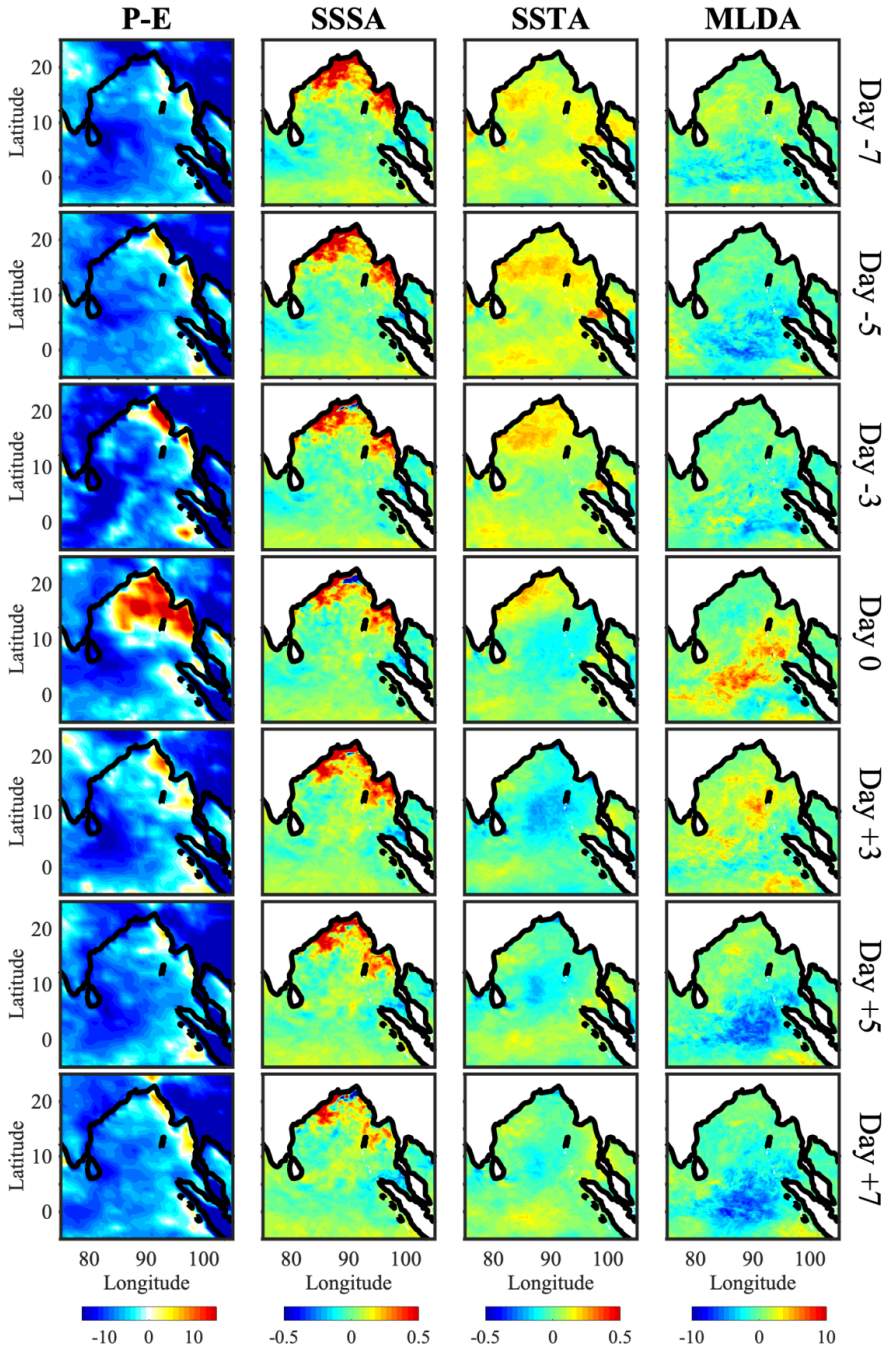

Figure 4.6. Unfiltered QBWISO composites of GPM precipitation minus ECMWF evaporation (P-E; mm day^{-1}), NEMO SSS anomalies (NEMO SSSA), NEMO SST anomalies (NEMO SSTA; °C), and NEMO MLD anomalies (NEMO MLDA; m) for May-October 2016-2018.

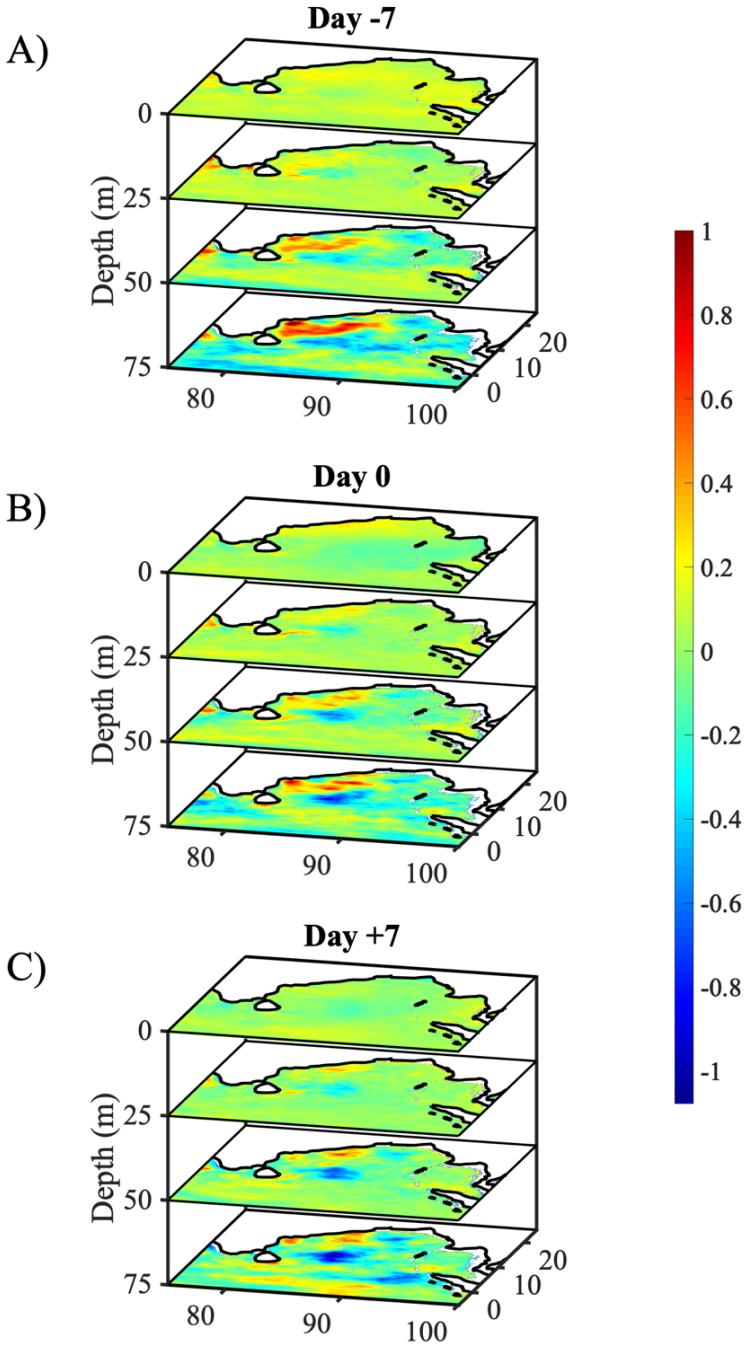

Figure 4.7. Unfiltered NEMO temperature anomaly composites with depth for Day -7 (A; °C), Day 0 (B; °C), and Day +7 (C; °C) of the QBWISO in the Bay of Bengal for May-October of 2016-2018.

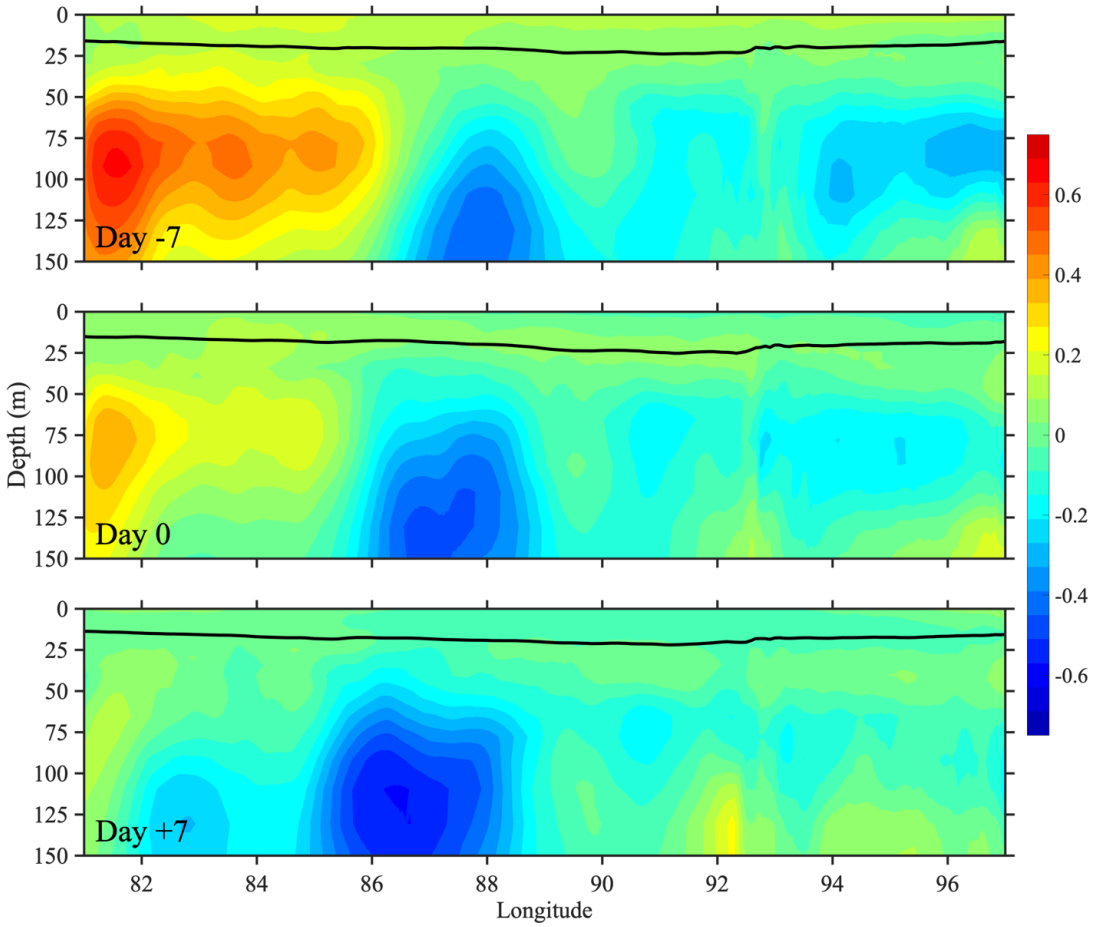

Figure 4.8. Unfiltered composite cross-sections of NEMO temperature anomalies with depth (shaded; °C) with NEMO MLD (black line; m) in the central Bay of Bengal (10-15°N) for Day -7 (top), Day 0 (middle), and Day +7 (bottom) of the QBWISO for May-October 2016-2018.

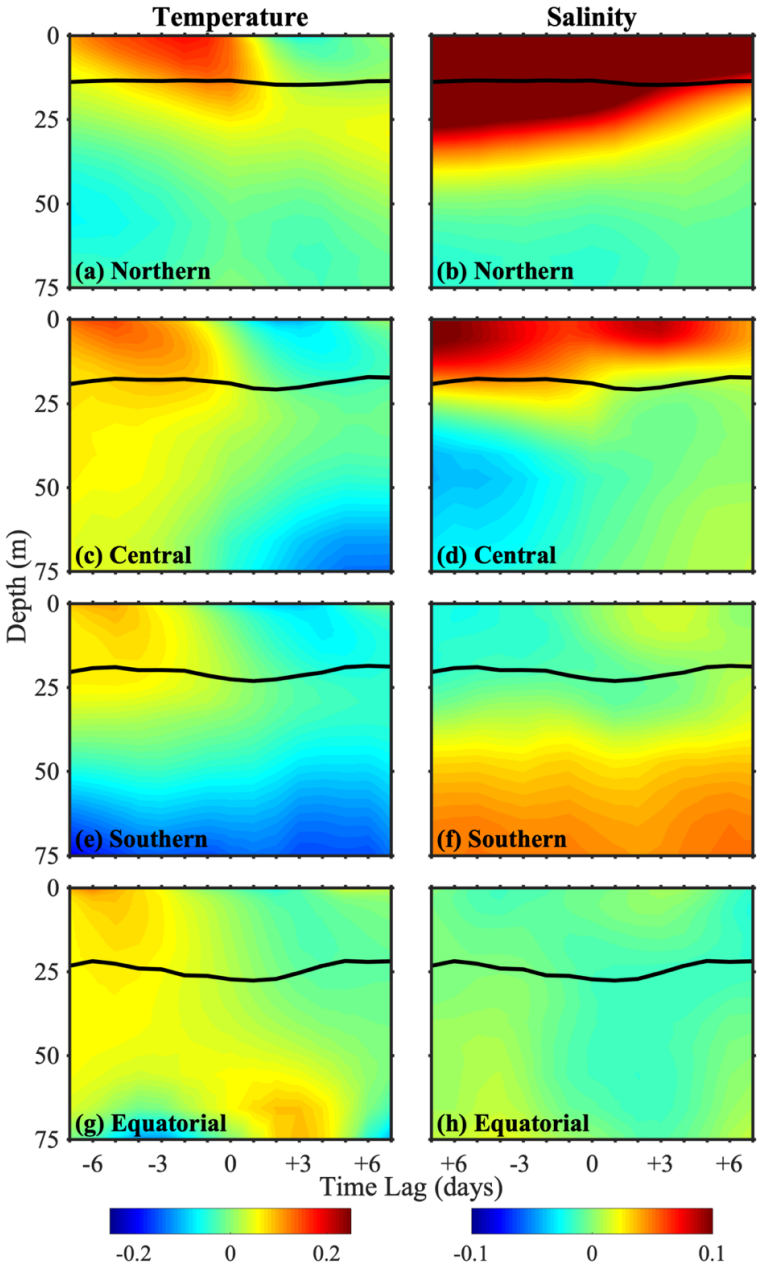

Figure 4.9. Unfiltered QBWISO composite with depth for NEMO temperature (left; shaded; °C) and salinity (right; shaded) anomalies overlaid with NEMO MLD (black line; m), box-averaged in the (a-b) Northern (85-100°E, 15-20°N), (c-d), Central (85-100°E, 10-15°N), (e-f) Southern (85-100°E, 5-10°N), and (g-h) Equatorial (85-100°E, 0-5°N) Bay of Bengal for May-October 2016-2018.

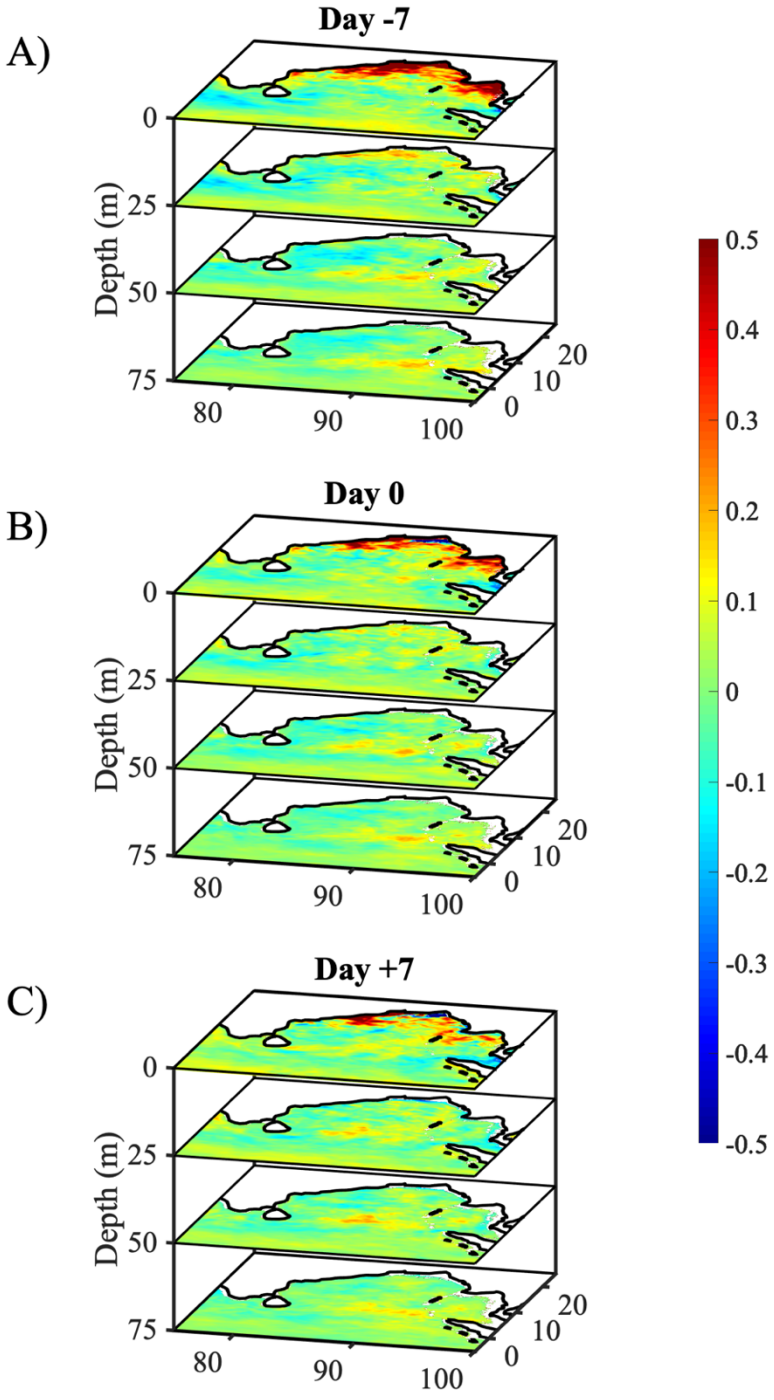

Figure 4.10. As in Figure 4.7, but for NEMO salinity anomalies.

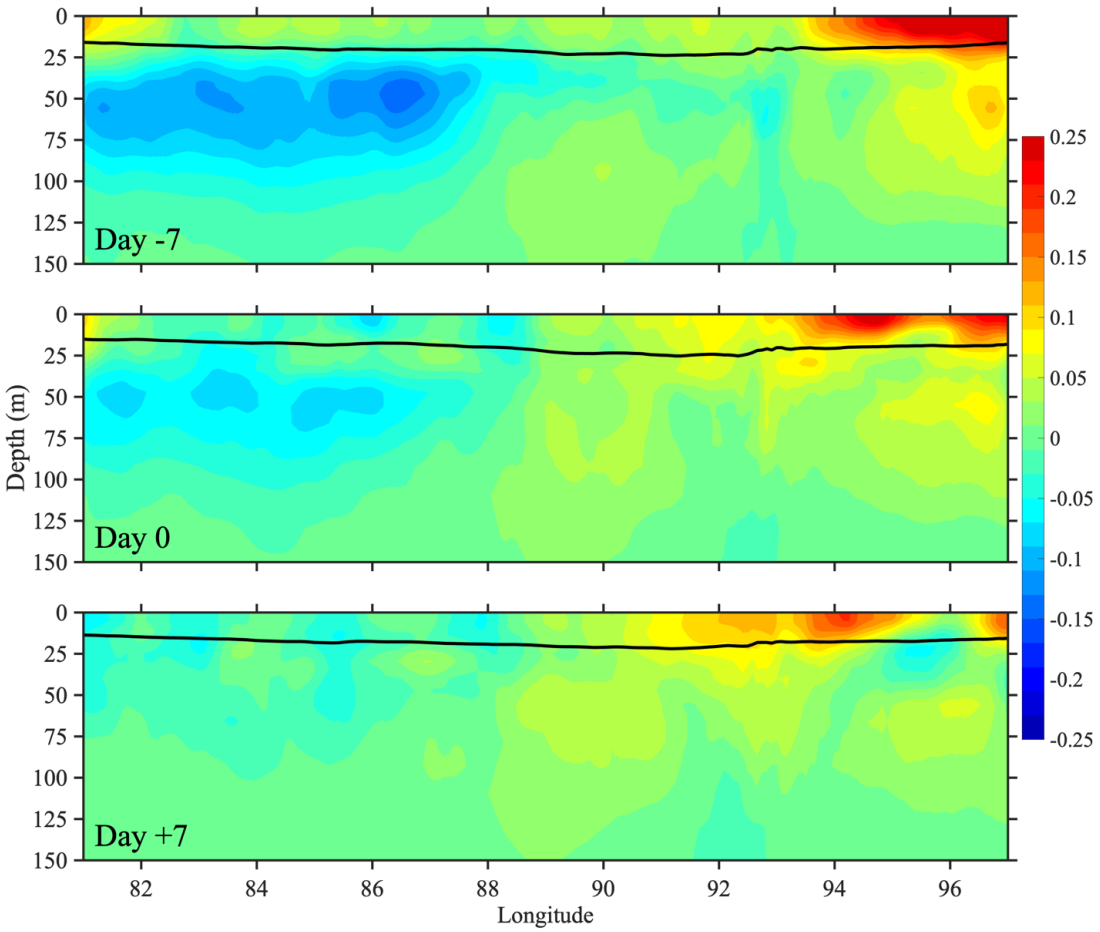

Figure 4.11. As in Figure 4.8, but for NEMO salinity anomalies (shaded).

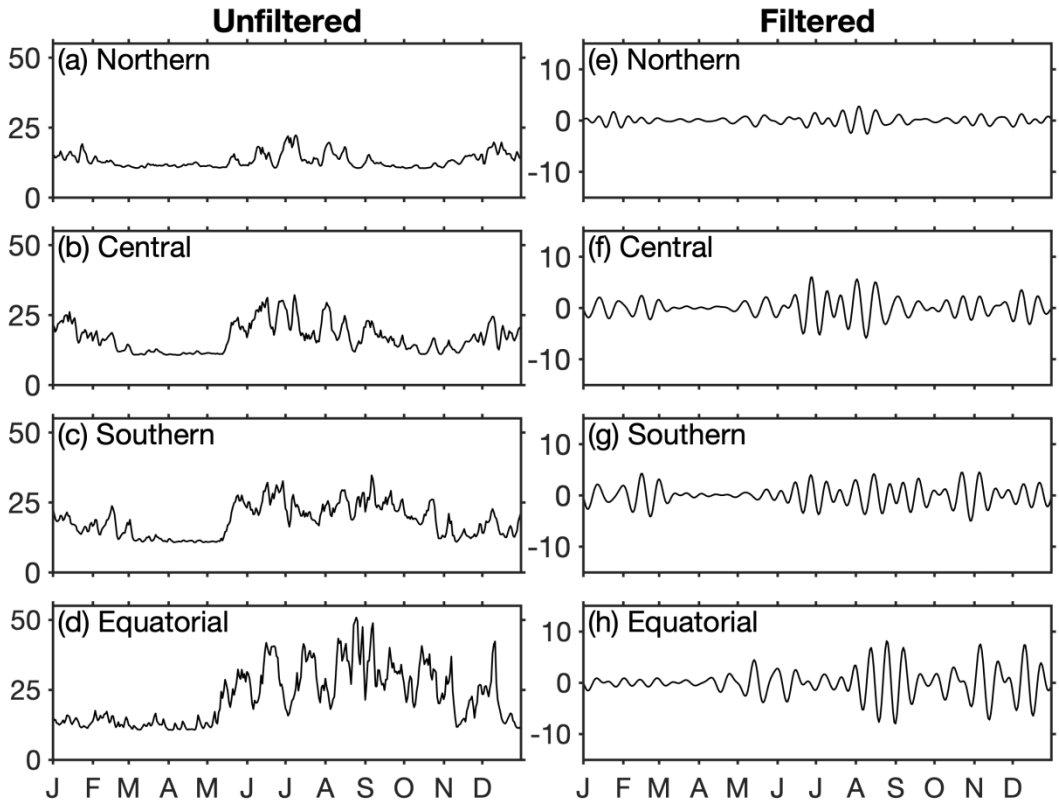

Figure 4.12. Unfiltered (left) and 10-20 day bandpass filtered (right) NEMO MLD (m) for 2016 in the (a, e) Northern (85-100°E, 15-20°N), (b, f), Central (85-100°E, 10-15°N), (c, g) Southern (85-100°E, 5-10°N), and (d, h) Equatorial (85-100°E, 0-5°N) Bay of Bengal.

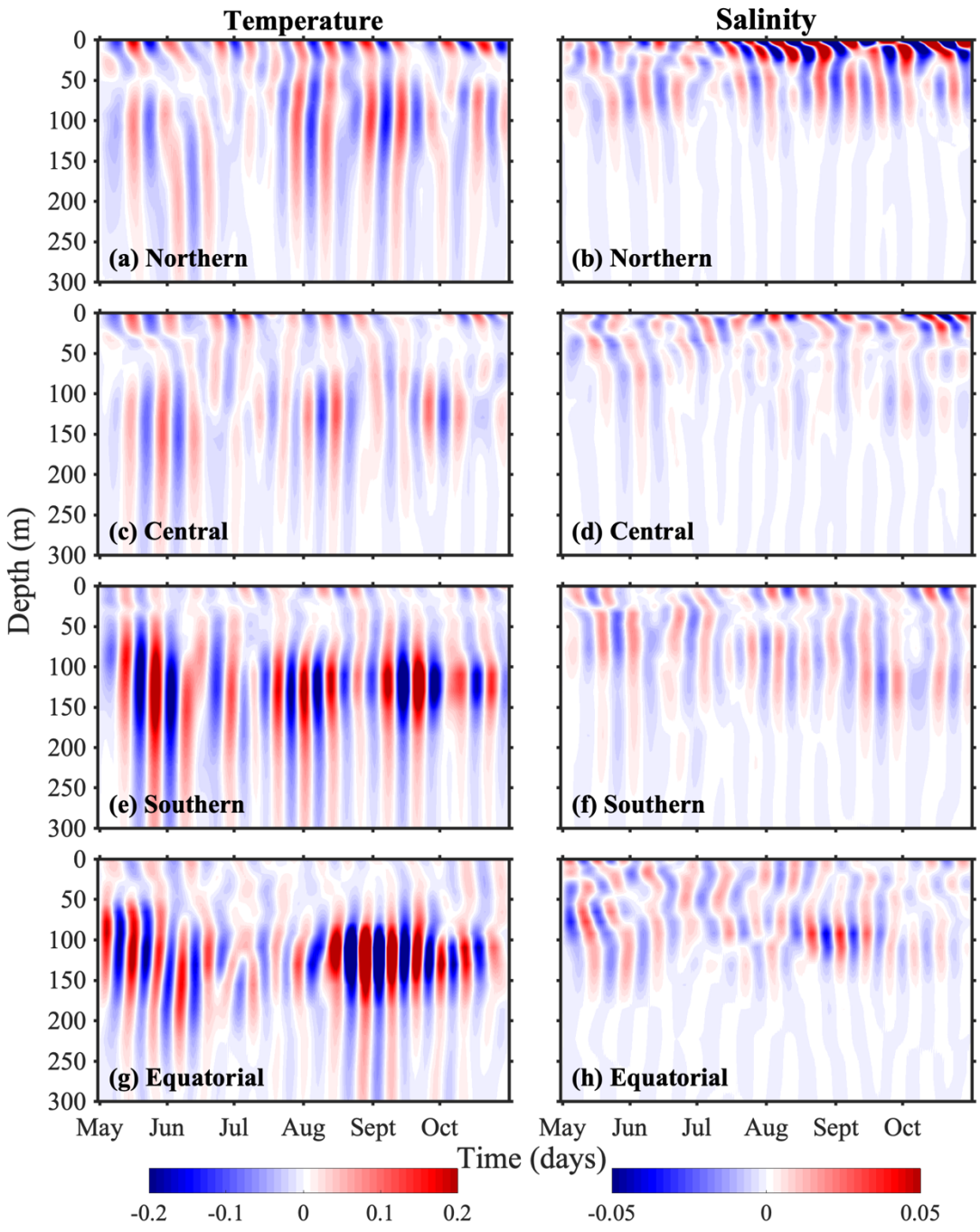

Figure 4.13. 10-20-day bandpass filtered depth-time sections for NEMO temperature (left; °C) and salinity (right; shaded) anomalies, box-averaged in the (a-b) Northern (85-100°E, 15-20°N), (c-d), Central (85-100°E, 10-15°N), (e-f) Southern (85-100°E, 5-10°N), and (g-h) Equatorial (85-100°E, 0-5°N) Bay of Bengal for May-October 2016.

CHAPTER 5

MESOSCALE EDDY VARIABILITY AND ITS LINKAGE TO DEEP CONVECTION OVER THE BAY OF BENGAL USING SATELLITE ALTIMETRIC OBSERVATIONS[4]

---

[4]Roman-Stork, H. L., Subrahmanyam, B., & C. B. Trott (2019). Mesoscale Eddy Variability and its Linkage to Deep Convection over the Bay of Bengal using Satellite Altimetric Observations, Advances in Space Research, https://doi.org/10.1016/j.asr.2019.09.054

ABSTRACT

In the Bay of Bengal (BoB), surface circulation is strongly influenced by the Indian Monsoon and notable local eddying that modulates the East India Coastal Current (EICC). In this study, we apply an eddy tracking algorithm to 25 years (1993-2018) of satellite altimetric observations to identify, analyze, and track mesoscale eddies in the BoB from their generation to dissipation. We compare the characteristics and trajectories of these eddies during the southwest (SW) and northeast (NE) monsoon seasons and during the pre- and post-SW monsoon periods to better understand the seasonality of the local eddy field. We find high eddy generation in the eastern BoB associated with instability induced by coastal Kelvin waves and the westward propagating Rossby waves, but we found the most robust eddies in the western BoB around the EICC. Ocean heat content (OHC) in the BoB was compared with warm-core eddies and we find that warm-core eddies drive changes in OHC. We also compared the eddy field during strong and weak SW monsoon forcing and with varying Indian Ocean Dipole (IOD) and El Niño-Southern Oscillation (ENSO) conditions, finding a statistically significant relationship with warm-core eddies and sea surface temperatures (SSTs; $R^2 = 91\%$) and outgoing longwave radiation (OLR; $R^2 = 88\%$) during periods of strong ENSO and IOD forcing. To understand the impact of these eddies on local atmospheric convection we found the composite surface structure of anticyclonic and cyclonic eddies of warm-core and cold-core SSTs, finding a close relationship between the eddy-composite SSTs and OLR.

5.1 INTRODUCTION

The Indian Monsoon system is one of the most dynamically complex systems in the world with a southwest (SW) monsoon in the boreal summer (June-September) and a northeast (NE) monsoon in the boreal winter (November-February). The monsoon seasons are named for the prevailing direction of the low-level winds over India, which reverse twice annually, similar to a large-scale land-sea breeze, making this one of the most unique systems in the world.

The Bay of Bengal (BoB) in the northeastern Indian Ocean is home to many of the most important air-sea dynamics associated with the Indian Monsoon system. The northern BoB's air-sea processes and mixed layer dynamics are driven primarily by freshwater fluxes from river runoff (Ramachandran et al., 2018). Along the western coast of the BoB, the East India Coastal Current (EICC), the western boundary current in the BoB, carries fresher waters from the BoB during the NE monsoon and seasonally reverses to transport more saline waters from the Arabian Sea into the BoB during the SW monsoon season (Schott and McCreary, 2001). Additionally, intraseasonal, interannual, and interdecadal oscillations act on the BoB, altering mixed-layer dynamics and convection in the region (Schott and McCreary, 2001).

Given the complexity and importance of the BoB in monsoon variability, there have been a number of studies investigating the current and eddy dynamics in the region (Chen et al., 2012; Cheng et al., 2018; Cui et al., 2016; Dandapat and Chakraborty, 2016; Gulakaram et al., 2018; Hacker et al., 1998; Patnaik et al., 2014; Sreenivas et al., 2012). While most studies have focused on the biological implications of eddies in the region, an

increasing number of studies in recent years have begun to focus on the role mesoscale eddies play in air-sea processes, storm intensification, and convection (Chen et al., 2012; Cheng et al., 2013; Cui et al., 2016; Dandapat and Chakraborty, 2016; Gopalan et al., 2000; Gulakaram et al., 2018; Patnaik et al., 2014; Sreenivas et al., 2012; Trott et al., 2018).

Patnaik et al. (2014) examined eddies in the EICC region during the two transition seasons between monsoons (April to May and then October to November) and their relation to tropical cyclone intensification in the region. This study used enthalpy fluxes to quantitatively examine the role of eddies in tropical cyclone intensification, finding that warm-core eddies were able to significantly (260%) increase the intensity of a tropical storm in October of 1999 in the BoB. Such research suggests that eddies in the BoB, and indeed the type of eddies in the BoB, can play a critical role in the strength and intensification of convective to synoptic scale disturbances and storms in the region. Dandapat and Chakraborty (2016) investigated the three-dimensional properties of mesoscale eddies in the western BoB using satellite altimetry. This study analyzed the spatial distribution of both anticyclonic (AE) and cyclonic (CE) eddies in the western BoB, finding that AEs dominate the central western BoB while CEs dominate the northwestern BoB. It was also found that AEs tended to be larger in size, but shorter lived than CEs, and that CEs were more likely to be generated during the SW monsoon season due to wind (Dandapat and Chakraborty, 2016). This study also noted the strong importance of wind stress in eddy generation, suggesting once more that intraseasonal and interannual variability should play a significant role in eddy variability.

Cheng et al. (2018) explored the depth, structure, dynamics, and generation of eddies in the central BoB using a combination of satellite observations, moored buoys, and

model simulations. Their research suggested that eddies have the highest amplitude in the thermocline, which in turn suggested that vertical motion of the thermocline is associated with eddy variability and generation. Their analysis using a 1½ layer model again confirmed the critical importance of wind stress and equatorial wind forcing in eddy formation, noting the geographic importance of the Myanmar bump and Andaman Island in the location of eddy generation (Cheng et al., 2018).

There have been a number of studies that focused on the connection between mesoscale eddies and deep ocean convection in various basins (Chanut et al., 2008; Cuxart et al., 2000; Legg et al., 2002), but few have addressed a connection to atmospheric convection. A recent study by Gulakaram et al. (2018) examined the connection between eddies and atmospheric convection in the BoB during the 2009 and 2013 SW monsoon seasons. They found that the CEs in the BoB were strongly influenced by the strength of the downwelling equatorial and coastal Kelvin waves that propagate in the BoB, with stronger Kelvin waves producing stronger eddies (Gulakaram et al., 2018). This same study also compared eddies with atmospheric convection, using a composite comparison and time series analysis to find a 4-day lag between outgoing longwave radiation (OLR) and AEs.

Several other studies have looked into the role of upwelling and downwelling Kelvin waves in the BoB on various time scales (Nienhaus et al., 2012; Sreenivas et al., 2012). It was found that the timing of these Kelvin waves were strongly related to the phase of the El Niño-Southern Oscillation (ENSO) and Indian Ocean Dipole (IOD), which in turn influenced sea level anomalies (SLA) in the BoB (Sreenivas et al., 2012). The results of Gulakaram et al. (2018) and of this study further prove that the phases of these oscillations

play a role in eddy variability and may also contribute to eddy-associated convection in the BoB.

Given the incredibly complex nature of eddy dynamics in the BoB, research is required into the spatiotemporal distribution of eddies and their connection to convection and interannual variability within the BoB. The goal of this paper is to investigate the role of planetary waves and interannual variability on mesoscale eddies and convection in the BoB. We will develop a comprehensive climatology of eddy variability within the BoB, as well as present an analysis of the processes involved in the creation of the observed eddy fields, including ENSO and the IOD. Finally, we will explore the connection between the observed mesoscale eddies with localized atmospheric convection and precipitation, finding that eddy-related convection can be strongly related to the ENSO and IOD phase the year prior. This research is conducted using 25 years of blended daily altimetric observations in the BoB and an eddy tracking methodology that emphasizes the necessity for high spatial resolution altimetric observations, such as from the upcoming Surface Water Ocean Topography (SWOT) mission, for monsoon studies and predictability. This paper is organized as follows: Section 5.2 presents the data and methodology used, Section 5.3 discusses the results and findings of this research, and Section 5.4 presents the major conclusions of this study.

5.2 DATA & METHODS

A. SATELLITE OBSERVATIONS

Sea level anomalies (SLA) were obtained from the Copernicus Marine and Environment Monitoring Service (CMEMS; marine.copernicus.eu) with a global grid

spacing of 0.25° at daily intervals from 1993 through 2018. This dataset is derived from a combination of TOPEX/POSEIDON, HY2, Jason-1, Jason-2, Jason-3, ENVISAT, Saral/AltiKa, ERS 1/2, and GFO satellite missions and is referenced to a 20-year mean from 1993-2012 (LeTraon et al., 1998; Ducet et al., 2000).

Sea surface temperatures (SSTs) are from the Optimum Interpolation Sea Surface Temperature (OISST) V2 dataset developed by the National Oceanic and Atmospheric Administration (NOAA) and the National Climatic Data Center (NCDC) using the Advanced Very High-Resolution Radiometer (AVHRR; Reynolds et al., 2007). This daily product is also at a global grid spacing of 0.25°.

Outgoing longwave radiation (OLR) from 1993-2017 are from the interpolated daily product provided by NOAA (available at https://www.esrl.noaa.gov/psd/data/gridded/data.interp_OLR.html) and for 2018 use measurements from NOAA-15 (which are integrated into the NOAA interpolated product and has full global coverage twice daily) to get the most accurate remotely sensed OLR at a global grid spacing of 2.5°.

NOAA's depth-integrated heat content products can be found at https://www.nodc.noaa.gov/OC5/3M_HEAT_CONTENT/ with a 1° horizontal resolution. We used the seasonal (3 month) product integrated over 0-700 m depth from 1993 to 2018. These estimates are primarily based off of Argo temperature measurements and is fully described in Levitus et al. (2012).

The atmospheric climate reanalysis datasets used in this study are maintained by the European Centre for Medium-Range Weather Forecasting (ECMWF). We have used

the global daily precipitation products, which span the years 1979-present at a horizontal resolution of 1°.

B. EDDY TRACKING METHODOLOGY

To identify and track the eddies, an eddy tracking algorithm was applied to daily SLA fields derived from satellite altimetry. Well described in Pegliasco et al. (2015), this approach finds each local maximum (for AEs) and minimum (for CEs), then extends to the largest closed contour to define the eddy edge (Chaigneau et al., 2009, 2008). To be a valid eddy, each closed contour must contain at least four connected grid points, which is a minimum radius of about 20 km (Trott et al., 2018). This method is advantageous over other commonly used methods (Chaigneau et al., 2008; Yi et al., 2014; Souza et al., 2011) as it is threshold-free and identifies a smaller number of false eddies (Trott et al., 2018). It also provides a more accurate eddy shape (Trott et al., 2018).

Next, eddy trajectories were constructed using a cost function (CF):

$$CF_{e_1,e_2} = \sqrt{\left(\frac{\Delta R - \overline{\Delta R}}{\sigma_{\Delta R}}\right)^2 + \left(\frac{\Delta A - \overline{\Delta A}}{\sigma_{\Delta A}}\right)^2 + \left(\frac{\Delta EKE - \overline{\Delta EKE}}{\sigma_{\Delta EKE}}\right)^2} \quad (5.1)$$

where ΔR, ΔA, and ΔEKE are the differences in radius (R), amplitude (A), and eddy kinetic energy (EKE), respectively, between intersecting eddies (Pegliasco, 2015). The average values ($\overline{\Delta R}$, $\overline{\Delta A}$, and $\overline{\Delta EKE}$) and standard deviations ($\sigma_{\Delta R}, \sigma_{\Delta A}$, and $\sigma_{\Delta EKE}$) were determined from thousands of identified eddy parts. Warm (cold) core eddies were defined when average SSTs within one eddy radius were warmer (cooler) than the average SSTs of waters between one and three radii from the eddy center, signifying the temperature of the waters surrounding each eddy.

In this study, the blended daily SLA product is used in its original daily format so as to identify, track, and analyze eddies on all time scales, including the transient eddies within the BoB. The influence of the monsoon system and prevalence of synoptic-scale weather systems, such as tropical cyclones, in the northern Indian Ocean lends itself to the creation of many transient eddies, for which a daily product is necessary (Trott et al., 2018, 2019). The daily interpolated SLA product is generated from the combined altimetry constellation, and thus inherently contains a fair amount of noise which can lend itself to the identification of false eddies. While this can contribute to uncertainty in our methodology, the number of real eddies identified vastly outweighs the false positives. While we acknowledge this uncertainty, as we intend to discuss the connection between eddy variability and convection, a daily product is necessary as convection in the BoB changes rapidly and a 3-day or 7-day product would not adequately capture the desired convection and precipitation.

C. Wavelet Analysis

To statistically analyze the relationship between eddy variability and large-scale climatic oscillations, wave coherence analysis was performed following the methodology of Grinsted et al., (2004). Wavelets are often used to analyze time series in time-frequency space and to identify dominant periods of oscillation within a signal. The most useful approach for our purposes is the wave coherence plot. Wave coherence is analogous to taking a correlation coefficient (R^2) for two time series in time-frequency as applied to a Morlet wavelet, and has the same scale of 0 to 1, with the value expressed describing the amount of variance explained. This manner of wave coherence plot also contains phase arrows, which can describe whether the two time series are in phase (pointing right), out

of phase (pointing left), and whether the first time series leads (down) or lags (up). A cone of influence is included to indicate where edge effects disallow for statistical significance.

5.3 RESULTS

Though eddies are transient features, they often generate in the BoB in response to several forcing mechanisms on seasonal time scales, such as monsoonal wind reversals and the development and propagation of coastal Kelvin waves, both of which influence the seasonal climatology of SLA and surface currents (Figure 5.1). The EICC experiences seasonal intensification as a response to both remote and local forcings. While one would expect the currents to respond exclusively to changes in monsoonal wind forcing, there are four sources of current and eddy generation in this region: along-shore winds, Ekman pumping in the central BoB, forcing from the eastern and northern BoB (typically attributed to coastal Kelvin waves), and remote forcing from the equatorial Indian Ocean (McCreary et al., 1996; Shankar et al., 1996; Sherin et al., 2018).

Climatologically, the EICC flows equatorward with a peak transport of 3 Sv during the NE monsoon (Figure 5.1a) and poleward during the SW monsoon season with a peak transport of 5 Sv (Figure 1b; Sherin et al., 2018). Climatological SLA reveals some large eddies in the western BoB that for much of the year cause the EICC to hug the east coast of India, but during the SW monsoon (Figure 5.1b), cause it to meander offshore, which is extremely important for the exchange of water masses between the Arabian Sea and the BoB (Durand et al., 2007; Jensen, 2001; Shankar et al., 2002; Shetye et al., 1996). In March, the EICC reaches its highest flow of approximately 7 Sv (Figure 1c; Sherin et al., 2018). There is a clear zonal pattern between the Kelvin waves in the eastern BoB and the

EICC the western BoB. The northward propagating EICC persists during April-May shows signs of weakening in May, deteriorates further during June-July, and disappears by August. The collapse of the winds at the end of the SW monsoon that accounts for the southward EICC in the fall and winter along the southern coast (McCreary et al., 1993). Ekman pumping over the Bay, local alongshore winds, and remote forcing from the equator all contribute to the circulation of the BoB.

A. Eddy Characteristics

The combined altimetric observations from 1993-2018 provide an unprecedented insight into the dynamic characteristics of mesoscale eddies in the BoB. The eddy tracking methodology described in Section 5.2.B was able to identify the abundance, size, amplitude, EKE, and region of eddy generation of all mesoscale eddies in this region over this time period, allowing for a multidecadal analysis of eddy characteristics in the BoB (Figure 5.2). Though there are previous studies on eddy tracking in this region, this is the first study to employ this particular methodology. Overall, we find that there are more AEs than CEs, but AEs tend to possess larger radii and lower amplitudes; however, CEs have much higher EKEs, particularly those along the EICC and those off the coast of Sri Lanka. Similar studies looking at mesoscale eddies in the BoB agree with the results of Figure 5.2 that the most robust eddies in the BoB are found in the western bay, which is extremely significant for fluctuations in the EICC and determining the pathways of water mass exchange between the two basins of the northern Indian Ocean (Cui et al., 2016; Dandapat and Chakraborty, 2016). In this region, eddies possess markedly higher radii (Figure 2 c-d), amplitudes (Figure 5.2e-f), and EKEs (Figure 5.2g-h). In the western bay, baroclinic instability of the EICC can help generate eddies (Cheng et al., 2018) and there is notable

eddying that develops within meanders of the mean flow (Chen et al., 2012; Cheng et al., 2013). In this region, turbulent eddying processes result in 30-50% of sea level variability (Sérazin et al., 2015). Circulation in the western BoB is highly geostrophic, with a local Rossby number of 0.006 (Dandapat and Chakraborty, 2016). The maximum number of eddies (as well as the highest number of eddy generations) are in the eastern bay, indicating that the coastal Kelvin and Rossby waves are an eddy generation mechanism for small-scale eddies (Cheng et al., 2018).

During the SW monsoon, the Arabian Sea, the BoB's western counterpart, experiences seasonally strong eddying due to increased local wind forcing. Conversely, the BoB is known for strong surface stratification during this time due to high precipitation and weaker low-level winds (Shetye et al., 1996). Positive wind stress curl from June through September over the BoB favors the generation of CEs as it triggers local surface divergence and upwelling (Dandapat and Chakraborty, 2016). While there is also a decrease in AE amplitudes, there is an increase in CE amplitudes which drives increased local EKEs due to the stronger local geostrophic currents. It is possible that this increase in cyclonic eddy amplitudes is due to upwelled waters along the eastern coast of India being trapped by downwelling coastal Kelvin waves which arrive in this region concurrently with the SW monsoon.

The cyclonic eddy seen east of Sri Lanka in Figure 5.1 is clearly identifiable in Figure 5.3 d, f, h. Due to its positioning and potential to redirect the pathway of the EICC, the climatological presence of this eddy is an important finding of this research. This eddy has been previously noted a semi-permanent feature of the Sri Lanka Dome region in the BoB that develops during the SW monsoon season due to cyclonic wind stress (Burns et

al., 2017). That we can track this feature using our methodology is an important finding, as the Sri Lanka Dome can contribute to EICC movement and local cyclogenesis (Burns et al., 2017). Eddy generation for AEs is extremely high along the eastern and northern coasts of the Bay and is constrained much closer to the coastline than in the full-year characteristics (Figure 5.2). The characteristics of eddies in the BoB during the SW monsoon show basin-wide eddy radii are smaller than the annual eddy radii (Figure 5.3).

Compared to the SW monsoon, the BoB is generally less energetic in the NE monsoon, as seen in the eddy characteristics in Figure 5.4. Eddies of both circulation types are seasonally weaker throughout the basin, owing to a combination of weaker winds and a change in current direction. As with the SW monsoon season, CEs have higher EKE than AEs; however, AEs are more abundant, have larger radiuses overall, and higher amplitudes. This is due to the negative wind stress curl seen during this time over the western BoB (Dandapat and Chakraborty, 2016). We find that the 18°N separation of anticyclonic eddies identified by Gangopadhyay et al. (2013) seen in the annual eddy characteristics (Figure 5.2) is most prominent during the NE monsoon season (Figure 5.4). CE generation is tightly constrained to the eastern Bay, with locally high eddy generation about 93°E and 13°N.

Compared to the monsoon periods the pre-SW monsoon period (March to May) is markedly different (Figure 5.5). The most striking characteristics of this time are the lack of large-radius CEs and the extremely high EKE in the western BoB. The EICC is seasonally high during the pre-SW monsoon time, as is the eddy field in the western BoB. The favorability of the western BoB to high-energy CE development is due to high sensitivity to the positive wind stress curl (Dandapat and Chakraborty, 2016). The EICC

flows along the western boundary of AEs that develop in the western BoB, hence the locally strong amplitudes, radii, and EKEs, reflected in the SLA and geostrophic current climatology of Figure 5.1. This intermonsoon period contrasts the pre-NE monsoon period in October (figure not shown), which is a very weak intermonsoon period, meaning it has a weak EICC and corresponding weak eddy field. The high EKE associated with pre-SW monsoon CEs is due to a combination of the arrival of the first upwelling Kelvin wave in the region and the strong EICC at this time (Nienhaus et al., 2012). Additionally, Nuncio and Kumar (2012) found that strong cyclonic circulation during this time period is due to the instability of cross-shore density gradients in the EICC in early February.

B. EDDY TRAJECTORIES

In addition to eddy characteristics, eddy trajectories were found for the eddy field in the BoB. To observe the behavior of multiple eddy size classes, these trajectories were divided by small (10-20 cm), medium (20-30 cm) and large (30-40 cm) amplitudes. Amplitudes greater than 40 cm were omitted as there were only sparse measurements (less than five over the entire period of 1993 to 2018). Trajectories were followed from generation to dissipation.

For the full year climatology, eddies with amplitudes between 10 and 20 cm were abundant throughout the full basin (Figure 5.6). There were more AEs of this amplitude, but the number of CEs was greater than that of AEs for the 20-30 cm and 30-40 cm amplitude ranges. AEs overall have a tendency to be larger than the CEs, as shown in the box plots in Figure 5.6. While the lower amplitude eddies have only a slight difference in size range, the higher amplitude CEs (30-40 cm) have a more refined range of sizes

between 100 and 150 km, compared to the AEs of the same amplitude that have a range of radiuses between 50 and 175 km. This occurs in all seasons (Figure 5.7; Figure 5.8; Figure 5.9). These results are similar to those of Dandapat and Chakraborty (2016), who also found AEs to have larger radiuses, especially during the SW monsoon season due to wind stress.

This same study also found AEs to have a shorter lifespan, as does ours, with there being more CEs that last 100+ days than AEs. Overall, however, the mean lifetime is very similar, with CEs lasting ~17 days and AEs lasting ~16 days. We find that eddies tend to have a radius range of 100-500 km and a range of lifespans from 2-250 days. It is important that we are able to track these short-lived eddies with lifespans less than 7 days, as synoptic-scale weather events and localized convection can be influenced by the eddy field and contribute to monsoon precipitation. This finding is critically important as it emphasizes the role high temporal resolution altimetric observations can play in monsoon forecasting and predictability.

The trajectories of many larger-amplitude eddies were initiated in the eastern BoB and propagated westward, seeming to follow along coastlines, with a particularly high concentration of CE trajectories in the EICC region. The upwelling mechanism in the eastern BoB is due to local Kelvin waves, to be discussed in detail in Section 5.3.D. The reasons for this propagation are generally attributed to advection, the beta effect, topography, or a combination of these factors (Chen et al., 2012). Additionally, the propagation speed is expected to be proportional to the vertical stratification (Chen et al., 2012). This frequently results in increased propagation speeds closer to the equatorial BoB

(Chen et al., 2012). Few eddies are generated in the southern BoB due to the low Coriolis force that is unable to maintain a robust dynamic balance (Chen et al., 2012).

Though the full year trajectories show little difference in abundance between eddy types, the imbalance between a higher number of AEs at lower amplitudes and a higher number of cyclonic eddies at higher amplitudes is stronger in the SW monsoon season, as well as the discrepancy between radius size in higher amplitude eddies (Figure 5.7). During the SW monsoon, there are more than double the number of cyclonic eddies at 20-30 cm amplitude and approximately double the CEs with amplitudes between 30-40 cm, although they are smaller than the AEs (Figure 5.7k; Figure 5.7l). The most robust eddies generate in the northeastern BoB and propagate westward along the EICC and coastal region, with several reaching their demise all the way down to the coast of Sri Lanka. This consistency in eddy propagation direction results in a probability of eddy presence in the western BoB on the order of 50-75% (Chen et al., 2012). The SW monsoon season also sees the highest amplitude CEs during the year, which follow this same general path.

As in the SW monsoon season, much of the eddy generation during the NE monsoon season is in the eastern BoB with westward propagation (Figure 5.8); however, there is a noticeable difference in the propagation direction of the 20-30 cm amplitude eddies, where there is some eddy generation at about 6-8°N and then some northwestward propagation, consistent with the observations of Chen et al. (2012), who found that these eddies travel at velocities ranging from 2.0-11.0 cm/s. These eddies propagate at speeds significantly slower than local Rossby waves due to their nonlinear behavior (Chelton et al., 1998; Gill, 1982). The greatest difference between monsoon trajectories, however, is

in the number of AEs versus CEs. During the NE monsoon season there are nearly double the number of 20-30 cm and 30-40 cm AEs, largely due to wind and EICC direction.

In the pre-SW monsoon time, there is a higher number of AEs with amplitudes of 10-20 cm and a higher number of cyclonic eddies with amplitudes of 20-30 cm (Figure 5.9). Only the mid-size cyclonic eddies show some northwestward propagation from the equatorial regions. Most CEs generate in the northeastern BoB and propagate westward while there was some AE generation along the west coast of the BoB (Figure 5.9c). Eddy trajectories during October revealed a disproportionately high number of low-amplitude eddies when compared with the other seasons (figure not shown). This was the only time period with no cyclonic eddies with amplitudes in the 30-40 cm range (and only 4 AEs of this size). The low-amplitude AEs are primarily generated about 10°N and propagate westward, whereas the low-amplitude CEs are more spread out.

These trajectory finds are largely consistent with recent studies by Dandapat and Chakraborty (2016) and Cheng et al. (2018) in the western and central BoB respectively. Our calculated eddy trajectories shared the same generation locations and spatial densities but tended to propagate farther than in the previous studies. This may be due to the different bounds used for calculations and for the different eddy tracking methodologies.

C. Coastal Kelvin waves and Rossby waves

In the BoB, equatorial Kelvin waves separate into coastal Kelvin waves upon reaching approximately one Rossby radius of deformation from the eastern boundary of the equatorial Indian Ocean (Rao et al., 2010). There are four coastal Kelvin waves per year—two upwelling and two downwelling. The first upwelling coastal Kelvin wave shows

the highest amplitudes in the northern Bay and occurs throughout the NE monsoon and the pre-SW monsoon months. These upwelling coastal Kelvin waves are characterized by negative SLA anomalies and arrive in late January in the BoB where they take roughly 120 days to propagate around the basin (Nienhaus et al., 2012; Rao et al., 2010). These coastal Kelvin waves also in turn generate Rossby waves, which can trigger eddy generation (Nienhaus et al., 2012). Given the timing of these Kelvin waves between January and April, their presence is undoubtedly responsible for much of the eddy variability and generation seen during the NE monsoon period and the pre-SW monsoon period.

The first downwelling coastal Kelvin waves are characterized by positive SLA and arrive in the BoB in late April to early May. They are strongest during May, which allows them to significantly contribute to eddy formation during the pre-SW monsoon period and the SW monsoon period. The strong EKE associated with the pre-SW monsoon CEs, and the strength of the eddy field in May, are due to the second downwelling coastal Kelvin wave, which arrives in the eastern BoB in October-December (Figure 5.10).

While the downwelling branch of the coastal Kelvin waves in the BoB also extend throughout the full eastern boundary of the Bay, their equatorial amplitudes are much larger than their upwelling counterparts, or even when compared to the first downwelling Kelvin wave, with a depth of 150 m. It has been shown by previous studies (Chen et al., 2012; Rao et al., 2010; Sreenivas et al., 2012) that this Kelvin wave is generally the strongest of the coastal Kelvin waves to propagate through the BoB and is the only coastal Kelvin wave strong enough to reach the southeastern Arabian Sea. This Kelvin wave arrives in the BoB in early October during the pre-NE monsoon transition period when wind stress perturbations in the equator are much wider, which contributes to the strength of the Kelvin

wave response. As the EICC is also flowing southward during this time, it is in the correct orientation to work constructively with the Kelvin wave to facilitate EICC flow propagation (Rao et al., 2010). It is due to these factors that the second downwelling Kelvin wave results in the strongest Rossby wave response and is thought to be one of the primary generation mechanisms for eddy activity in the western BoB in the pre-SW monsoon season (Chen et al., 2012; Rao et al., 2010; Sreenivas et al., 2012).

A time-longitude plot of SLA in the BoB at 15°N shows the westward propagation of these Rossby waves as they are generated in the eastern BoB and radiate out from the coast (Figure 5.11) with a speed of 0.054 m/s. These waves are characterized by increased SLAs from June to January in the eastern BoB and decreased SLAs from late December or January to April as they radiate from the eastern BoB (indicated by a black line in Figure 5.11). The waves can then propagate westward across the BoB in response to the arrival of the second downwelling Kelvin wave and generate high amplitude eddies in the western BoB along the EICC region, which we have shown to have the highest EKE in the BoB.

Through a comparison of El Niño, La Niña, positive IOD, and negative IOD years, we can see a difference in the Rossby wave response to the second downwelling Kelvin wave in the BoB when these oscillatory phases work constructively or destructively (Figure 5.11). The weakest downwelling Rossby wave response occurs during concurrent El Niño and positive IOD years (Figure 5.11a). When this occurs, the equatorial wind stress is anomalously eastward (Rao et al., 2010), which weakens the downwelling Kelvin wave and instead strengthens the upwelling Kelvin waves, creating an upwelling Rossby wave response in the BoB (Sreenivas et al., 2012), which can be seen in the low positive SLA. When there is both an El Niño and negative IOD phase, the El Niño still weakens the

equatorial wind stress response but the SST temperature gradient in the Indian Ocean is such that there is still a second downwelling Kelvin wave in August and September, triggering the Rossby wave response in the BoB, but a much weakened one (Figure 5.11b).

La Niña years overall show a much stronger downwelling Rossby wave response in the BoB. As with the El Niño year, however, a positive IOD year still creates an anomalously easterly flow towards the Arabian Sea during August and September, weakening the equatorial wind stress, and creating a slightly weakened downwelling Kelvin wave (Figure 5.11c). The resulting Rossby wave in the BoB will still be stronger than during an El Niño year, however, as the ENSO signal overwhelms the IOD signal, creating a signal that is stronger than the combination of El Niño and a negative IOD year. The strongest downwelling Rossby wave response occurs following a year with both La Niña and a negative IOD phase. The combination of an enhanced Walker-type circulation in the Indian Ocean with stronger westerly wind stress from the negative IOD phase creates the correct conditions for strong downwelling Kelvin waves in October, which then leads to a very strong downwelling Rossby wave in the BoB in response to an equally strong coastal Kelvin wave (Figure 5.11d).

As strong second downwelling Kelvin waves propagating around the coast of the BoB are the only ones strong enough to reach the Arabian Sea, it follows that an enhanced Kelvin wave signal following a La Niña and negative IOD year will produce stronger flow along the EICC into the Arabian Sea (Sherin et al., 2018). The strength of the flow of the EICC into the Arabian Sea in the pre-NE monsoon period strongly influences the salinity stratification in the southeastern Arabian Sea in winter and spring, which contributes to the strength of the monsoon onset vortex over Kerala in early June (Shenoi et al., 1999). The

combination of ENSO, IOD, and planetary wave propagation in the previous year can strongly contribute to the timing of the monsoon onset in Kerala through modulation of the freshwater flux into the southeastern Arabian Sea.

The timing of these Rossby waves and the eddy generation in the BoB is consistent with a response to the arrival of the second downwelling coastal Kelvin wave, which typically in the BoB around mid-October and propagates around the BoB through December, triggering the Rossby wave response (Figure 5.11). It is the strength and timing of these second downwelling coastal Kelvin waves that triggers much of the eddy activity seen in the pre-SW monsoon period around the EICC region in the western BoB. More energetic downwelling Rossby waves can contribute to the creation of stronger eddy fields in the western BoB, which contribute to convection, which can in turn contribute to monsoon precipitation.

D. OCEAN HEAT CONTENT

In addition to planetary wave propagation, ocean heat content (OHC) strongly contributes to SST variability and eddy core temperatures. In order to assess the seasonality of OHC in the BoB, OHC is analyzed from NOAA's seasonal, depth-integrated OHC product (Figure 5.12e). As the most significant eddying in the western BoB occurs during the spring months, it is notable that the western BoB has high OHC during the spring months and has lower heat content values during the winter months. It is interesting to note that the spatial distribution of OHC in the BoB does not often coincide with areas of eddy generation, though the lack of coastal coverage in the depth-integrated product may cause EICC and other coastal processes to be missing from the calculated values. It should be

noted, however, that the region with the highest amplitudes and EKE values, the western BoB, experiences the greatest changes in OHC, suggesting a connection between eddy size, EKE, and available heat, which could possibly form a link to convection.

When combined with the arrival and timing of the Rossby wave response to the second downwelling Kelvin wave (Figure 5.10, 5.12), it is clear that the OHC conditions, EKE availability from the EICC, and arrival of the Rossby wave create the perfect scenario for increased strong warm-core eddy activity. This phenomenon has been noted by a recent study by Gulakaram et al. (2018), who also found that a stronger monsoon year's BoB eddy field would be forced by stronger planetary waves in the Indian Ocean and the BoB, creating more AEs and longer-lived CEs, with the opposite being true for a weaker monsoon year. These warm-core eddies in turn have the correct conditions to facilitate convection of the western BoB and India, and the Gulakaram et al. (2018) study found there to be a 4-day lag correlation between OLR and AEs in the BoB. Warm-core eddies generating convection in the western BoB would help explain the seasonal heat loss during the SW monsoon season (Figure 5.12b), as convection would transfer heat from the ocean to the atmosphere. Additionally, larger warm-core eddies would logically have higher OHC values associated with them. As our analysis has shown AEs, especially higher amplitude AEs, to be larger than CEs, it follows that the large warm-core AEs in the BoB would have higher OHC values (Kumar and Chakraborty, 2011; Sadhuram et al., 2012).

Given the relationship between OHC, SST, and eddies, it is useful to compare the number of warm-core eddies in the BoB compared to the OHC from 1993-2018 (Figure 5.13). We find that the overall pattern of OHC in the BoB is weakly related to the number of warm-core eddies in the basin when taken for the whole 25 year period ($R^2 = 0.1524$).

The wave coherence analysis reveals a much more complex relationship. We find that warm-core eddies and OHC are correlated with 95% confidence following a strong El Niño and IOD event, most notably following the 1997-1998 El Niño. During this time, phase arrows indicate that OHC and warm-core eddies are anti-phased and that warm-core eddies slightly lag OHC. The 1997-1998 El Niño and positive IOD event was one of the strongest in recent memory. This is reflected in the warm-core eddies (close to the mean) compared with the OHC (very low), suggesting that other processes contributed to the number of warm-core eddies that year. A similar pattern is seen following the 2015-2016 El Niño event, where again there is a statistically significant correlation (95% confidence) between OHC and warm-core eddies, which may persist for several years following the event. Conversely, there was a strong La Niña in 2010-2011, which is characterized by a period of high OHC and near-mean warm-core eddies, as well as a strong correlation on a seasonal time scale, which would coincide with the IOD period. This suggests that ENSO and the IOD both have a strong influence on OHC values in the region, but less so on the relative abundance of warm-core eddies in the BoB.

Given the apparent relationship between OHC and warm-core eddies, it is then useful to consider deep convection in the BoB. Basic thermodynamics suggest that higher OHC would lead to warmer waters and higher SSTs, triggering deep convection. It has been shown that OHC and warm-core eddies are related and are impacted by ENSO and IOD (Figure 5.13), and thus it stands to reason that warm-core eddies and deep convection should be closely connected. We can explore this connection by isolating warm-core eddies that are surface- and subsurface-intensified.

E. DEEP CONVECTION

As it is possible to extract the vertical structure of eddies with respect to surface- and subsurface-intensification from their surface SLA and SST signatures (Assassi et al., 2016; Trott et al., 2019), we have compiled composites of warm- and cold-core anticyclonic and cyclonic eddies (Figure 5.14). Not unsurprisingly, there was a higher number of surface-intensified eddies of both circulation types, which is typical of highly stratified regions (Dandapat and Chakraborty, 2016). To better understand local convection in these eddy regions, we have also included a composite of OLR. OLR is a commonly used proxy for convection and when compared with the composite eddy SST anomaly (SSTA) signature, it should help describe the relationship between eddies in the BoB and deep convection. In the composites, for all eddy SLA and SSTA types, the OLR is locally low when the SSTA is locally high and vice-versa. OLR is not a perfect proxy for convection, however, and merely means that clouds are present in that region. When we also include precipitation observations, OLR and precipitation follow very different patterns, with there being a clear lag between OLR and precipitation values.

In comparing surface- and subsurface- intensified eddies, we can see the clearest contrast between the cold-core eddy OLR signatures. In subsurface-intensified cold-core CEs, the OLR values are generally fairly low, with higher values above the cold-core and lower values below the center where SSTs are warmer, actually showing both the highest precipitation values and lowest OLR values (Figure 5.14g-h). The cold core AEs, however, are surface intensified and have the highest OLR values of any of the eddy types, as well as the lowest precipitation values (Figure 5.14o-p). Compared to these, the warm-core

eddies show little difference between cyclonic and anticyclonic or surface- and subsurface-intensified.

A previous study by Gulakaram et al. (2018) compared OLR and precipitation over composite AEs and CEs and did a lag-correlation to find a 4-day lag with OLR compared to AEs, and also found that AEs during strong monsoons could produce precipitation rates as much as 2 mm/day more than during strong monsoon years. Compared with this study, our results show a climatologically weak signal in precipitation over eddies that seems to only loosely follow the warm-core eddy locations.

To better understand the role of SSTs and convection, we can measure the climatological OHC for the BoB during all four times of the year, (Figure 5.12). Climatological conditions show that the lowest heat content values are present in the western BoB, especially during the pre-NE monsoon season and then, to a lesser extent, during the NE monsoon season. The overwhelming maximum in OHC occurs during the pre-SW monsoon period in the western BoB, where the highest EKE for CEs and most eddy trajectories occur. This suggests that warm-core CEs (and subsurface-intensified cold-core CEs) in that region during this time have more than enough energy necessary to trigger convection and higher precipitation rates.

In the BoB SSTs exceed 28°C almost throughout the SW monsoon (Gadgil, 2003; Shenoi et al., 2002) making it favorable for convection throughout the season. Convection does not, however, occur all the time, resulting in a poor correlation between SST and rainfall over the Indian Ocean (Gadgil, 2003).

F. EDDY VARIABILITY DUE TO ENSO AND IOD EVENTS

The Indian Ocean and BoB are responsive to multiple climatic events, including ENSO and the IOD, as seen in Figure 5.11. Here we compare the total annual number of AEs and CEs for 1993 to 2018 using an annual average of NOAA's Oceanic Niño Index (ONI) for ENSO (Figure 5.15) and the Dipole Mode Index (DMI) for the IOD (Figure 5.16). The average number of AEs is consistently higher from 1993-2010, after which there is some fluctuation between a higher number of cyclonic and a higher number of AEs. The lowest number of AEs coincides with the strong 1997-1998 IOD/ENSO event, consistent with a weakened downwelling Rossby wave (Figure 5.11a). AEs and the ONI have a moderate negative correlation (R^2 = -0.4402) and AEs and the DMI have a weaker positive correlation (R^2 = 0.1097). Conversely, CEs and the ONI have a weak negative correlation (R^2 = -0.1683), whereas CEs and the DMI have a slightly stronger relationship (R^2 = 0.3163).

To further analyze the relationship between eddies and the ONI and DMI, wave coherence is calculated to see how the relationship changes over time. The ONI and AEs have one of the strongest relationships, consistently being anticorrelated and in phase with a longer period of oscillation from 1993-2006 with 95% confidence. After 2006, however, this relationship changes completely so that the two are in phase and positively correlated with 95% confidence after 2011 with a dominant period of less than 3 years (Figure 5.15). This same relationship does not hold true for CEs, which remain weakly correlated on short time scales for most of the 25-year period.

Though not always the case, La Niña years generally produce more eddies than El Niño years. A previous study by Sreenivas et al. (2012) showed that the timing of the coastal Kelvin waves in the BoB is strongly related to ENSO phase, and thus the role ENSO forcing plays on modulating eddy dynamics in the BoB is through the second downwelling coastal Kelvin waves. Another study showed that there was an 18-month lag between eddying and ENSO phase, concluding that there was no relationship (Chen et al., 2012), but this calculated lag was due to the timing of the planetary wave reponse, which is delayed from ENSO phase to eddy generation.

Wave coherence was also calculated for eddies and the DMI (Figure 5.16). Unlike the ONI, which showed a stark contrast between AEs and CEs, the DMI and eddies seem to have a more temporally consistent relationship, with the strongest correlations occuring for both after 2006, spanning ten years, although this occurs for CEs first. Both have a dominant period of 4 years with 95% confidence during the 21st century and are in phase with the DMI. CEs, have higher correlations on shorter time scales at the beginning of the record. There is tendency for higher correlations to occur with La Niña conditions, suggesting an interplay between ENSO and the IOD on eddy behavior. In comparing the number of warm core eddies (both anticyclonic and cyclonic) using wavelet coherenc analysis, we also found a statistically signficant relationship during ENSO and IOD years to 95% confidence, further adding credence to our theory (figure not shown). In comparing both basin-averaged OLR and SST to the number of warm-core eddies, we find that from 1998 to 2001, then from 2010 to 2014, and in 2016 there is a strong relationship between SST (R^2 = 91%), OLR (R^2 = 88%) and the number of warm-core eddies with a dominant periodicity of 2-6 years, consistent with ENSO and IOD forcing. These time periods were

also either during or immediatley following a La Niña, further suggesting the connection between La Niña forcing of planetary waves and eddy-induced convection.

To further describe the variability between ENSO and IOD phases, we compare the eddy fields in the BoB following a concurrent El Niño and positive IOD years (1998; Figure 5.17) and following a La Niña and negative IOD year (2011; Figure 5.18). As in the Rossby wave propagation associated with their generation, there is a dramatic difference between the eddy fields. Following the weak downwelling Rossby wave in the BoB generated during the El Niño and positive IOD year, cyclonic eddies are low amplitude and anticyclonic eddies have large regions of negative SLA. Conversely, the SST fields are both higher magnitude than the mean eddy field in Figure 5.13. The most notable result of the low Rossby wave response, however, would be the OLR response to the eddy field. All eddy types, save subsurface-intensified CEs, have large positive OLR values and low precipitation values associated with them, suggesting that overall eddying during this year is characterized by clear skies and low precipitation.

Compared with Figure 5.17, Figure 5.18 describes much higher amplitude eddies with more moderate temperature profiles, yet a more climatological OLR response, similar to the one seen in Figure 5.13. That being said, the OLR response in Figure 5.18 favors lower values over higher, which is more indicative of deep convection in the area. Unlike following the El Niño/Positive IOD year, the OLR following the La Niña/Negative IOD year does not appear to favor a specific eddy type, nor does it differentiate between subsurface- or surface-intensified eddies; there are slightly lower OLR values for CEs, but AEs have more precipitation associated with them.

Overall, it is clear that the eddy field following the suppressed (enhanced) Rossby wave response during an El Niño/Positive IOD (La Niña/Negative IOD) year favors clear skies (convection) and lower (higher) precipitation values where there are eddies. This suggests a connection between the Rossby wave-induced eddies and deep convection in the BoB, modulated on interannual timescales by ENSO and IOD processes.

5.4 CONCLUSION

The EICC, coastal Kelvin waves, and the associated Rossby waves play an important role in eddy variability, and large-scale climate oscillations and modes of interannual variability, such as ENSO and the IOD, play a statistically significant role in modulating these processes, as shown through wavelet analysis. These relationships evolve through time, however, and are strongly interrelated. These modes of variability can work either constructively or destructively together to alter the eddy field of the following pre-SW monsoon and SW monsoon season by modulating the equatorial wind stress in the Indian Ocean and influencing the timing and strength of the second downwelling Kelvin wave, which typically arrives in the BoB in October. This coastal Kelvin wave propagates around the BoB and reaches the Arabian Sea in early winter, with the strength of flow influenced by the direction of the EICC. These Kelvin waves generate a downwelling Rossby wave response in the BoB in October or November, taking several months to propagate across the BoB before triggering significant eddying in the pre-SW monsoon season into the SW monsoon season proper. These eddies can then help influence convection in the western BoB and contribute to monsoonal rainfall.

The weakest eddying and convection is seen following a year when a positive IOD and El Niño are concurrent due to the anomalously eastern wind in the equatorial Indian Ocean, which causes the second downwelling Kelvin and Rossby waves to be small to nonexistent. Conversely, the strongest eddying and convection is seen following a negative IOD and La Niña season the previous year, which enhances the westerly wind anomalies in the equatorial Indian Ocean, creating a strong downwelling Kelvin and Rossby wave response and resultant eddy field.

The timing of the arrival of the Rossby wave in the western BoB and the eddy generation with resultant convection the year following a particular phase of ENSO and IOD suggests a possible explanation for the imperfect prediction of monsoon precipitation amounts during an El Niño or La Niña year. The modulation of the EICC by the second downwelling Kelvin wave, and therefore by the combination of ENSO and IOD processes, suggests that these processes influence the transport of reasonably fresh water from the BoB into the southeastern Arabian Sea region in late winter. This can in turn influence the development of the Arabian Sea Mini Warm Pool and the monsoon onset vortex, influencing the strength and timing of SW monsoon onset over Kerala.

As most tropical depressions, cyclones, and low-pressure systems that contribute to rainfall over the northern Indian Ocean and Indian subcontinent are generated over the BoB, it is critical that we develop a better understanding of the processes that influence deep convection in the BoB. Our use of a blended daily altimetric product to track eddies and connect them to convection emphasizes the potential use for altimetry in Indian monsoon studies and predictability. While the daily product is necessarily noisy and may produce false eddies and uncertainty, the majority of the eddies produced will have real

physical meaning and be reflective of the real dynamics in the region. As the altimetric constellation is improved with the addition of the SWOT mission, we will have higher spatial resolution observations to improve our daily altimetry products, which will improve the robustness of our eddy tracking methodology and results. In understanding the dynamic relationship between eddy variability in the BoB, ENSO and IOD processes, deep atmospheric convection, and precipitation, we can begin to paint a clearer picture of the mechanisms that govern deep convection, storm development, and precipitation in the BoB.

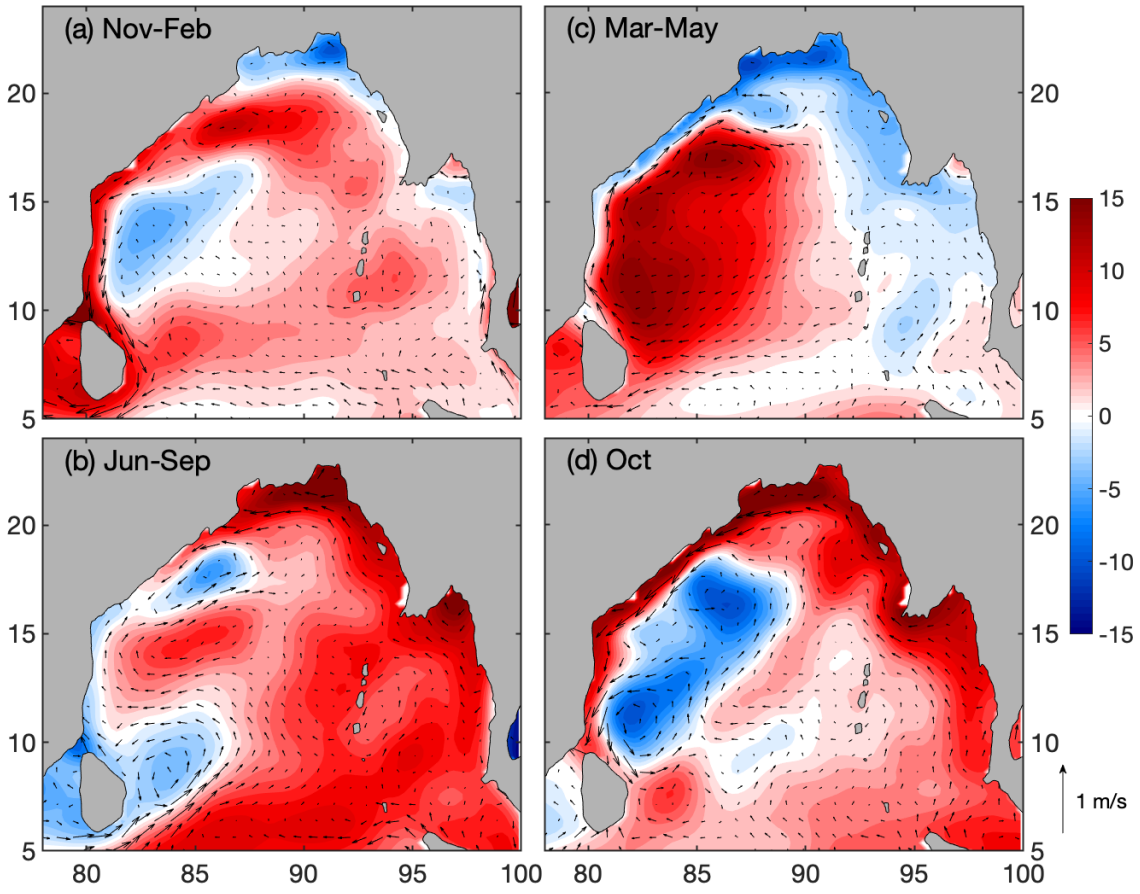

Figure 5.1. Climatological SLA (in cm) and associated geostrophic current vectors from altimetry (m/s) during 1993-2018 for (a) Northeast monsoon (November-February), (b) Southwest monsoon (June-September), (c) March-May, and (d) October.

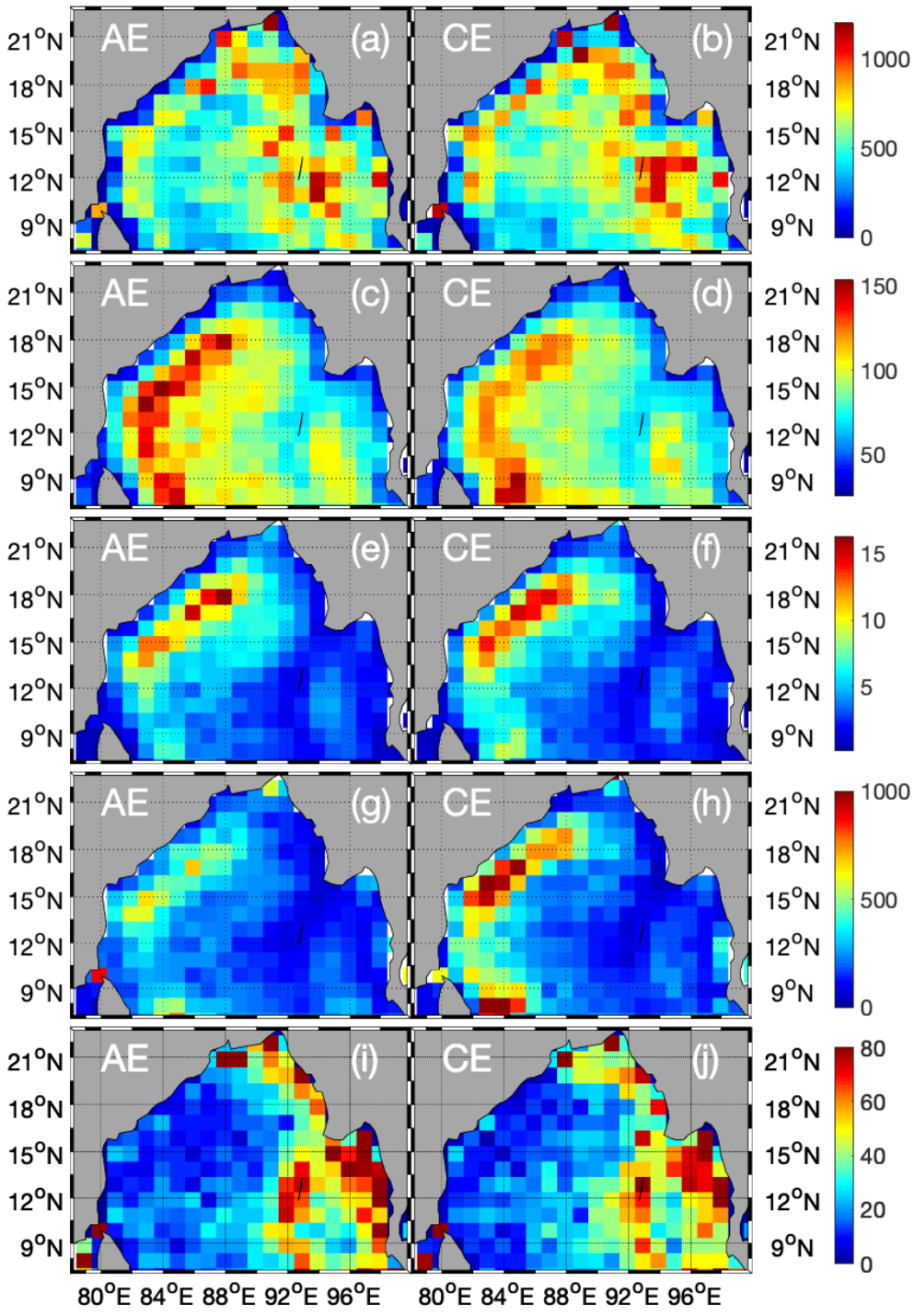

Figure 5.2. Mean spatial distribution of eddy characteristics from 1993-2018 for AEs (left panel) and CEs (right panel). (a-b) Number of eddies; (c-d) radius (in km); (e-f) amplitude (in cm); (g-h) EKE (in $cm^2\ s^{-2}$); (i-j) Number of eddy generation.

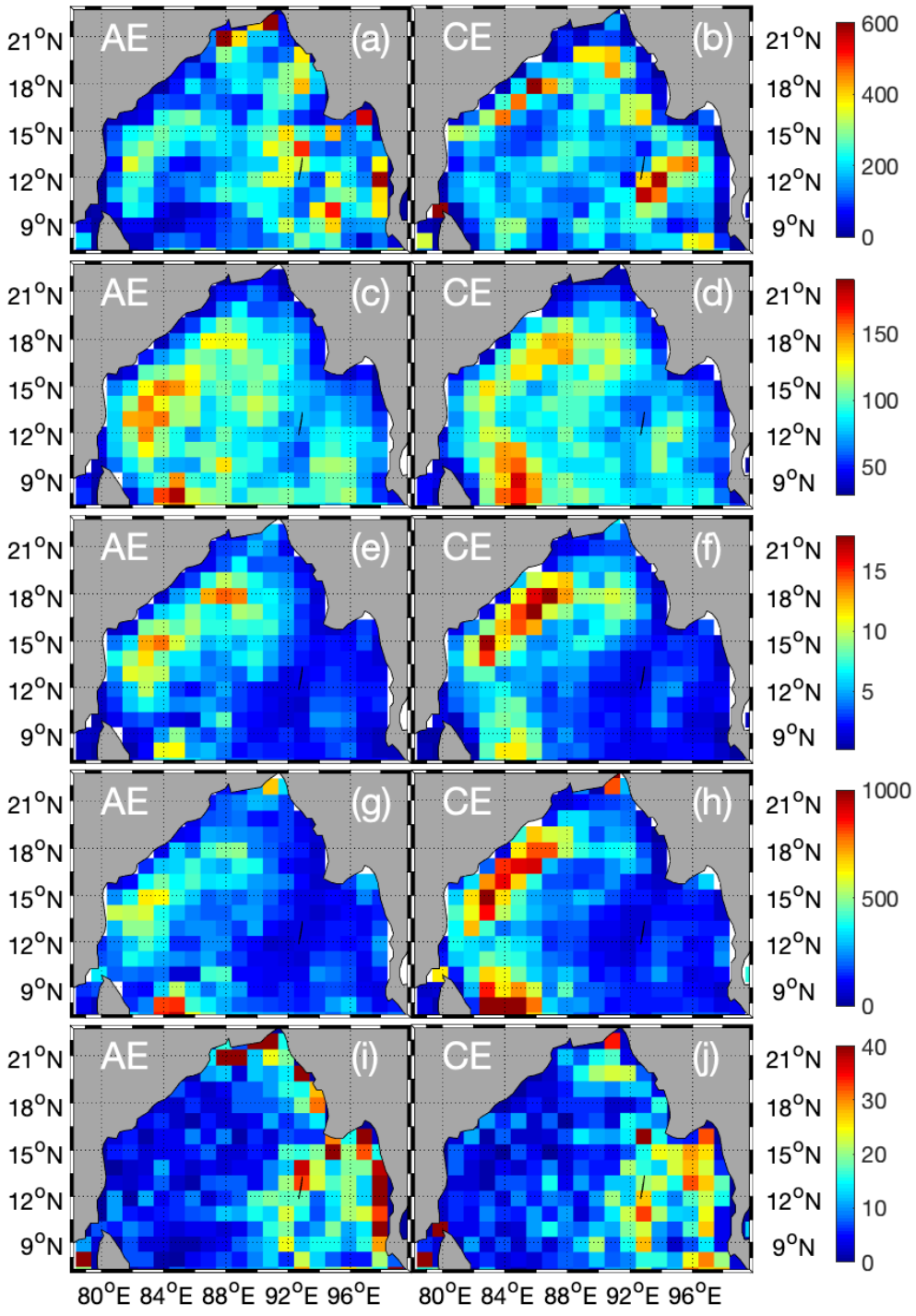

Figure 5.3. Mean spatial distribution of eddy characteristics for the Southwest monsoon season (Jun-Sep) from 1993-2018 for AEs (left panel) and CEs (right panel). (a-b) Number of eddies; (c-d) radius (in km); (e-f) amplitude (in cm); (g-h) EKE (in $cm^2\ s^{-2}$); (i-j) Number of eddy generation.

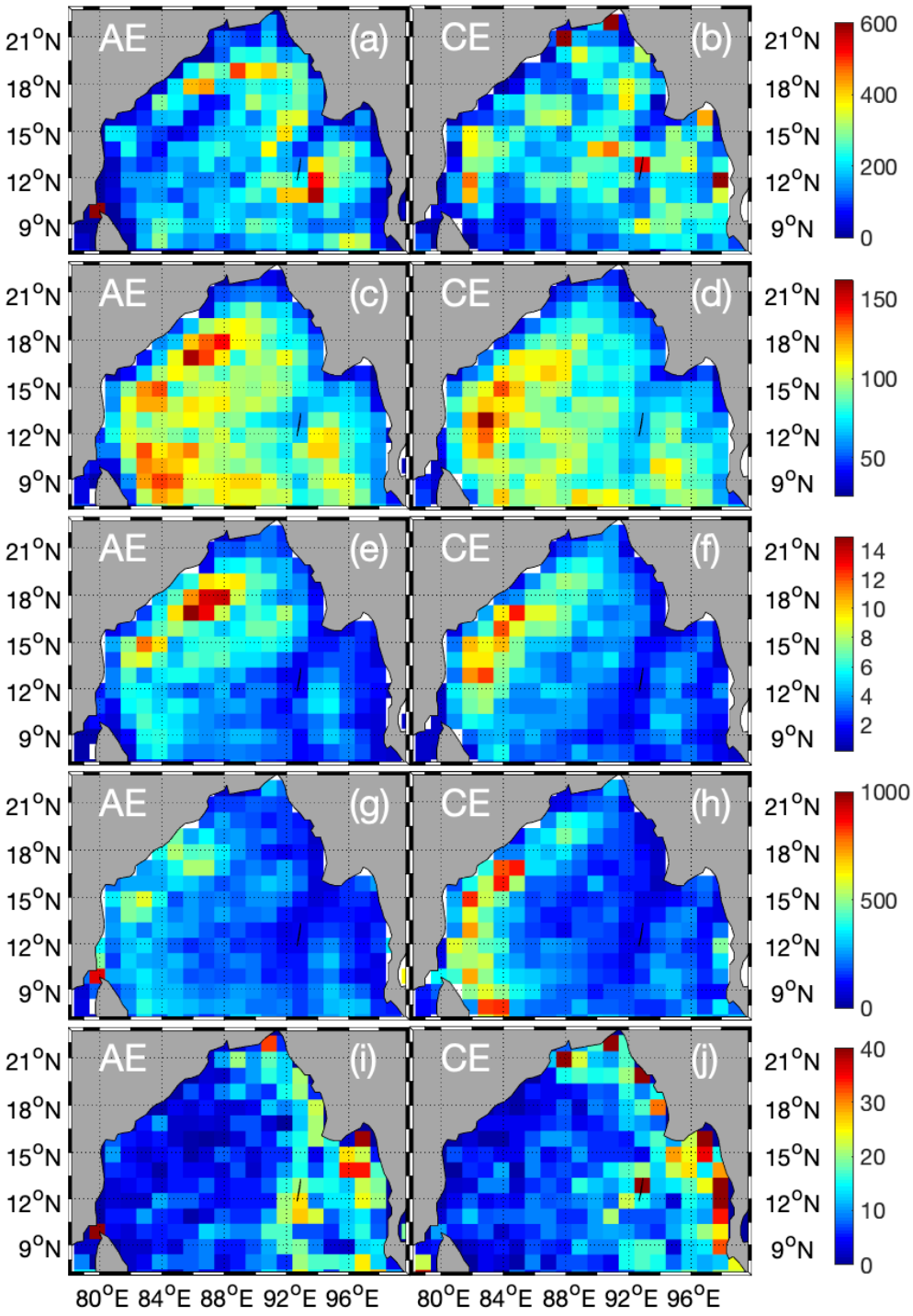

Figure 5.4. Mean spatial distribution of eddy characteristics for the Northeast monsoon season (Nov-Feb) from 1993-2018 for AEs (left panel) and CEs (right panel). (a-b) Number of eddies; (c-d) radius (in km); (e-f) amplitude (in cm); (g-h) EKE (in $cm^2\ s^{-2}$); (i-j) Number of eddy generation.

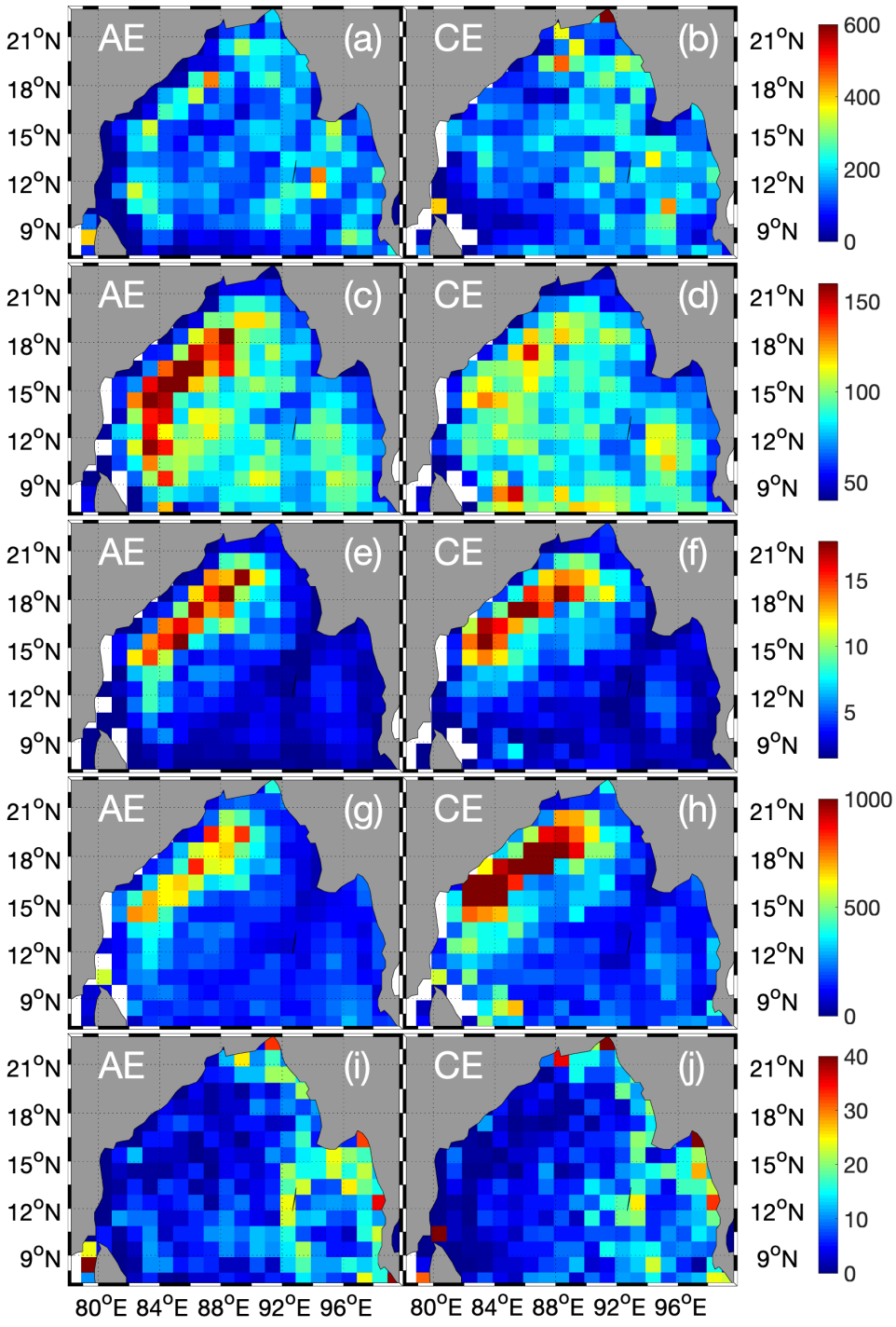

Figure 5.5. Mean spatial distribution of eddy characteristics for the intermonsoon period (Mar-May) from 1993-2018 for AEs (left panel) and CEs (right panel). (a-b) Number of eddies; (c-d) radius (in km); (e-f) amplitude (in cm); (g-h) EKE (in cm^2 s^{-2}); (i-j) Number of eddy generation.

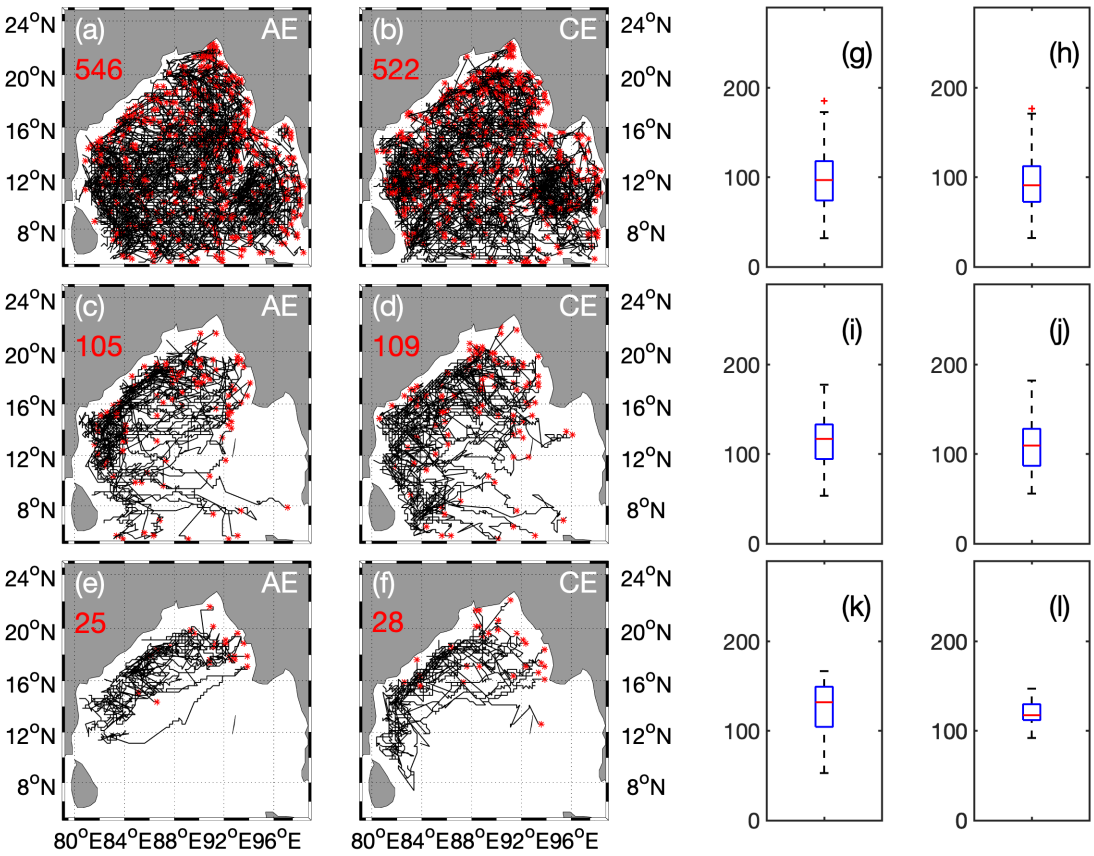

Figure 5.6. Total annual eddy trajectories from 1993-2018 for AEs (left) and CEs (middle) for 10-20 cm (a-b), 20-30 (c-d), 30-40 (e-f), and box plots of radius (km; right), with (g) corresponding to (a), (h) to (b), and so on. Red stars indicate genesis location and black lines to indicate eddy trajectories. Red numbers are the number of eddies shown.

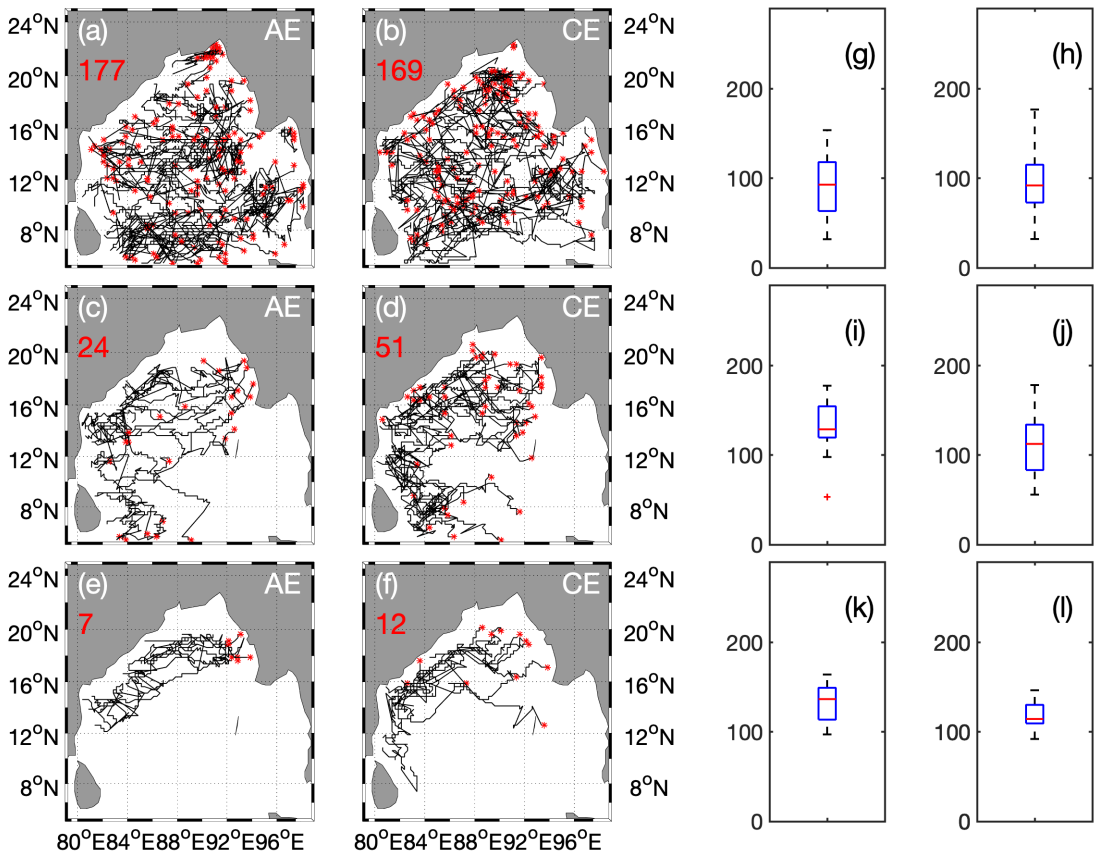

Figure 5.7. SW monsoon eddy trajectories from 1993 to 2018 for AEs (left) and CEs (middle) for 10-20 cm (a-b), 20-30 (c-d), 30-40 (e-f), and box plots of radius (km; right), with (g) corresponding to (a), (h) to (b), and so on. Red stars indicate genesis location and black lines to indicate eddy trajectories. Red numbers are the number of eddies shown.

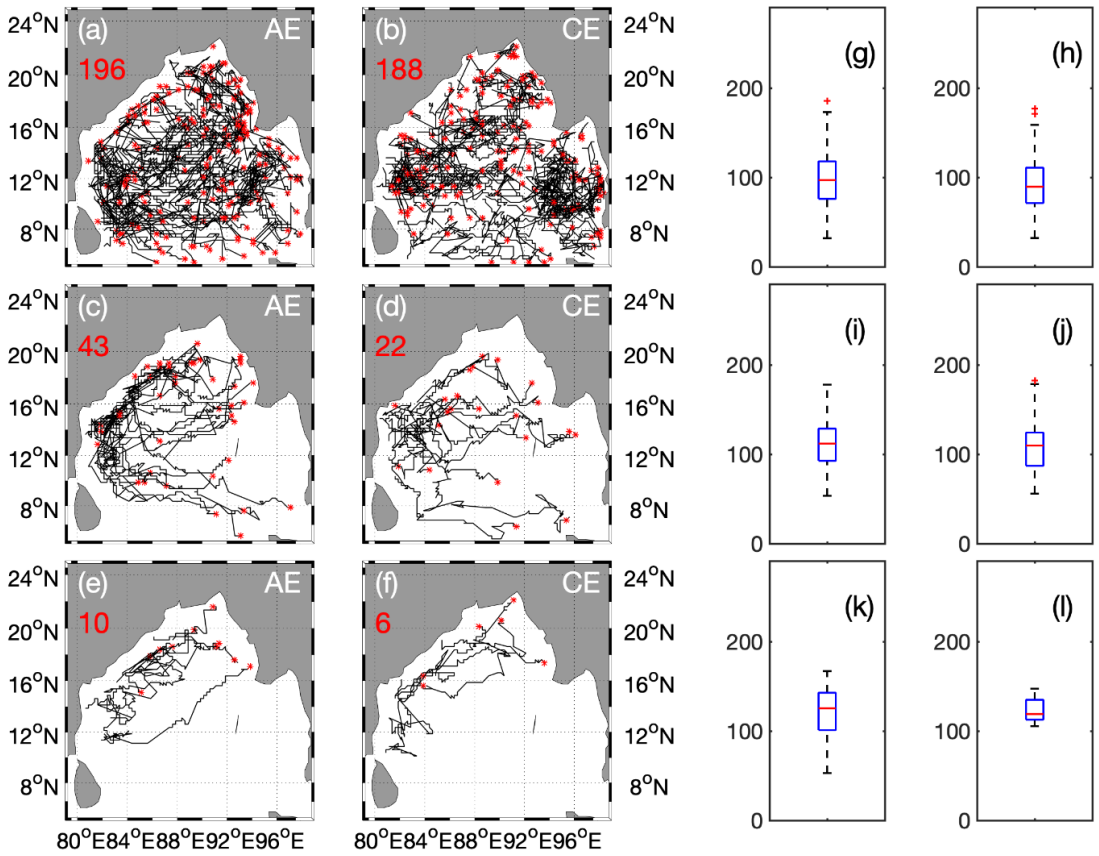

Figure 5.8. NE Monsoon eddy trajectories from 1993-2018 for AEs (left) and CEs (middle) for 10-20 cm (a-b), 20-30 (c-d), 30-40 (e-f), and box plots of radius (km; right), with (g) corresponding to (a), (b) to (h), and so on. Red stars indicate genesis location and black lines to indicate eddy trajectories. Red numbers are the number of eddies shown.

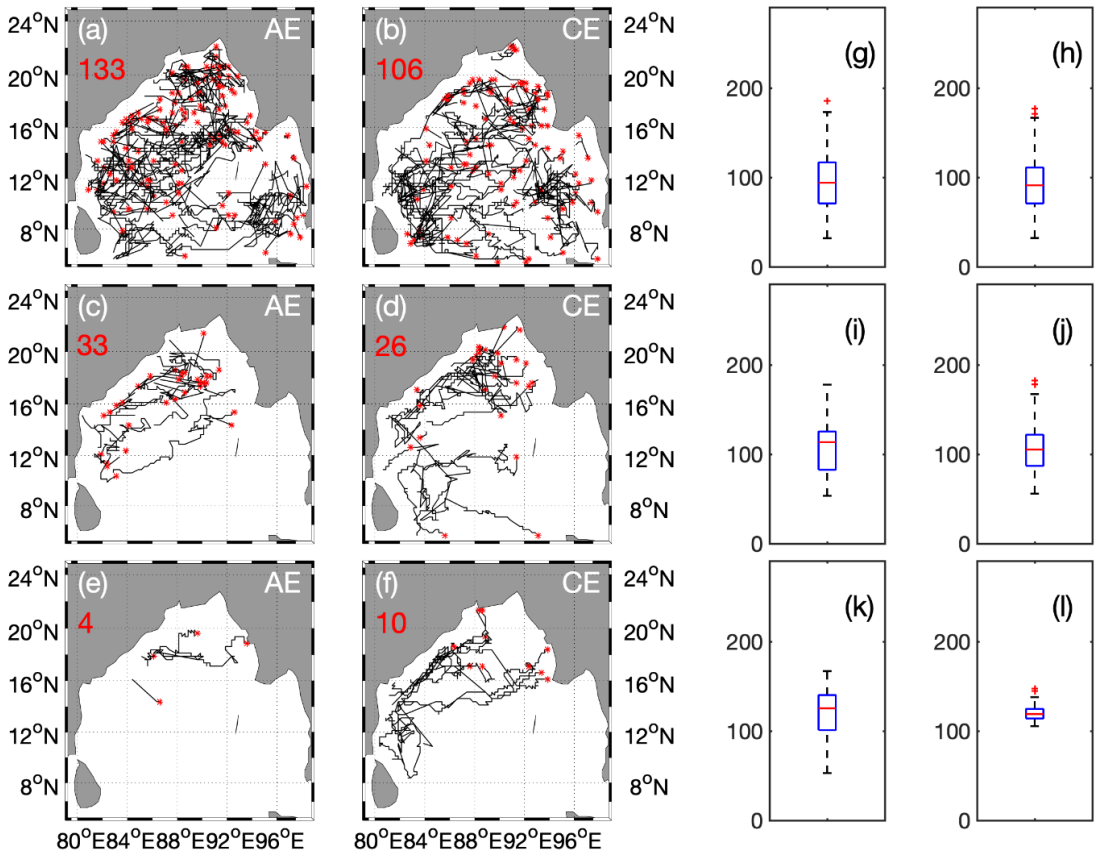

Figure 5.9. Total MAM eddy trajectories from 1993-2018 for AEs (left) and CEs (middle) for 10-20 cm (a-b), 20-30 (c-d), 30-40 (e-f), and box plots of radius (km; right), with (g) corresponding to (a), (h) to (b), and so on. Red stars indicate genesis location and black lines to indicate eddy trajectories. Red numbers are the number of eddies shown.

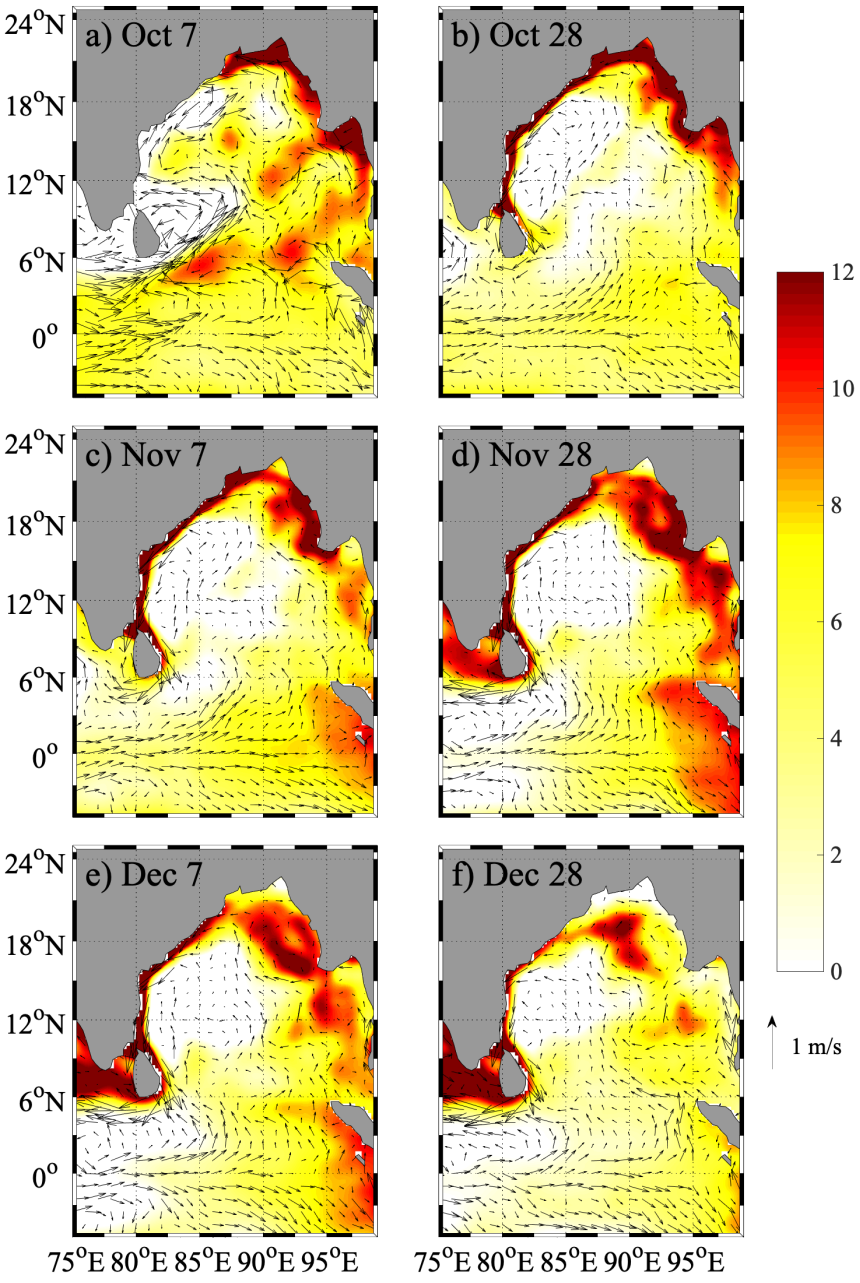

Figure 5.10. A 25-year average of the second downwelling coastal kelvin wave propagation in the Bay of Bengal roughly every three weeks from (a) Oct 7 to (f) Dec 28, from 1993 to 2018 in AVISO SLA (cm; shaded) with geostrophic currents overlaid outside of 3°N-3°S, and ageostrophic currents between 3°N-3°S (black vectors; m/s). Only positive SLA values are shown to isolate the downwelling signature.

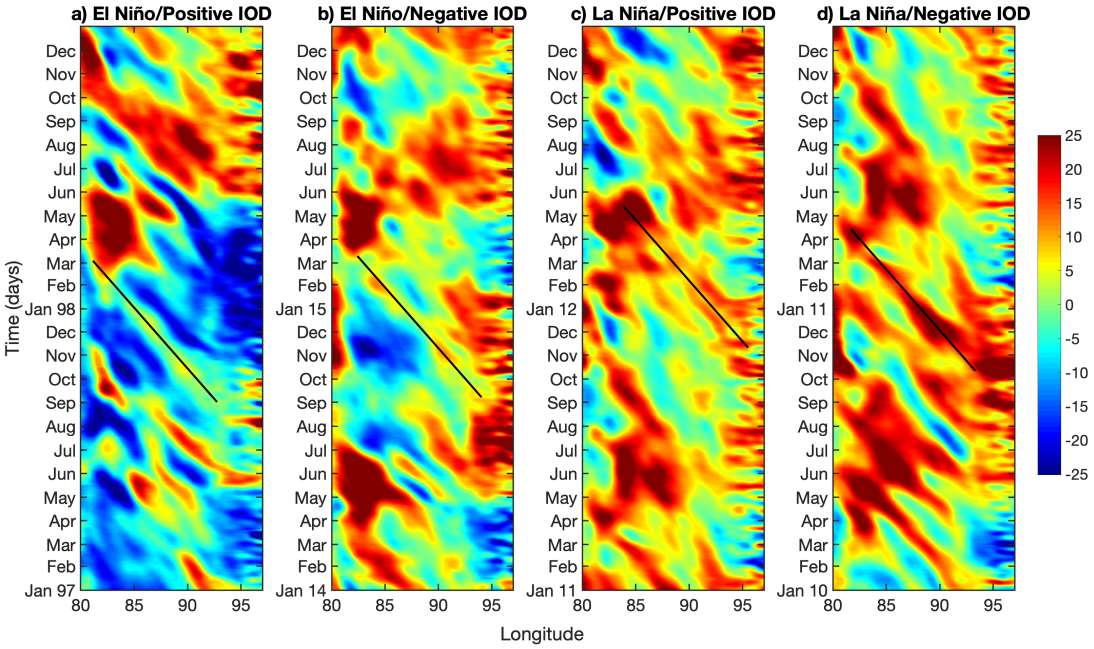

Figure 5.11. Time-longitude plots at 15°N of Rossby waves in SLA (cm) in the BoB during a) an El Niño and positive IOD year (1997-1998), b) an El Niño and negative IOD year (2014-2015), c) a La Niña and positive IOD year (2011-2012), and d) a La Niña and negative IOD year. Black lines indicate Rossby wave propagation.

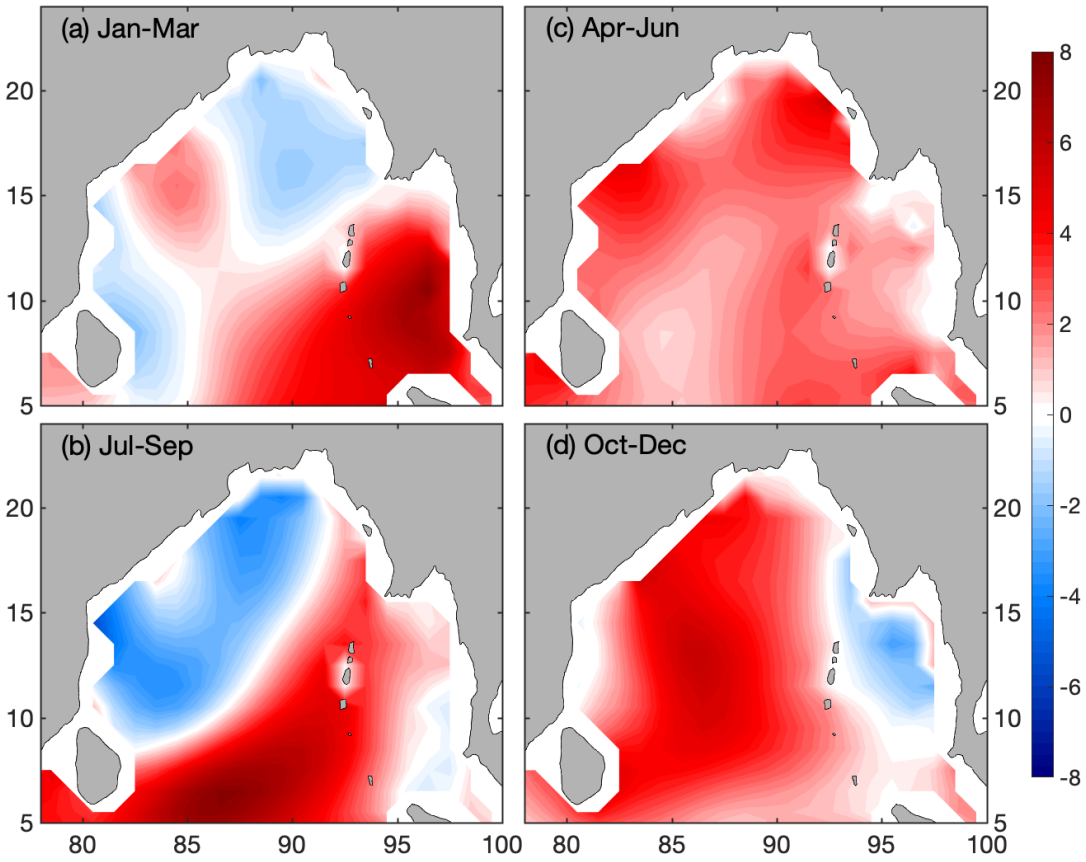

Figure 5.12. Climatological depth-integrated ocean heat content averaged over 1993-2018 seasonally. Units for ocean heat content are in $x10^{19}$ J.

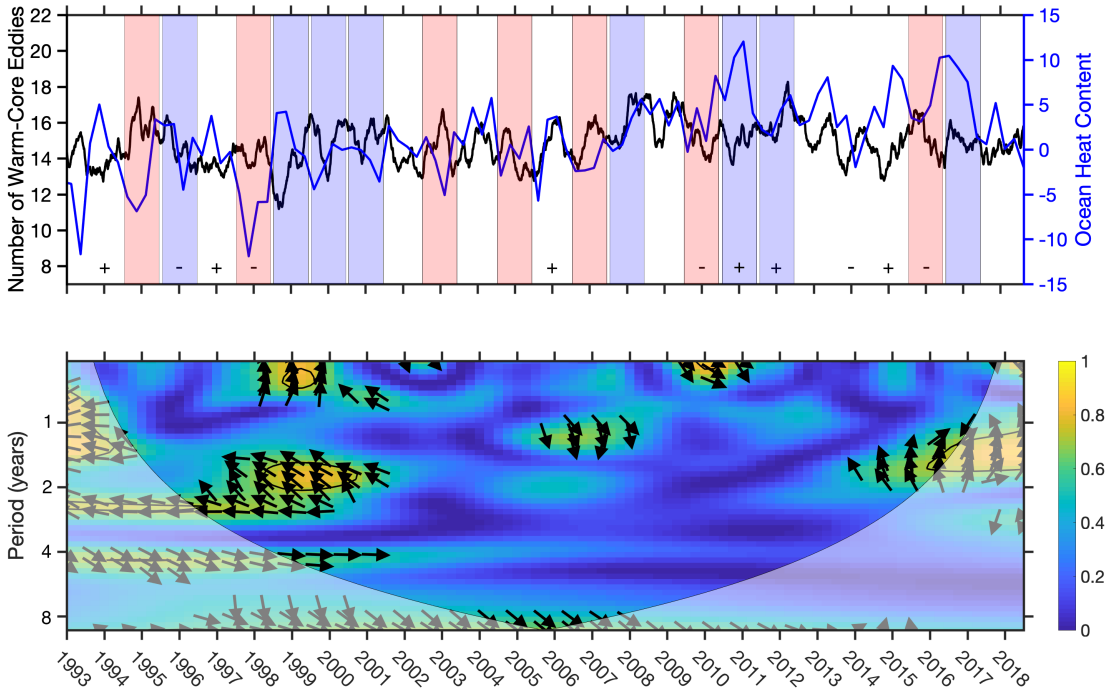

Figure 5.13. (Top) Number of warm-core eddies in the BoB (blue) and basin-wide OHC (black) from 1993-2018. Units for OHC are in $x10^{19}$ J. (Bottom) wave coherence plot of warm core eddies and OHC (R^2 shaded). Phase arrows indicate whether the two time series are in phase (right), anti-phase (left), or if the eddies lead (down) or lag (up) OHC. White shading indicates the cone of influence where the length of the time series does not allow for statistical significance due to edge effects. Black outlines indicate 95% confidence. Colored bars indicate El Niño years (red) and La Niña years (blue), whereas IOD years are indicated by a + or – for positive and negative IOD phases respectively.

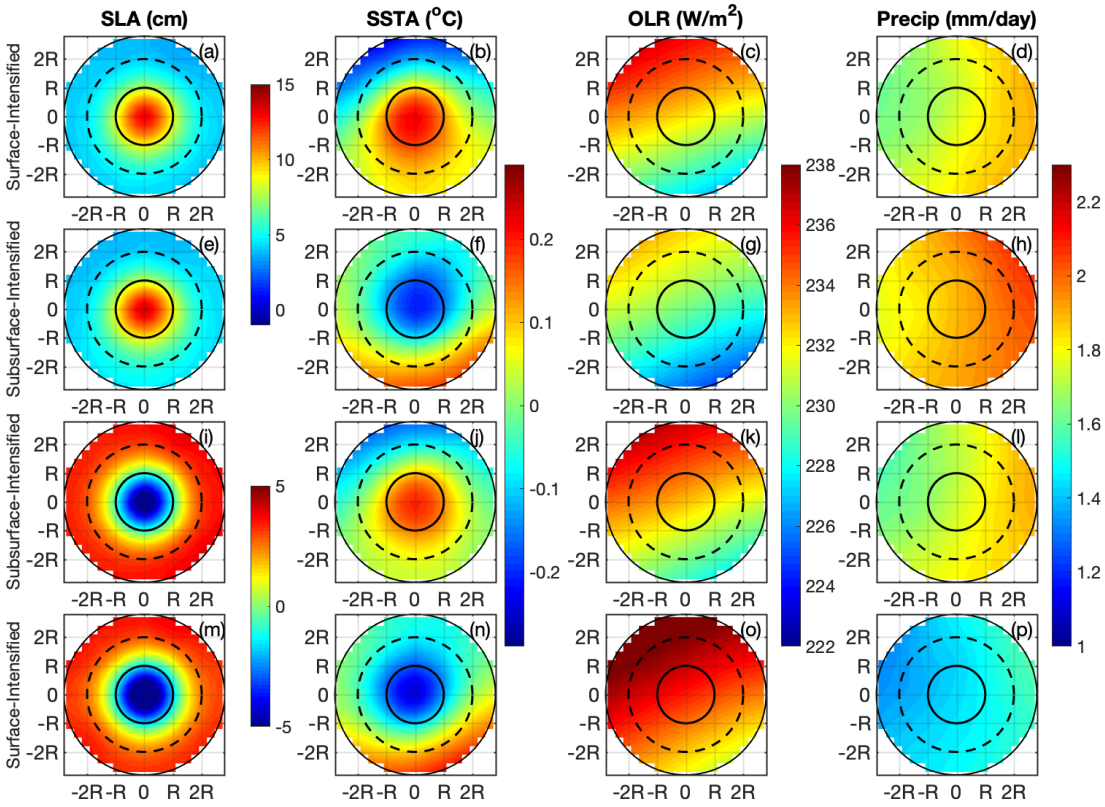

Figure 5.14. Eddy composites with normalized radius from 1993 to 2018 in the Bay of Bengal in SLA (left; cm), SSTA (left middle; °C), OLR (right middle; W/m^2), and precipitation (right; mm/day) for (a-d) surface intensified, warm core AEs, (e-h) subsurface-intensified, cold core AEs, (i-l) subsurface intensified, warm core CEs, and (m-p) surface intensified, cold core CEs.

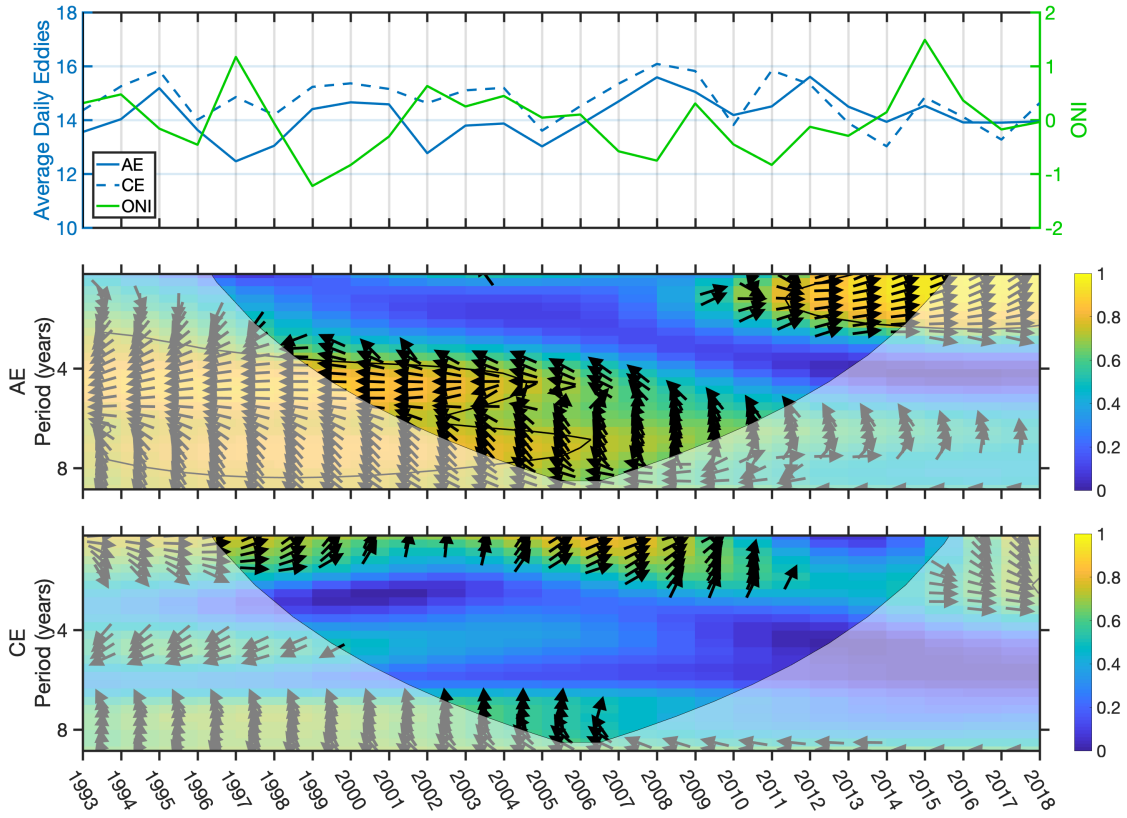

Figure 5.15. (Top) Total annual AEs (solid blue) and CEs (dashed blue) in the Bay of Bengal compared to the annual mean ONI ENSO index (°C; solid green) from 1993 to 2018, where the total number of eddies is taken to be the average number of eddies in a day for each year. Wave coherence plots of (middle) the ONI and AEs (R^2 shaded) and of (bottom) the ONI and CEs. Phase arrows indicate whether the two time series are in phase (right), anti-phase (left), or if the eddies lead (down) or lag (up) the ONI. White shading indicates the cone of influence where the length of the time series does not allow for statistical significance due to edge effects. Black outlines indicate 95% confidence.

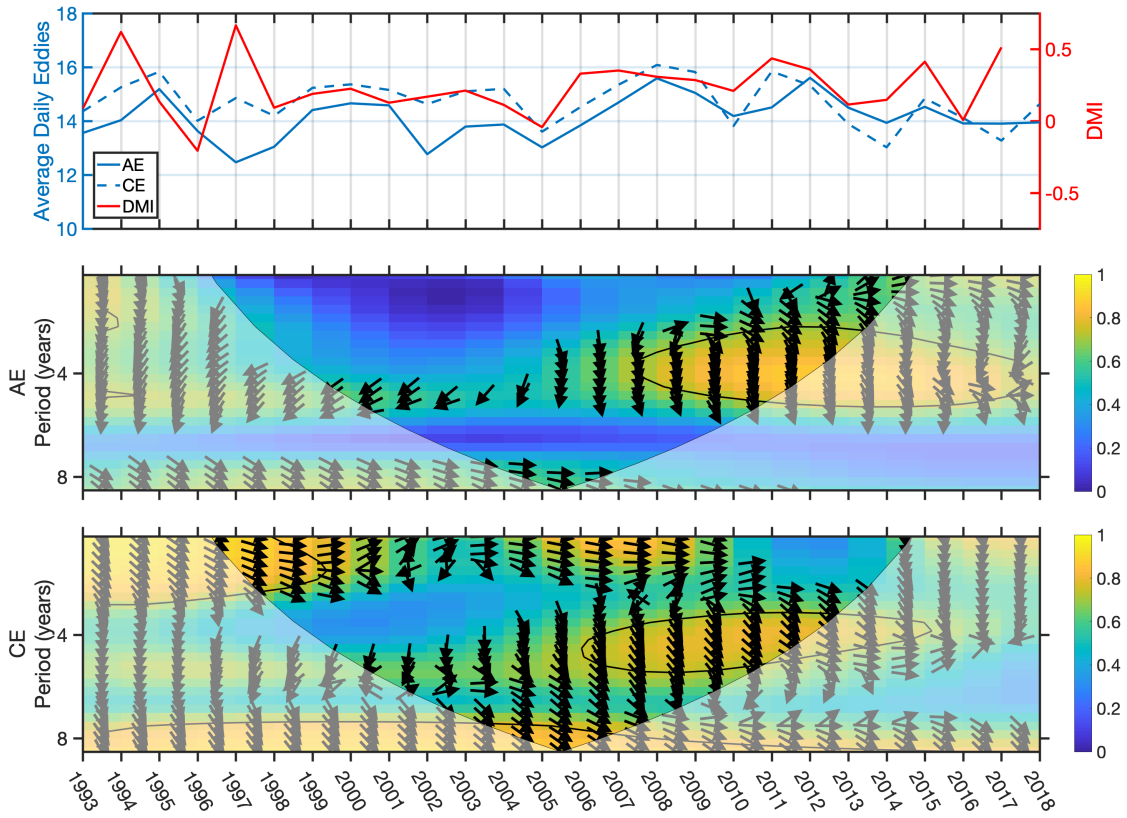

Figure 5.16. Total annual AEs (solid blue) and CEs (dashed blue) in the Bay of Bengal compared to the annual mean DMI IOD index (°C; solid red) from 1993 to 2017, where the total number of eddies is taken to be the average number of eddies in a day for each year. Wave coherence plots of (middle) the DMI and AEs (R^2 shaded) and of (bottom) the DMI and CEs. Phase arrows indicate whether the two time series are in phase (right), anti-phase (left), or if the eddies lead (down) or lag (up) the DMI. White shading indicates the cone of influence where the length of the time series does not allow for statistical significance due to edge effects. Black outlines indicate 95% confidence.

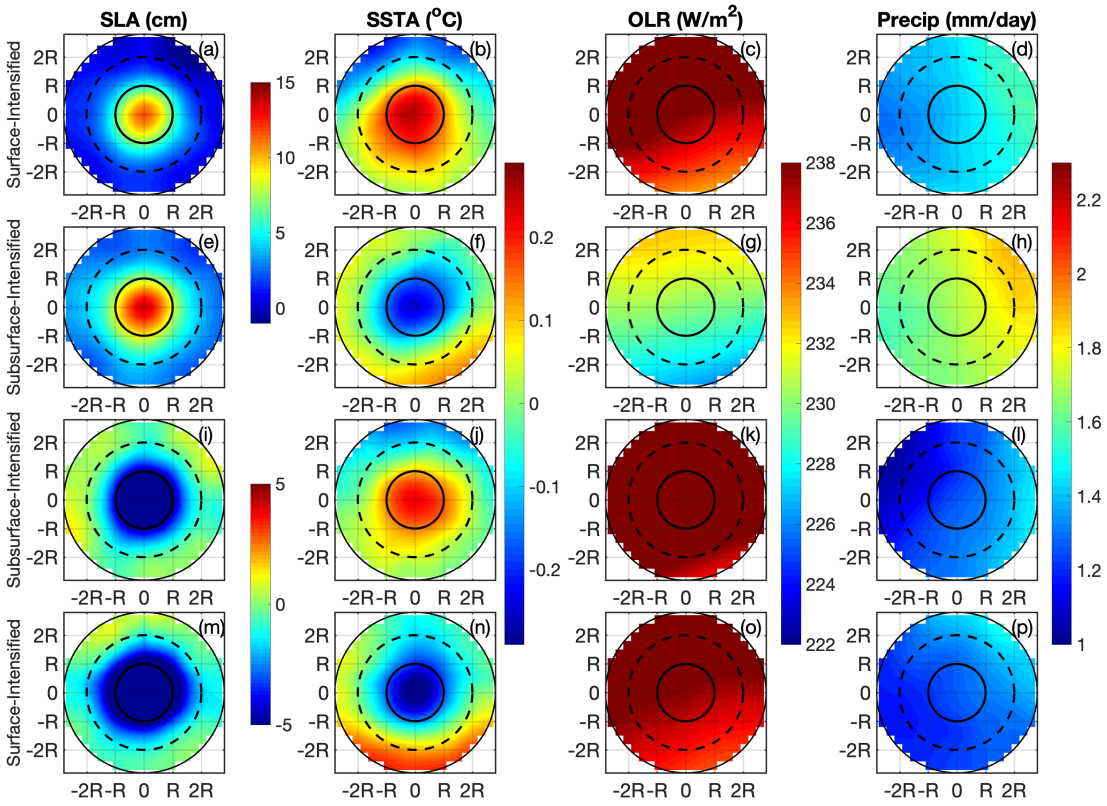

Figure 5.17. Eddy composites with normalized radius for 1998 in the Bay of Bengal in SLA (left; cm), SSTA (left middle; °C), OLR (right middle; W/m^2), and precipitation (right; mm/day) for (a-d) surface intensified, warm core AEs, (e-h) subsurface-intensified, cold core AEs, (i-l) subsurface intensified, warm core CEs, and (m-p) surface intensified, cold core CEs.

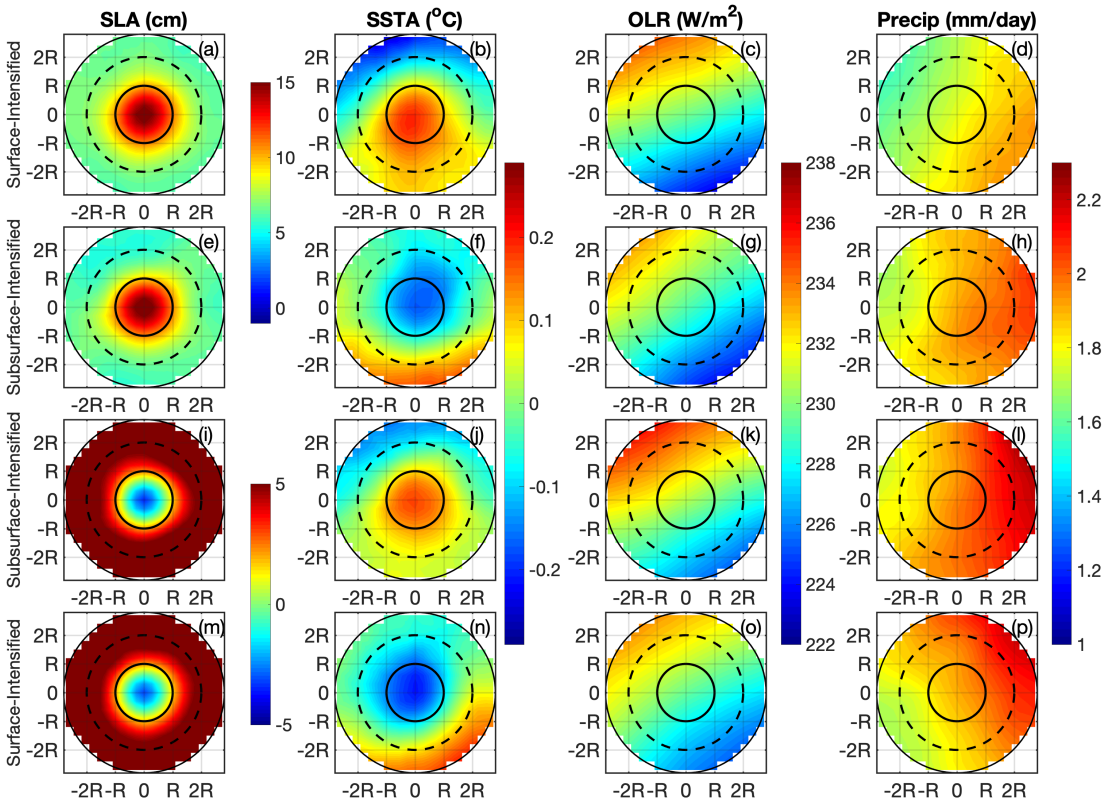

Figure 5.18. Eddy composites with normalized radius for 2011 in the Bay of Bengal in SLA (left; cm), SSTA (left middle; °C), OLR (right middle; W/m^2), and precipitation (right; mm/day) for (a-d) surface intensified, warm core AEs, (e-h) subsurface-intensified, cold core AEs, (i-l) subsurface intensified, warm core CEs, and (m-p) surface intensified, cold core CEs.

CHAPTER 6

CONCLUSIONS

This dissertation has focused on the physical oceanographic processes and air-sea interactions associated with monsoon onset, intraseasonal oscillations, and mesoscale eddies in the Bay of Bengal and Indian Ocean. This research has employed a combination of reanalysis, ocean models, and satellite observations of both the atmosphere and ocean in order to understand these processes. While each chapter has focused on a different facet of monsoon processes in the Indian Ocean, they all highlight the continued necessity for high spatial and temporal resolution ocean satellite observations and for these observations to be included in modeled forecasts of the monsoon and intraseasonal oscillations. The southwest monsoon and its associated intraseasonal oscillations directly impact the economics, agriculture, fisheries, national security, and well-being of over a billion people in India and its neighbors, so it remains critically important that we further our understanding of monsoon processes and the Indian Ocean. It is the hope of the author that the findings in this dissertation will not only help to improve monsoon forecasting and monitoring but spread awareness for our continued need to do so.

In Chapter 2, the role of salinity and freshwater transport in the southeastern Arabian Sea in the establishment of the Arabian Sea Mini Warm Pool and monsoon onset was explored. It was found that the freshwater contribution of EICC was greater during weak and normal monsoon regimes than during strong monsoon regimes, when the NEC

played a greater role. During weak and normal monsoon years, the freshwater entering the southeastern Arabian Sea was more confined to the coast, which resulted in a deeper barrier layer, but a smaller warm pool. By contrast, the composite strong monsoon regime had a more spread out fresh pool that was more persistent, which resulted in a shallower barrier layer, but a stronger warm pool and stronger onset. In analyzing trends in onset parameters, it was found that a long-term decrease in atmospheric moisture flux from the sea surface, freshwater transport, and wind in conjunction with an increase in OHC contributed to the lack of strong monsoons after 1994. Additionally, prevailing IOD and ENSO conditions favored weak monsoons during this time period, which influenced these observed changes in physical parameters, and also created the conditions necessary for the observed patterns in monsoon strength. Most importantly, this was the first study to establish the importance of freshwater transport into the southeastern Arabian Sea by the NEC in determining monsoon onset and establishment of the Arabian Sea Mini Warm Pool, as well as to provide a physical basis for the lack of strong monsoons after 1994.

In Chapter 3, the need for high spatial and temporal resolution satellite observations was highlighted as satellite observations of oceanic (SLA, SSS, SST) and atmospheric parameters (precipitation and wind) were used to monitor the 30-90-day, 10-20-day, and 3-7-day ISOs in the Indian Ocean. Through this multiparameter approach, it was found that an MRG wave in the eastern equatorial Indian Ocean triggered the genesis of the southern cell of the 10-20-day double cell structure, which was a novel finding. Furthermore, it was found that surface winds from the northern cell of the double cell structure modulate the coastal Kelvin waves in the Bay of Bengal. The 3-7-day oceanic signal was low amplitude overall, but it was found that SSS from satellites could more adequately capture these

events due to the larger satellite swath. From these findings, it was concluded that higher spatial resolution observations of SLA, such as those from NASA's upcoming SWOT mission were necessary in order to adequately capture these 3-7-day events, as well as to improve our understanding of coastal processes, such as those impacted by 10-20-day events.

The 10-20-day ISO was further explored in Chapter 4, which focused on understanding how this atmospheric ISO is translated into the Bay of Bengal. It was found that the 10-20-day ISO has a stronger SSS signature in the northern Bay than in other regions of the Bay due to the patterns of enhanced/suppressed convection associated with the double cell, as well as the positioning of the northernmost cell of the double cell structure. Furthermore, it was found that winds from the northernmost cell induce upwelling in the central Bay up to four days following the height of precipitation, which causes a slight salinification and cooling of SSTs. The most novel finding of this study, however, was the discovery that the 10-20-day signal in temperature can be felt in the Bay down to 250 m depth, suggesting that there are biweekly oscillations in the thermocline associated with this mode of variability. In salinity, there is a slight increase around the thermocline in the central and southern Bay, which further suggests that the subsurface Arabian Sea high salinity water mass is affected by this mode of variability.

The investigation into mesoscale eddy variability in the Bay of Bengal in Chapter 5 revealed that the most energetic eddies occur around the EICC region, particularly during the pre-monsoon months. It was further discovered that warm-core eddy variability in the Bay helps to drive changes in OHC, which has implications for monsoon rainfall, tropical cyclones, and ISOs. As the Rossby waves radiated by the second downwelling coastal

Kelvin wave in the Bay can significantly impact the eddy field in the western Bay, the Rossby wave propagation during concurrent ENSO and IOD phases were explored, along with the resultant composite eddy field. Through this multiparameter analysis, it was found that the season following an El Niño and positive IOD would result in a weaker Rossby wave, lower amplitude eddies, and a suppressed precipitation response associated with these eddies. In contrast, the season following a La Niña and negative IOD resulted in a stronger Rossby wave, higher amplitude eddies, and an enhanced precipitation response associated with these eddies. This study was significant in that it was the first to analyze 25-years of eddy variability and characteristics in the Bay, as well as the first to connect Bay of Bengal eddy variability to the strength of a previous year's ENSO and IOD phase through Rossby wave propagation.

While this work addressed a variety of important questions in monsoon studies, there remain many unanswered questions that are worthy of further study. In particular, further work is needed to establish the role of IOD and ENSO asymmetry in barrier layer development in the Indian Ocean, especially in the southeastern Arabian Sea. Further ISO research should also focus on connecting these meteorological and physical oceanographic phenomena to biological processes, such as using ocean color data to observe the oceanic response to the upwelling associated with the 10-20-day ISO. Additionally, this work has emphasized the need for higher resolution satellite observations, particularly of SSS and SLA, the latter of which NASA's upcoming SWOT mission may prove instrumental in accomplishing. High resolution ocean color observations from NASA's Moderate Resolution Imaging Spectroradiometer (MODIS), Visible and Infrared Imager/Radiometer Suite (VIIRS), and the upcoming Plankton, Aerosol, Cloud, and ocean Ecosystem (PACE)

mission will be able to resolve these ISO processes and submesoscale systems. These higher resolution observations will not only help monitor the 3-7-day ISO, but also will also help in a multiparameter analysis and tracking of submesoscale eddies and systems in the Bay of Bengal, which will further our understanding of air-sea dynamics on intraseasonal timescales.

REFERENCES

Aagaard, K., & Carmack, E. C. (1989). The role of sea ice and other fresh water in the Arctic circulation. *Journal of Geophysical Research*, *94*(C10), 14485. https://doi.org/10.1029/jc094ic10p14485

Agarwal, N., Chakraborty, A., Mallick, S., Buckley, J., Shesu, V., & Society, T. O. (2016). Large-scale air-sea coupling processes in the Bay of Bengal using space-borne observations. *Oceanography*, *29*(2), 192–202.

Agarwal, N., Sharma, R., Basu, S., Parekh, A., Sarkar, A., & Agarwal, V. K. (2007). Bay of Bengal summer monsoon 10-20 day variability in sea surface temperature using model and observations. *Geophysical Research Letters*, *34*(6). https://doi.org/10.1029/2007GL029296

Aiguo Dai, & Kevin E. Trenberth. (2002). Estimates of Freshwater Discharge from Continents : Latitudinal and Seasonal Variations. *Journal of Hydrometeorology*, *3*, 660–687. https://doi.org/10.1175/1525-7541(2002)003<0660:EOFDFC>2.0.CO;2

Aiyyer, A. R., & Molinari, J. (2003). Evolution of mixed Rossby-gravity waves in idealized MJO environments. *Journal of the Atmospheric Sciences*, *60*(23), 2837–2855. https://doi.org/10.1175/1520-0469(2003)060<2837:EOMRWI>2.0.CO;2

Ajayamohan, R. S., Annamalai, H., Luo, J. J., Hafner, J., & Yamagata, T. (2011). Poleward propagation of boreal summer intraseasonal oscillations in a coupled model: Role of

internal processes. *Climate Dynamics*, *37*(5), 851–867. https://doi.org/10.1007/s00382-010-0839-6

Aparna, S. G., McCreary, J. P., Shankar, D., & Vinayachandran, P. N. (2012). Signatures of Indian Ocean Dipole and El Niño-Southern Oscillation events in sea level variations in the Bay of Bengal. *Journal of Geophysical Research: Oceans*, *117*(10), 1–13. https://doi.org/10.1029/2012JC008055

Assassi, C., Morel, Y., Vandermeirsch, F., Chaigneau, A., Pegliasco, C., Morrow, R., et al. (2016). An Index to Distinguish Surface- and Subsurface-Intensified Vortices from Surface Observations. *Journal of Physical Oceanography*, *46*, 2529–2552. https://doi.org/10.1175/JPO-D-15-0122.1

Atlas, R., Oceanic, N., Hoffman, R. N., & Leidner, S. M. (2009). Development of a new cross-calibrated, multi-platform (CCMP) ocean surface wind product. *AMS 13th Conference on Integrated Observing and Assimilation Systems for Atmosphere, Oceans, and Land Surface (IOAS-AOLS)*, (January).

Atlas, R., Hoffman, R. N., Ardizzone, J., Leidner, S. M., Jusem, J. C., Smith, D. K., & Gombos, D. (2011). A cross-calibrated, multiplatform ocean surface wind velocity product for meteorological and oceanographic applications. *Bulletin of the American Meteorological Society*, *92*(2), 157–174. https://doi.org/10.1175/2010BAMS2946.1

Bernard, B., Madec, G., Penduff, T., Molines, J. M., Treguier, A. M., Le Sommer, J., et al. (2006). Impact of partial steps and momentum advection schemes in a global ocean circulation model at eddy-permitting resolution. *Ocean Dynamics*, *56*(5–6), 543–567. https://doi.org/10.1007/s10236-006-0082-1

Bhat, G. S., Gadgil, S., Hareesh Kumar, P. V., Kalsi, S. R., Madhusoodanan, P., Murty, V. S. N., et al. (2001). BOBMEX: The Bay of Bengal Monsoon experiment. *Bulletin of the American Meteorological Society*, *82*(10), 2217–2243. https://doi.org/10.1175/1520-0477(2001)082<2217:BTBOBM>2.3.CO;2

de Boyer Montégut, C., Madec, G., Fischer, A. S., Lazar, A., & Iudicone, D. (2004). Mixed layer depth over the global ocean: An examination of profile data and a profile-based climatology. *Journal of Geophysical Research C: Oceans*, *109*(12), 1–20. https://doi.org/10.1029/2004JC002378

Burns, J. M., Bulusu, S., & Murty, V. S. N. (2017). On the dynamics of the Sri Lanka Dome in the Bay of Bengal. *Journal of Geophysical Research : Oceans*, *122*(9), 7737–7750. https://doi.org/10.1002/2017jc012986

Carton, J. A., Chepurin, G. A., Chen, L., & Grodsky, S. A. (2018). Improved global net surface heat flux. *Journal of Geophysical Research: Oceans*, *123*(5), 3144–3163. https://doi.org/10.1002/2017JC013137

Carton, J. A., Chepurin, G. A., & Chen, L. (2018). SODA3: A new ocean climate reanalysis. *Journal of Climate*, *31*(17), 6967–6983. https://doi.org/10.1175/JCLI-D-17-0149.1

Chacko, K.V., Hareesh Kumar, P.V., Ramesh Kumar, M. R., Mathew, B., & Bannur, V. M. (2012). A Note on Arabian Sea Warm Pool and its Possible Relation with Monsoon Onset over Kerala. *Journal of Scientific and Research Publications, 2(12), 286-289.*

Chaigneau, A., Gizolme, A., & Grados, C. (2008). Mesoscale eddies off Peru in altimeter records: Identification algorithms and eddy spatio-temporal patterns. *Progress in Oceanography*, *79*(2–4), 106–119. https://doi.org/10.1016/j.pocean.2008.10.013

Chaigneau, A., Eldin, G., & Dewitte, B. (2009). Eddy activity in the four major upwelling systems from satellite altimetry (1992-2007). *Progress in Oceanography*, *83*(1–4), 117–123. https://doi.org/10.1016/j.pocean.2009.07.012

Chanut, J., Barnier, B., Large, W., Debreu, L., Penduff, T., Molines, J. M., & Mathiot, P. (2008). Mesoscale Eddies in the Labrador Sea and Their Contribution to Convection and Restratification. *Journal of Physical Oceanography*, *38*(8), 1617–1643. https://doi.org/10.1175/2008JPO3485.1

Chatterjee, A., Shankar, D., McCreary, J. P., & Vinayachandran, P. N. (2013). Yanai waves in the western equatorial Indian Ocean. *Journal of Geophysical Research: Oceans*, *118*(3), 1556–1570. https://doi.org/10.1002/jgrc.20121

Chatterjee, P., & Goswami, B. N. (2004). Structure, genesis and scale selection of the tropical quasi-biweekly mode. *Quarterly Journal of the Royal Meteorological Society*, *130*(599 PART B), 1171–1194. https://doi.org/10.1256/qj.03.133

Chelton, D. B., Deszoeke, R. A., Schlax, M. G., El Naggar, K., & Siwertz, N. (1998). Geographical Variability of the First Baroclinic Rossby Radius of Deformation. *Journal of Physical Oceanography*, *28*, 443–460. https://doi.org/10.1017/CBO9781107415324.004

Chen, G., Wang, D., & Hou, Y. (2012). The features and interannual variability mechanism of mesoscale eddies in the Bay of Bengal. *Continental Shelf Research*, *47*, 178–185. https://doi.org/10.1016/j.csr.2012.07.011

Chen, G., Han, W., Li, Y., McPhaden, M. J., Chen, J., Wang, W., & Wang, D. (2017). Strong Intraseasonal Variability of Meridional Currents near 5 ° N in the Eastern Indian Ocean : Characteristics and Causes. *Journal of Physical Oceanography*, *47*, 979–998. https://doi.org/10.1175/JPO-D-16-0250.1

Chen, T.-C., & Chen, J.-M. (1993). The 10–20-Day Mode of the 1979 Indian Monsoon: Its Relation with the Time Variation of Monsoon Rainfall. *Monthly Weather Review*. https://doi.org/10.1175/1520-0493(1993)121<2465:TDMOTI>2.0.CO;2

Cheng, X., Xie, S. P., McCreary, J. P., Qi, Y., & Du, Y. (2013). Intraseasonal variability of sea surface height in the Bay of Bengal. *Journal of Geophysical Research: Oceans*, *118*(2), 816–830. https://doi.org/10.1002/jgrc.20075

Cheng, X., McCreary, J. P., Qiu, B., Qi, Y., & Du, Y. (2017). Intraseasonal-to-semiannual variability of sea-surface height in the eastern, equatorial Indian Ocean and southern Bay of Bengal. *Journal of Geophysical Research: Oceans*, *122*, 4051– 4067. https://doi.org/10.1002/2016JC012662

Cheng, X., McCreary, J. P., Qiu, B., Qi, Y., Du, Y., & Chen, X. (2018). Dynamics of Eddy Generation in the Central Bay of Bengal. *Journal of Geophysical Research: Oceans*, *123*(9), 6861–6875. https://doi.org/10.1029/2018JC014100

Cui, W., Yang, J., & Ma, Y. (2016). A statistical analysis of mesoscale eddies in the Bay of Bengal from 22–year altimetry data. *Acta Oceanologica Sinica*, *35*(11), 16–27. https://doi.org/10.1007/s13131-016-0945-3

Cullather, R. I., & Bosilovich, M. G. (2011). The moisture budget of the polar atmosphere in MERRA. *Journal of Climate*, *24*(11), 2861–2879. https://doi.org/10.1175/2010JCLI4090.1

Cuxart, J., Bougeault, P., & Redelsperger, J. L. (2000). A turbulence scheme allowing for mesoscale and large-eddy simulations. *Quarterly Journal of the Royal Meteorological Society*, *126*(562), 1–30. https://doi.org/10.1002/qj.49712656202

D'Addezio, J. M., Subrahmanyam, B., Nyadjro, E. S., & Murty, V. S. N. (2015). Seasonal Variability of Salinity and Salt Transport in the Northern Indian Ocean. *Journal of Physical Oceanography*. https://doi.org/10.1175/jpo-d-14-0210.1

D'Addezio, J. M., & Subrahmanyam, B. (2018). Evidence of organized intraseasonal convection linked to ocean dynamics in the Seychelles–Chagos thermocline ridge. *Climate Dynamics*, *0*(0), 0. https://doi.org/10.1007/s00382-018-4087-5

Dandapat, S., & Chakraborty, A. (2016). Mesoscale Eddies in the Western Bay of Bengal as Observed from Satellite Altimetry in 1993-2014: Statistical Characteristics, Variability and Three-Dimensional Properties. *IEEE Journal of Selected Topics in Applied Earth Observations and Remote Sensing*, *9*(11), 5044–5054. https://doi.org/10.1109/JSTARS.2016.2585179

Deb, S. K., Kishtawal, C. M., Kumar, P., Kiran Kumar, A. S., Pal, P. K., Kaushik, N., & Sangar, G. (2016). Atmospheric Motion Vectors from INSAT-3D: Initial quality assessment and its impact on track forecast of cyclonic storm NANAUK. *Atmospheric Research*, *169*, 1–16. https://doi.org/10.1016/j.atmosres.2015.09.010

Deepa, R., & Oh, J. H. (2014). Indian summer monsoon onset vortex formation during recent decades. *Theoretical and Applied Climatology*, *118*, 237–249. https://doi.org/10.1007/s00704-013-1057-z

Ducet, N., Le Traon, P. Y., & Reverdin, G. (2000). Global high-resolution mapping of ocean circulation from TOPEX/Poseidon and ERS-1 and -2. *Journal of Geophysical Research: Oceans*, *105*(C8), 19477–19498. https://doi.org/10.1029/2000jc900063

Durand, F., Shankar, D., de Boyer Montégut, C., Shenoi, S. S. C., Blanke, B., & Madec, G. (2007). Modeling the barrier-layer formation in the southeastern Arabian Sea. *Journal of Climate*, *20*(10), 2109–2120. https://doi.org/10.1175/JCLI4112.1

Durand, M., Fu, L. L., Lettenmaier, D. P., Alsdorf, D. E., Rodriguez, E., & Esteban-Fernandez, D. (2010). The surface water and ocean topography mission: Observing terrestrial surface water and oceanic submesoscale eddies. *Proceedings of the IEEE*, *98*(5), 766–779. https://doi.org/10.1109/JPROC.2010.2043031

Entekhabi, D., Njoku, E. G., O'Neill, P. E., Kellogg, K. H., Crow, W. T., Edelstein, W. N., et al. (2010). The soil moisture active passive (SMAP) mission. *Proceedings of the IEEE*, *98*(5), 704–716. https://doi.org/10.1109/JPROC.2010.2043918

Fore, A. G., Yueh, S. H., Tang, W., Stiles, B. W., & Hayashi, A. K. (2016). Combined Active/Passive Retrievals of Ocean Vector Wind and Sea Surface Salinity With SMAP. *IEEE Transactions on Geoscience and Remote Sensing*, *54*(12), 7396–7404. https://doi.org/10.1109/TGRS.2016.2601486

Fu, X., Wang, B., Waliser, D. E., & Tao, L. (2007). Impact of Atmosphere–Ocean Coupling on the Predictability of Monsoon Intraseasonal Oscillations. *Journal of the Atmospheric Sciences*, *64*(1), 157–174. https://doi.org/10.1175/JAS3830.1

Gadgil, S. (2003). The Indian Monsoon and Its Variability. *Annual Review of Earth and Planetary Sciences*, *31*(1), 429–467. https://doi.org/10.1146/annurev.earth.31.100901.141251

Gadgil, S., & Asha, G. (1992). Intraseasonal Variation of the Summer Monsoon I:Observational Aspects. *Journal of the Meteorological Society of Japan*.

Gadgil, S., & Joseph, P. V. (2003). On breaks of the Indian monsoon. *Proceedings of the Indian Academy of Sciences, Earth and Planetary Sciences*, *112*(4), 529–558. https://doi.org/10.1007/BF02709778

Gangopadhyay, A., Bharat Raj, G. N., Chaudhuri, A. H., Babu, M. T., & Sengupta, D. (2013). On the nature of meandering of the springtime western boundary current in the Bay of Bengal. *Geophysical Research Letters*, *40*(10), 2188–2193. https://doi.org/10.1002/grl.50412

Gerken, T., Babel, W., Herzog, M., Fuchs, K., Sun, F., Ma, Y., et al. (2015). High-resolution modelling of interactions between soil moisture and convective

development in a mountain enclosed Tibetan Basin. *Hydrology and Earth System Sciences*, *19*(9), 4023–4040. https://doi.org/10.5194/hess-19-4023-2015

Gill, A. E. (1982). Atmosphere - ocean dynamics. *NEW YORK, U.S.A., ACADEMIC PRESS INC., 1982*.

Gimeno, L., Drumond, A., Nieto, R., Trigo, R. M., & Stohl, A. (2010). On the origin of continental precipitation. *Geophysical Research Letters*. https://doi.org/10.1029/2010GL043712

Gimeno, L., Dominguez, F., Nieto, R., Trigo, R., Drumond, A., Reason, C. J. C., et al. (2016). Major Mechanisms of Atmospheric Moisture Transport and Their Role in Extreme Precipitation Events. *Annual Review of Environment and Resources*, *41*(1), 117–141. https://doi.org/10.1146/annurev-environ-110615-085558

Girishkumar, M. S., Ravichandran, M., & Han, W. (2013). Observed intraseasonal thermocline variability in the Bay of Bengal. *Journal of Geophysical Research: Oceans*, *118*(7), 3336–3349. https://doi.org/10.1002/jgrc.20245

Girishkumar, M. S., Joseph, J., Thangaprakash, V. P., Pottapinjara, V., & McPhaden, M. J. (2017). Mixed Layer Temperature Budget for the Northward Propagating Summer Monsoon Intraseasonal Oscillation (MISO) in the Central Bay of Bengal. *Journal of Geophysical Research: Oceans*, *122*(11), 8841–8854. https://doi.org/10.1002/2017JC013073

Gopalan, A. K. S., Krishna, V. V. G., Ali, M. M., & Sharma, R. (2000). Detection of Bay of Bengal eddies from TOPEX and in situ observations. *Journal of Marine Research*, *58*, 721–734.

Goswami, B. N., & Chakravorty, S. (2017). *Dynamics of the Indian Summer Monsoon Climate* (Vol. 1). https://doi.org/10.1093/acrefore/9780190228620.013.613

Goswami, B. N., Sengupta, D., & Suresh Kumar, G. (1998). Intraseasonal oscillations and interannual variability of surface winds over the Indian monsoon region. *Proceedings of the Indian Academy of Sciences, Earth and Planetary Sciences*. https://doi.org/10.1007/BF02842260

Goswami, B. N., Ajayamohan, R. S., Xavier, P. K., & Sengupta, D. (2003). Clustering of synoptic activity by Indian summer monsoon intraseasonal oscillations. *Geophysical Research Letters*, *30*(8), 1–4. https://doi.org/10.1029/2002GL016734

Grinsted, A., Moore, J. C., & Jevrejeva, S. (2004). Application of the cross wavelet transform and wavelet coherence to geophysical time series. *Nonlinear Processes in Geophysics*, *11*, 561–566.

Grunseich, G., & Subrahmanyam, B. (2013). Detection of the Madden-Julian Oscillation in the Indian Ocean From Satellite Altimetry. *IEEE Geoscience and Remote Sensing Letters*, *10*(3), 441–445. https://doi.org/10.1109/LGRS.2012.2208261

Grunseich, G., Subrahmanyam, B., & Arguez, A. (2011). Influence of the Madden-Julian Oscillation on sea surface salinity in the Indian Ocean. *Geophysical Research Letters*, *38*(17), 1–9. https://doi.org/10.1029/2011GL049047

Grunseich, G., Subrahmanyam, B., Murty, V. S. N., & Giese, B. S. (2011). Sea surface salinity variability during the Indian Ocean Dipole and ENSO events in the tropical Indian Ocean. *Journal of Geophysical Research: Oceans*, *116*(11), 1–14. https://doi.org/10.1029/2011JC007456

Grunseich, G., Subrahmanyam, B., & Wang, B. (2013). The madden-julian oscillation detected in aquarius salinity observations. *Geophysical Research Letters*, *40*(20), 5461–5466. https://doi.org/10.1002/2013GL058173

Guan, B., Lee, T., Hlakides, D. J., & Waliser, D. E. (2014). Aquarius surface salinity and the Madden-Julian Oscillation: The role of salinity in surface layer density and potential energy. *Geophysical Prospecting*, *41*(April), 6413–6419. https://doi.org/10.1002/2014GL061184.

Gulakaram, V. S., Vissa, N. K., & Bhaskaran, P. K. (2018). Role of mesoscale eddies on atmospheric convection during summer monsoon season over the Bay of Bengal: A case study. *Journal of Ocean Engineering and Science*, *3*(4), 343–354. https://doi.org/10.1016/j.joes.2018.11.002

Hacker, P., Firing, E., Hummon, J., & Gordon, L. (1998). Bay of Bengal currents during the northeast monsoon monsoon is compared to the output of a high-resolution , Description. *Geophysical Research Letters*, *25*(15), 2769–2772.

Han, W., Liu, W. T., & Lin, J. (2006). Impact of atmospheric submonthly oscillations on sea surface temperature of the tropical Indian Ocean. *Geophysical Research Letters*, *33*(3), 6–9. https://doi.org/10.1029/2005GL025082

Hendon, H. H., Liebmann, B., & Glick, J. D. (1998). Oceanic Kelvin waves and the Madden-Julian oscillation. *Journal of the Atmospheric Sciences*, *55*(1), 88–101. https://doi.org/10.1175/1520-0469(1998)055<0088:OKWATM>2.0.CO;2

Huang, N. E., & Wu, Z. (2008). a Review on Hilbert-Huang Transform : Method and Its Applications. *Reviews of Geophysics*, *46*(2007), 1–23. https://doi.org/10.1029/2007RG000228.1.INTRODUCTION

Huffman, G. J., Adler, R. F., Arkin, P., Chang, A., Ferraro, R., Gruber, A., et al. (1997). The Global Precipitation Climatology Project (GPCP) Combined Precipitation Dataset. *Bulletin of the American Meteorological Society*, *78*(1), 5–20. Retrieved from http://dx.doi.org/10.1175%2F1520-0477%281997%29078%3C0005%3ATGPCPG%3E2.0.CO%3B2

India Meteorological Department. (2019). Monsoon: 2019 Daily Rainfall Series. Retrieved from http://www.imd.gov.in/pages/monsoon_main.php.

Jensen, T. G. (2001). Arabian Sea and Bay of Bengal exchange of salt and tracers in an ocean model. *Geophysical Research Letters*, *28*(20), 3967–3970. https://doi.org/10.1029/2001GL013422

Joseph, P. V., & Sijikumar, S. (2004). Intraseasonal variability of the low-level jet stream of the Asian summer monsoon. *Journal of Climate*, *17*(7), 1449–1458. https://doi.org/10.1175/1520-0442(2004)017<1449:IVOTLJ>2.0.CO;2

Karmakar, A., Parekh, A., Chowdary, J. S., & Gnanaseelan, C. (2018). Inter comparison of Tropical Indian Ocean features in different ocean reanalysis products. *Climate Dynamics*, *51*, 119–141. https://doi.org/10.1007/s00382-017-3910-8

Kikuchi, K., & Wang, B. (2009). Global perspective of the quasi-biweekly oscillation. *Journal of Climate*, *22*(6), 1340–1359. https://doi.org/10.1175/2008JCLI2368.1

Kikuchi, K., Wang, B., & Kajikawa, Y. (2012). Bimodal representation of the tropical intraseasonal oscillation. *Climate Dynamics*, *38*(9–10), 1989–2000. https://doi.org/10.1007/s00382-011-1159-1

Krishnamurti, T. N., & Ardanuy, P. (1980). The 10 to 20-day westward propagating mode and "Breaks in the Monsoons." *Tellus*. https://doi.org/10.3402/tellusa.v32i1.10476

Krishnamurti, T. N., & Bhalme, H. N. (1976). Oscillations of a Monsoon System. Part I. Observational Aspects. *Journal of the Atmospheric Sciences*. https://doi.org/10.1175/1520-0469(1976)033<1937:OOAMSP>2.0.CO;2

Krishnamurti, T. N., Jana, S., Krishnamurti, R., Kumar, V., Deepa, R., Papa, F., et al. (2017). Monsoonal intraseasonal oscillations in the ocean heat content over the surface layers of the Bay of Bengal. *Journal of Marine Systems*, *167*, 19–32. https://doi.org/10.1016/j.jmarsys.2016.11.002

Kumar, B., & Chakraborty, A. (2011). Movement of seasonal eddies and its relation with cyclonic heat potential and cyclogenesis points in the Bay of Bengal. *Natural Hazards*, *59*(3), 1671–1689. https://doi.org/10.1007/s11069-011-9858-9

Kurian, J., & Vinayachandran, P. N. (2007). Mechanisms of formation of the Arabian Sea mini warm pool in a high-resolution Ocean General Circulation Model. *Journal of Geophysical Research: Oceans*, *112*(5), 1–14. https://doi.org/10.1029/2006JC003631

Large, W. G., & Yeager, S. G. (2009). The global climatology of an interannually varying air - Sea flux data set. *Climate Dynamics*, *33*(2–3), 341–364. https://doi.org/10.1007/s00382-008-0441-3

Lawrence, D. M., & Webster, P. J. (2002). The boreal summer intraseasonal oscillation: Relationship between northward and eastward movement of convection. *Journal of the Atmospheric Sciences*, *59*(9), 1593–1606. https://doi.org/10.1175/1520-0469(2002)059<1593:TBSIOR>2.0.CO;2

Legg, S., McWilliams, J., & Gao, J. (2002). Localization of Deep Ocean Convection by a Mesoscale Eddy. *Journal of Physical Oceanography*, *28*(5), 944–970. https://doi.org/10.1175/1520-0485(1998)028<0944:lodocb>2.0.co;2

Levine, R. C., & Turner, A. G. (2012). Dependence of Indian monsoon rainfall on moisture fluxes across the Arabian Sea and the impact of coupled model sea surface temperature biases. *Climate Dynamics*, *38*, 2167–2190. https://doi.org/10.1007/s00382-011-1096-z

Levitus, S., Antonov, J. I., Boyer, T. P., Baranova, O. K., Garcia, H. E., Locarnini, R. A., et al. (2012). World ocean heat content and thermosteric sea level change (0-2000m), 1955-2010. *Geophysical Research Letters*, *39*(10), 1–5. https://doi.org/10.1029/2012GL051106

Li, K., Liu, Y., Li, Z., Yang, Y., Feng, L., Khokiattiwong, S., et al. (2018). Impacts of ENSO on the Bay of Bengal Summer Monsoon Onset via Modulating the Intraseasonal Oscillation. *Geophysical Research Letters*, *45*(10), 5220–5228. https://doi.org/10.1029/2018GL078109

Li, Y., Han, W., & Lee, T. (2015). Intraseasonal sea surface salinity variability in the equatorial Indo-Pacific Ocean induced by Madden-Julian oscillations. *Journal of Geophysical Research: Oceans*, *120*, 2233–2258. https://doi.org/10.1002/2014JC010647

Li, Y., Han, W., Hu, A., Meehl, G. A., & Wang, F. (2018). Multidecadal changes of the upper Indian ocean heat content during 1965-2016. *Journal of Climate*, *31*(19), 7863–7884. https://doi.org/10.1175/JCLI-D-18-0116.1

Li, Y., Han, W., Wang, W., & Ravichandran, M. (2016). Intraseasonal variability of sst and precipitation in the Arabian Sea during the Indian summer monsoon: Impact of ocean mixed layer depth. *Journal of Climate*, *29*(21), 7889–7910. https://doi.org/10.1175/JCLI-D-16-0238.1

Li, Y., Han, W., Wang, W., Zhang, L., & Ravichandran, M. (2018). The Indian summer monsoon intraseasonal oscillations in CFSv2 forecasts: Biases and importance of improving air-sea interaction processes. *Journal of Climate*, *31*(14), 5351–5370. https://doi.org/10.1175/JCLI-D-17-0623.1

Madden, R. A., & Julian, P. R. (1971). Detection of a 40-50 Day Oscillation in the Zonal Wind in the Tropical Pacific. *Journal of the Atmospheric Sciences*, *28*, 702–708.

Madec, G. (2011). NEMO Ocean Engine: version 3.3, (27), 1–332. Retrieved from http://www.nemo-ocean.eu/About-NEMO/Reference-manuals%5Cnpapers2://publication/uuid/73E7FF17-99BE-4B10-A823-0037C823EF6E

Masunaga, H. (2007). Seasonality and regionality of the Madden-Julian Oscillation, Kelvin wave, and equatorial Rossby wave. *Journal of the Atmospheric Sciences*, *64*(12), 4400–4416. https://doi.org/10.1175/2007JAS2179.1

Matthews, A. J. (2008). Primary and successive events in the Madden-Julian Oscillation, *134*(April), 439–453. https://doi.org/10.1002/qj.224

McCreary, J P, Han, W., Shankar, D., & Shetye, S. R. (1996). Dynamics of the East India Coastal Current 2. Numerical Solutions. *Journal of Geophysical Research*, *101*(C6), 13993–14010.

McCreary, J. P., Kundu, P. K., & Molinari, R. L. (1993). A numerical investigation of dynamics, thermodynamics and mixed-layer processes in the Indian Ocean. *Progress in Oceanography*, *31*(3), 181–244. https://doi.org/10.1016/0079-6611(93)90002-U

Miyama, T., McCreary, J. P., Sengupta, D., & Senan, R. (2006). Dynamics of biweekly oscillations in the equatorial Indian Ocean. *Journal of Physical Oceanography*, *36*(5), 827–846. https://doi.org/10.1175/JPO2897.1

Momin, I. M., Mitra, A. K., Mahapatra, D. K., Rajagopal, E. N., & Harenduprakash, L. (2013). Indian Ocean simulation results from NEMO global ocean model. *Indian Journal of Marine Sciences*, *42*, 425–430.

Murakami, M. (1976). Analysis of Summer Monsoon Fluctuations over India. *Journal of the Meteorological Society of Japan*, *54*(1), 15–31. https://doi.org/10.2151/jmsj1965.54.1_15

Murty, V. S. N., Suryanarayana, A., & Rao, D. P. (1993). Current structure and volume transport across 12N in the Bay of Bengal. *Indian Journal of Marine Sciences*, *22*(March), 12–16.

Murty, V. S. N., Subrahmanyam, B., Tilvi, V., & O'Brien, J. J. (2004). A new technique for the estimation of sea surface salinity in the tropical Indian Ocean from OLR. *Journal of Geophysical Research C: Oceans*, *109*(12), 1–26. https://doi.org/10.1029/2003JC001928

Nagamani, P. V., Ali, M. M., Goni, G. J., Udaya Bhaskar, T. V. S., Mccreary, J. P., Weller, R. A., et al. (2016). Heat content of the Arabian Sea Mini Warm Pool is increasing. *Atmospheric Science Letters*, *17*(1), 39–42. https://doi.org/10.1002/asl.596

Neema, C. P., Hareeshkumar, P. V., & Babu, C. A. (2012). Characteristics of Arabian Sea mini warm pool and Indian summer monsoon. *Climate Dynamics*, *38*(9–10), 2073–2087. https://doi.org/10.1007/s00382-011-1166-2

Nienhaus, M. J., Subrahmanyam, B., & Murty, V. S. N. (2012). Altimetric Observations and Model Simulations of Coastal Kelvin Waves in the Bay of Bengal. *Marine Geodesy*, *35*(SUPPL. 1), 190–216. https://doi.org/10.1080/01490419.2012.718607

Nuncio, M., & Kumar, S. P. (2012). Life cycle of eddies along the western boundary of the Bay of Bengal and their implications. *Journal of Marine Systems*, *94*, 9–17. https://doi.org/10.1016/j.jmarsys.2011.10.002

Nyadjro, E. S., & Subrahmanyam, B. (2016). Spatial and temporal variability of central Indian Ocean salinity fronts observed by SMOS. *Remote Sensing of Environment*, *180*, 146–153. https://doi.org/10.1016/j.rse.2016.02.049

Nyadjro, E. S., Subrahmanyam, B., & Shriver, J. F. (2011). Seasonal variability of salt transport during the Indian Ocean monsoons. *Journal of Geophysical Research: Oceans*. https://doi.org/10.1029/2011JC006993.

Nyadjro, E. S., Subrahmanyam, B., Murty, V. S. N., & Shriver, J. F. (2012). The role of salinity on the dynamics of the Arabian Sea mini warm pool. *Journal of Geophysical Research: Oceans*, *117*(9), 1–12. https://doi.org/10.1029/2012JC007978

Ordoñez, P., Gallego, D., Ribera, P., Peña-Ortiz, C., & García-Herrera, R. (2016). Tracking the Indian summer monsoon onset back to the preinstrument period. *Journal of Climate*, *29*(22), 8115–8127. https://doi.org/10.1175/JCLI-D-15-0788.1

Ortega, S., Webster, P. J., Toma, V., & Chang, H. R. (2017). Quasi-biweekly oscillations of the South Asian monsoon and its co-evolution in the upper and lower troposphere. *Climate Dynamics*, *49*(9–10), 3159–3174. https://doi.org/10.1007/s00382-016-3503-y

Pai, D. S., & Rajeevan, M. (2009). Summer monsoon onset over Kerala : *Journal of Earth System Science*, *118*(2), 1–13. https://doi.org/10.1007/s12040-009-0020-y

Paris, M. L., & Subrahmanyam, B. (2018). Role of El Niño Southern Oscillation (ENSO) Events on Temperature and Salinity Variability in the Agulhas Leakage Region. *Remote Sensing*, *10*(127), 1–19. https://doi.org/10.3390/rs10010127

Patnaik, K. V. K. R. K., Maneesha, K., Sadhuram, Y., Prasad, K. V. S. R., Ramana, T. V, & Rao, V. B. (2014). East India Coastal Current induced eddies and their interaction with tropical storms over Bay of Bengal. *Journal of Operational Oceanography*, *7*(1), 58–68. https://doi.org/10.1080/1755876X.2014.11020153

Penduff, T., Juza, M., Brodeau, L., Smith, G. C., Barnier, B., Molines, J. M., et al. (2010). Impact of global ocean model resolution on sea-level variability with emphasis on interannual time scales. *Ocean Science*, *6*(1), 269–284. https://doi.org/10.5194/os-6-269-2010

Pegliasco, C., Chaigneau, A., & Morrow, R. (2015). Main eddy vertical structures observed in the four major Eastern Boundary Upwelling Systems. *Journal of Geophysical Research: Oceans*, *120*(9), 6008–6033. https://doi.org/10.1002/2015JC010950

Penduff, Thierry, Sommer, J. Le, Barnier, B., Tréguier, A., Penduff, T., Sommer, J. Le, et al. (2007). Influence of numerical schemes on current-topography interactions in 1 / 4 ° global ocean simulations To cite this version : HAL Id : hal-00331131.

Pillai, P. A., & Chowdary, J. S. (2016). Indian summer monsoon intra-seasonal oscillation associated with the developing and decaying phase of El Niño. *International Journal of Climatology*, *36*(4), 1846–1862. https://doi.org/10.1002/joc.4464

Prend, C. J., Seo, H., Weller, R. A., & Farrar, J. T. (2018). Impact of freshwater plumes on intraseasonal upper ocean variability in the Bay of Bengal. *Deep-Sea Research Part II: Topical Studies in Oceanography*, (November). https://doi.org/10.1016/j.dsr2.2018.09.007

Ramachandran, S., Tandon, A., Mackinnon, J., Lucas, A. J., Pinkel, R., Waterhouse, A. F., et al. (2018). Submesoscale Processes at Shallow Salinity Fronts in the Bay of Bengal: Observations during the Winter Monsoon. *Journal of Physical Oceanography*, *48*(3), 479–509. https://doi.org/10.1175/JPO-D-16-0283.1

Rao, R. R., & Sivakumar, R. (1999). On the possible mechanisms of the evolution of a mini-warm pool during the pre-summer monsoon season and the genesis of onset vortex in the south-eastern Arabian Sea. *Quarterly Journal of the Royal Meteorological Society*. https://doi.org/10.1256/smsqj.55502

Rao, R. R., Girish Kumar, M. S., Ravichandran, M., Rao, A. R., Gopalakrishna, V. V., & Thadathil, P. (2010). Interannual variability of Kelvin wave propagation in the wave guides of the equatorial Indian Ocean, the coastal Bay of Bengal and the southeastern Arabian Sea during 1993-2006. *Deep-Sea Research Part I: Oceanographic Research Papers*, *57*(1), 1–13. https://doi.org/10.1016/j.dsr.2009.10.008

Rao, R. R., Jitendra, V., GirishKumar, M. S., Ravichandran, M., & Ramakrishna, S. S. V. S. (2015). Interannual variability of the Arabian Sea Warm Pool: observations and governing mechanisms. *Climate Dynamics*, *44*, 2119–2136. https://doi.org/10.1007/s00382-014-2243-0

Rao, S. A., Saha, S. K., Pokhrel, S., Sundar, D., Dhakate, A. R., Mahapatra, S., et al. (2011). Modulation of SST, SSS over northern Bay of Bengal on ISO time scale. *Journal of Geophysical Research: Oceans*, *116*(9), 1–11. https://doi.org/10.1029/2010JC006804

Reynolds, R. W., Smith, T. M., Liu, C., Chelton, D. B., Casey, K. S., & Schlax, M. G. (2007). Daily high-resolution-blended analyses for sea surface temperature. *Journal of Climate*, *20*(22), 5473–5496. https://doi.org/10.1175/2007JCLI1824.1

Roman-Stork, H. L., Subrahmanyam, B., & Murty, V. S. N. (2019). Quasi-biweekly oscillations in the Bay of Bengal in observations and model simulations. *Deep-Sea Research Part II: Topical Studies in Oceanography*, (June), 104609. https://doi.org/10.1016/j.dsr2.2019.06.017

Roundy, P. E. (2008). Analysis of convectively coupled Kelvin waves in the Indian ocean MJO. *Journal of the Atmospheric Sciences*, *65*(4), 1342–1359. https://doi.org/10.1175/2007JAS2345.1

Roundy, P. E., Schreck, C. J., & Janiga, M. A. (2009). Contributions of convectively coupled equatorial Rossby waves and Kelvin waves to the real-time multivariate MJO indices. *Monthly Weather Review*, *137*(1), 469–478. https://doi.org/10.1175/2008MWR2595.1

Sadhuram, Y., Maneesha, K., & Murty, T. V. R. (2012). Intensification of Aila (May 2009) due to a warm core eddy in the north Bay of Bengal. *Natural Hazards*, *63*(3), 1515–1525. https://doi.org/10.1007/s11069-011-9837-1

Samson, G., Masson, S., Durand, F., Terray, P., Berthet, S., & Jullien, S. (2017). Roles of land surface albedo and horizontal resolution on the Indian summer monsoon biases in a coupled ocean–atmosphere tropical-channel model. *Climate Dynamics*. https://doi.org/10.1007/s00382-016-3161-0

Sanchez-Franks, A., Kent, E. C., Matthews, A. J., Webber, B. G. M., Peatman, S. C., & Vinayachandran, P. N. (2018). Intraseasonal variability of air-sea fluxes over the Bay of Bengal during the Southwest Monsoon. *Journal of Climate*, *31*(17), 7087–7109. https://doi.org/10.1175/JCLI-D-17-0652.1

Sankar, S., Kumar, M. R. R., & Reason, C. (2011). On the relative roles of El Nino and Indian Ocean Dipole events on the Monsoon Onset over Kerala. *Theoretical and Applied Climatology*, *103*(3–4), 359–374. https://doi.org/10.1007/s00704-010-0306-7

Schott, F. A., & McCreary, J. P. (2001). The monsoon circulation of the Indian Ocean. *Progress in Oceanography*, *51*(1), 1–123. https://doi.org/10.1016/S0079-6611(01)00083-0

Senan, R., Sengupta, D., & Goswami, B. N. (2003). Intraseasonal “monsoon jets” in the equatorial Indian Ocean. *Geophysical Research Letters*, *30*(14), 1–4. https://doi.org/10.1029/2003GL017583

Sengupta, D., Parampil, S. R., Bhat, G. S., Murty, V. S. N., Babu, V. R., Sudhakar, T., et al. (2008). Warm pool thermodynamics from the Arabian Sea Monsoon Experiment (ARMEX). *Journal of Geophysical Research: Oceans*. https://doi.org/10.1029/2007JC004623

Sengupta, D., Senan, R., & Goswami, B. N. (2001). Origin of intraseasonal variability of circulation in the tropical central Indian Ocean. *Geophysical Research Letters*, *28*(7), 1267–1270. https://doi.org/10.1029/2000GL012251

Sengupta, D., & Ravichandan, M. (2001). Oscillations of the Bay of Bengal SST during the 1998 summer monsoon. *Geophys. Res. Lett.*, *28*(10), 2033–2036. https://doi.org/10.1029/2000GL012548

Sengupta, D., Goswami, B. N., & Senan, R. (2001). Atmosphere during the Asian Summer Monsoon /,• ASST. *Geophysical Research Letters*, *28*(21), 4127–4130.

Sengupta, D, Senan, R., Murty, V. S. N., & Fernando, V. (2004). A biweekly mode in the equatorial Indian Ocean. *Journal of Geophysical Research C: Oceans*, *109*(10), 1–12. https://doi.org/10.1029/2004JC002329

Sérazin, G., Penduff, T., Grégorio, S., Barnier, B., Molines, J.-M., & Terray, L. (2015). Intrinsic Variability of Sea Level from Global Ocean Simulations: Spatiotemporal Scales. *Journal of Climate*, *28*(10), 4279–4292. https://doi.org/10.1175/jcli-d-14-00554.1

Serreze, M. C., Barrett, A. P., Slater, A. G., Woodgate, R. A., Aagaard, K., Lammers, R. B., et al. (2006). The large-scale freshwater cycle of the Arctic. *Journal of Geophysical Research: Oceans*, *111*(11), 1–19. https://doi.org/10.1029/2005JC003424

Shankar, D., McCreary, J. P., Han, W., & Shetye, S. R. (1996). Dynamics of the East India Coastal Current 1. Analytic solutions forced by interior Ekman pumping and local

alongshore winds. *Journal of Geophysical Research C: Oceans*, *101*(C6), 13975–13991. https://doi.org/10.1029/96JC00559

Shankar, D., & Shetye, S. R. (1997). On the dynamics of the Lakshadweep high and low. *Journal of Geophysical Research*, *102*(C6), 12,551-12,562.

Shankar, D., Vinayachandran, P. N., & Unnikrishnan, A. S. (2002). The monsoon currents in the north Indian Ocean. *Progress in Oceanography*, *52*(1), 63–120. https://doi.org/10.1016/S0079-6611(02)00024-1

Sharmila, S., Pillai, P. A., Joseph, S., Roxy, M., Krishna, R. P. M., Chattopadhyay, R., et al. (2013). Role of ocean-atmosphere interaction on northward propagation of Indian summer monsoon intra-seasonal oscillations (MISO). *Climate Dynamics*, *41*(5–6), 1651–1669. https://doi.org/10.1007/s00382-013-1854-1

Shenoi, S. S. C., Shankar, D., & Shetye, S. R. (2002). Differences in heat budgets of the near-surface Arabian Sea and Bay of Bengal: Implications for the summer monsoon. *Journal of Geophysical Research*, *107*(C6), 5-1-5–14. https://doi.org/10.1029/2000JC000679

Shenoi, S., Shankar, D., Gopalakrishna, V., & Durand, F. (2005). Role of ocean in the genesis and annihilation of the core of the warm pool in the southeastern Arabian Sea. *Mausam*, *56*(1), 147–160.

Shenoi, S. S. C., Shankar, D., & Shetye, S. R. (1999). On the sea surface temperature high in the Lakshadweep Sea before the onset of the southwest monsoon. *Journal of Geophysical Research: Oceans*, *104*(C7), 15703–15712. https://doi.org/10.1029/1998jc900080

Sherin, V. R., Durand, F., Gopalkrishna, V. V., Anuvinda, S., Chaitanya, A. V. S., Bourdallé-Badie, R., & Papa, F. (2018). Signature of Indian Ocean Dipole on the western boundary current of the Bay of Bengal. *Deep-Sea Research Part I: Oceanographic Research Papers*, *136*(June), 91–106. https://doi.org/10.1016/j.dsr.2018.04.002

Shetye, S. R., Gouveia, A. D., Shankar, D., Shenoi, S. S. C., Vinayachandran, P. N., Sundar, D., et al. (1996). Hydrography and circulation in the western Bay of Bengal during the northeast monsoon. *Journal of Geophysical Research C: Oceans*, *101*(C6), 14011–14025. https://doi.org/10.1029/95JC03307

Shoup, C. G., Subrahmanyam, B., & Roman-Stork, H. L. (2019). Madden-Julian Oscillation-Induced Sea Surface Salinity Variability as Detected in Satellite-Derived Salinity. *Geophysical Research Letters*, *46*(16), 9748–9756. https://doi.org/10.1029/2019gl083694

Smedsrud, L. H., Ingvaldsen, R., Nilsen, J. E. Ø., & Skagseth, Ø. (2010). Heat in the Barents Sea: Transport, storage, and surface fluxes. *Ocean Science*, *6*(1), 219–234. https://doi.org/10.5194/os-6-219-2010

Sobel, A. H., & Maloney, E. D. (2000). Effect of ENSO and the MJO on western North Pacific tropical cyclones. *Geophysical Research Letters*, *27*(12), 1739–1742. https://doi.org/10.1029/1999GL011043

Souza, J. M. A. C., De Boyer Montégut, C., & Le Traon, P. Y. (2011). Comparison between three implementations of automatic identification algorithms for the quantification and characterization of mesoscale eddies in the South Atlantic Ocean. *Ocean Science*, *7*(3), 317–334. https://doi.org/10.5194/os-7-317-2011

Sprintall, J., Gordon, A. L., Murtugudde, R., & Susanto, R. D. (2000). A semiannual Indian Ocean forced Kelvin wave observed in the Indonesian seas in May 1997. *Journal of Geophysical Research*, *105*(C7), 17,217-17,230.

Sreenivas, P., Gnanaseelan, C., & Prasad, K.V.S.R. (2012). Influence of El Niño and Indian Ocean Dipole on sea level variability in the Bay of Bengal. Glob. Planet. Change. 80-81, 215-225. https://doi.org/10.1016/j.gloplacha.2011.11.001.

Straub, K. H. (2013). MJO initiation in the real-time multivariate MJO index. *Journal of Climate*, *26*(4), 1130–1151. https://doi.org/10.1175/JCLI-D-12-00074.1

Subrahmanyam, B., Trott, C. B., & Murty, V. S. N. (2018). Detection of Intraseasonal Oscillations in SMAP Salinity in the Bay of Bengal. *Geophysical Research Letters*, (2011), 1–9. https://doi.org/10.1029/2018GL078662

Subrahmanyam, B., Trott, C. B., & Murty, V. S. N. (2018). Detection of Intraseasonal Oscillations in SMAP Salinity in the Bay of Bengal. *Geophysical Research Letters*, (2011), 1–9. https://doi.org/10.1029/2018GL078662

Subrahmanyam, B., Roman-Stork, H.L., & Murty, V. S. N. (2020). Response of the Bay of Bengal to 3-7-day synoptic oscillations during the southwest mosnoon of 2019, *Journal of Geophysical Research: Oceans*, 125, e2020JC016200, https://doi.org/10.1029/2020JC016200

Suhas, E., Neena, J. M., & Goswami, B. N. (2013). An Indian monsoon intraseasonal oscillations (MISO) index for real time monitoring and forecast verification. *Climate Dynamics*, *40*(11–12), 2605–2616. https://doi.org/10.1007/s00382-012-1462-5

Le Traon, P. Y., Nadal, F., & Ducet, N. (1998). An improved mapping method of multisatellite altimeter data. *Journal of Atmospheric and Oceanic Technology*, *15*(2), 522–534. https://doi.org/10.1175/1520-0426(1998)015<0522:AIMMOM>2.0.CO;2

Trott, C. B., Subrahmanyam, B., Chaigneau, A., & Delcroix, T. (2018). Eddy Tracking in the Northwestern Indian Ocean During Southwest Monsoon Regimes. *Geophysical Research Letters*, *45*, 6594–6603. https://doi.org/10.1029/2018GL078381

Trott, C. B., Subrahmanyam, B., Chaigneau, A., & Roman-Stork, H. L. (2019). Eddy-induced Temperature and Salinity Variability in the Arabian Sea. *Geophysical Research Letters*, *46*(5), 2734–2742. https://doi.org/10.1029/2018GL081605

Trott, C. B., & Subrahmanyam, B. (2019). Detection of intraseasonal oscillations in the Bay of Bengal using altimetry. *Atmospheric Science Letters*, 1–10. https://doi.org/10.1002/asl.920

Trott, C. B., Subrahmanyam, B., Roman-Stork, H. L., Murty, V. S. N., & Gnanaseelan, C. (2019). Variability of Intraseasonal Oscillations and Synoptic Signals in Sea Surface

Salinity in the Bay of Bengal. *Journal of Climate*, *32*(20), 6703–6728. https://doi.org/10.1175/jcli-d-19-0178.1

Uppala, S. M., Kållberg, P. W., Simmons, A. J., Andrae, U., da Costa Bechtold, V., Fiorino, M., et al. (2005). The ERA-40 re-analysis. *Quarterly Journal of the Royal Meteorological Society*, *131*(612), 2961–3012. https://doi.org/10.1256/qj.04.176

Vecchi, G. A., & Harrison, D. E. (2002). Monsoon breaks and subseasonal sea surface temperature variability in the Bay of Bengal. *Journal of Climate*, *15*(12), 1485–1493. https://doi.org/10.1175/1520-0442(2002)015<1485:MBASSS>2.0.CO;2

Vinayachandran, P. N., & Shetye, S. R. (1991). The warm pool in the Indian Ocean. *Proceedings of the Indian Academy of Sciences - Earth and Planetary Sciences*. https://doi.org/10.1007/BF02839431

Vinayachandran, P. N., Murty, V. S. N., & Ramesh Babu, V. (2002). Observations of barrier layer formation in the Bay of Bengal during summer monsoon. *Journal of Geophysical Research: Oceans*, *107*(C12), SRF 19-1-SRF 19-9. https://doi.org/10.1029/2001JC000831

Vinayachandran, P. N., Shankar, D., Kurian, J., Durand, F., & Shenoi, S. S. C. (2007). Arabian Sea mini warm pool and the monsoon onset vortex. *Current Science*.

Waliser, D. E., Murtugudde, R., Strutton, P., & Li, J. L. (2005). Subseasonal organization of ocean chlorophyll: Prospects for prediction based on the Madden-Julian Oscillation. *Geophysical Research Letters*, *32*(23), 1–4. https://doi.org/10.1029/2005GL024300

Wang, B., & Xie, X. (1997). A Model for the boreal summer intraseasonal oscillation. *Journal of the Atmospheric Sciences*, *54*(1), 72–86. https://doi.org/10.1175/1520-0469(1997)054<0072:AMFTBS>2.0.CO;2

Wang, B., Webster, P., Kikuchi, K., Yasunari, T., & Qi, Y. (2006). Boreal summer quasi-monthly oscillation in the global tropics. *Climate Dynamics*, *27*(7–8), 661–675. https://doi.org/10.1007/s00382-006-0163-3

Wang, B., Ding, Q., & Joseph, P. V. (2009). Objective Definition of the Indian Summer Monsoon Onset. *Journal of Climate*, *22*, 3303–3316. https://doi.org/10.1175/2008JCLI2675.1

Wang, X., & Chen, G. (2017). Quasi-Biweekly oscillation over the South China sea in late summer: Propagation dynamics and energetics. *Journal of Climate*, *30*(11), 4103–4112. https://doi.org/10.1175/JCLI-D-16-0533.1

Webber, B. G. M., Matthews, A. J., & Heywood, K. J. (2010). A dynamical ocean feedback mechanism for the Madden-Julian Oscillation. *Quarterly Journal of the Royal Meteorological Society*, *136*(648), 740–754. https://doi.org/10.1002/qj.604

Webber, B. G. M., Matthews, A. J., Heywood, K. J., & Stevens, D. P. (2012). Ocean Rossby waves as a triggering mechanism for primary Madden-Julian events. *Quarterly Journal of the Royal Meteorological Society*, *138*(663), 514–527. https://doi.org/10.1002/qj.936

Webster, P. J., Bradley, E. F., Fairall, C. W., Godfrey, J. S., Hacker, P., Houze Jr., R. A., et al. (2002). The Jasmine Pilot Study. *Bulletin of the American Meteorological Society*, *83*(11), 1603-1630+1559. https://doi.org/10.1175/BAMS-83-11-1603

Webster, Peter J., Clark, C., Cherikova, G., Fasullo, J., Han, W., Loschnigg, J., & Sahami, K. (2002). The monsoon as a self-regulating coupled ocean-atmosphere system. *International Geophysics*, *83*(C), 198–219. https://doi.org/10.1016/S0074-6142(02)80168-1

Wheeler, M. C., & Hendon, H. H. (2004). An All-Season Real-Time Multivariate MJO Index: Development of an Index for Monitoring and Prediction. *Monthly Weather Review*, *132*(8), 1917–1932. https://doi.org/10.1175/1520-0493(2004)132<1917:AARMMI>2.0.CO;2

Wheeler, M., & Kiladis, G. N. (1999). Convectively Coupled Equatorial Waves: Analysis of Clouds and Temperature in the Wavenumber–Frequency Domain. *Journal of the Atmospheric Sciences*, *56*(3), 374–399. https://doi.org/10.1175/1520-0469(1999)056<0374:CCEWAO>2.0.CO;2

Wijffels, S. E., Schmitt, R. W., Bryden, H. L., & Stigebrandt, A. (1992). Transport of Freshwater by the Oceans. *Journal of Physical Oceanography*. https://doi.org/10.1175/1520-0485(1992)022<0155:tofbto>2.0.co;2

Wu, Z., & Huang, N. E. (2009). Ensemble Empirical Mode Decomposition :, *1*(1), 1–41. https://doi.org/10.1515/BMT.2010.030

Yi, J., Du, Y., He, Z., & Zhou, C. (2014). Enhancing the accuracy of automatic eddy detection and the capability of recognizing the multi-core structures from maps of sea level anomaly. *Ocean Science*, *10*(1), 39–48. https://doi.org/10.5194/os-10-39-2014

Zhang, C. (2005). Madden-Julian Oscillation. *Reviews of Geophysics*. https://doi.org/10.1029/2004RG000158

Zhang, Y., & Du, Y. (2012). Seasonal variability of salinity budget and water exchange in the northern Indian Ocean from HYCOM assimilation. *Chinese Journal of Oceanology and Limnology*, *30*(6), 1082–1092. https://doi.org/10.1007/s00343-012-1284-7

Zhang, Z., Zhan, Y., Wang, W. (2017). Bay of Bengal salinity stratification and Indian summer monsoon intrasesonal oscillation: 1. Intraseasonal variability and causes. *Journal of Geophysical Research: Oceans*, *122*, 4291–4311. https://doi.org/10.1002/2013JC009262.Received

Zhou, L., & Murtugudde, R. (2013). Impact of Northward-Propagating Intraseasonal Variability on the Onset of Indian Summer Monsoon. *Journal of Climate*, *27*(1992), 126–139. https://doi.org/10.1175/JCLI-D-13-00214.1

Zuo, H., Balmaseda, M. A., Tietsche, S., Mogensen, K., & Mayer, M. (2019). The ECMWF operational ensemble reanalysis-analysis system for ocean and sea ice: A description of the system and assessment. *Ocean Science*, *15*(3), 779–808. https://doi.org/10.5194/os-15-779-2019

APPENDIX A

COPYRIGHT PERMISSIONS

A.1 CHAPTER 2 COPYRIGHT PERMISSIONS

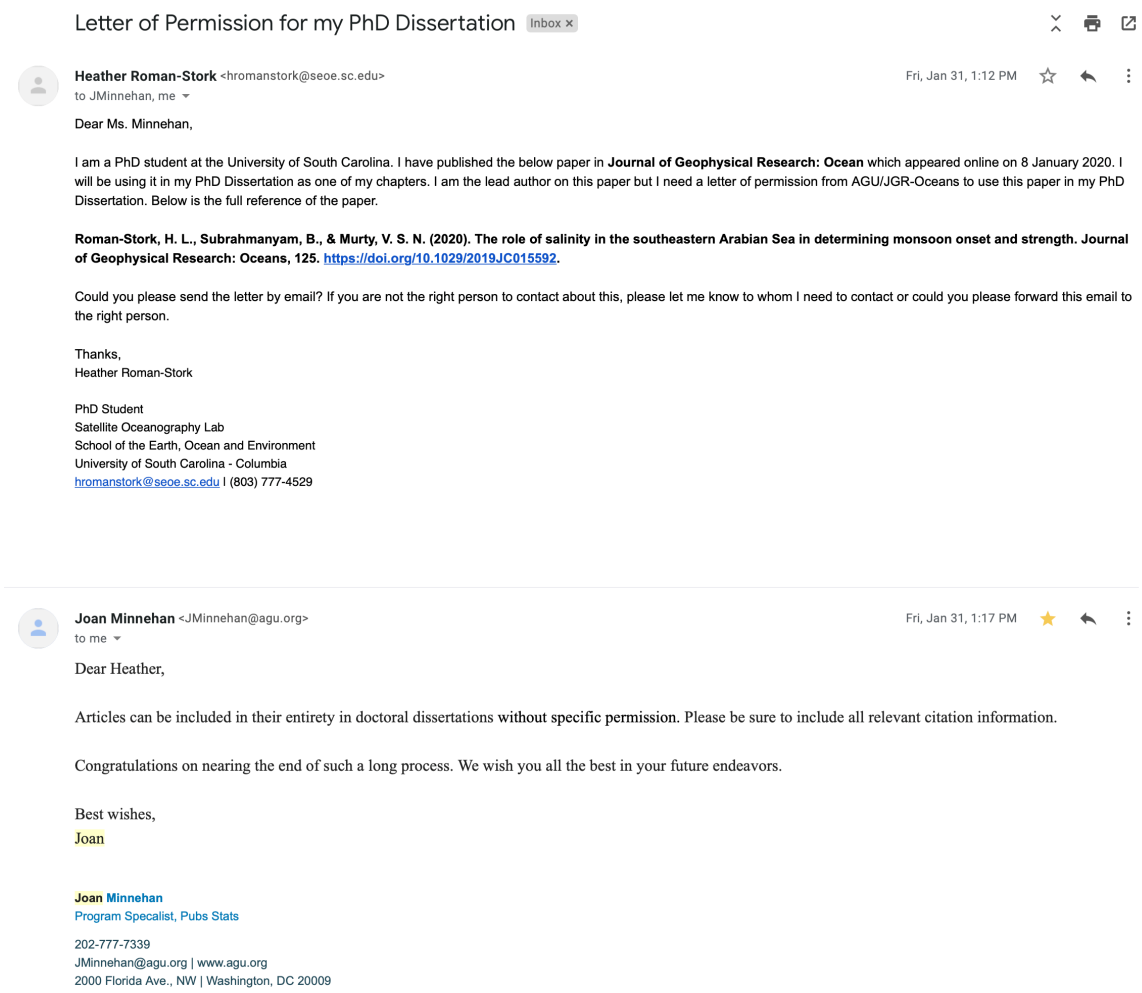

Letter of Permission for my PhD Dissertation Inbox ×

Heather Roman-Stork <hromanstork@seoe.sc.edu> Fri, Jan 31, 1:12 PM
to JMinnehan, me

Dear Ms. Minnehan,

I am a PhD student at the University of South Carolina. I have published the below paper in **Journal of Geophysical Research: Ocean** which appeared online on 8 January 2020. I will be using it in my PhD Dissertation as one of my chapters. I am the lead author on this paper but I need a letter of permission from AGU/JGR-Oceans to use this paper in my PhD Dissertation. Below is the full reference of the paper.

Roman-Stork, H. L., Subrahmanyam, B., & Murty, V. S. N. (2020). The role of salinity in the southeastern Arabian Sea in determining monsoon onset and strength. Journal of Geophysical Research: Oceans, 125. https://doi.org/10.1029/2019JC015592.

Could you please send the letter by email? If you are not the right person to contact about this, please let me know to whom I need to contact or could you please forward this email to the right person.

Thanks,
Heather Roman-Stork

PhD Student
Satellite Oceanography Lab
School of the Earth, Ocean and Environment
University of South Carolina - Columbia
hromanstork@seoe.sc.edu I (803) 777-4529

Joan Minnehan <JMinnehan@agu.org> Fri, Jan 31, 1:17 PM
to me

Dear Heather,

Articles can be included in their entirety in doctoral dissertations without specific permission. Please be sure to include all relevant citation information.

Congratulations on nearing the end of such a long process. We wish you all the best in your future endeavors.

Best wishes,
Joan

Joan Minnehan
Program Specalist, Pubs Stats

202-777-7339
JMinnehan@agu.org | www.agu.org
2000 Florida Ave., NW | Washington, DC 20009

A.2 CHAPTER 3 COPYRIGHT PERMISSIONS

Letter of Permission for my PhD Dissertation Inbox ×

Heather Roman-Stork <hromanstork@seoe.sc.edu> Mon, Feb 24, 10:05 AM
to JMinnehan, bcc: me

Dear Ms. Minnehan,

I am a PhD student at the University of South Carolina. I have published the below paper in **Journal of Geophysical Research: Oceans** which appeared online on 5 February 2020. I will be using it in my PhD Dissertation as one of my chapters. I am the lead author on this paper but I need a letter of permission from AGU/JGR-Oceans to use this paper in my PhD Dissertation. Below is the full reference of the paper.

Roman-Stork, H. L., Subrahmanyam, B., & Trott, C. B. (2020). Monitoring intraseasonal oscillations in the Indian Ocean using satellite observations. Journal of Geophysical Research: Oceans, 125, e2019JC015891. https://doi.org/10.1029/2019JC015891

Could you please send the letter by email? If you are not the right person to contact about this, please let me know to whom I need to contact or could you please forward this email to the right person.

Thanks,
Heather

--
Heather Roman-Stork

PhD Student
Satellite Oceanography Lab
School of the Earth, Ocean and Environment
University of South Carolina - Columbia
hromanstork@seoe.sc.edu | (803) 777-4529

Publications <publications@agu.org> Mon, Feb 24, 10:09 AM
to me

Dear Heather,

Articles can be included in their entirety in doctoral dissertations without specific permission. Please be sure to include all relevant citation information.

Congratulations on nearing the end of such a long process. We wish you all the best in your future endeavors.

Best wishes,
Joan

A.3 CHAPTER 4 COPYRIGHT PERMISSIONS

Copyright Clearance Center | RightsLink®

Home | Help | Email Support | Sign in | Create Account

Quasi-biweekly oscillations in the Bay of Bengal in observations and model simulations

Author: Heather L. Roman-Stork,Bulusu Subrahmanyam,V.S.N. Murty

Publication: Deep Sea Research Part II: Topical Studies in Oceanography

Publisher: Elsevier

Date: October 2019

Please note that, as the author of this Elsevier article, you retain the right to include it in a thesis or dissertation, provided it is not published commercially. Permission is not required, but please ensure that you reference the journal as the original source. For more information on this and on your other retained rights, please visit: https://www.elsevier.com/about/our-business/policies/copyright#Author-rights

BACK | CLOSE WINDOW

A.4 CHAPTER 5 COPYRIGHT PERMISSIONS